CMMoST 2023

7TH INTERNATIONAL CONFERENCE ON

Mechanical Models in Structural Engineering

29 November - 01 December 2023

Escuela de Ingenierías Industriales
Universidad de Málaga

EXTENDED ABSTRACTS

UNIVERSIDAD DE MÁLAGA

UNIVERSIDAD DE GRANADA

UNIVERSIDAD D SEVILLA

7^{th} International Conference on Mechanical Models in Structural Engineering

CMMOST 2023

Extended Abstracts

Málaga, November 2023

Editors

Germán Castillo López	Universidad de Málaga
Luisa María Gil Martín	Universidad de Granada
Enrique Hernández Montes	Universidad de Granada
Margarita Cámara Pérez	Universidad de Sevilla
Víctor Compán Cardiel	Universidad de Sevilla
Andrés Sáez Pérez	Universidad de Sevilla

Coordination and design

Felipe García Sánchez	Universidad de Málaga
Juan Francisco Carbonell Márquez	Universidad de Málaga

Publisher

Manuel Alejandro Fernández Ruiz — Universidad de Málaga
Escuela de Ingenierías Industriales.
Arquitecto Francisco Peñalosa 6, 29071
Málaga (Spain)
mafernandez@uma.es — +34 951 953 281

Printed by: Godel Impresiones Digitales, S.L.
Printed in Spain
ISBN digital: 978-84-19214-79-9
Depósito Legal: GR-1761-2023

UNIVERSIDAD DE MÁLAGA

UNIVERSIDAD DE GRANADA

UNIVERSIDAD D SEVILLA

SPONSORS


cemosa
Ingeniería y Control


Spanish Group
IABSE


MAPEI


málaga
CONVENTION
BUREAU


metro
Málaga


copicentro
www.copicentro.net


COPITI
Colegio Oficial de Peritos e Ingenieros
Técnicos Industriales de Málaga


Colegio Oficial de Ingenieros Industriales
de Andalucía Oriental


ESCUELA DE
INGENIERÍAS
INDUSTRIALES

CONTENTS

ORGANIZATION

Organizers

Germán Castillo López	Universidad de Málaga
Luisa María Gil Martín	Universidad de Granada
Enrique Hernández Montes	Universidad de Granada
Margarita Cámara Pérez	Universidad de Sevilla
Víctor Compán Cardiel	Universidad de Sevilla
Andrés Sáez Pérez	Universidad de Sevilla

Local committee

José Bernardo Beltrán Ramos	Universidad de Málaga
Juan Francisco Carbonell Márquez	Universidad de Málaga
Manuel Alejandro Fernández Ruiz	Universidad de Málaga
Felipe García Sánchez	Universidad de Málaga
José Manuel García-Manrique Ocaña	Universidad de Málaga
Antonio González Herrera	Universidad de Málaga
Antonia María Lima Rodríguez	Universidad de Málaga
José Alberto Martín Romero	Universidad de Málaga
María Eugenia Parrón Rubio	Universidad de Málaga
Consolación Pedraza Rodríguez	Universidad de Málaga
Francisca Pérez García	Universidad de Málaga
Miguel Troyano Moreno	Universidad de Málaga

Conference Secretariat

Juan Francisco Carbonell Márquez	Universidad de Málaga
Germán Castillo López	Universidad de Málaga
Felipe García Sánchez	Universidad de Málaga

Scientific committee

Eduardo Bayo Pérez	Universidad de Navarra, Spain
David Becerra Alonso	Universidad Loyola, Spain
Federico Carlos Buroni Cuneo	Universidad de Sevilla, Spain
Antoni Cladera Bohigas	Universitat de les Illes Balears, Spain
Chiara Coletti	Università di Padova, Italy
Miguel Fernández Ruíz	Universidad Politécnica de Madrid, Spain
Enrique García Macías	Universidad de Granada, Spain
María Dolores Gómez Pulido	Inst. Eduardo Torroja de la Construcción (CSIC), Spain
Salvador Ivorra Chorro	Universidad de Alicante, Spain
Javier Fernando Jiménez Alonso	Universidad de Sevilla, Spain
Mahdi Kioumarsi	Oslo Metropolitan University, Norway
María Jesús Lamela Rey	Universidad de Oviedo, Spain
Manuel López López	Universidade da Coruña, Spain
Antolín Lorenzana Iban	Universidad de Valladolid, Spain
Orlando Maeso Fortuny	Universidad de Las Palmas de Gran Canaria, Spain
Alvaro Magdaleno González	Universidad de Valladolid, Spain
Antonio Marí Bernat	Universidad Politècnica de Catalunya, Spain
Stefano Miccoli	Università della Svizzera Italiana (USI), Italy
Pedro Miguel Sosa	Universitat Politècnica de València, Spain
Iván Muñoz Díaz	Universidad Politécnica de Madrid, Spain
Javier Naranjo Pérez	Universidad Politécnica de Madrid, Spain
Eva Oller Ibars	Universidad Politècnica de Catalunya, Spain
Pablo Pachón García	Universidad de Sevilla, Spain
Michele Palermo	Università di Bologna, Italy
Stravroula Pantazopoulou	University of York, Canada
Miguel José Pereira das Dores Santos de Oliveira	Universidade do Algarve, Portugal
Luis Rodríguez de Tembleque Solano	Universidad de Sevilla, Spain
Esperanza Rodríguez Mayorga	Universidad de Sevilla, Spain
Mario Rodríguez Rodríguez	Universidad Nacional Autónoma de México, Mexico
Manuel Romero García	Universitat Politècnica de València, Spain
Alexander Safonov	Skoltech Faculty, Russia
Roger Señís López	Universidad Politècnica de Catalunya, Spain
José Manuel Soria Herrera	Universidad Politécnica de Madrid, Spain
Alberto Taliercio	Politecnico di Milano, Italy
Antonio Tomás Espín	Universidad Politécnica de Cartagena
Chengxiang Yu	Universidad de Castilla La Mancha, Spain

PREFACE

Málaga, November 2023

Dear Friends and Colleagues,

Welcome to the 7th International Conference on Mechanical Models in Structural Engineering (CMMoST 2023), which will be held at the Escuela de Ingenerías Industriales of the University of Malaga from the 29th of November to the 1st of December 2023 in Málaga (Spain).

CMMoST 2023 is a scientific event organized by the University of Malaga in conjunction with the University of Sevilla and the University of Granada. Previous successful conferences were held in Granada (2011 and 2013), Sevilla (2015), Madrid (2017), Alicante (2019) and Valladolid (2021).

The CMMoST conferences constitute an excellent opportunity for researchers and professionals to present research projects and results and also to share experiences in the areas of Structural Engineering from the identification of innovative applications and novel solution techniques to the development of new mathematical procedures, the study of structural materials or addressing educational issues in technical degrees.

The present document is a collection of extended abstract that were accepted for oral presentation at CMMoST 2023 after peer-review. In this edition 57 contributions from 163 authors are programmed in 14 sessions. Two plenary sessions have also been scheduled.

The aim of this congress has always been to promote research carried out by pre-doctoral researchers and research in educational innovation in the topics of the congress. To this end, two awards have been established, one for the best paper presented by a pre-doctoral author and the other for educational innovation in the topics of the congress. Finally, 11 papers will compete for the award for the best paper presented by a pre-doctoral author and 8 for educational innovation.

We warmly thank all the contributors, authors, plenary speakers and sponsors of the event and wish this conference will offer you fruitful scientific debates and a pleasant stay in the city of Málaga.

The conference organizers would also like to express their gratitude to Vice-Rectorate for Research and Transfer, for its support through the University of Malaga's II Plan for Research, Transfer and Scientific Dissemination.

PLENARY SPEAKERS

Filippo Ubertini

Filippo Ubertini is a Full Professor of Structural Design at the Department of Civil and Environmental Engineering of University of Perugia, Italy, where he teaches Structural Design and Earthquake Engineering and where he coordinates the International PhD Program in Civil and Environmental Engineering. He graduated cum laude in Civil Engineering at University of Perugia in 2005 and received his PhD in Civil Engineering from University of Pavia in 2009. He was visiting scholar at Columbia University in 2008. Author of more than 135 papers published in high impact international journals, his research is mainly focused on structural health monitoring, with emphasis on physics-based methods, smart materials and applications to earthquake engineering, bridge engineering and cultural heritage structures. He is a member of the editorial board of Mechanical Systems and Signal Processing and of other international journals, and he has been member of the scientific committees of several international conferences. He is Vice-President of the Italian "FABRE" Consortium that is leading national research on multilevel risk classification and monitoring of civil infrastructures, with multimillion funding achieved in the last two years. He has been PI of several international and national research projects and plenary/semi-plenary/keynote speaker at prestigious international conferences, including TEST&E 2022, Eurodyn 2020 and CBPAT 2020. Dr. Ubertini has been awarded by the Italian Association for Wind Engineering in 2010 and has received best papers awards in EVACES 2011 and IOMAC 2019.

Plenary title:

Monitoring-based structural prognosis through physics-informed learning strategies: applications in Civil Engineering.

Noemi Jiménez Redondo

MSc Industrial Engineering (Universidad Pontificia Comillas, 1991) and PhD Industrial Engineering (Universidad de Málaga, 1999). In 1991, she joined the Railway Division of Abengoa. In 1992, she started working as a Research Assistant for Instituto de Investigación Tecnológica (Universidad Pontificia Comillas) in the area of electrical energy systems. In 1993 she joined University of Málaga as a lecturer and researcher in the areas of power electronics and electrical energy systems. In 1999 she became Assistant Professor and in 2001 Associate Professor of University of Malaga. In 2007 she joined CEMOSA, as an external consultant, to build a Research & Innovation department. Since January 2010 she is on unpaid leave from the University of Malaga and works full time for CEMOSA as the Director of the Research Innovation department. She has extensive experience in R&I projects funded by the European Commission since 2010, both as coordinator and partner. Her current areas of interest include transport infrastructures (along the whole life cycle), energy efficiency and buildings and smart grids, as well as digitalization and data science in relation to the mentioned fields. She is the coordinator of the European Smart Green Rail Joint Venture (eSGR JV), a Founder Member of Europe's Rail JU and the Representative of eSGR JV in the Governing Board and System and Innovation Programme Board of the referred JU. She is a member of the Steering Committee of the European Construction Technology Platform (ECTP). She is member of the Executive Management Committee of CEMOSA.

Plenary title:

Towards more digital and sustainable infrastructures. CEMOSA's experiences.

Extended Abstracts

A simplified approach for modelling failure propagation of steel structures

Marin, Lorenzo[1]; Makoond, Nirvan[1]; Setiawan, Andri[1]; Buitrago, Manuel[1]; Adam, Jose M.[1]

ABSTRACT

Assessing the likelihood of progressive collapse in buildings resulting from the local failure of individual structural elements is challenging, especially in steel buildings. Engineers invest significant effort in modelling various connections between structural members, requiring detailed 3D solid elements. The complexity and computation time increase exponentially when analysing an entire building instead of local subassemblies. This study presents a practical methodology for modelling steel structures to predict progressive collapse rapidly. It adopts the distributed plastic hinges approach and is able to accurately simulate large deformations expected in collapse scenarios. Suitable experimental tests were selected to validate the proposed methodology, revealing the sensitivity of predictions to modelling assumptions such as the positioning of the hinges, the plastic length of each hinge, the cross-section discretisation and the material definition. Finally, a set of recommendations for the simplified modelling of steel structures is provided for practising engineers working in the progressive collapse domain.

Keywords: Progressive collapse, Steel structures, Modelling strategies, Computational modelling, Simplified approach.

1. INTRODUCTION

In some buildings, the local failure of primary structural components can lead to the progressive collapse of the entire structure if other components cannot withstand additional loads redistributed to them following the initial failure. This has been observed in the collapse of large steel structures like the Plasco Building (Tehran, Iran) and The Twin Towers of the World Trade Center (NY, USA). Engineers usually need to develop detailed and complex models that require high computational costs to analyse such scenarios.

This article proposes a simplified but sufficiently accurate approach to assess the possibility of progressive collapse occurring due to the initial failure of primary structural components. The aim is to reduce computational costs and model complexity while still being able to reliably predict the successive failure of structural components. To achieve this, the numerical models must be able to capture key failure modes of beams and columns under the combined effect of axial loads and bending moments. As such, the predicted structural response using the proposed approach is compared in this article to that observed during suitable experimental tests to verify that the resulting errors are acceptable.

[1] *ICITECH, Universitat Politècnica de València (Spain). lomavil@upv.es (Corresponding author), ncmakoon@upv.es; asetiaw1@upv.es; mabuimo1@upv.es; joadmar@upv.es*

2. SIMPLIFIED MODELLING STRATEGY

The proposed simplified modelling strategy provides insight into the overall behaviour of a building up to the initiation of collapse. Collapse is a systems problem, requiring a good representation of the interaction between elements to assess their failure.

The modelling approach involves representing the steel structure using 2D elements (frame objects). For this study, primary beam-column connections are considered as being entirely rigid (suitable for overstrength joints), while joints between secondary and primary beams are modelled as pinned.

2.1. Fiber Hinges

The nonlinear behaviour during the collapse of a steel building is evaluated by using fiber hinges. These hinges discretize the cross-section into fibers with different constitutive relations, allowing changes in the moment-rotation behaviour and plastic deformation to be considered. Each hinge is defined by its length, by the number of fibers in the cross-section, and by a material constitutive law for each fiber. The hinge length determines the distance over which the element's plastic properties (rotation and axial deformation) develop [1]. The area of each fiber depends on a geometric ratio, which is always kept below five and preferably below three. This ratio indirectly determines the number of fibers making up the section. Additionally, the material's constitutive relationships are established based on the stress-strain curve of steel. Adequate definition of the number of hinges, their location, the material's constitutive relationships, and hinge length are crucial to ensure computational efficiency and accuracy.

2.2. Modelling of columns

As the main vertical loadbearing elements of a framed building, it is of the utmost importance to accurately represent the failure of columns. These elements are subjected to high axial loads, so their failure is governed either by their first buckling mode or by yielding. Experimental tests on two different column specimens with three different pairs of boundary conditions [2] have been chosen to assess the suitability of the proposed approach. The columns have the following characteristics: L_1=1.15 m, $f_{y,1}$=292.3 MPa (height and yield strength of the first type of column specimens); L_2=1.42 m, $f_{y,2}$= 281.3 MPa (height and yield strength of the second type of column specimens). In the first study (Pin-Pin), failure always occurs due to buckling. In the second (Pin-Fix) and third studies (Fix-Fix), the failure is produced by yielding of the steel profile.

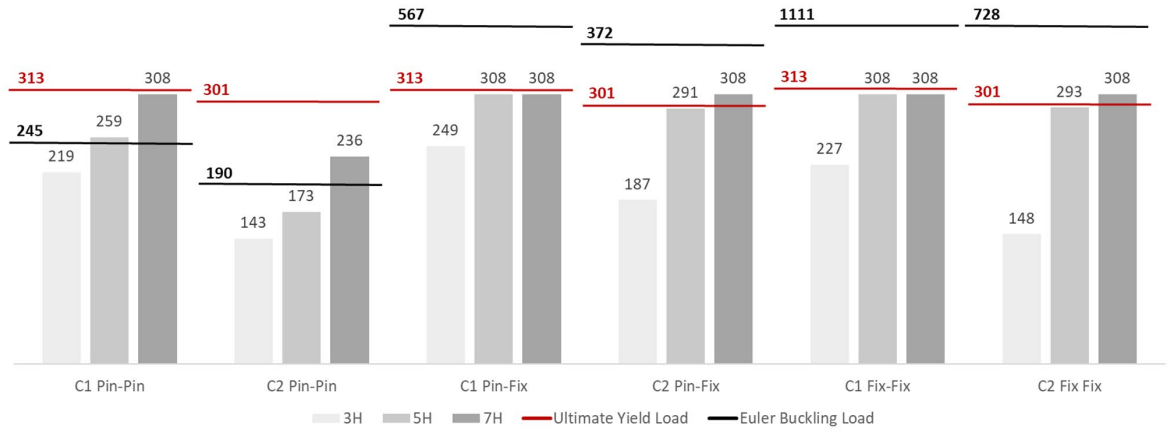

Figure 1. *Comparison of the ultimate load obtained with different simplified models (with 3,5 and 7 fiber hinges along the column height) and those obtained in the experimental tests. All values in kN.*

In Figure 1, different simplified models are evaluated for each of the previously described experimental studies, where the columns have 3, 5, and 7 equally distributed hinges along their height. The results reveal that it is most suitable to use 5 hinges, leading to a relative error of less than 3% for all tests.

2.3. Modelling of beams

The behaviour of beams under extreme events is dominated by catenary actions, unlike normal conditions where bending governs. The experimental test involving the substructure shown in Figure 2 (a) was chosen to evaluate the proposed simulation strategy. The test involved removing the central column and applying a constant downward load until the beam element ruptures. The specimen was designed with rigid joints to avoid connection failure during the test [3].

Appropriate definition of material properties is crucial for the simulation to produce accurate predictions. Parameters such as the yield strength and strain, the stress and strain at the onset of necking, and the ultimate strength and strain must be defined. Ideally, having the complete stress-strain curve of the materials would be best, although this is sometimes not possible. Figure 2 (c) shows the vertical load-displacement relation recorded at the node of the removed column during the experiment compared to those predicted by simplified models with different material properties. All these models were defined with 21 hinges per beam (Figure 2 (b)). The different materials evaluated are: S355 Minimum (defined based on minimum ductility requirements specified in [4]), S355 Global (defined based on mean characteristics of steel elements reported in [3]), and S355 Local (each member defined with its mechanical material characteristics as reported in [3]). Results reveal that knowing at least the average characteristics of the steel used is essential to accurately evaluate the overall behaviour of the entire structure. The S355 local material was chosen for the analysis presented in the remainder of this section since it corresponds to the most accurate representation of the test specimen.

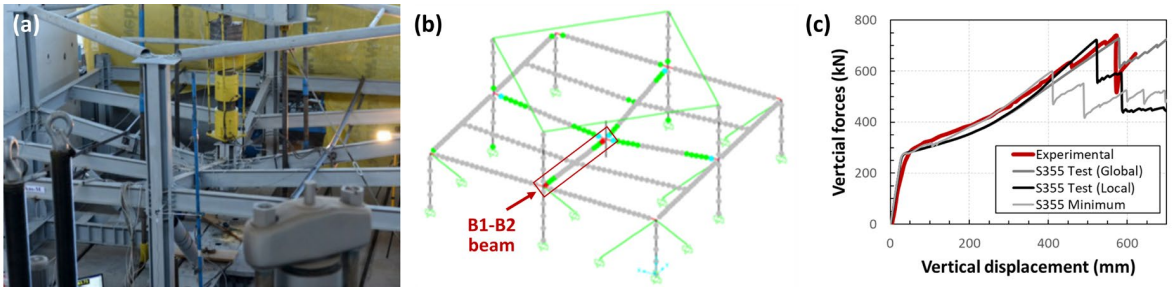

Figure 2. *(a) Specimen at the end of the test [5]; (b) Simplified model at initial rupture of a member; (c) Comparison between experimental and model results in beam B1-B2 with different σ – ε curves.*

It is crucial to evaluate yielding along the entire beam length using a sufficient number of hinges to detect beam failure. This is because of the specific features of cross-sections used for steel structures and the material's remarkable ability to absorb plastic energy. As a result, a section that is yielding experiences substantial deformations that can significantly affect the behaviour of adjacent elements. Figure 3 compares measured responses during the experimental test to the predictions of simplified models with 11, 21, and 31 hinges along each beam length. Specifically, the evolution of vertical forces, bending moments, and axial loads as the vertical displacement of the central beam increases are reported. Based on the results, the 21-hinge model is deemed as being the most suitable choice as it exhibits lower relative errors overall.

It is worth highlighting that the behaviour of the hinges at each end of the beam is particularly important due to stress concentrations that occur at the connection locations. This behaviour depends strongly on the hinge length defined for these hinges. Through iteration, it has been found that it is suitable to set the hinge length at these locations to one-third of the depth of the beam section. As shown for the case of 11 hinges in Figure 3, incorrect results are obtained in the failure evaluation if this adjustment is not implemented.

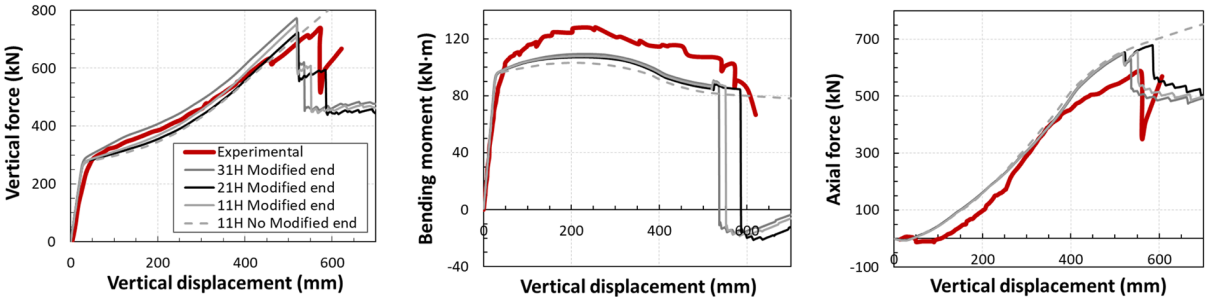

Figure 3. *Comparison between experimental results and model results with different numbers of hinges: 11 (with and without modified end hinges), 21 and 31. Vertical force, bending moment, axial force - vertical displacement, in beam B1-B2 (left to right).*

3. CONCLUSIONS

Evaluating building collapse typically requires complex simulations involving tedious modelling and high computational costs. A simplified modelling approach using fiber hinges has been proposed to assess the failure of steel-framed buildings. It has been found that using 5 hinges in columns and 21 hinges in beams can predict the behaviour of these components with sufficient accuracy during the early stages of collapse. This configuration significantly reduces computational costs, while still providing sufficient accuracy to facilitate a clear and simple identification of the failure initiation.

ACKNOWLEDGEMENTS

This article is part of a project (Endure) that has received funding from the European Research Council (ERC) under the European Union's Horizon 2020 research and innovation programme (Grant Agreement No. 101000396).

REFERENCES

[1] I. Computers and Structures, CSI (2017). Analysis Reference Manual For SAP2000®, ETABS®, SAFE® and CSiBridge®. Berkeley, California, USA.

[2] Johnston, B. G., Cheney,L. T. (1942). Steel columns of rolled wide-flange section progress report no. 2. AISC Research Report, 59, 42-3.

[3] Dinu, F., Marginea, I., Dubina, D., & Petran, I. (2016). Experimental testing and numerical analysis of 3D steel frame system under column loss. *Engineering Structures*, *113*, *59-70*.

[4] CEN European Committee for Standardization (2013). EN 1993-1-1: Eurocode 3 Design of steel structures. Part 1-1: General rules and rules for buildings.

A stochastic data-driven model for the vertical Ground Reaction Force modelling.

García-Terán, José María[1]; Peláez, César[1]; Magdaleno, Álvaro[1]

ABSTRACT

In this work, a statistical approach is proposed to model and generate the vertical component of the GRFs of pedestrians while walking. The method makes use of some recorded data, which are registered by means of a pair of instrumented load insoles, to model the individual steps (left and right separately). Additionally, the double support phase, which occurs when both feet are on the ground, is analyzed and modelled to generate complete vertical GFRs which could be used to simulate the pedestrian action on a structure. The methodology is applied to a registered GRF to obtain the corresponding stochastic model to show its ability to capture the specific walking characteristics of the walking person and its usefulness to generate equivalent virtual GRFs.

Keywords: data-driven model; vertical GRF; human loading; instrumented insoles

1. INTRODUCTION

Walking is a human activity that may cause dynamic issues in slender structures. Due to its stochastic nature, it is challenging to develop accurate models that help to predict the known as ground reaction forces, or GRFs. Several authors have dealt with this problem before. In [1], a comprehensive literature review about the topic is presented, demonstrating the activity during the past decades. Many modern methods [2,3] assume a shape or a function that represent the GRF and propose ways to obtain their parameters to generate realistic virtual forces.

In this work, a novel approach is proposed to develop a stochastic model of the vertical GRFs from a set of recorded data. A pair of low-cost instrumented insoles is used to register the necessary data, which is processed in order to get first a model that reproduce isolated steps and then, concatenate them to form a virtual version of the applied force. A comparison between virtual and real GRFs is provided to show the quality of the model.

2. METHODOLOGY AND RESULTS

In this chapter the methodology from registering the data to generating virtual GRFs is explained together with the results of an application example.

2.1. Data acquisition procedure

The data required to develop the stochastic model are registered with a pair of instrumented insoles (Fig. 1a). They can be managed, configured and data can be collected by means of an ad-hoc app that

[1] *ITAP. Universidad de Valladolid (SPAIN). josemaria.gteran@uva.es (corresponding author); cesar.pelaez@estudiantes.uva.es; alvaro.magdaleno@uva.es*

also helps to wirelessly connect the insoles to the smartphone via Bluetooth. The same app is used to register and export the data. The procedure to gather data is as follows: first, the user puts the insoles inside the shoes; then, the insoles need to be calibrated by following the instructions in the app; finally, the user can start registering data and start walking. For the purposes of this work, at least 100 steps are necessary in order to get stochastically meaningful data. At the end of the recording, data is exported into an ASCII file where two force vectors are included, one per foot, together with the timestamp of every pair of force samples. An example of the recording can be seen in Fig. 1b, where the typical shape of the walking forces can be clearly appreciated.

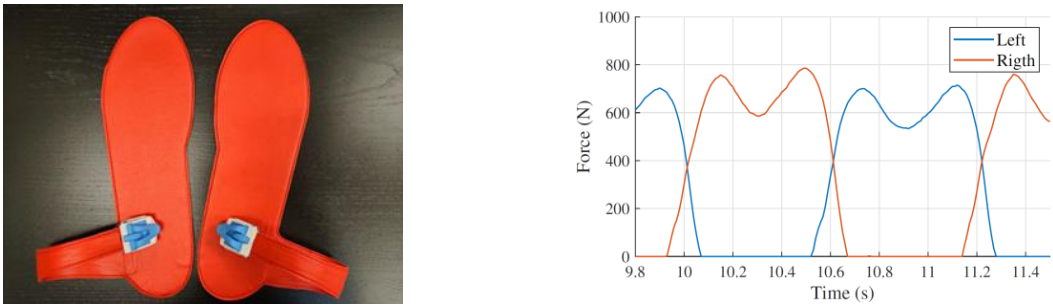

(a) (b)

Figure 1. *(a) Insoles used to register the data; (b) example of registered data*

2.2. Steps modelling

Before obtaining the stochastic model that represents the way a person walks, the registered data is first pre-processed in order to remove possible tendencies the data may have and filter high-frequency noise from both force vectors. Then, an algorithm devoted to detecting when every step starts and ends is run to isolate them. This algorithm is based on a threshold: the first point that exceeds that threshold is saved as the first point of the step (number 5 in Fig. 2a), while the last point before descending under the threshold is kept as the sample at which the step ends (number 4 in Fig. 2b). The whole force vectors are processed, and all the steps are identified in this way, leading to two sets of steps, left and right. Each step has a different number of samples and duration, as shown in Fig. 3.

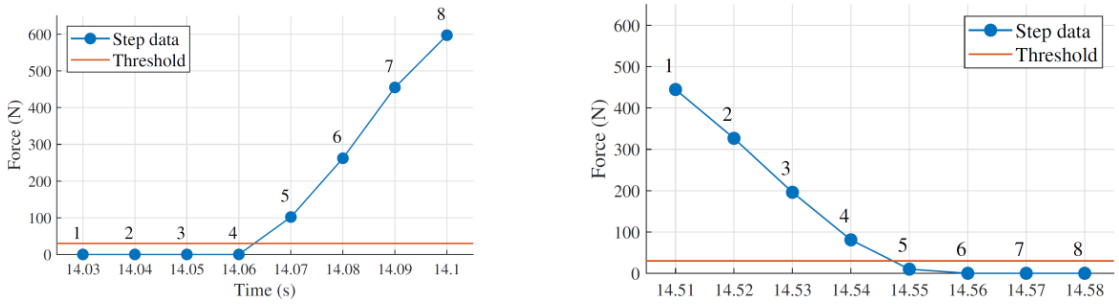

(a) (b)

Figure 2. *Example of detection of a step (a) starting and (b) ending*

Before going on, outlier steps are detected and removed to avoid contaminating the final model. This can be easily done by checking the duration of the steps (removing the outlier values) and some geometrical aspects. In the latter case, every step is verified to have two (and only two) local maxima and one local minimum lying between them. Also, after the normalization and scaling procedure described next, the precise time instants at which these maxima and minimum occur can also be checked to remove some more steps, if needed.

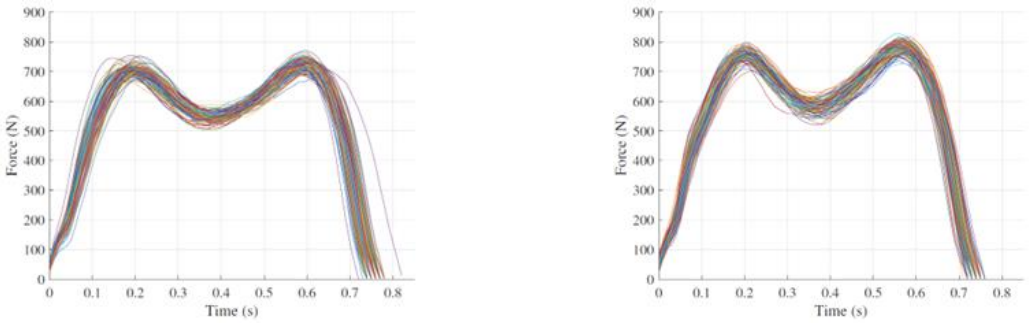

(a) (b)

Figure 3. *Example of detected steps: (a) left steps; (b) right steps*

The time vector of each step is then normalized so they all last 1 s. However, the normalization factor of each step is saved to undo this normalization process when generating new steps. After that, each step is resampled in order to all have the same length, N. In this state, all the steps are described by samples that occur at the same N time instants. The core of the stochastic model consists in treating the force at each normalized instant as a random variable, with its own mean and standard deviation value. The mean values of all the normalized left steps can be seen in Fig. 5a. Moreover, the ensemble of N variables is assumed to follow a multivariate normal distribution that can be modelled through a vector of mean values, one per time instant, and a covariance matrix. This covariance matrix is a square $N \times N$ matrix that represents how each variable is related or varies with the rest ones. The diagonal terms of this matrix represent the variance values of each random variable. Fig. 4 depicts the covariance matrix with colors proportional to their numerical value, as shown. They are associated to the steps of Fig. 3a (left steps) in two different scenarios: $N = 100$ (Fig. 4a) and $N = 400$ (Fig. 4b). As can be seen, the matrix barely changes with the value N, only affecting the resolution of the picture.

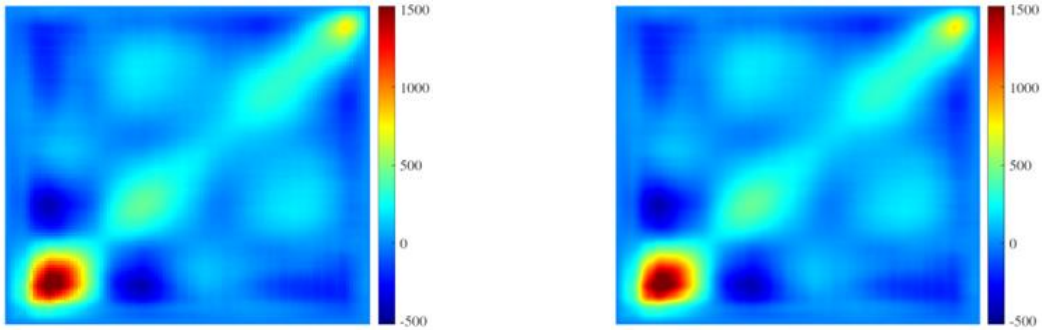

(a) (b)

Figure 4. *Example of covariance matrix for (a)* $N = 100$ *and (b)* $N = 400$

The model formed by the covariance matrix and the mean vector is useful to generate isolated normalized steps, as shown in Fig. 5b. However, in order to complete the whole GRF, the normalization must be undone. To do so, a set of normalization factors can be generated with the mean and standard deviation of the experimental ones, assuming they follow a normal distribution.

2.3. GRF generation

Finally, the virtual steps need to be concatenated in order to form the complete GRF. To do so, the time separating each other must be controlled. To do so, two new random variables are defined: the overlapping time between a right step and a left step, and the same time between a left step and a right step. This two times, where both feet are on the ground, can be directly measured from the experimental data and their mean and standard deviation computed. With those values, a set of new overlapping time values can be generated to form the new vectors.

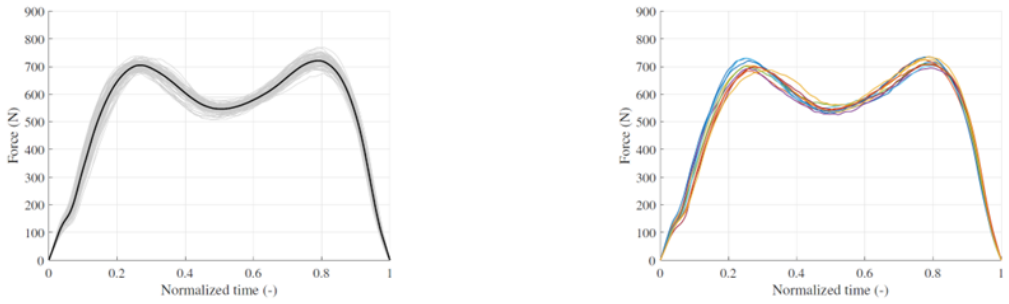

(a) (b)

Figure 5. *(a) Experimental steps with their mean value and (b) generated steps*

The forming procedure is as follows: a step is assigned to start at $t = 0\ s$. It lasts a certain amount of time, ending at $t = t_1$. Then, the first step of the other foot is assigned to start at $t = t_1 - \Delta t_1$, where Δt_1 represents the overlapping time. The procedure is repeated until the desired number of steps have been concatenated. As a result, two vectors of left and right virtual vertical GRFs are obtained and can be resampled if required. Fig. 6 shows the sum of both vectors, i.e., the total vertical GRF both virtual and experimental, for comparison. As can be seen, they are similar to each other.

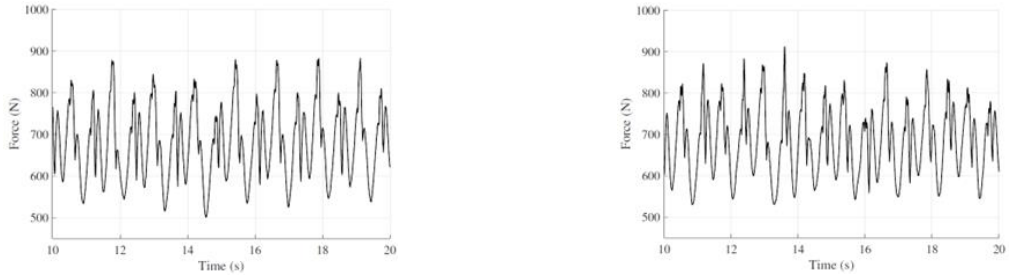

(a) (b)

Figure 6. *(a) Experimental GRF and (b) virtual GRF*

3. CONCLUSIONS

A methodology has been developed to obtain a stochastic model from the experimental data of GRF associated to a walking person. The model first generates isolated normalized steps very similar to the ones used to obtain it and then, concatenates a number of them to form the virtual GRF. This virtual GRF, as shown, is very similar to the one used to develop the model, but not identical due to the stochastic nature of the model that reproduces the stochastic nature of the walking activity.

ACKNOWLEDGEMENTS

The authors wish to acknowledge to the AEI, Spanish Government (10.13039/501100011033), and to "ERDF A way of making Europe", for the partial support through the grant PID2022-140117NB-I00.

REFERENCES

[1] Racic, V., Pavic, A. & Brownjohn, J. M. (2009). Experimental identification and analytical modelling of human walking forces: Literature review. *Journal of Sound and Vibration, 326(1-2), 1-49*.

[2] García-Diéguez, M., Racic, V. & Zapico-Valle, J.L. (2021). Complete statistical approach to modelling variable pedestrian forces induced on rigid surfaces. *Mechanical Systems and Signal Processing, 159, 107800.*

[3] Pancaldi, F., Bassoli, E., Milani, M. & Vincenzi, L. (2021). A statistical approach for modeling individual vertical walking forces. *Applied Sciences, 11(21), 10207.*

Advances in the determination of the mechanical properties of thin membranes through dynamic tests

Lima-Rodriguez, Antonia[1]; Caminos, Luis[1]; Gonzalez-Herrera, Antonio[1]; Garcia-Manrique, Jose[1]

ABSTRACT

The mechanical properties of thin membranes can be determined by non-destructive dynamic tests. When a membrane is subjected to sound pressure, it vibrates according to its natural modes. These vibration modes depend directly on their mechanical characteristics, including Young's modulus. The interaction between sound waves and the membrane (mechanical-acoustic coupling) is complex and requires a thorough study: For this reason, it is necessary to evaluate different aspects that influence in the natural frequencies present in the response. Among these parameters are: the position of the sound source, the measurement points, the geometry and dimensions of the material, the frequency range or the quantities to be measured, among others. This work presents the first results of a new case study with more data of excited frequencies and measurement points, to improve the precision of the results obtained.

Keywords: mechanical properties, membrane, dynamic test, natural frequencies, sound source.

1. INTRODUCCIÓN

Cada vez hay un mayor número de aplicaciones que involucran materiales de membranas delgadas, lo cual aumenta la necesidad de una mejor comprensión de su comportamiento. Hay una amplia cantidad de estudios para conocer las propiedades mecánicas de este tipo de materiales, desde el ensayo de tracción [1], el análisis de curvas tensión-deformación [2] o técnicas de nano y microindentación [3]. Aunque estas pruebas arrojan resultados interesantes, tienen limitaciones debido a su naturaleza destructiva.

En un estudio anterior [4], se determinó una metodología basada en un ensayo dinámico no destructivo, para identificar las frecuencias naturales y relacionarlas con las propiedades mecánicas, en concreto con el módulo de Young del material. En este estudio inicial se utilizó membranas circulares y en la configuración de ensayo la fuente de sonido se colocó a 90º respecto del plano de la membrana y de su centro. Sin embargo, aparecieron dificultades en el ensayo, como la presencia de frecuencias de resonancia asociadas al soporte de la membrana.

El presente estudio tiene como objetivo mejorar la configuración anterior, acotando los resultados. Para ello se realiza un ensayo más complejo, colocando la fuente de sonido a 45º, y rompiendo de esta manera la simetría axial del problema. Esto permite detectar una mayor cantidad de frecuencias en la

[1] *Departamento de Ingeniería Civil, de Materiales y Fabricación. Universidad de Málaga. tlima@uma.es "(Corresponding author). lfcaminos@uma.es. agh@uma.es. josegmo@uma.es.*

respuesta de la membrana. También se utiliza un segundo micrófono para analizar la influencia de las resonancias asociadas al entorno del experimento.

2. MÉTODO DE TRABAJO

En el ensayo experimental, una fuente de sonido estimula a una membrana circular de 15 mm de diámetro, del material que se desea ensayar. Los parámetros del experimento están basados en recomendaciones de investigaciones previas. La Fig. 1 muestra un esquema de la configuración del ensayo.

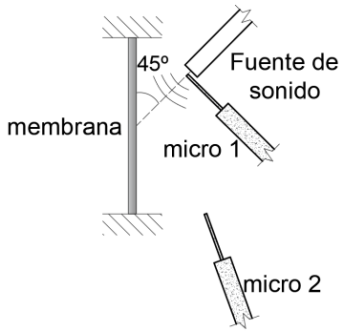

Figura 1. *Configuración del ensayo.*

Para obtener los datos experimentales, se utilizó el mismo equipo que en estudios anteriores [4], usándose un vibrómetro láser Doppler para medir la respuesta de velocidad de puntos de la membrana. En este trabajo se muestran datos del centro de la membrana y de un punto adicional en el soporte, para medir la excitación del conjunto. El micrófono 2 se utilizó para monitorear el sonido ambiental.

Las respuestas de los puntos estudiados se analizan mediante la representación de las funciones de respuesta en frecuencia (FRF) en velocidad, respecto a la presión que se aplica en la fuente de sonido. También se aplica el método de ajuste circular, basado en los diagramas de Nyquist, para obtener las frecuencias de resonancia presentes en la respuesta. Una vez obtenidas las frecuencias de resonancia de la membrana de forma experimental, éstas se pueden relacionar de forma analítica, con las propiedades mecánicas del material, en concreto el módulo de Young, y obtener de esta manera su valor [4,5].

3. RESULTADOS OBTENIDOS

En la Fig. 2 están representadas las FRF en velocidad para el centro de la membrana y un punto en el soporte. El rango de frecuencias mostradas va desde 0 a 4 kHz.

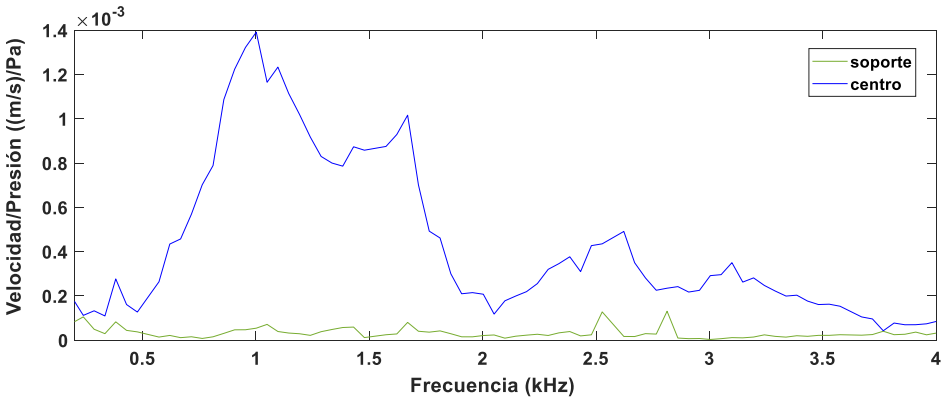

Figura 2. *Función de transferencia en velocidad.*

Se observa en la figura que no es fácil identificar los valores exactos de los picos por la existencia de varios picos cercanos. Los primeros picos se pueden tomar entorno a los valores: 400 Hz, 1000 Hz y 1600 Hz.

En la Fig. 3, se ha representado la presión del micrófono 2 respecto a la presión del micrófono 1, en función de la frecuencia.

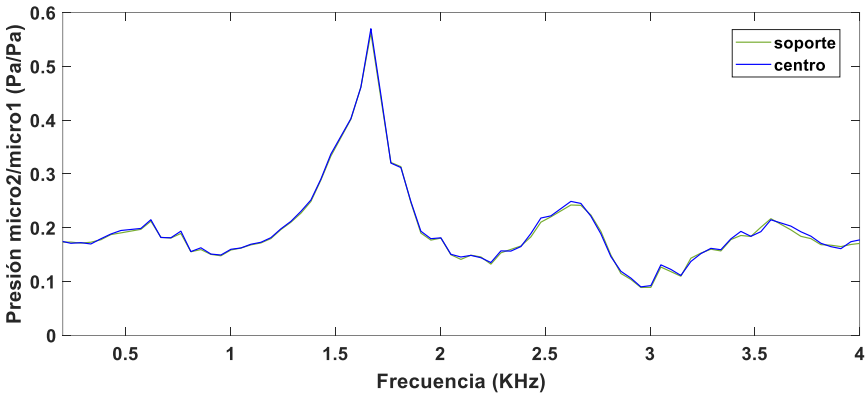

Figura 3. *Presión en el micrófono 2 respecto a la presión en el micrófono 1.*

En esta figura se observa que los primeros picos de la gráfica corresponden, aproximadamente, con los valores: 1600 Hz y 2600 Hz. Estas son frecuencias asociadas al entorno acústico.

En la Fig. 4 están representados los diagramas de Nyquist para el punto central y el soporte. Se observa que los puntos siguen formas de círculos.

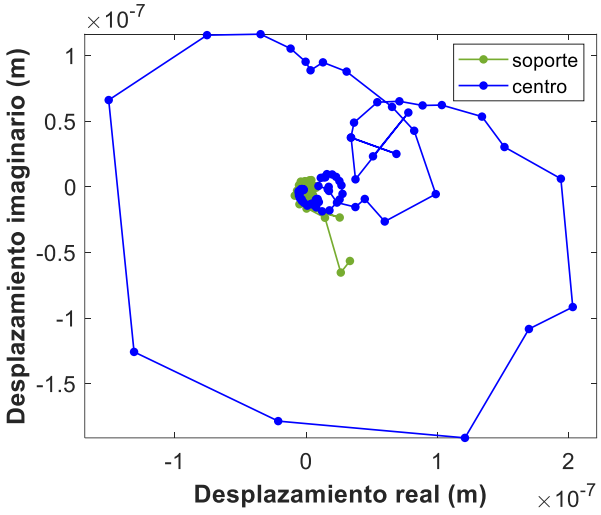

Figura 3. *Diagrama de Nyquist.*

Las frecuencias obtenidas con el método de Nyquist para las frecuencias de hasta 2600 Hz, están dadas en la Tabla 1. También se han incluido las frecuencias asociadas al entorno acústico.

Tabla 1. Frecuencias obtenidas con el método de ajuste circular y frecuencias del entorno acústico

Frecuencias (Hz) centro	Frecuencias (Hz) soporte	Frecuencias (Hz) micrófono 2
393.52	358.63	1600
1026.98	1064.81	2600
1117.94	1440.34	
1551.65	1663.60	
1650.94	1845.37	
2038.74	2805.32	
2599.59	2815.71	

Desechando las frecuencias del soporte y del entorno, las que se pueden asociar a la membrana serían las de color azul en la tabla, cuyos valores están en torno a 1000 Hz y 2000 Hz. Aunque la frecuencia en torno a 1000 Hz está presente en el soporte, aparece doble en la respuesta de la membrana, y se puede considerar como frecuencia natural de la misma.

4. CONCLUSIONES

Después de analizar los resultados, se puede concluir que, con una mayor complejidad en el ensayo se obtiene más información, aunque también se complica la interpretación de los resultados. Con una configuración más compleja que en las del estudio anterior [4], se pueden obtener más datos válidos, y estos podrían arrojar resultados más precisos para el cálculo del módulo de Young.

También se analiza la influencia de las resonancias asociadas al soporte del sistema y al entorno, captadas por un segundo micrófono. Se concluye que las frecuencias asociadas al soporte y al entorno acústico están presentes en la respuesta de la membrana, y estos valores tienen que ser descartados.

AGRADECIMIENTOS

Agradecimiento a la Universidad de Málaga por la financiación recibida.

REFERENCIAS

[1] Ding, X., Ko, W. H., & Mansour, J. M. (1990). Residual stress and mechanical properties of boron-doped p+-silicon films. *Sensors and Actuators: A. Physical, 23(1–3), 866–871*.

[2] Benson-Martin, J., Zammaretti, P., Bilic, G., Schweizer, T., Portmann-Lanz, B., Burkhardt, T., … Ochsenbein-Kölble, N. (2006). The Young's modulus of fetal preterm and term amniotic membranes. *European Journal of Obstetrics and Gynecology and Reproductive Biology, 128(1–2), 103–107*.

[3] Huang, G., Daphalapurkar, N. P., Gan, R. Z., & Lu, H. (2008). A method for measuring linearly viscoelastic properties of human tympanic membrane using nanoindentation. *Journal of Biomechanical Engineering, 130(1)*.

[4] Lima-Rodriguez, A., Garcia-Manrique, J., Dong, W., & Gonzalez-Herrera, A. (2022). A Novel Methodology to Obtain the Mechanical Properties of Membranes by Means of Dynamic Tests. *Membranes, Vol 12*.

[5] Timoshenko, S. (1928). Vibration problems in engineering. New York.

AI-driven approach for automated OMA of large-scale structures

Hernández-González, Israel Alejandro[1]; García-Macías, Enrique[1]

ABSTRACT

The pressing challenge posed by the management of ageing infrastructure has motivated the growing adoption of Structural Health Monitoring (SHM) systems as an effective means for preventive maintenance. Specifically, SHM systems exploiting Operational Modal Analysis (OMA) are gaining popularity owing to their non-destructive nature and minimum intrusiveness. Nonetheless, their widespread adoption for the management of infrastructural systems faces efficiency hurdles, including large computational demands and substantial expert intervention. In this context, recent advances in artificial intelligence (AI) offer vast potential for revolutionizing various sectors across Industry and Science, including the possibility of developing new smart maintenance methods. In this light, this work introduces an innovative AI-based Blind Source Separation (BSS) technique for fast OMA of structures. The ability of the proposed approach for conducting fast automated OMA with minimum computational demand is demonstrated through a real-world bridge, the Montecastelli Bridge in Italy.

Keywords: Artificial Intelligence, Blind Source Identification, Operational Modal Analysis, Structural Health Monitoring.

1. INTRODUCTION AND THEORETICAL FUNDAMENTALS

Output-only OMA represents a continuous area of development with diverse applications in Structural Engineering. Over the past decades, research efforts have focused on the development of automated OMA procedures compatible with long-term SHM, Stochastic Subspace Identification (SSI) methods emerging as the most successful ones [1]. However, both in their covariance-driven or data-driven versions, SSI approaches are computationally demanding and require substantial expert intervention. Such limitations hamper their widespread use for SHM of infrastructural networks at a regional scale. In this context, recent advancements in AI hold vast potential for revolutionizing various sectors across Science and Technology, including the potential for solving the scalability limitations of current OMA techniques.

Motivated by the new possibilities of AI, this work presents and innovative AI-based OMA approach. The developed approach consists of a deep neural network (NN) trained in a supervised fashion by a BSS method. In general, BSS methods aim to identify a set of independent components (ICs), $\mathbf{s}(t)$, hidden within the raw acceleration acquisitions, $\mathbf{x}(t)$. To this aim, the acceleration data are assumed as a linear mixture of the ICs as $\mathbf{x}(t) = \mathbf{A}\mathbf{s}(t)$, where $\mathbf{A} \in \mathbb{C}^{m \times n}$ represents the transformation matrix (mixing matrix), and m and n are the number of measurement channels and ICs, respectively. Among the various BSS approaches in the literature (refer to [2] for a thorough state-of-the-art review), the second-order blind identification (SOBI) algorithm is adopted herein. The SOBI algorithm involves two

[1] *Department of Structural Mechanics and Hydraulic Engineering. University of Granada (SPAIN). israela42@correo.ugr.es; enriquegm@.ugr.es (Corresponding author).*

steps: (i) whitening of $\mathbf{x}(t)$ into a zero-mean unit-variance time series $\mathbf{z}(t)$; and (ii) identification of ICs producing diagonal time-shifted covariance matrices of $\mathbf{z}(t)$, i.e., $\mathbf{R}_{\mathbf{z}}(\tau) = \mathrm{E}\{z(t)\mathbf{z}(t+\tau)^{\mathrm{T}}\}$. The latter is often achieved by the joint approximate diagonalization (JAD) technique [3], which finds the diagonalization matrix $\boldsymbol{\Psi}$ by solving the following optimization problem in Eq. (1) over p covariance matrices:

$$\boldsymbol{\Psi}^{\mathrm{T}}\mathbf{R}_{\mathbf{z}}(\tau_i)\boldsymbol{\Psi} \approx \text{diagonal}, 1 \le i \le p \;\Rightarrow \min_{\boldsymbol{\Psi}} \sum_{i}^{p} \text{off}\left(\boldsymbol{\Psi}^{\mathrm{T}}\mathbf{R}_{\mathbf{z}}(\tau_i)\boldsymbol{\Psi}\right). \tag{1}$$

Once solved, the mixing matrix can be readily obtained as in Eq. (2):

$$\mathbf{A} = \left(\mathbf{E}\mathbf{D}^{1/2}\right)^{-1}\boldsymbol{\Psi}\,, \tag{2}$$

where $\mathbf{E}$ and $\mathbf{D}$ stand for the eigenvalue and eigenvector matrices of $\mathbf{R}_{\mathbf{x}}(0)$. It is important to remark that the ICs and the matrix $\mathbf{A}$, which contains the mode shapes of the system, are in general complex value. This is achieved if, instead of working with the real acceleration acquisitions $\mathbf{x}(t)$, one works with the analytical signal extracted by its Hilbert transform. Through simple algebraic manipulations, it is straightforward to identify that the acceleration records can be obtained as $\mathbf{x}(t) = \mathbf{A}_R\boldsymbol{s}_R(t) + \boldsymbol{A}_I\boldsymbol{s}_I(t)$, subindexes "*R*" and "*I*" denoting the real and imaginary parts of the corresponding terms. It is therefore concluded that the acceleration records are linearly related to the real and imaginary parts of the ICs through the counterparts of the modal matrix. This finding suggests the possibility of developing a deep NN combining two branches to reproduce both the real and imaginary parts of the ICs. In addition, combining these two branches through a linear fully connected layer, the weights of the neurons before the output layer can be directly understood as the real and imaginary parts of matrix $\mathbf{A}$.

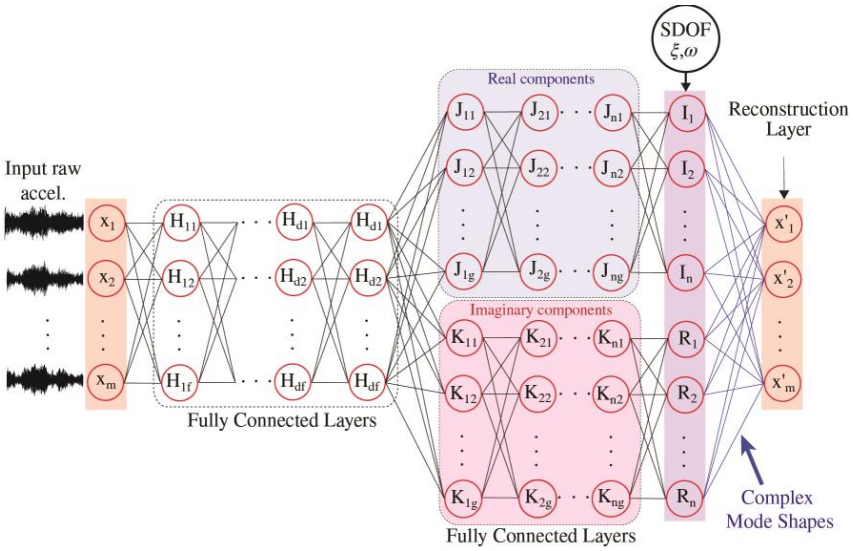

Figure 1. *Architecture of the developed MTL-DNN for fast BSS-OMA of structures.*

From the previous findings, the architecture of the developed feedforward MTL-DNN is sketched in Fig. 1. The input of the MTL-DNN correspond to the acceleration time series $\mathbf{x}(t)$. This is followed by a set of dense layers, which simulate the whitening and JAD processes. Dropout layers are used to reduce the overfitting of the NN. The activation functions used for the hidden layers are set to "*tanh*", except that the penultimate layer uses the linear transfer function "*linear*". The cost function is defined as a L^2 regularized version of the sum of squared errors in terms of the real/imaginary parts of the ICs and the

reconstructed acceleration data. Backpropagation Adam optimization is used to update the weights and biases of the NN. Finally, once the independent components are identified, the corresponding resonant frequencies and damping ratios are automatically extracted by the Ibrahim Time-domain (ITD) method.

2. NUMERICAL RESULTS AND DISCUSSION

The developed *MTL-DNN* is utilized for the OMA of a real-world in-operation structure, the Montecastelli Bridge. The Montecastelli Bridge is a reinforced concrete arch bridge crossing the Tiber River between the localities of Città di Castello and Umbertide (Italy). An ambient vibration test (AVT) reported in reference [4] was conducted on February 22, 2012, with the aim of identifying its main modal characteristics. The monitoring system consisted of 9 high-sensitivity (10 V/g) uniaxial piezoelectric accelerometers monitoring the vertical accelerations of the deck as depicted in Fig. 2.

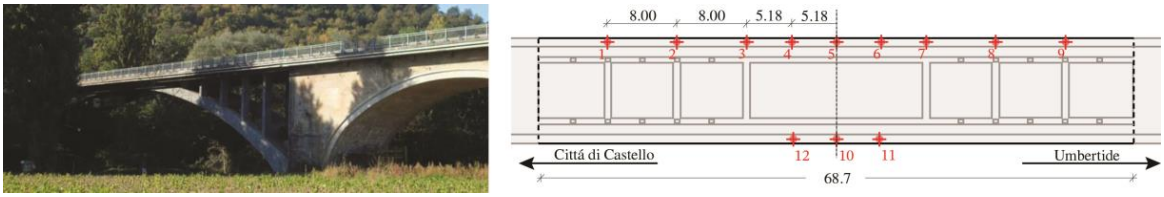

Figure 2. *View of the Montecastelli Bridge and sensors layout.*

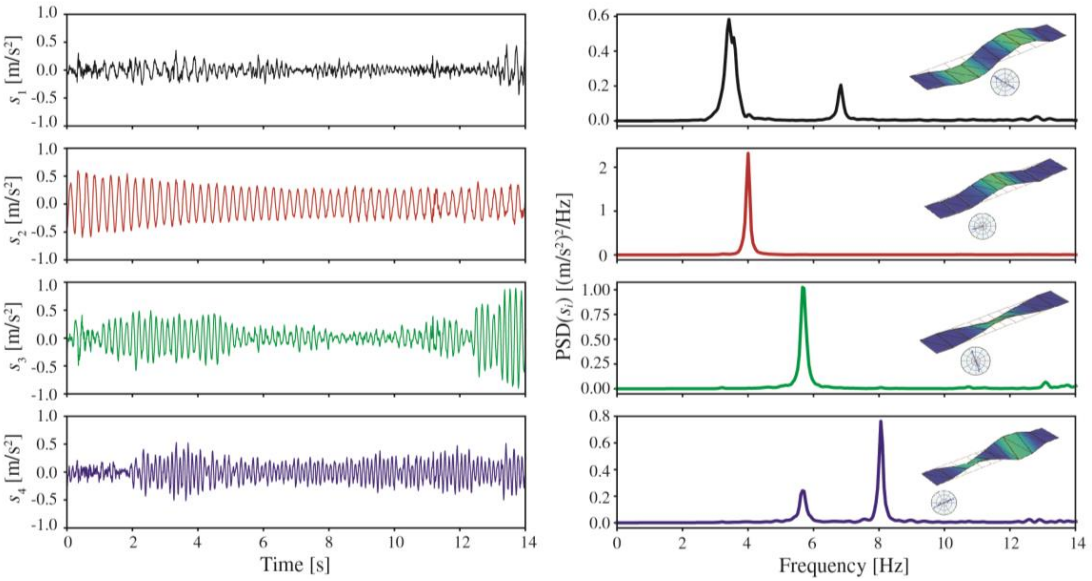

Figure 3. *First four independent components extracted by the proposed MTL-DNN in the Montecastelli Bridge.*

Thirty min-long acceleration records (sampling acquisition of 200 Hz) are used to test the MTL-DNN. The first four ICs extracted by the NN are reported in Fig. 3. Note that the NN successfully extracts almost harmonic sources, with an accuracy level comparable to standard SOBI. Up to nine modes are successfully identified in the frequency broadband up to 15 Hz as reported in Table 1, including 4 vertical bending (V*i*) and 5 torsional (T*i*) modes. Note that the developed MTL-DNN approach provides very close agreements with respect to the Data-SSI results from [4], with maximum relative differences in terms of frequency below 0.3%. Conversely, differences in terms of damping ratios are considerably larger, although given the low excitation levels registered in the experimental campaign, such differences are expectable. Indeed, maximum differences of 5% are found between MTL-DNN

and standard SOBI, thereby we can conclude that the AI model has been trained with accuracy. In addition, the developed NN can effectively reproduce the complex nature of the mode shapes as indicated with the corresponding mode phase collinearity (MPC) values in Table 1. Finally, although omitted due to space constraints, the model assurance criterion (MAC) values between the modes identified by MTL-DNN and Data-SSI are roughly 1 in all cases.

Table 1. Comparison of the modal properties of the Montecastelli Bridge estimated by MTL-DNN and Data-SSI [4]

	MTL-DNN			Data-SSI			
Label	Freq [Hz]	Damp. [%]	MPC	Freq [Hz]	Rel. Diff [%]	Damp. [%]	Rel. Diff [%]
V1	3.41	3.50	99.1	3.41	0.08	2.60	34.62
V2	3.40	1.23	99.5	4.00	-0.04	0.80	53.75
T1	5.69	1.71	95.9	5.71	-0.31	1.22	40.16
T2	6.84	1.15	96.7	6.83	0.02	1.14	0.88
V3	7.76	2.28	95.5	7.76	-0.02	1.61	41.61
T3	8.03	0.75	89.8	8.03	0.02	0.70	7.14
V4	10.42	1.33	98.7	10.41	0.03	0.78	70.51
T4	11.15	1.23	97.6	11.15	0.01	0.78	57.69
T5	13.84	1.12	95.4	13.84	0.01	0.9	24.44

3. CONCLUSIONS

This work has reported the development of an innovative AI-based OMA approach for rapid modal identification of structures. The fundamentals of BSS are encapsulated in the architecture of the network, including two different branches trained in a multi-task fashion for reproducing both the real and imaginary components of the mode shapes. The effectiveness of the developed approach has been tested in a real-world in-operation bridge, the Montecastelli Bridge. The presented results demonstrate the efficacy of the developed network, achieving modal identification results with comparable accuracy to the well-established Data-SSI algorithm, but with almost instantaneous identification capabilities.

ACKNOWLEDGEMENTS

This work has been supported by the Spanish Ministry of Science and Innovation through the research project ''BRIDGEXT - Life-extension of ageing bridges: Towards a long-term sustainable Structural Health Monitoring'' (Ref. PID2020-116644RB-I00).

REFERENCES

[1] Rainieri, C., & Fabbrocino, G. (2010). Automated output-only dynamic identification of civil engineering structures. *Mechanical Systems and Signal Processing*, 24(3), 678-695.

[2] Sadhu, A., Narasimhan, S., & Antoni, J. (2017). A review of output-only structural mode identification literature employing blind source separation methods. *Mechanical Systems and Signal Processing*, 94, 415-431.

[3] McNeill, S. I., & Zimmerman, D. C. (2008). A framework for blind modal identification using joint approximate diagonalization. *Mechanical Systems and Signal Processing*, 22(7), 1526-1548.

[4] Ubertini, F., Materazzi, A. L., Gentile, C., & Pelliccia, F. (2012). Automatic identification of modal parameters: Application to a reinforced concrete arch bridge. Proceedings of the EACS.

An efficient strategy for modeling the human auditory system from Micro-Computed Tomography Imaging.

Caminos, Luis[1]; Chaves, Gonzalo[1]; Lima-Rodriguez, Antonia[1]; Garcia-Manrique, Jose[1]; Gonzalez-Herrera, Antonio[1]

ABSTRACT

Finite Element modeling is a widely used methodology to build numerical models and simulate the behavior of the human auditory system; this has allowed essential advances in understanding the biomechanics of that complex system. There are two key points in modeling: the construction of an adequate geometry that allows efficient meshing and the correct use of mechanical properties of the materials. This research aims to show a new strategy for automating the build Finite Element Model process of the human auditory system using the FEM from Micro-Computed Tomography (Micro-CT) Imaging. The idea behind this methodology is to build a Finite Element Model with a computational and temporal low cost. This work allowed us to design the first semi-automatic algorithm to build a finite element model of the human middle ear that will later be used to incorporate the other components of the auditory system for different types of studies.

Keywords: human hearing, middle ear, finite element model

1. INTRODUCTION

The intricate human auditory system necessitates the application of finite element models for comprehension [1]. Nevertheless, generating these models is a challenging undertaking that demands precise geometry creation and optimal coupling between components. Proportions must remain accurate to avoid meshing issues, while the element count should be balanced to achieve computational efficiency. This study seeks to automate the process of constructing the finite element model for the human auditory system, serving as a crucial initial step towards this objective.

A semi-automatic algorithm is designed to build a finite element model of the human middle ear (tympanic membrane, ossicular chain, tendons, and ligaments). The geometric model is built from images taken from Micro-CT provided by the University of Antwerp [2].

Although some human decisions are necessary, the process has been designed and partially automated. The following sections provide a brief description of the methodology, results, and conclusions.

[1] *Departamento de Ingeniería Civil, de Materiales y Fabricación. Universidad de Málaga (España). lfcaminos@uma.es* (Corresponding author). *chaves.h.gonzalo@gmail.com. tlima@uma.es. josegmo@uma.es. agh@uma.es*

2. METODOLOGY

The structure of the algorithm is shown in Fig. 1. It is divided into four stages that are described below.

2.1. Input data

The input data is obtained from Micro-CT of the auditory system, in our case provided by [2]. These data are ***.stl*** files of the tympanic membrane, ossicular chain, ligaments, and tendons that were generated through Micro-CT image processing, the latter is outside the scope of this research.

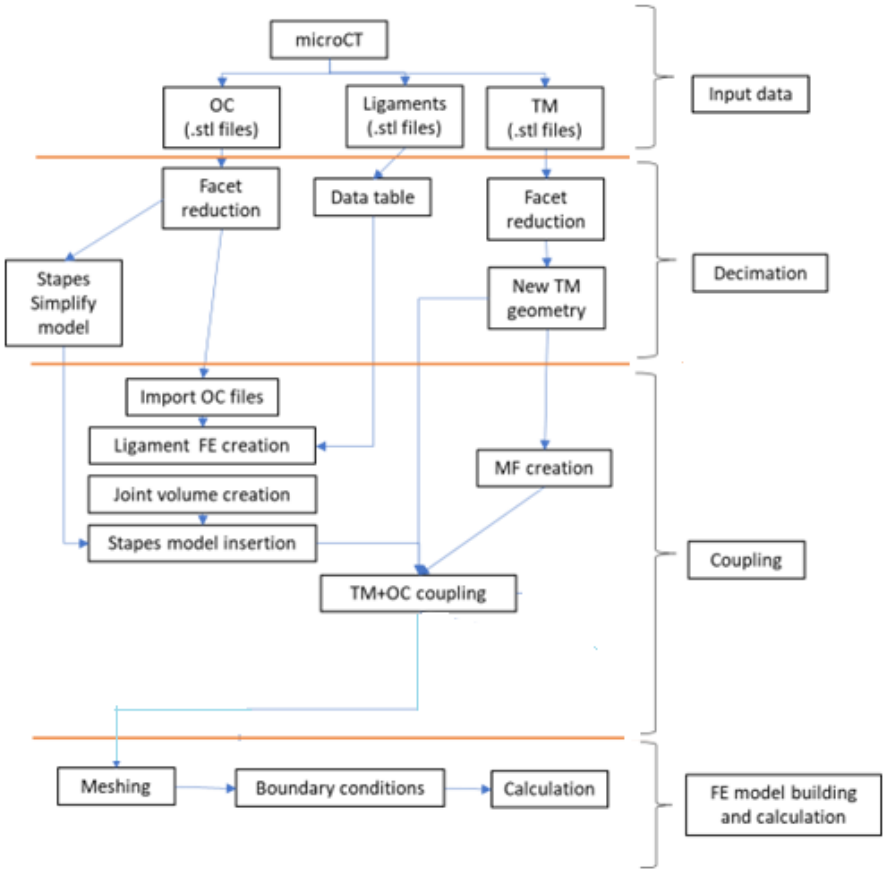

Figure 1. *Algorithm structure*

2.2. Decimation

For FE modeling and calculation, Micro-CT images provide detailed geometries. However, this increases computational cost and it's unclear if the results are of high quality. Thus, a decimation process is necessary to reduce external geometry facet numbers.

For this task, a routine is programmed in MATLAB software. The volumes of the malleus, incus, stapes, and tympanic membrane are treated, and new decimated geometries are constructed in the form of CAD files for the tympanic membrane and ossicles, or data tables for ligaments and tendons in the form of bars.

2.3. Coupling

This stage of the algorithm is the most complex since, each new geometry must be spatially positioned and coupled. Even when the original data comes from the same specimen, this procedure is not easy. This is the point where decision-making automation is most complex. We need to couple geometries with different characteristics, adding ligament, articulation, and at the same time ensuring that the meshing step can be performed efficiently.

2.4. FE model building and calculation.

The methodology used allows different models of material properties to be introduced to each of the parts that make up the system. In this research, this information was taken from the literature and previous works of our research team [3]. It is well known that the tympanic membrane is a critical component in the behavior of the human middle ear, for this reason, a convergence study is necessary [4]. The form factor (relationship between the element and the thickness of the TM) used is 3. On the other hand, the meshing of the other components is done in a specific order.

3. RESULTS

Below are some results from each stage of the algorithm. Fig. 2(a) shows the change in the geometry of the malleus through a faceting process using Matlab; a significant reduction in the number of polygons that make up the solid can be observed.

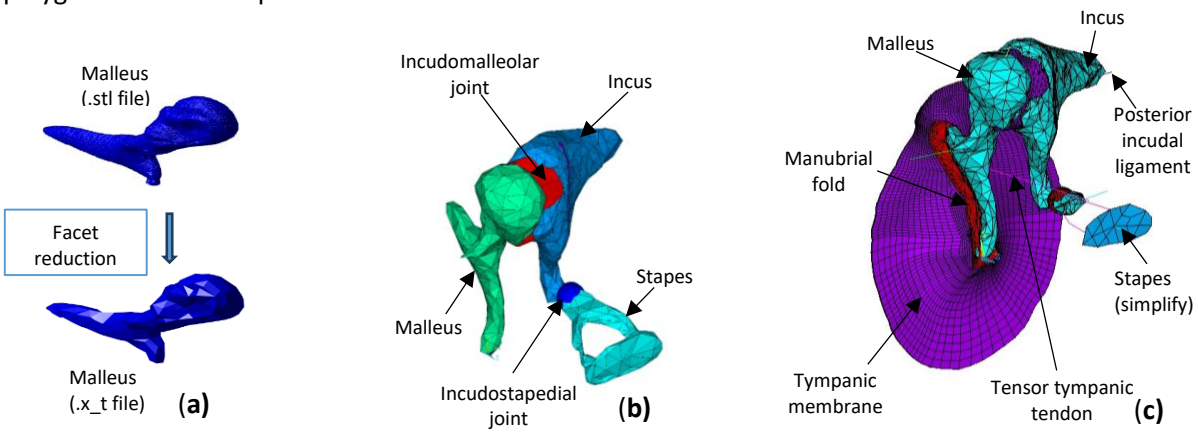

Figure 2. ***(a)*** *Malleus facet reduction.* ***(b)*** *Ossicular chain and joints coupling.* ***(c)*** *Middle ear FEM*

Fig. 2(b) shows the coupling of the ossicular chain and joints. This stage is one of the most complex. Some decisions such as generating contact areas could not be automated.

The complete FEM of the middle ear is shown in Fig. 2(c). Some important simplifications can be observed, such as the use of beam elements for models.

A harmonic analysis was conducted from 100 to 10.000 Hz using the FEM. A uniform harmonic 80 dB_{SPL} stimulus pressure was applied to the lateral side of the eardrum. The amplitude of stapes footplate displacements versus frequency is shown in Fig. 3 compared with experimental measurements [5]. It can be seen that the model curve and the experimental curve are very close.

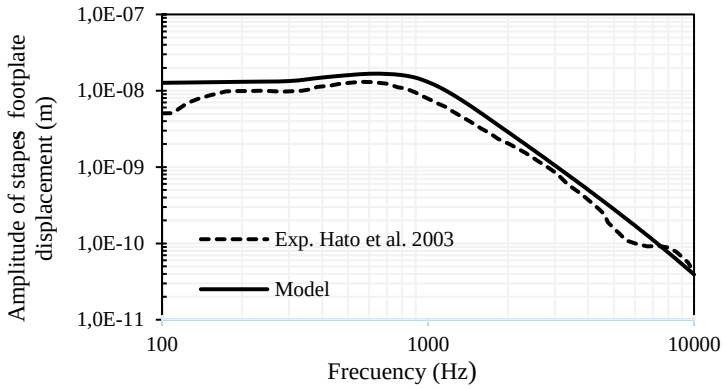

Figure 3. *Amplitude of stapes footplate displacement vs. frequency*

4. CONCLUSIONS

This article describes a methodology to build, from Micro-CT images, a numerical model of the human middle ear. This process is not fully automated because human decisions must be included in the algorithm.

The model obtained could be validated by comparing it with the numerical response of a harmonic analysis and experimental measurements taken from the specialized literature.

This work is the first step in the automation-building process of a numerical model of the human auditory system from images taken from patients with auditory pathologies.

REFERENCES

[1] Garcia-Manrique, J., Furlong, C., Gonzalez-Herrera, A., Cheng. JT., (2023). Numerical model characterization of the sound transmission mechanism in the tympanic membrane from a high-speed digital holographic experiment in transient regime. *Acta Biomaterialia, 159, 63–73.*

[2] Biophysics and biomedical physics. University of Antwerp. https://www.uantwerpen.be/en/research-groups/bimef/.

[3] Caminos, L., Garcia-Manrique, J., Lima-Rodriguez, A., Gonzalez-Herrera, A. (2018). Analysis of the mechanical properties of the human tympanic membrane and its influence on the dynamic behaviour of the human hearing system. *Applied Bionics and* Biomechanics, *2018, 1736957*.

[4] Volandri, G., Di Puccio, F., Forte, P., Carmignani, C. (2011). Biomechanics of the tympanic membrane. *Journal of Biomechanics, 44, 1219–1236*.

[5] Hato N, Stenfelt S, Goode RL. (2003). Three-Dimensional Stapes Footplate Motion in Human Temporal Bones. *Audiology and Neurotology, 8, 140–52*.

Analysis of the structural safety and proposals for intervention of a historic building: La Casa Rubio, Cartagena, Spain

Tomás, Antonio[1]; Sánchez-Olivares, Gregorio[1]; Parra, Carlos[2]

ABSTRACT

The objective of this contribution is to analyse the structural safety and propose possible strengthening interventions in the Casa Rubio, a 19th century building in El Algar, Cartagena, Spain. This study should serve as a basis for the subsequent municipal project to rehabilitate the building for public use, but always avoiding major interventions to preserve the historical and architectural value of the building. A finite element model has been implemented to analyse the behaviour of the structure under vertical and seismic actions. In the case of gravity actions, interventions are proposed on the cast iron columns, on certain wooden elements, such as beams and part of the floor slabs, and on those masonry elements bearing stresses exceeding the strength of the material. In the case of seismic action, strategies are proposed for the masonry elements by means of perimeter strapping and a bracing system for the most deformable parts of the building.

Keywords: historic building, structural assessment, rehabilitation, strengthening, seismic resistance

1. INTRODUCCIÓN

En este trabajo se analiza la seguridad estructural y se aportan propuestas de intervención para la Casa Rubio, un inmueble modernista del s. XIX ubicado en la localidad de El Algar, Cartagena, España (Fig. 1a), ante el propósito de la corporación municipal de dotarlo de espacios administrativos y de uso público.

Las plantas baja y primera son trapezoidales, siendo la segunda planta cruciforme y rematando el edificio una sobreelevación o linterna central. Las cubiertas inclinadas apoyan sobre correas de madera y están acabadas con teja cerámica plana o alicantina (Fig. 1b).

La estructura del edificio está compuesta por diversos subsistemas estructurales, los cuales han sido objeto de intervenciones parciales a lo largo del s. XX (muro perimetral, núcleo interior, forjados de madera y de hormigón, pilares interiores de fundición y de acero, vigas de madera y metálicas, y estructuras de cubierta). Estos subsistemas están dispuestos en diferentes direcciones, formando un conjunto rígido tridimensional (Fig. 2), cuya misión es la de recibir, soportar y transmitir las diferentes acciones a las que está sometido el edificio.

[1] *Departamento de Ingeniería Minera y Civil. Universidad Politécnica de Cartagena (SPAIN). antonio.tomas@upct.es (Corresponding author). gregorio.sanchez@upct.es*

[2] *Departamento de Arquitectura y Tecnología de la Edificación. Universidad Politécnica de Cartagena (SPAIN). carlos.parra@upct.es*

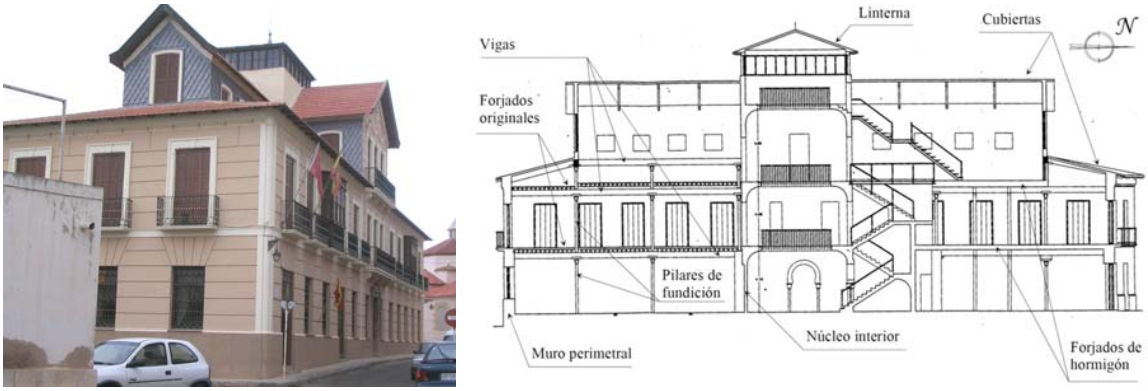

(a) (b)

Figura 1. *Casa Rubio. (a) Vista Sureste. (b) Sección Norte-sur.*

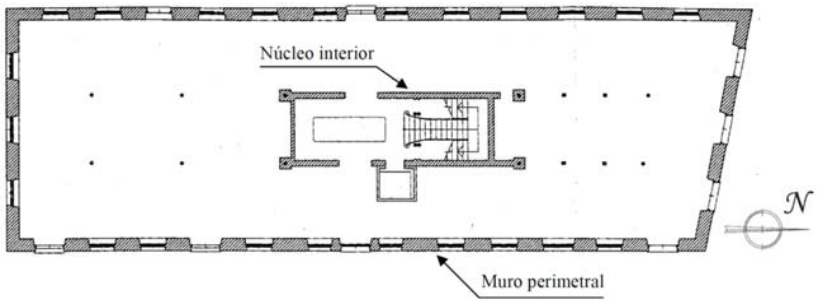

Figura 2. *Planta estructural.*

2. ANÁLISIS Y COMPROBACIONES ESTRUCTURALES

2.1. Modelo

A partir de estudios previos e inspecciones del edificio en su estado actual se ha propuesto un modelo estructural del inmueble (Fig. 3) empleando el *software* ETABS® [1], en donde predominan mayoritariamente los elementos de fábrica [2]. Se ha empleado análisis estático para las acciones gravitatorias y análisis dinámico lineal modal para la acción sísmica. En base a las necesidades transmitidas por el Ayuntamiento, la sobrecarga de uso adoptada es 3 kN/m^2, correspondiente a zonas de acceso público con mesas y sillas y zonas administrativas.

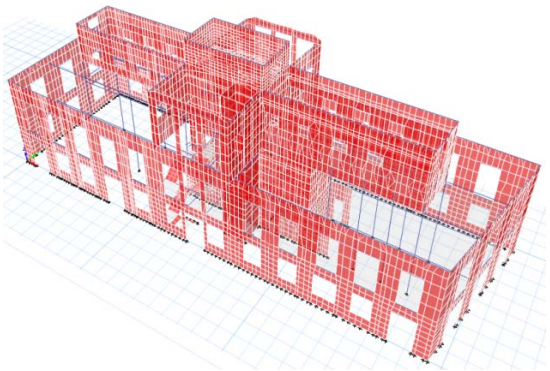

Figura 3. *Modelo de elementos finitos mediante el software ETABS®.*

2.2. Resultados

2.2.1. Análisis de la respuesta estructural frente a cargas verticales

Se han obtenido tensiones y realizado diversas comprobaciones de resistencia: (i) estado tensional en los muros de fábrica, considerándose un valor de 1,33 MPa como límite para la tensión de compresión media en la fábrica (valor reducido debido al escaso conocimiento del estado del material); (ii) tensiones en la base de los muros que se transmiten a la cimentación y, de esta, al terreno, siendo el valor de la tensión admisible 0,35 MPa según el estudio geotécnico realizado; y (iii) el valor del axil en los pilares de fundición, que se compara con la resistencia del material -hierro de fundición-, considerando el valor límite frente a pandeo [3] y, de nuevo, el axil que se transmite a la cimentación y, de esta, al terreno.

En la Fig. 4a se observan las tensiones normales en los muros de fábrica, yendo la escala cromática desde violeta (-1,2 MPa) a azul (1,2 MPa). La presencia de la escalera de hormigón añadida posteriormente en la zona Este del núcleo central, junto con la abertura de huecos de puertas en sus paños, provoca concentración de tensiones, tanto de compresión como de tracción, de valor máximo 2,6 MPa.

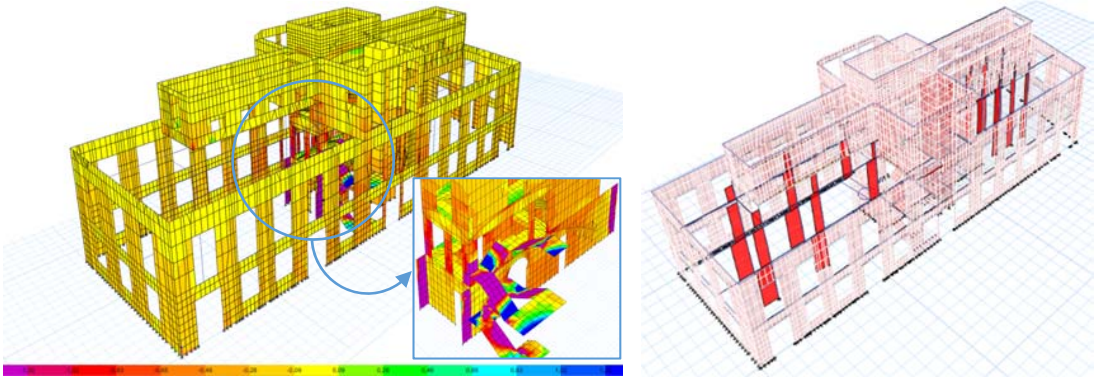

(a) (b)

Figura 4. *Resultados del análisis. (a) Estado tensional normal en los muros de fábrica (muro perimetral y núcleo interior). (b) Esfuerzo axil en pilares.*

Los elementos más afectados por la nueva sobrecarga son las columnas de fundición del ala Sur. En la Fig. 4b se puede apreciar la variación del axil en ellas, apareciendo el valor máximo (482,33 kN) en una de las dos columnas interiores (en la zona Norte los axiles son menores por haberse dispuesto, con posterioridad, cuatro pilares de refuerzo de acero laminado). La tensión máxima transmitida por las columnas al terreno es 438,48 kN/m^2, superior a la tensión admisible 0,35 MPa. Para obtener esta cifra, con la escasa información disponible, se ha estimado un tamaño de cimentación de 1,0×1,1 m. Frente a este nivel de incertidumbre se considera necesario, y así se transmite a la administración local, efectuar ulteriores catas y evaluar la posibilidad de que sea necesario un refuerzo de la cimentación (el tamaño mínimo para el cumplimiento de la tensión admisible sería 1x1,4 m).

2.2.2. Análisis de la respuesta estructural frente a sismo

Tras realizar un análisis modal con el espectro de respuesta de la norma española, se aprecia que los tres primeros modos movilizan el ala Sur del edificio (Fig. 5a-c), por ser esta la parte más deformable, siendo el cuarto modo el que comienza a movilizar el ala Norte -el brazo de la planta cruciforme- (Fig. 5d). En términos de desplazamientos, destacar que los nodos en las extremidades superiores del brazo Sur de la planta segunda sufren movimientos en horizontal d_X = 1,9 mm, d_Y = 68,2 mm, y en vertical d_Z = 4,7 mm, lo que provocaría el despegue del muro a lo largo del contacto con el cuerpo central, provocando un mecanismo lábil y, consecuentemente, el colapso. El coronamiento Sur del muro perimetral sufre un desplazamiento d_Y = 46,1 mm, provocando un desplome relativo 1/185 y, por tanto, la rotura de la fábrica.

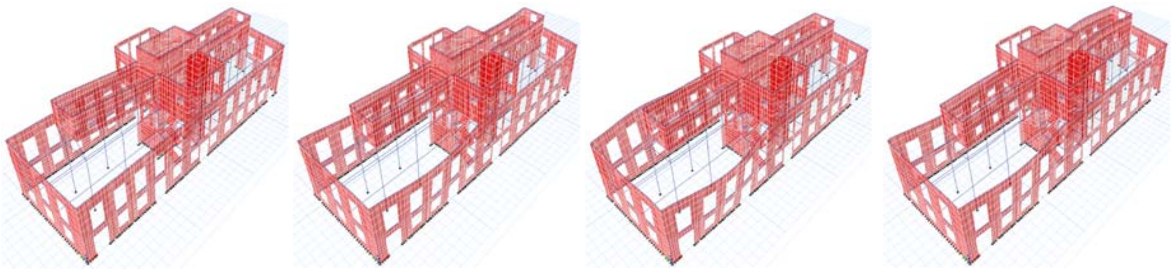

(a) (b) (c) (d)

Figura 5. *Modos de deformación. (a) Primero. (b) Segundo. (c) Tercero. (d) Cuarto.*

3. CONCLUSIONES Y PROPUESTAS DE REFUERZO

Se ha analizado la estructura de la Casa Rubio, un edificio modernista del s. XIX ubicado en Cartagena, mediante modelos de cálculo que han puesto en evidencia los puntos más críticos en su comportamiento resistente, tanto bajo cargas verticales como, sobre todo, bajo la acción sísmica.

A continuación, se enumeran de modo resumido las propuestas de refuerzo, procurando la menor intervención posible que preserve el genuino patrimonio arquitectónico del edificio:

(i) elementos estructurales de fábrica: al aparecer tensiones que superan la resistencia del material, se propone volver a cegar ciertos huecos en el núcleo central mediante piezas de fábrica de adecuada resistencia, recuperando de este modo la distribución homogénea de las cargas en esa zona del edificio;

(ii) elementos de madera de las vigas y del forjado del ala Sur: al no poder asegurar suficiente margen de seguridad frente a esfuerzos de flexión ante el nuevo valor de la sobrecarga de uso, se propone reconvertir las secciones de madera a secciones mixtas hormigón-madera, aunque garantizando la correcta transmisión de esfuerzos mediante conectores y aplicando una adecuada protección impermeabilizante a la madera;

(iii) columnas de fundición: para adecuar el edificio a las cargas verticales impuestas por el nuevo uso previsto, se propone reforzarlas mediante un encamisado exterior con perfiles tubulares de acero laminado; y

(iv) estrategias de refuerzo sísmico de los elementos estructurales de fábrica: se proponen zunchos perimetrales y un sistema de arriostramiento de las partes más deformables del edificio a través de cruces de San Andrés, poniendo especial atención en el adecuado diseño de las conexiones entre los elementos existentes y los añadidos.

REFERENCIAS [CALIBRI, 11PT, NEGRITA, MAYÚSCULA, ALINEADO A LA IZQUIERDA]

[1] ETABS. (2013). [Software]. Extended three dimensional analysis of building systems. Berkeley: Computers & Structures, Inc.

[2] Lourenço, P.B., Rots, J.G., & Blaauwendraad, J. (1998). Continuum model for masonry: parameter estimation and validation. *Journal of Structural Engineering, ASCE, 124(6), 642-652*.

[3] Rondal, J., & Rasmussen, K.J.R. (2004). On the strength of cast iron columns. *Journal of Constructional Steel Research, 60, 1257-1270*.

Analytical stiffness of demountable joints with welded studs

García, Ismael[1]; López-Colina, Carlos[2]; Serrano, Miguel Angel[2]; Vigón, Paula[2]

ABSTRACT

Designing detachable joints between I-section beams and tubular section columns is not a straight-forward task. This arises from the fact that placing bolts inside the hollow section of the column can sometimes be challenging due to the inaccessibility of its interior. In response to this issue, the research community has put forth various types of connections, including bolted joints with welded studs. These are of particular interest due to their ease of execution on the construction site and their ability to be disassembled. This article presents an analytical model based on the components method to estimate the stiffness of beam to column joints and column to base plate joints with welded studs. These equations have been validated through a comparison with results obtained in full-scale experimental tests. The findings demonstrate that the stiffness can be estimated using the proposed equations with a reasonable level of accuracy.

Keywords: demountable joints; welded studs; joint characterization.

1. INTRODUCCIÓN

En un contexto de emergencia climática global, la necesidad de reducir las emisiones de carbono se ha vuelto apremiante. La industria de la construcción es una de las principales contribuyentes a estas emisiones debido a la gran cantidad de energía y recursos naturales que consume, así como a los desechos y la contaminación que genera durante la construcción y la demolición de edificios [1].

Una estrategia efectiva para abordar este desafío es promover la práctica de desmontar y reutilizar elementos estructurales en lugar de desecharlos después de la vida útil de un edificio. Esto no solo reduce la necesidad de fabricar nuevos materiales, lo que ahorra energía y recursos, sino que también disminuye tanto la cantidad de desechos que terminan en vertederos como la contaminación asociada con la producción de nuevos materiales de construcción [2].

La reutilización de componentes estructurales puede incluir la recuperación de vigas, pilares, muros y otros elementos clave que, si se mantienen en buenas condiciones, pueden integrarse en nuevos proyectos de construcción. Esto no solo reduce la demanda de recursos naturales, sino que también disminuye las emisiones de carbono relacionadas con la extracción, la producción y el transporte de nuevos materiales. Sin embargo, al diseñar uniones metálicas desmontables entre vigas IPE y pilares de sección tubular, pueden surgir dificultades debido a la inaccesibilidad del interior del tubo, lo que puede convertirse en un problema durante el proceso de ejecución. Para solventar este inconveniente, varios

[1] *Dpto. construcciones arquitectónicas, ingeniería del terreno y mecánica de los medios continuos y teoría de estructuras. Universidad de Valladolid (España). garciaismael@uva.es (Corresponding author).*
[2] *Departamento de Construcción e Ingeniería de Fabricación. Universidad de Oviedo (España). lopezpcarlos@uniovi.es; serrano@uniovi.es; uo194830@uniovi.es*

autores han propuesto la utilización de uniones con pernos soldados [3]–[5]. En este trabajo se estudia la rigidez de uniones viga-pilar y pilar-placa base diseñadas con angulares y pernos soldados. Las unio- nes viga-pilar son ejecutadas con angulares de alas desiguales L 120×80×10 y pernos roscados de mé- trica 16 mm y calidad K800 previamente soldados en la cara del pilar tubular. Los pernos conectan el pilar con el ala corta de los angulares superiores e inferiores, mientras que el ala larga de los angulares se atornilla al ala de la viga mediante tornillos estándar, como se puede ver en la Fig. 1 izda. Se realizaron un total de 6 uniones viga-pilar, divididas en tres casos en cada uno. En el primer conjunto, se utilizó una viga HEB 200 en combinación con un tubo SHS 200, en el cual se varió el espesor del tubo desde 6 mm hasta 10 mm. En el segundo conjunto, se empleó una viga laminada IPE 300 junto con un tubo SHS 200, y de manera similar, se varió el espesor del tubo de 6 mm a 10 mm en tres ocasiones distintas, tal y como se puede ver en la Tabla 1.

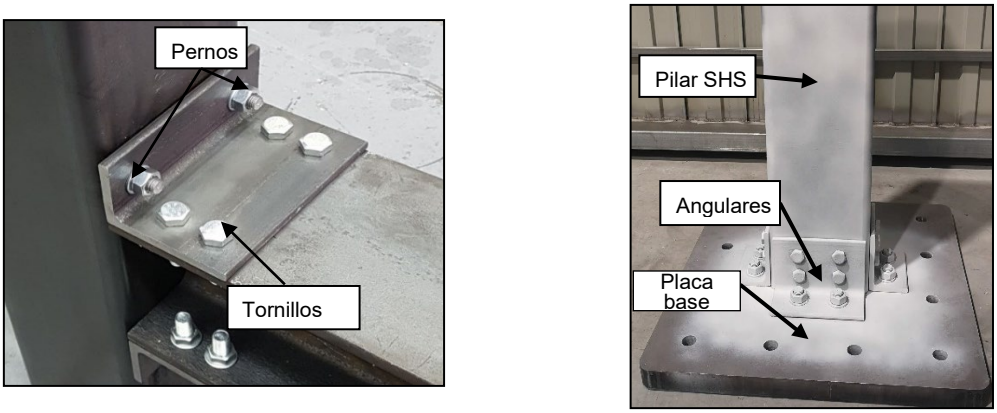

Figura 1. *Ejemplo de unión viga-pilar (izquierda) y pilar-placa base (derecha) ejecutadas con casquillos de angular y pernos soldados.*

Las uniones pilar- placa base están formadas por un tubo (pilar) conectado a la placa base mediante cuatro angulares del tipo L 120×80×10 en las que cada angular se conecta con cada una de las caras del tubo (Fig. 1 dcha). Se fabricaron un total de tres uniones pilar-placa base a escala real. La placa base consistió siempre en una chapa de acero de 600×600×40 mm mientras que, para estudiar el comporta- miento de diferentes geometrías de pilares, se prepararon tres probetas (BM1, BM2 y BM3) con un pilar de sección cuadrada SHS 200 al que se le fue variando el espesor del tubo, formando así probetas con espesores de pared del tubo de 6 mm, 8 mm y 10 mm. Para favorecer el montaje, los angulares fueron más cortos que el ancho del tubo correspondiente, siendo de 180 mm para las caras de ancho 200 mm. Cada angular se conectó al pilar por su ala larga mediante 4 tornillos comerciales TR 16 de calidad 10.9. El ala corta de cada angular se conectó a la placa base con 2 pernos soldados de rosca métrica, diámetro 20 mm, longitud 35 mm y calidad K800. Tanto las uniones viga-pilar como las uniones pilar-placa base están diseñadas para ser desmontables y están pensadas para su posterior reutilización.

2. RIGIDEZ DE LAS UNIONES

Las probetas se ensayaron ante cargas monotónicas crecientes hasta rotura. Los ensayos se llevaron a cabo en un marco de ensayos multiposicional. Para aplicar la carga se utilizó un actuador hidráulico marca Ibertest GIB 500-MD2W con capacidad de carga máxima de 500 kN en compresión y 300 kN en tracción. Se aplicó un desplazamiento en el extremo de la viga (en uniones viga-pilar) o en el extremo del pilar (en uniones pilar-base) hasta provocar el agotamiento de la unión. En el caso de las uniones

viga-pilar, fue el pilar el que se fijó al marco, mientras en el caso de las uniones base-pilar fue la base la que se ancló al marco. La curva momento-rotación experimental se obtuvo con ayuda de un equipo de correlación digital de imágenes, a partir de la cual se determinó la rigidez inicial experimental, $S_{j,ini,EXP}$, que se muestra en la tabla 2 tanto para las uniones viga-pilar como para las uniones pilar-placa base. La tabla 1 muestra la geometría de las uniones ensayadas viga-pilar y placa-base con datos de los tubos, viga, angulares, tornillos y pernos soldados junto con la relación de anchos entre el ala de la viga y el ala del pilar en estas uniones.

Tabla 1. Geometría de las uniones viga-pilar (SMS) y pilar-placa base (BM).

Probeta	Tubo	Viga	Casquillos	Tornillos	Pernos	Relación β $[b_b/b_0]$
SMS1	SHS 200.6	HEB 200	L120×80×10	8×M16 8.8	4 M16×40 K800	1
SMS2	SHS 200.8	HEB 200	L120×80×10	8×M16 8.8	4 M16×40 K800	1
SMS3	SHS 200.10	HEB 200	L120×80×10	8×M16 8.8	4 M16×40 K800	1
SMS4	SHS 200.6	IPE 300	L120×80×10	8×M16 8.8	4 M16×40 K800	0.75
SMS5	SHS 200.8	IPE 300	L120×80×10	8×M16 8.8	4 M16×40 K800	0.75
SMS6	SHS 200.10	IPE 300	L120×80×10	8×M16 8.8	4 M16×40 K800	0.75
BM1	SHS 200.6	-	L120×80×10	16x M16 10.9	8 M20×35 K800	-
BM2	SHS 200.6	-	L120×80×10	16x M16 10.9	8 M20×35 K800	-
BM3	SHS 200.8	-	L120×80×10	16x M16 10.9	8 M20×35 K800	-

Para determinar la rigidez analítica de las uniones viga-pilar, se realizó una adaptación mejorada del modelo propuesto por el EC3-1-8 para perfiles abiertos. Los componentes que se consideraron fueron la cara lateral a cortante (k_1), las caras laterales a tracción y compresión (k_2 y k_3), la cara frontal a compresión ($k_{4,C}$), la cara frontal a tracción ($k_{4,T}$), el angular a flexión (k_6) y los pernos a tracción (k_{10}). Se determinaron los coeficientes de rigidez de acuerdo con las expresiones propuestas en el Eurocódigo 3 [6] para los componentes k_1, k_6, y k_{10} mientras que para los componentes $k_{4,T}$ y $k_{4,C}$ y k_2, y k_3 se siguieron las ecuaciones propuestas por Lozano [7] y por López-colina [8], respectivamente. Los resultados de la rigidez analítica $S_{j,an}$ para las uniones viga-pilar se muestran en la tabla 2.

Tabla 2. Resultados de las uniones viga-pilar (SMS) y pilar-placa base (BM).

Unión	$S_{j,ini,EXP}$ [kNm/rad]	$S_{j,an}$ [kNm/rad]	$S_{j,an}/S_{j,ini,EXP}$
SMS1	1973	1935	0,98
SMS2	2801	2708	0,97
SMS3	3671	3212	0,87
SMS4	2050	1941	0,95
SMS5	3795	3203	0,84
SMS6	4945	4220	0,85
BM1	5661	6095	1,08
BM2	5979	6089	1,02
BM3	6924	6085	0,88

Para el cálculo de la rigidez inicial de las uniones pilar-placa base se ha seguido el procedimiento general propuesto en el Eurocódigo 3 para uniones con chapa frontal con dos o más filas de tornillos a tracción. En este trabajo se modelizaron las uniones pilar-placa base teniendo en cuenta los componentes del angular a flexión (k_6) y los pernos a tracción (k_{10}). Al estar pretensados los tornillos, los coeficientes de rigidez debidos a los tornillos a cortante y a los tornillos a aplastamiento se supusieron

infinito, siguiendo las recomendaciones propuestas en el Eurocódigo 3. Los resultados de la rigidez analítica $S_{j,an}$ para las uniones pilar-placa base se muestran en la tabla 2.

De los resultados experimentales se puede observar que, en las probetas formadas por una misma sección de tubo, pero con diferente espesor, la rigidez inicial aumentó ligeramente a medida que aumentaba el espesor del tubo. Este aumento es más notable en el caso de las uniones viga-pilar que en el de las uniones pilar-placa base.

3. CONCLUSIONES

Los modelos analíticos propuestos para la estimación de la rigidez inicial en las uniones viga-pilar y pilar-placa base reprodujeron con una concordancia razonable los resultados de rigidez obtenidos en los ensayos. Estos resultados permiten extender el método de los componentes a uniones no consideradas actualmente en los códigos de diseño. Su inclusión, podría promover el uso de un sistema de edificación desmontable y reutilizable que contribuiría a la sostenibilidad del proceso constructivo de los edificios.

AGRADECIMIENTOS

Los autores agradecen la financiación recibida por parte de la Agencia Estatal de Investigación a través del proyecto BIA2017-83467-P y a través del contrato predoctoral PRE2018-084273, así como al CIDECT mediante el proyecto 5CF.

REFERENCIAS

[1] D. 2010/31/CE, *Directive 2010/31/EU of the European Parliament and of the Council of 19 May 2010 on the energy performance of buildings*. 2010.

[2] T. O'Grady, R. Minunno, H. Y. Chong, and G. M. Morrison. (2021). Design for disassembly, deconstruction and resilience: A circular economy index for the built environment. *Resources, Conservation and Recycling*, 175, 105847.

[3] D. Vandegans and J. Janss (1996). Connection between steel beams and concrete filled R.H.S. based on the stud technique (threaded stud). *Connections in Steel Structures III*, 67–76.

[4] L. C. Neves, L. Simões da Silva, and P. C. G. da S. Vellasco. (2002). Experimental behaviour of end plate I-beam to concrete-filled rectangular hollow section column joints. *Advances in Steel Structures (ICASS '02)*. 253–260.

[5] M. A. Serrano-López, C. López-Colina, Y. C. Wang, M. Lozano, I. García, and F. L. Gayarre. (2021). An experimental study of I beam-RHS column demountable joints with welded studs. *Journal of Constructional Steel Research*, 182, 106651.

[6] "EN 1993-1-8:2005 - Eurocode 3: Design of steel structures - Part 1-8: Design of joints". (2005). *Eurocode 3*.

[7] M. Lozano. (2019). *The component method applied to welded beam-column joints between open profiles and structural tubes. Doctoral thesis, in spanish. Original title: El método de los componentes aplicado a uniones viga-pilar soldadas entre perfiles abiertos y tubo estructural*.

[8] C. López-Colina, M. A. Serrano, M. Lozano, F. L. Gayarre, J. M. Suárez, and T. Wilkinson (2019) Characterization of the main component of equal width welded I-beam-to-RHS-column connections. *Steel and Composite Structures*. 32, 337-346.

Automatic creation of Moodle repositories for personalized evaluation of learning results in Strength of Materials subject

Cifuentes-Rodríguez, Jaime[1]; Gutiérrez-Posada, Víctor[1] ; Ubero-Martínez, Iván [1]; Vallepuga-Espinosa, José [1]

ABSTRACT

Strength of Materials is a compulsory subject in Engineering and Architecture Schools. This subject is susceptible to numerous graphic representations, both in theoretical explanations as in the problem statements and their proposed solution. An increasing number of universities are using the Moodle virtual platform as the basis for learning and skill evaluation The personalized graphic representation of problem statements in a Moodle questionnaire is a challenge, as it requires a very important number of statements in order to individualize it for each student. With this aim, we propose a MATLAB-based tool to automatically generate personalized Moodle questionnaires that allow evaluating the students learning process by solving Strength of Materials problems. The tool allows the choice of the complexity degree of each problem in real time, together with a scaled visualization of the solution. Thus, student and teacher simultaneously obtain a better idea of the student´s learning progress.

Keywords: Strength of materials, Moddle, Matlab, teaching strategies and innovation

1. INTRODUCCIÓN

La Resistencia de Materiales tiene como finalidad elaborar métodos simples de cálculo, aceptables desde el punto de vista práctico, de los elementos típicos más frecuentes de las estructuras y elementos de máquinas, empleando para ello diversos procedimientos aproximados. Para ello se introducen hipótesis simplificativas, que pueden ser justificadas comparando los resultados de cálculo con los ensayos, o con los obtenidos aplicando la teoría de la elasticidad. [1]. Por la naturaleza de esta disciplina, la evaluación del aprendizaje ha de ser procedural [2], y para ello es necesario disponer de un repositorio de ejercicios adecuado. La construcción de un repositorio es una tarea especialmente laboriosa para el docente, pues la casuística es muy variada y la cantidad de problemas que se pueden plantear es prácticamente ilimitada. Una vez construido el repositorio de ejercicios se pueden utilizar, entre otras, la evaluación mediante test o mediante preguntas de respuesta corta para evaluar el aprendizaje [3].

La herramienta presentada propone dar respuesta a un problema típico de Resistencia de Materiales, como es la determinación de las leyes de esfuerzos cortantes y flectores y la ecuación de la elástica de una viga isostática de sección constante.

[1] *Departamento de tecnología minera, topográfica y estructuras. Universidad de León (España). jcifr@unileon.es (Corresponding author). vgutp@unileon.es. iubem@unileon.es. jvale@unileon.es.*

Para explicar todo lo anteriormente expuesto mostramos un problema típico en la enseñanza la Resistencia de Materiales como es el caso de la determinación de las leyes de esfuerzos cortantes y momentos flectores junto con la ecuación de la elástica de una viga isostática. [3]

2. PROBLEMA DE DETERMINACIÓN DE LEYES DE ESFUERZOS Y ECUACIÓN DE LA ELÁSTICA

2.1. Planteamiento del problema

El problema planteado consiste en la determinación de las leyes de esfuerzos cortantes y flectores y de la elástica de las vigas de sección constante de la Fig. 1. Se supone que el módulo de elasticidad es constante.

Figura 1. *Vigas correspondientes a los problemas propuestos. Las cargas están dadas en kN y las longitudes en m*

2.2. Resolución

Las leyes de esfuerzos cortantes y momentos flectores son obtenidas a partir de las conocidas ecuaciones de equilibrio [4], Eqs. (1-2) y ecuación de la elástica mediante Eq. (3).

$$\frac{dC_y(x)}{dx} = -q_y(x) \tag{1}$$

$$\frac{dM_z(x)}{dx} = C_y(x) \tag{2}$$

$$EI_z \frac{d^2y}{dx^2} = -M_z(x) \tag{3}$$

donde $C_y(x)$ y $M_z(x)$ son el esfuerzo cortante y el momento flector respectivamente.

2.3. Salida de resultados

La salida de resultados es la mostrada en la Fig. 2. En ella se puede observar:

- Resultado de las reacciones del problema.
- Representaciones gráficas y valores más significativos de las leyes de esfuerzos cortantes y momentos flectores.
- Expresiones analíticas e intervalos de validez de los mismos.
- Representación gráfica y valores más significativos de la elástica del problema.
- Representación analítica e intervalos de validez de la misma.

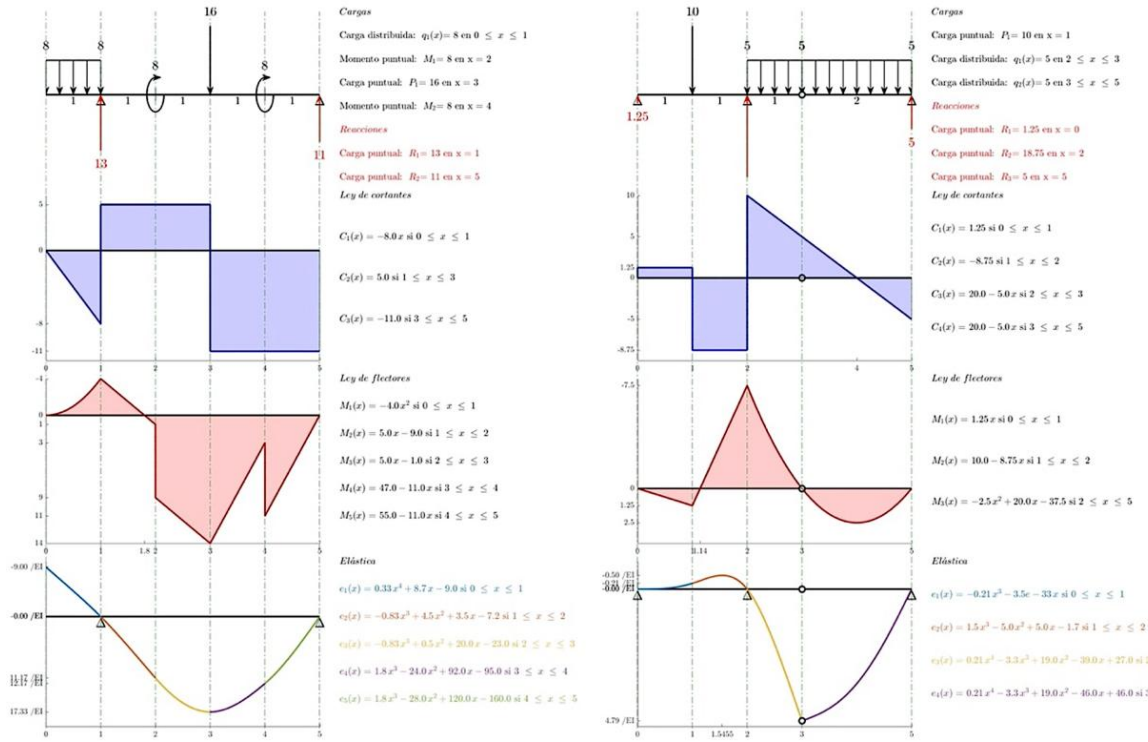

Figura 2. *Salida de resultados correspondientes a los problemas planteados.*

3. IMPLEMENTACIÓN PARA MOODLE

Las preguntas de un cuestionario de Moodle se generan automáticamente mezclando diagramas individuales de cuatro problemas resueltos previamente con la herramienta creada. La Fig. 3 muestra en Moodle dos preguntas tipo en donde se debe señalar el diagrama de esfuerzos cortantes y el diagrama de momentos flectores correcto para la viga del enunciado. De igual manera, en las preguntas de la Fig. 4 se solicita la correspondencia entre los diagramas de cortantes y flectores, así como la correspondencia correcta entre los diagramas de flectores y la elástica.

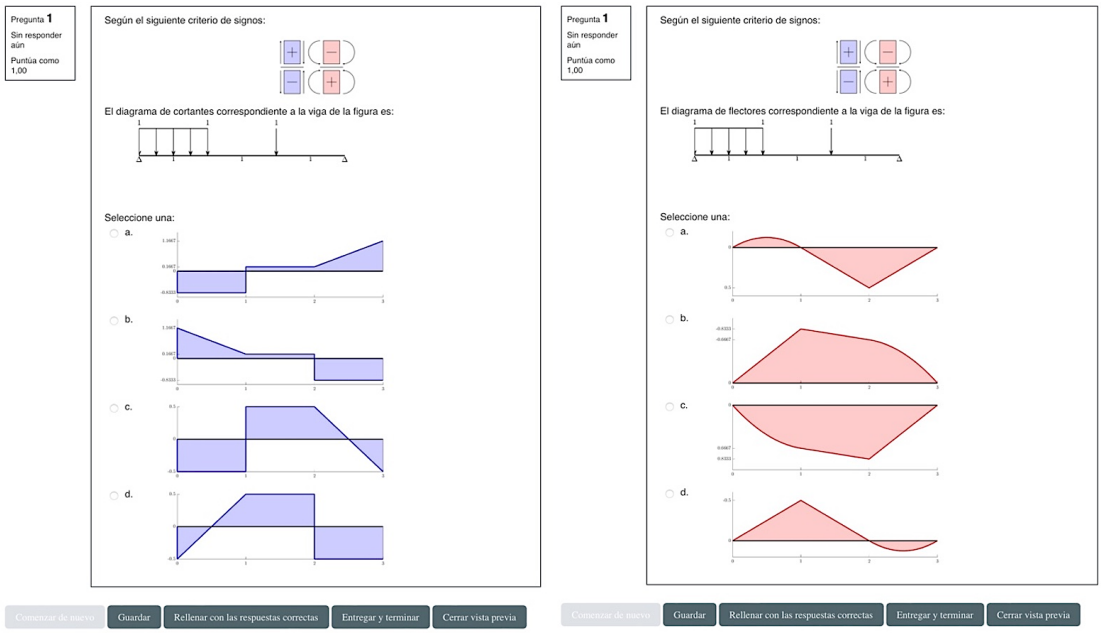

Figura 3. *Visualización en Moodle de los cuestionarios de esfuerzos cortantes y momentos flectores.*

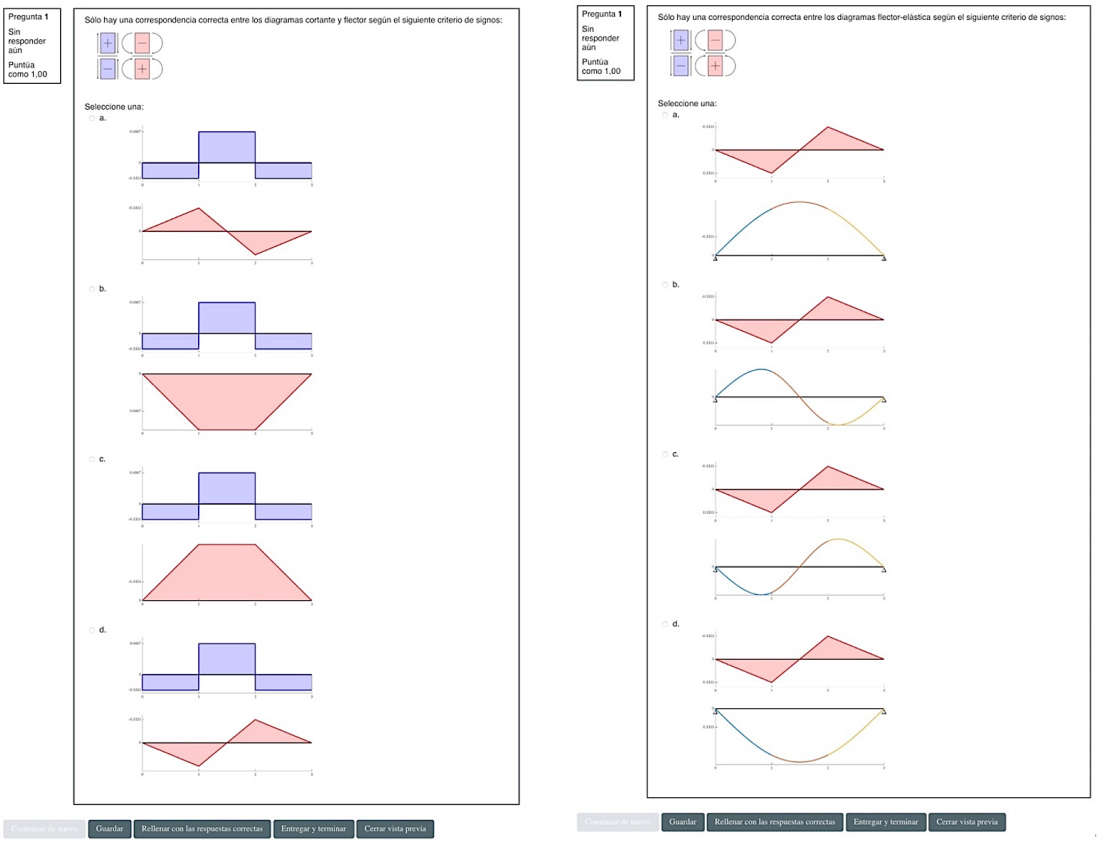

Figura 4. *Visualización en Moodle de los cuestionarios de correspondencias entre diagramas.*

4. CONCLUSIONES Y TRABAJO FUTURO

Se ha comprobado que una herramienta de simulación matemática como Matlab permite la generación y resolución analítica de problemas relacionados con la Resistencia de Materiales, lo que la hace idónea a la hora de la implementación personalizada de preguntas para ser incluidas en cuestionarios Moodle.

La continuación de este trabajo contempla el establecimiento de métricas adecuadas para evaluar su impacto en los resultados de aprendizaje y para verificar su utilidad en entornos de enseñanza reglada. Además, se mejorará la herramienta para que contemple otros de problemas de Resistencia de Materiales (geometría de masas, determinación eje neutro, núcleo central, etc.).

REFERENCIAS

[1] Stiopin, P. A., & Mora, P. G. (1979). Resistencia de materiales. Editorial Mir Moscú.

[2] Hernando M., Guzmán E., Conejo R., (2013). Measuring Procedural Knowledge in Problem Solving Environments with Item Response Theory. *Artificial Intelligence in Education, (pp. 653-656)*.

[3] Abellán M., Gisbert M. (2012). Los cuestionarios del entorno Moodle: su contribución a la evaluación virtual formativa de los alumnos de matemáticas de primer año de las titulaciones de Ingeniería, *RUSC. Universities and Knowledge Society Journal, vol 9, iss 1, (pp. 166-183)*.

[4] Timoshenko, S. (1957). Resistencia de Materiales Primera Parte. Delgado Tomas, (trad.).

Automatically generating problems/exams for structural engineering courses using MS Excel® and FastTest PlugIn for Moodle

Huerta, Milagros[1]; Fernández-Ruiz, Manuel Alejandro[2]; Núñez-Almagro, Javier Jacob[1]; Requena-García de la Cruz, María Victoria[1]

ABSTRACT

Since the onset of the COVID-19 pandemic, higher education has undergone substantial changes in the way classes are conducted and students are evaluated. This impact has been particularly pronounced in the realm of engineering disciplines. Adapting teaching and assessment methodologies became essential in response to confinement measures. For many engineering courses, creating analogous problems or exams with varying data yet maintaining the same complexity has proven to be a labour-intensive task for educators. This study aims to leverage digital platforms, such as Moodle with the FastTest PlugIn, to enhance student monitoring and evaluation while reducing the grading workload for professors. Problems have been devised using MS Excel, preserving identical structures while data is automatically altered. These problems are integrated into Moodle for assessment. Although the initial preparation demands time, this investment pays off in the grading of exercises and exams, benefiting both professors and students.

Keywords: Higher Education, Teaching Innovation, Moodle, Excel, structural engineering problems.

1. INTRODUCCIÓN

Debido a la situación de pandemia provocada por el COVID-19, uno de los retos a los que nos hemos enfrentado los docentes ha sido tener que pasar, sin previo aviso y sin preparación (tanto del profesorado como del alumnado), de una docencia totalmente presencial a otra totalmente a distancia. Para ello, ha sido fundamental el uso de sistemas de gestión del aprendizaje (Learning Management System, LMS) [1]. A pesar de la era digital en la que nos encontramos, algunos de los factores principales que hace que el profesorado no utilice algún LMS son, tanto el tiempo que hay que dedicar a elaborar las tareas, como la necesidad de algunos conocimientos informáticos para poder usarlos [2].

Por otro lado, a la hora de realizar un examen presencial, ya existía preocupación por parte del profesorado sobre las prácticas deshonestas del alumnado [3]. Tras la llegada del COVID-19 junto con la evaluación a distancia, esta preocupación se vio incrementada. De hecho, se han publicado numerosos artículos al respecto [4], mostrando muchos métodos que diferentes universidades y docentes de manera particular utilizaban para tratar de disminuir las prácticas deshonestas del alumnado durante la evaluación. Tras hacer una revisión sobre el uso de exámenes online para evaluar el aprendizaje del siglo XXI, en [5] se recomiendan algunas estrategias para evitar prácticas académicas deshonestas

[1] *Department of Mechanical Engineering and Industrial Design. University of Cadiz (Spain). milagros.huerta@uca.es (Corresponding author). jacob.nunez@uca.es. mariavictoria.requena@uca.es.*

[2] *Department of Civil, Materials and Manufacturing Engineering. University of Málaga (Spain). mafernandez@uma.es*

durante el desarrollo de los exámenes. Entre ellas cabe resaltar la estrategia de usar múltiples versiones de un examen. De esta forma, cada estudiante tiene un examen diferente, para lo cual es muy importante el uso de las plataformas LMS. Además, en [5] se llega a la conclusión de que, cuando se usa la evaluación a distancia de manera efectiva, puede ser muy valiosa en la evaluación del aprendizaje del siglo XXI. El problema es que, para poder desarrollar e implementar un buen examen online, se suele dedicar más tiempo en preparar el examen online que en el contenido de las preguntas, además de la falta de preparación del profesorado en este tipo de actividades.

En este trabajo se muestra cómo se han preparado diferentes tipos de ejercicios de ingeniería estructural (extrapolable a cualquier contenido) que se corrigen automáticamente, usando MS Excel® y el *FastTest PlugIn* para generar preguntas parametrizadas con los cuestionarios de Moodle [6].

2. METODOLOGÍA

Para poder desarrollar muchos problemas iguales, pero con datos diferentes, en primer lugar, se ha usado MS Excel® para elaborar los problemas de estructuras, de manera que los datos del problema sean variables y los resultados se calculen automáticamente, como se muestra en la Fig. 1.

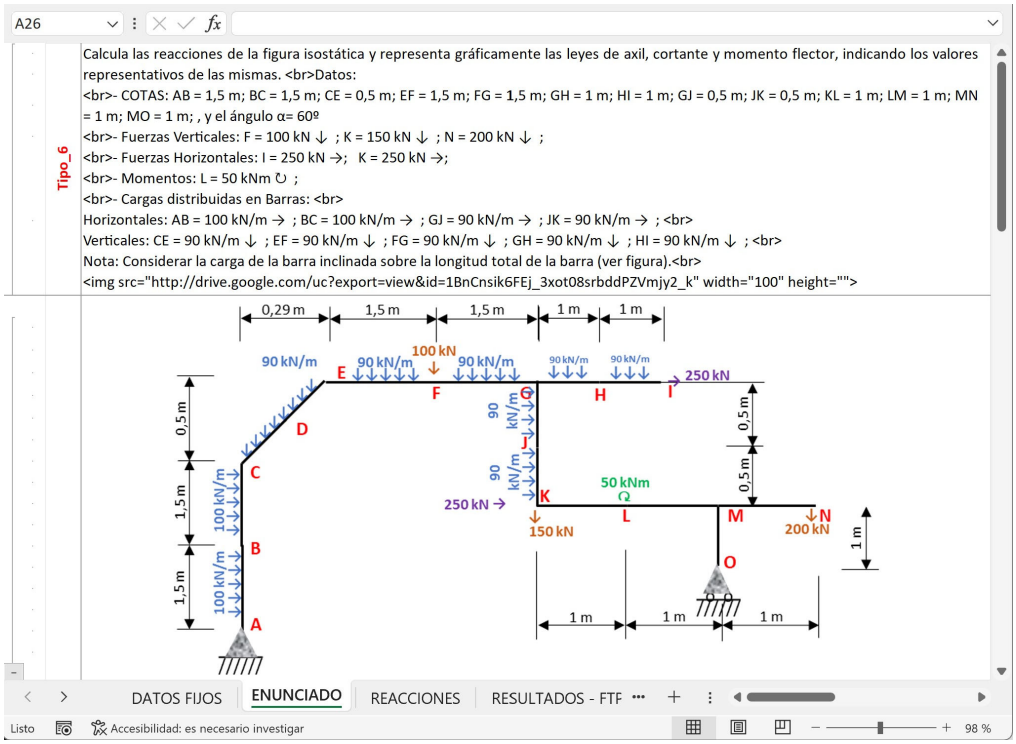

Figura 1. *Ejemplo de un problema preparado en MS Excel® de un pórtico, con datos aleatorios.*

Los datos de los diferentes problemas se pueden introducir a mano con unos datos concretos, o se pueden generar automáticamente con unos intervalos de valores concretos, usando la función de MS Excel® "ALEATORIO.ENTRE(*Valor mínimo*; *Valor máximo*)". Esta última opción es la mejor para generar muchos problemas diferentes sin que se repitan, aunque se han usado ambas propuestas. De este mismo problema, se han sacado varios diferentes (una viga con un pilar, una viga sola, una viga empotrada, etc.), simplemente haciendo cero algunos valores de cotas y cargas.

A continuación, se ha utilizado el complemento *FastTest PlugIn*, para generar preguntas tipo CLOZE de Moodle. Con ellas, el profesorado puede definir múltiples preguntas dentro de un mismo enunciado (generando espacios en blanco), asignando una puntuación a cada pregunta. Los estudiantes deben responder rellenando los espacios y Moodle evaluará todo automáticamente asignando la puntuación en función de las respuestas correctas. Las preguntas pueden ser de opción múltiple, respuesta corta o numérica, permitiendo a ésta última introducir un margen de error (tolerancia). En la Fig. 2, se muestra el problema con los códigos necesarios para poder exportarlo a Moodle, usando *FastTest PlugIn*. Aunque pueda parecer muy complejo, la codificación de las preguntas tipo CLOZE se generan automáticamente con el "FORMULARIO Códigos CLOZE" que tiene *FastTest PlugIn*. Usando este complemento, el profesorado no tiene que saber nada sobre la codificación de las preguntas tipo CLOZE.

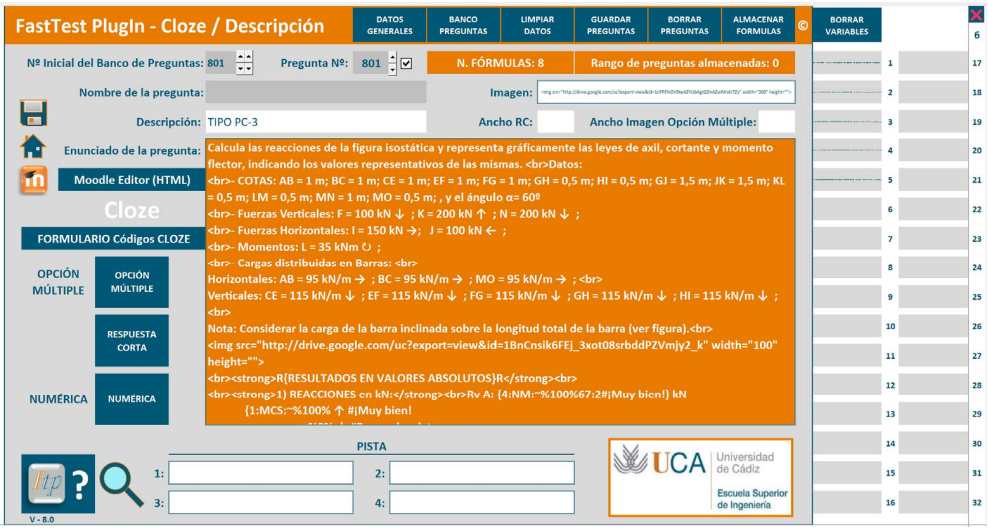

Figura 2. *Ejemplo del problema del pórtico preparado con FastTest PlugIn.*

Por último, para que el alumnado pueda seleccionar en Moodle qué diagrama corresponde a cada barra (axil, cortante y momento flector), se han preparado todas las combinaciones de posibles diagramas y se han codificado para que el programa los elija automáticamente según los datos obtenidos para cada barra y tipo de diagrama. La elaboración de estas imágenes ha llevado un tiempo, pero ya sirve para cualquier problema en el que se quiera que los estudiantes trabajen con diagramas. En la Fig. 3 se muestra cómo visualizan los estudiantes el problema y los diferentes datos que tiene que introducir.

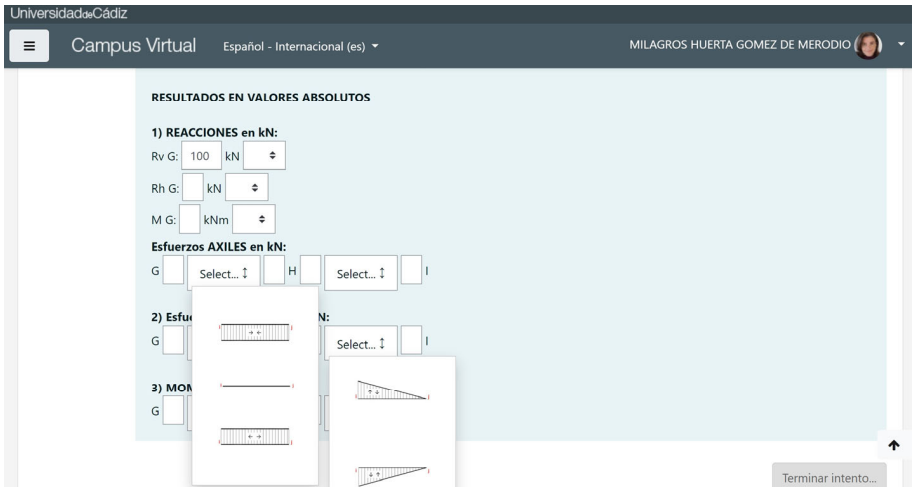

Figura 3. *Ejemplo un problema con selección de diagramas, tal y como se visualiza en la plataforma Moodle.*

En las preguntas tipo CLOZE de Moodle, no existe directamente la opción de poder incluir un menú desplegable con imágenes. Para poder realizar esta opción hay que incluir un script que se incluye directamente si se utiliza el complemento *FastTest PlugIn*. Tras preparar varios tipos de problemas, se han preparado grandes bancos de preguntas para las asignaturas de Resistencia de Materiales tanto en la Universidad de Cádiz como en la de Málaga. En primer lugar, se puso a los estudiantes a que realizaran una prueba de evaluación online. Una vez pasada dicha prueba, se puso los ejercicios a disposición del alumnado para que practicaran (sin nota), con un número ilimitado de intentos.

3. CONCLUSIONES

La principal conclusión que se ha sacado con este trabajo es que, a pesar de que ha llevado cierto tiempo desarrollar los primeros problemas (al menos el primero de cada tipo), este tiempo se amortiza a corto plazo, pues ahorra mucho tiempo de corrección. Para clases masificadas, el tiempo invertido se amortiza más rápidamente. Por otro lado, dado que en la docencia universitaria presencial se suele hacer la evaluación final de manera presencial, esta metodología sirve para la evaluación continua, pudiendo poner a los estudiantes a realizar los ejercicios tanto en sesiones presenciales como desde su casa. Habiendo un examen final con el que se pueda comprobar que el estudiante ha adquirido los conocimientos necesarios para aprobar la asignatura. En este caso, se les puede dejar que hagan los ejercicios en su casa, indicándoles que, si no sacan una nota mínima en el examen final presencial, no pueden aprobar. Por último, esta metodología ha tenido muy buena acogida por parte del alumnado, pues podían realizar el mismo ejercicio con datos diferentes y podía ir practicando y tener el resultado y la corrección en el momento de cerrar el cuestionario. Además, un comentario de uno de los estudiantes cuando se les preguntó qué les parecía la metodología ha sido que le ha venido muy bien poder realizar ejercicios de diagramas que se corrijan automáticamente, pues es algo que les cuesta mucho entender y con estos problemas tienen la solución al instante.

REFERENCIAS

[1] Al-Fraihat, D., Joy, M., Masadeh, R. & Sinclair, J. (2020). Evaluating E-learning systems success: An empirical study. *Comput Human Behav, 102, 67–86.*

[2] Pazos, A. J. B., Ruiz, B. C. & Pérez, B. M. (2020). Digital transformation of university teaching in communication during the covid-19 emergency in Spain: An approach from students' perspective. *Revista Latina de Comunicación Social, 78, 265–287*.

[3] Comas, R., Sureda, J., Casero, A. & Morey, M. (2011). La integridad académica entre el alumnado universitario Español. *Estudios Pedagógicos, 37, 207–225.*

[4] Shakeel, A., Shazli, T., Salman, M. S., Naqvi, H. R., Ahmad, N. & Ali, N. (2021). Challenges of unrestricted assignment-based examinations (ABE) and restricted open-book examinations (OBE) during COVID-19 pandemic in India: An experimental comparison. *Human Behav and Emerg Tech, 1050–1066.*

[5] Boitshwarelo, B., Reedy, A.K. & Billany, T. (2017). Envisioning the use of online tests in assessing twenty-first century learning: a literature review. *RPTEL 12, 16*.

[6] Huerta, M., Caballero-Hernández, J.A. & Fernández-Ruiz, M.A. (2022). Comparative Study of Moodle Plugins to Facilitate the Adoption of Computer-Based Assessments. *Applied Sciences (Switzerland), vol. 12, no. 18.*

Bars overlapping in tensegrity structures belonging to the Octahedron family

Carbonell-Márquez, Juan Francisco[1]; Fernández-Ruiz, Manuel Alejandro[1]

ABSTRACT

When performing the form-finding process of full-forms of tensegrity structures it is observed that beyond the double-expanded octahedron, struts overlapping occurs in space, making practicably impossible to materialize the tensegrity to employ it as a real structure. As the spatial coordinates of nodes that determine the geometry of the structure are provided as a linear combination of vectors composing a base of null space of the tensegrity force density matrix, an analytical study is carried out to check the existence of any combination of those vectors that avoids the overlapping of bars.

Keywords: tensegrity, octahedron family, form-finding, force density method.

1. INTRODUCTION

Tensegrity structures are, in general, spatial pin-jointed structures composed by compression (struts or bars) and tension (cables) elements which are pre-stressed so that the whole structure results free-standing and self-equilibrated [1]. The application of this kind of structures is becoming more and more widespread [2][3].

One of the key steps in the design of tensegrity structures is the form finding process. Although there are different approaches, as reviewed in [4], one of the most employed is the Force Density Method (FDM) proposed by Schek [5], based on the concept of force:length or force density ratio q to linearize the equations of equilibrium of the structure. The main equations in the FDM for a tensegrity structure are given by Eq. (1):

$$\begin{aligned} \mathbf{D}\cdot\mathbf{x}&=\mathbf{0}\\ \mathbf{D}\cdot\mathbf{y}&=\mathbf{0}\\ \mathbf{D}\cdot\mathbf{z}&=\mathbf{0} \end{aligned} \tag{1}$$

where $\mathbf{x}$, $\mathbf{y}$, and $\mathbf{z}$ are n-dimension vectors that contains the x, y and z coordinates of the n nodes composing the tensegrity, and $\mathbf{D}\in\mathbb{R}^{n\times n}$ is the so-called force density matrix which is constructed according to Eq. (2):

$$D_{ij}=\begin{cases}\sum_{k\in\Gamma} q_k & \text{for } i=j\\ -q_k & \text{if nodes } i \text{ and } j \text{ connected by member } k\\ 0 & \text{otherwise}\end{cases} \tag{2}$$

being Γ the set of members (cables and struts) connected to node i. The total number of members in the structure is denominated by m. Given that the equilibrium equations to be solved (Eq. (1)) are a system of homogeneous equations, the solution implies $\mathbf{D}$ not to be full rank. Therefore, a set of proper

[1] *Departamento de Ingeniería Civil, de Materiales y Fabricación. Universidad de Málaga (ESPAÑA). jfcarbonell@uma.es (Corresponding author), mafernandez@uma.es*

force densities q need to be sought in order to accomplish this fact. As proved by Zhang and Ohsaki [6], if a d-dimension tensegrity is to be obtained, the rank deficiency of $\mathbf{D}$ needs to be greater or equal to $d+1$.

2. THE OCTAHEDRON FAMILY

One of the main inputs to the FDM are the nodal connectivity and the force density assignation for the members composing the connectivity of the structure. In this work, the connectivity or topology of the Octahedron family [1] is employed to build up the structure. The Octahedron family is based on 4-nodes rhombical cells which are composed by four tensioned cables and a compressed strut. The construction of the structure is made so that each node only receives a compressed strut. All the members in the family are built by duplicating nodes, cables and struts from the first member, the octahedron, that consists of three rhombical cells, that is, six nodes linked by three compressed bars and twelve tensioned elements. Figure 1 shows the basic rhombical cells and the three first members of the family. It is observed that the bars in the structures in the Octahedron family are grouped in 3 three groups of equal length and parallel bars.

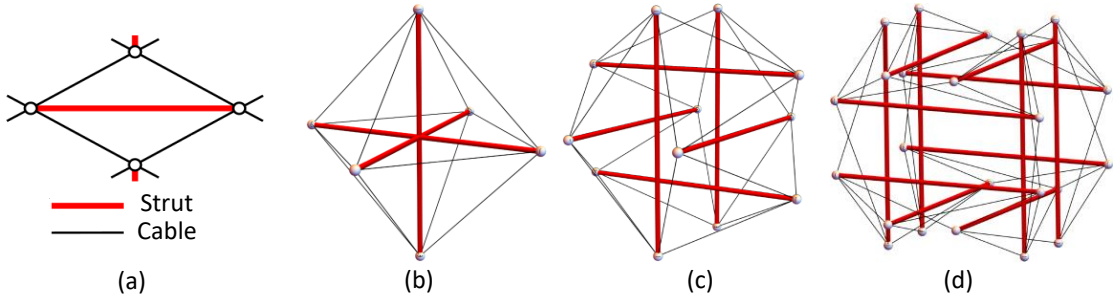

Figure 1. *The Octahedron family: (a) basic rhombical cell, (b) octahedron ($p=1$), (b) expanded octahedron ($p=2$), (c) double-expanded octahedron ($p=3$).*

An important aspect in the form-finding process of the different members of the Octahedron family is fullness. This is the property of the structure according to which there is no node with the same spatial coordinates as another in the structure. If this is accomplished, the structure is full. If not, then the structure is said to be folded. Fernández-Ruiz et al. [7] proposed that assigning all the same value of force density ratio, q_c, to the cables in the structure, and doing the same for the struts, q_s, then the following force density assignation leads to a 3D full form of the p-th member in the Octahedron family:

$$\frac{q_s}{q_c} = -\frac{p+1}{p} \tag{2}$$

The observed problem in the structures belonging to the Octahedron family appears when $p \geq 4$, that is, the triple-expanded octahedron. In those structures there are bars that overlap each other, as shown in Figure 2.

3. NODAL COORDINATES AS LINEAR COMBINATION OF BASE OF NULL SPACE OF $\mathbf{D}$ MATRIX

The force:length assignation performed by the relation given by Eq. (2) assures the matrix $\mathbf{D}$ rank deficiency of 4 to get a 3D tensegrity structure. By observing Eq. (1), the solutions $\mathbf{x}$, $\mathbf{y}$, and $\mathbf{z}$ are vectors which belong to the null space of matrix $\mathbf{D}$. Therefore, any linear combination of the vectors composing

a basis of the null space of $\mathbf{D}$ will provide a possible spatial realization of the tensegrity structure. If $\mathbf{e}^i \in \mathbb{R}^n$, with $i = \mathrm{I}, \ldots, \mathrm{IV}$, compose a basis of $\ker(\mathbf{D})$, then the nodal coordinates of the structure are given by:

$$\mathbf{j} = \sum_{i=\mathrm{I}}^{\mathrm{IV}} \alpha_j^i \cdot \mathbf{e}^i \tag{2}$$

with $j = x, y, z$, and α_j^i are twelve arbitrary real values chosen so that the vectors $\mathbf{x}, \mathbf{y}, \mathbf{z}$ are linearly independent. Different values of α_j^i will provide different geometries of the tensegrity structure.

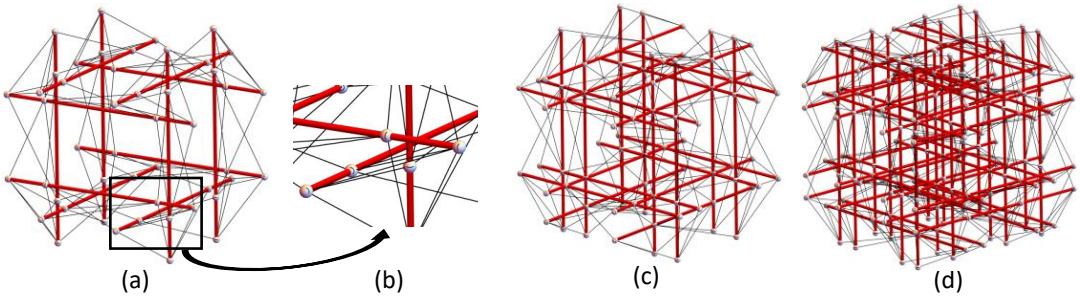

Figure 2. *Bars overlapping in the octahedron family when $p \geq 4$: (a) 3-expanded octahedron ($p = 4$), (b) detail of overlapped bars, (c) 4-expanded octahedron ($p = 5$), (d) 5-expanded octahedron ($p = 6$)..*

4. BARS OVERLAPPING AND LINEAR COMBINATION OF BASE OF NULL SPACE OF D MATRIX

By observation of the resulting structures when $p \geq 4$ and $\mathbf{X} = (\mathbf{x}, \mathbf{y}, \mathbf{z}) = \left(\mathbf{e}^i, \mathbf{e}^k, \mathbf{e}^l\right)$, with $i = \mathrm{I}, \ldots, \mathrm{IV}$, $k = \mathrm{I}, \ldots, \mathrm{IV}$, $l = \mathrm{I}, \ldots, \mathrm{IV}$, and $i \neq k \neq l$ it can be concluded that some bars in the structure are collinear and they overlap at some extent (Figure 2). Let us pay attention at to two of those overlapped bars, joining, say, nodes A and B and C and D. The parametric expression of the line defined by nodes A and B is:

$$\begin{aligned} x &= x_A + \gamma(x_B - x_A) = e_A^i + \gamma\left(e_B^i - e_A^i\right) = e_A^i + \gamma \Delta e_{AB}^i \\ y &= y_A + \gamma(y_B - y_A) = e_A^k + \gamma\left(e_B^k - e_A^k\right) = e_A^k + \gamma \Delta e_{AB}^k \\ z &= z_A + \gamma(z_B - z_A) = e_A^l + \gamma\left(e_B^l - e_A^l\right) = e_A^l + \gamma \Delta e_{AB}^l \end{aligned} \tag{3}$$

with $\gamma \in \mathbb{R}$. As the extremal node C of the other overlapped bar is on that line, then:

$$\begin{aligned} x_C &= e_C^i = e_A^i + \gamma_C \Delta e_{AB}^i \\ y_C &= e_C^k = e_A^k + \gamma_C \Delta e_{AB}^k \\ z_C &= e_C^l = e_A^l + \gamma_C \Delta e_{AB}^l \end{aligned} \Leftrightarrow \gamma_C = \frac{\Delta e_{AC}^i}{\Delta e_{AB}^i} = \frac{\Delta e_{AC}^k}{\Delta e_{AB}^k} = \frac{\Delta e_{AC}^l}{\Delta e_{AB}^l} \tag{4}$$

The question now is: is there any combination of α_j^i so that $(\mathbf{x}, \mathbf{y}, \mathbf{z}) \neq \left(\mathbf{e}^i, \mathbf{e}^k, \mathbf{e}^l\right)$ and node C of the overlapped bar changes its relative position to A and B and the overlapping disappears? If the nodal coordinates are given as a linear combination of a base of $\ker(\mathbf{D})$, Eq. (2), now the line AB remains:

$$j = \sum_{i=\mathrm{I}}^{\mathrm{IV}} \alpha_j^i \cdot e_A^i + \gamma \sum_{i=\mathrm{I}}^{\mathrm{IV}} \alpha_j^i \cdot \Delta e_{AB}^i \tag{5}$$

with $j = x, y, z$. Let us assume that the coordinates of the extremal node C of the other bar can be written as:

$$j_C = \sum_{i=\mathrm{I}}^{\mathrm{IV}} \alpha_j^i \cdot e_C^i = \sum_{i=\mathrm{I}}^{\mathrm{IV}} \alpha_j^i \cdot e_A^i + \gamma_j \sum_{i=\mathrm{I}}^{\mathrm{IV}} \alpha_j^i \cdot \Delta e_{AB}^i \quad (6)$$

with $j = x, y, z$. Therefore, if the extremal node C of the other bar is not on line AB, then $\gamma_x \neq \gamma_y \neq \gamma_z$. Rearranging Eq. (6) and considering that $\gamma_C = \frac{\Delta e_{AC}^i}{\Delta e_{AB}^i}$ (Eq. (4)):

$$\sum_{i=\mathrm{I}}^{\mathrm{IV}} \alpha_j^i \cdot \Delta e_{AC}^i = \gamma_j \sum_{i=\mathrm{I}}^{\mathrm{IV}} \alpha_j^i \cdot \Delta e_{AB}^i \Leftrightarrow \gamma_C \sum_{i=\mathrm{I}}^{\mathrm{IV}} \alpha_j^i \cdot \Delta e_{AB}^i = \gamma_j \sum_{i=\mathrm{I}}^{\mathrm{IV}} \alpha_j^i \cdot \Delta e_{AB}^i \quad (6)$$

Therefore $\gamma_C = \gamma_x = \gamma_y = \gamma_z$ and it can be concluded that for any linear combination of vectors composing a basis of $\ker(\mathbf{D})$, node C is always on line AB and retains its relative position with respect to the AB nodes. The same fact can be stated for the other extremal node D. So, the answer to the previously stated question is clear: no, bars AB and CD will always overlap no matter the chosen linear combination of basis of $\ker(\mathbf{D})$.

5. CONCLUSIONS

The form-finding process of tensegrity structures by means of FDM implies nodal coordinates of the structure to be calculated as a linear combination of vectors composing a basis of null space of the force density matrix $\mathbf{D}$. It has been shown that, although the Octahedron family is a very interesting source of tensegrity structures, a problem arises when dealing with high order members of the family: some bars overlap each other. It has been proven that no matter the chosen real coefficients to calculate the referred linear combination, the overlapping cannot be avoided, hindering the real materialization of the structure beyond the double-expanded octahedron.

REFERENCES

[1] Fernández-Ruiz, M.A., Hernández-Montes, E., Carbonell-Márquez, J.F., & Gil-Martín, L.M. (2019). Octahedron family: The double-expanded octahedron tensegrity. *International Journal of Solids and Structures, 165, 1-13.*

[2] Fraldi, M., Cutolo, A., Carotenuto, A.R., Palumbo, S., & Pugno, N. (2021). A lesson from earthquake engineering for selectively damaging cancer cell structures. *Journal of the Mechanical Behavior of Biomedical Materials*, *119*, *104533*.

[3] Bauer, J., Kraus, J.A., Crook, C., Rimoli, J.J., & Valdevit, L. (2021). Tensegrity metamaterials: toward failure-resistant engineering systems through delocalized deformation. *Advanced Materials, 33, 1-9*.

[4] Tibert, A.G., & Pellegrino, S. (2003). Review of form-finding methods for tensegrity structures. *International Journal of Space Structures, 18, 209-223*.

[5] Schek, H.-J. (1974). The force density method for form finding and computation of general networks. *Computer Methods in Applied Mechanics and Engineering, 3, 115-134.*

[6] Zhang, J.Y., & Ohsaki, M. (2005). Tensegrity Structures: Form, Stability, and Symmetry, p.300. Tokyo: Springer Japan.

[7] Fernández-Ruiz, M.A., M., Hernández-Montes, E., & Gil-Martín, L.M. (2022). Topological design of the octahedron tensegrity familiy. *Engineering Structures, 259, 114211*.

Boundary Elements Method applied to modeling and study of soil-foundation interaction using nonlinear elastic supports

Gutiérrez-Posada, Víctor[1]; Ubero-Martínez, Iván [1]; Cifuentes-Rodríguez, Jaime[1]; Vallepuga-Espinosa, José[1]

ABSTRACT

This work presents a numerical formulation to study the behavior of the soil which is modelled by elastic support as proposed by Winkler. In Winkler's model, normal tractions and normal displacements to the boundary of the solid are unknown, but both are related by the ballast coefficient. Moreover, tensile tractions are not allowed, increasing the non-linearity of the problem. The proposed formulation is based on Boundary Element Method (BEM) and it is applied to the resolution of 3D elastic problem.

Different soil types are modeled to analyze the relationship between the ballast coefficient and the material young's modulus. Thus, it is possible to determine the behavior of the foundation is rigid or flexible.

Finally, a double iterative procedure is used to obtain a solution which non tensile tractions in both foundation base and the pier-foundation common contact interphase.

Keywords: Boundary element method, Winkler support model, Nonlinear boundary condition

1. INTRODUCCIÓN

Las zapatas son un tipo de cimentación que consiste en ampliar la base de pilares para transmitir sus cargas al terreno. Uno de los tipos más utilizados son las zapatas aisladas, que trasmiten las cargas de un único pilar [1]. En 1867, Emil Winkler [2] propone por primera vez la relación entre las fuerzas de reacción y el movimiento de la zapata. Los soportes elásticos de Winkler modelizan el terreno mediante un muelle vertical y lineal cuya rigidez está determinada por el denominado coeficiente de Balasto o coeficiente de Winkler. Diversos trabajos se basan en el análisis de soportes tipo Winkler utilizando el Método de los Elementos de Contorno[3], [4].

2. SOLUCION TEÓRICA DEL PROBLEMA

Para el dimensionamiento de zapatas aisladas, el Código Técnico de la Edificación [5] propone el uso del concepto de rigidez relativa entre suelo-estructura, de tal forma que considera rígida la zapata si la distribución de tensiones es lineal y flexible en el caso contrario. Para unas dimensiones como las mostradas en la Fig. 1 se considera que la zapata es rígida cuando se cumple:

$$v \leq \frac{\pi}{4} \sqrt[4]{\frac{E_C I_C}{B K_{BC}}} \tag{1}$$

[1] *Departamento de tecnología minera, topográfica y de estructuras. Universidad de León (ESPAÑA). vgutp@unileon.es (Corresponding author). iubm@unileon.es. jcifr@unileon.es. jvale@unileon.es*

siendo v el vuelo de la zapata en cualquier dirección, E_C el módulo elástico del material de la zapata, I_C el momento de inercia de la sección de la zapata perpendicular a la dirección del vuelo considerado respecto a la horizontal que pasa por su centro de gravedad, B el ancho de la zapata en la dirección perpendicular al vuelo considerado, y K_{BC} el coeficiente de balasto a utilizar.

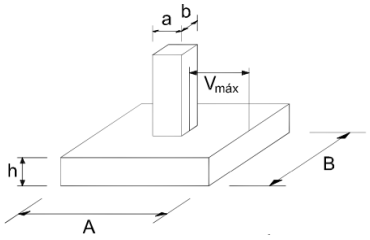

Figura 1. *Criterio de rigidez relativa para zapatas*

3. MÉTODO PROPUESTO

Se propone un método doblemente iterativo basado en la resolución del problema elástico de contacto en el cual, por un lado, se comprueba que no existen tracciones en la base de la zapata y en el caso de que aparezcan, se modifican las condiciones de contorno en dicha zona para permitir desplazamientos recalculando nuevamente el problema hasta encontrar una solución en la que no aparezca ninguna zona traccionada. Por otro lado, se analizan las tensiones en la zona de contacto pilar-cimentación, pudiendo llegar a una solución en la que solo aparezcan compresiones en dicha zona si se diera el caso de que el material o anclaje del pilar no soporta tracciones.

Además, en la zona de la zapata con apoyos Winkler, para establecer la condiciones de contorno, se desconoce el valor de la tensión y el desplazamiento en dichos nodos, pero se conoce la relación entre ellos mediante el denominado coeficiente de balasto. Esta relación se define como:

$$t_1 = - K_{BC} u_1 \tag{2}$$

siendo t_1 y u_1 la tensión y desplazamiento en cada nodo respectivamente.

4. EJEMPLO

En este ejemplo se considera un pilar aislado de acero sobre una zapata. Las dimensiones son mostradas en la Fig. 2 a). Las propiedades del material del pilar son E = 210 GPa y ν = 0,3 y del material de la cimentación son E = 25 GPa y ν = 0,3. Para su análisis mediante MEC se discretiza el contorno con elementos triangulares planos con el nodo situado en el baricentro. El mallado se puede ver en la Fig. 2 b). Se utilizan condiciones de simetría en los planos ZX e YZ para evitar discretizar dichos planos. En la parte superior del pilar se aplica una carga vertical hacia abajo de 10 MPa, con el resto de condiciones de contorno $t_1 = t_2 = t_3 = 0$. En la base se utilizan diferentes coeficientes de balasto, mostrados en la *Tabla 1.* Para estos valores se estudian las tensiones en la base comprobando que, de acuerdo con la

Eq. (1), la cimentación se comporta como rígida o flexible. Se grafican las tensiones en los nodos cercanos al eje de simetria, con coordenada x = 28,33 mm y con coordenada y = 14,58 mm para los diferentes coeficientes de balasto, dando una idea de cómo cambian estas en función del coeficiente de balasto utilizado. (Fig. 3).

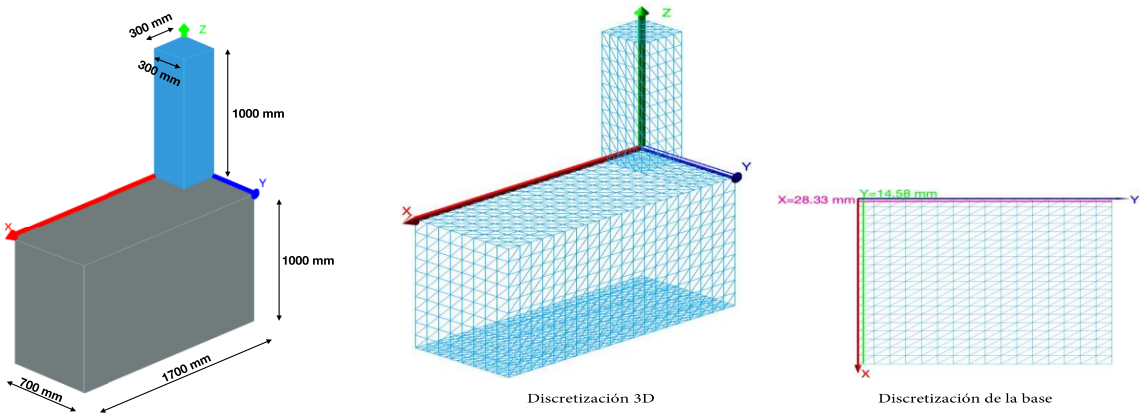

a) b)

Figura 2. a) *Geometría del problema*. **b)** *Discretización*

Tabla 1. Coeficiente de balasto utilizado

Tipo de Suelo	$\boldsymbol{K_{BC}[MPa/mm]}$
Arena media	0,04
Roca alterada	40
Roca sana	400

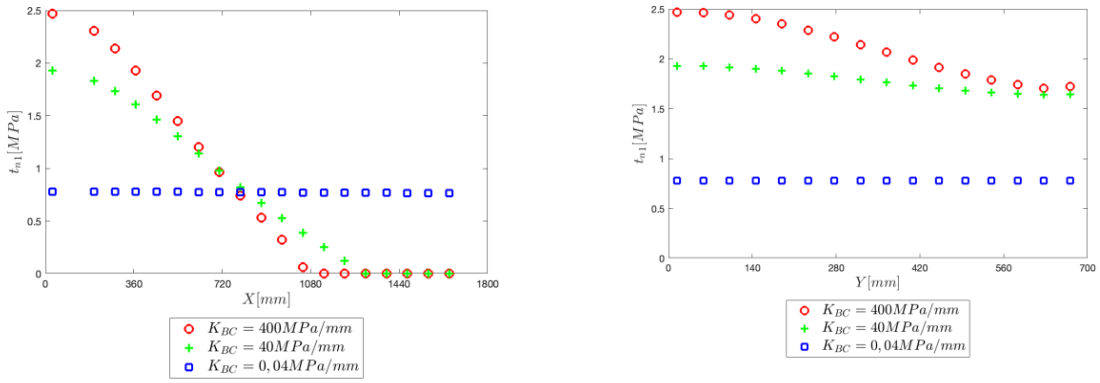

a) b)

Figura 3. *a) Tensiones para nodos con coordenada Y = 14,58 mm. b) Tensiones para nodos con coordenada X = 28,33 mm*

La Fig. 4 muestra la distribución de tensiones en la base de la cimentación para los diferentes valores del coeficiente de balasto considerado, señalando con una línea a partir de que valores la tensión es nula, es decir, la zapata se despega del terreno. La distribución se comporta de manera no lineal a medida que el valor del coeficiente de balasto aumenta, siendo completamente lineal para $\mathrm{k_{BC}} = 0{,}04\ \mathrm{MPa/mm}$, lineal solo en el eje Y para $\mathrm{k_{BC}} = 40\ \mathrm{MPa/mm}$ y no lineal en ambos ejes para $\mathrm{k_{BC}} = 400\ \mathrm{MPa/mm}$.

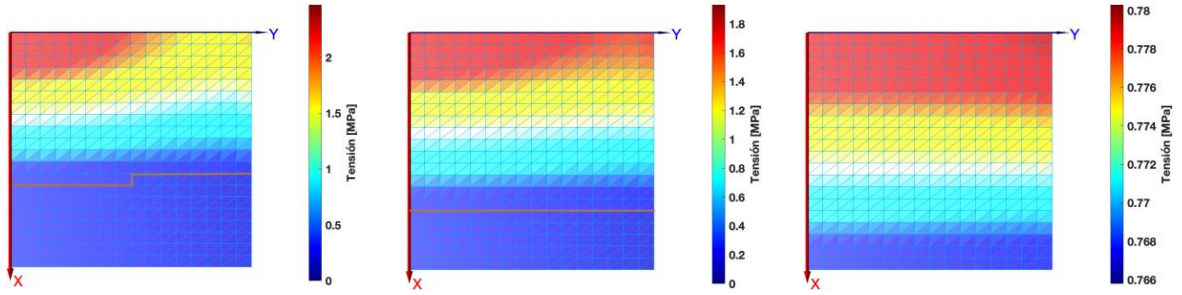

a) b) c)

Figura 4. *Distribución de tensiones en la base. a)* $K_{BC} = 400\ MPa/mm$. *b)* $K_{BC} = 40\ MPa/mm$. *c)* $K_{BC} = 0{,}04\ MPa/mm$.

5. CONCLUSIONES

La formulación propuesta cumple con lo expresado en la Eq. (1), es decir, muestra el comportamiento lineal o no lineal de la distribución de tensiones en la base de una cimentación teniendo en cuenta la relación entre las dimensiones de la misma, el módulo elástico del material y el coeficiente de balasto con el que se modela el suelo, por lo que se considera válida. Por lo tanto, se puede utilizar para estudiar el comportamiento de zapatas aisladas para cualquier tipo de suelo aplicando la teoría de Winkler.

REFERENCIAS

[1] Arboleda López, S. A., Marín Gil, M. I., Franco Álvarez, Y. A., y García Patiño, J. W. (2021). Cimentaciones: procesos constructivos y su diseño de ejecución. en Teknik. Medellín: Instituto Tecnológico Metropolitano.

[2] Winkler, E. (2016). Lehre von der elastizitat und festigkeit. Hansebook.

[3] Rashed, Y. F., Aliabadi, M. H., y Brebbia, C. A. (1998). The boundary element method for thick plates on a Winkler foundation, *Int. J. Numer. Methods Eng., vol. 41, n.º 8, pp. 1435-1462.*

[4] Vallepuga-Espinosa, J.,Sánchez-González, L., y Ubero-Martínez, I. (2019). Winkler Support Model and Nonlinear Boundary Conditions Applied to 3D Elastic Contact Problem Using the Boundary Element Method, *Acta Mech. Solida Sin., vol. 32, n.º 2, pp. 230-248*.

[5] Código Técnico de la Edificación (CTE) Documento Básico: Seguridad Estructural. Cimientos. (2019).

Calculation of the useful life of reinforced concrete structures from the mid-20th century, according to the standard ISO 15686.

Sánchez, Florinda[1]; Sanz, David[2]; Lagos, Francisco[1]

ABSTRACT

The durability of reinforced concrete structures depends on factors that are linked to environmental conditions, and maintenance that can lead to premature degradation in their life cycle. For buildings built in the modern era, it is of great value to calculate the useful life of reinforced concrete, based on qualitative data and non-destructive tests, which provide information on its current state, and the causes that causes deterioration; and in this sense, guide the choice of intervention measures to prevent further damage, and thus guarantee the survival of the asset in safe conditions of use. The useful life of two buildings for public use in Colombia dating from 1950 is calculated by the method proposed from the ISO 15686 Standard. The results guide an analysis methodology that can be replicated in other buildings of that time; as well as actions to prolong the useful life of these structures.

Keywords: Concrete structures, heritage building, useful life.

1. INTRODUCCIÓN

La norma ISO 15686 genera una metodología para estimar o predecir la obsolescencia de la vida útil de edificios y activos construidos, comparados con el número de años para el cual fue diseñado [1]. El análisis de condiciones relativas a la calidad del diseño, calidad de materiales de construcción, ejecución de obra, aspectos de uso, ambientes interiores y exteriores, mantenimiento, y restauración, como se presenta en la Tabla 1, ponderados por un valor de vida útil de referencia, arroja la vida útil estimada de un bien inmueble [2]. En la investigación que se presenta, se adopta la citada norma, para obtener el número de años de vida útil de dos edificaciones en concreto reforzado, catalogadas como inmuebles patrimoniales, que orientará a los órganos de decisión en las propuestas de buenas prácticas, basadas en evidencias alineadas con los objetivos específicos de usos futuros de estas edificaciones, dando prioridad a la seguridad de los habitantes sin detrimento de los valores patrimoniales del bien.

2. METODOLOGÍA

El estudio se propone desde el análisis de datos de carácter histórico recopilados en fuentes bibliográficas y archivos institucionales, con levantamiento de evidencias in situ, y análisis de muestras en laboratorio. Todos estos datos cuantitativos y cualitativos permiten calificar cada una de las siete

[1] *Facultad de ingeniería y arquitectura. Universidad Colegio Mayor de Cundinamarca (Colombia). florinda.sanchez@unicolmayor.edu.co (Corresponding author), flagos@unicolmayor.edu.co*

[2] *Departamento de construcción y tecnologías arquitectónicas. Universidad Politécnica de Madrid. david.sanz.arauz@upm.es*

condiciones citadas en norma ISO 15686. La revisión de planos históricos arroja datos para evaluar las modificaciones del diseño a lo largo de la vida del edificio desde su puesta en uso. Mediante el trabajo de campo se verifican las medidas de los elementos diseñados según planos históricos, adiciones y eliminaciones en la construcción, estado e integridad del sistema estructural. Se revisan también condiciones de ambiente intrínsecas y extrínsecas para identificar fuentes que propicien deterioro. De manera paralela se identifican lesiones y patologías producidas por el uso, o por factores externos, que pueden influir en el desempeño de las edificaciones y de sus componentes. En este sentido, las siete condiciones que determinan la vida útil estimada de un inmueble son: calidad de los diseños C1, calidad de los materiales C2, calidad de la ejecución de la obra C3, condiciones de uso C4, condiciones interiores y exteriores C5, mantenimiento C6, y restauración C7. De acuerdo con la metodología planteada por la ISO 15686, se obtendrá un valor de vida útil estimada VUE, tomando cada una de las condiciones encontradas en el inmueble, como factor multiplicador de la vida útil de referencia VUR Eq. (1).

$$VUE = VUR \times C1 \times C2 \times C3 \times C4 \times C5 \times C6 \times C7 \quad (1)$$

A cada una de las condiciones asociadas se asigna una clasificación de alto, medio, o bajo, representada en términos cuantitativos para el cálculo final de VUE así: 0.8 para deficiente, 1.0 para promedio, 1.2 para eficiente [3]. El valor de vida útil de referencia VUR o vida útil de diseño, se asocia con el certificado final, en el cual el arquitecto o constructor "certifica que la edificación entregada ha sido terminada según el proyecto aprobado y la documentación técnica que lo desarrolla" [4], lo que garantiza la estabilidad y solidez, útil para el fin previsto y la habitabilidad del inmueble [5]. El valor VUR en años, depende de la temporalidad prevista para la edificación, y el uso definido. Para estructuras de concreto reforzado, el Comité euro internacional del hormigón [6] proyecta una vida útil superior a los 50 años. De otra parte, el Instituto Geográfico Agustín Codazzi de Colombia IGAC, en la resolución 620 de 2008 [7] clasifica la vida útil de los inmuebles dependiendo del sistema constructivo. Por su parte, la Asociación Canadiense de Normas [8] establece valores entre 50 y 100 años dependiendo del uso. Los datos de las normas se muestran de manera comparativa en la *Tabla 1.*

Tabla 1. Vida útil de diseño para edificios

Norma	Descripción	Años
IGAC (2008)	Sistema estructural en mampostería, concreto o metálico	100
IGAC (2008)	Muros de carga	70
CSA (2001)	Uso residencial	50 a 99
CSA (2001)	Monumentos, edificios patrimoniales	Mas de 100
CEB-FIB (1995)	Concreto reforzado	Mas de 50

Como complemento del proceso, y en razón a la relación directa que hoy en día se tiene del ciclo de vida con el modelo de gestión por metodología Building Information Modeling BIM, se propone la integración de los datos de las siete condiciones de la Norma ISO 15686, utilizando el Manual de entrega de Información IDM, en los procesos y el flujo de información, durante el ciclo de vida de la edificación [9]. El IDM será la base para generar un mapa de procesos con aplicación en cada una de las dimensiones de HBIM para edificios patrimoniales [10]: 3D levantamiento arquitectónico, 4D evolución histórica, 5D diagnóstico, 6D mantenimiento, 7D conservación y restauración.

3. RESULTADOS

3.1. Comparativo entre edificio de 13 pisos para residencias universitarias, y templo para culto católico, los dos construidos entre 1950 y 1960 en concreto reforzado.

3.1.1. Condición: calidad de diseños del proyecto C1

La estructura del edificio fue diseñada en 1952 por el ingeniero Doménico Parma, pionero en el sistema en concreto reticular celulado para losas de entrepiso en Colombia [11] y director de los principales iconos de la época moderna como la torre Avianca en Bogotá. El proyecto arquitectónico estuvo a cargo de la firma Esguerra Sáenz Urdaneta y Suarez, reconocida oficina de arquitectura en el país a mediados del siglo XX. El templo fue diseñado en 1957, también por el ingeniero Doménico Parma, y el diseño arquitectónico con el manejo de concreto a la vista, tiene como autor a Germán Samper, discípulo de Le Corbusier. En esta condición, los dos casos reciben una clasificación alta, con un puntaje de 1.2.

3.1.2. Condiciones: calidad de los materiales C2 y calidad en la ejecución de obra C3

En el edificio se cuenta con datos cuantitativos de la resistencia media del concreto. Un valor corresponde a un estudio realizado en el año 2002 por extracción, corte y ensayo de núcleos que arrojó un valor de 20.2 MPa. En el mismo año se efectuó un estudio de ultrasonido con resultados promedio de 27 MPa. En el año 2022 se realizaron mediciones con esclerómetro, que arrojaron valores de 24.2 MPa. En el templo, las resistencias con esclerómetro arrojan valores promedio de 22.3 MPa. Teniendo en cuenta que, la resistencia de diseño de la época de los dos casos era de 21 MPa [12], se puede considerar una respuesta eficiente del concreto. De otra parte, el análisis petrográfico de una muestra de concreto extraída del edifico, arroja resultados analíticos que permiten decir que se trata de un concreto de árido de cuarzo puro con una gran porosidad intergranular, intragranular y por fisuras, con alteraciones por corrosión en los bordes. Se infiere que la porosidad presente en el concreto puede generar menor resistencia mecánica y mayor vulnerabilidad ante agentes nocivos del medio ambiente. Los datos de aceros de refuerzo arrojados por el ensayo de escaneo Ferroscan, indican la presencia de acero liso de ϕ7/8” en sentido vertical, y acero de ϕ 3/8” en sentido horizontal, en los elementos estructurales evaluados en los dos casos. Los flejes en los nudos de los pórticos son escasos, y se presentan fisuras por cortante en algunas vigas. Por la condición de calidad de los materiales, y calidad de la ejecución de obra se otorga una clasificación media, con un valor de 1.0 para los dos casos de estudio.

3.1.3. Condiciones de uso C4, condiciones interiores y exteriores C5, mantenimiento C6, y restauración C7

Según inspección visual y análisis del edificio, se encuentran en total abandono la mitad de los pisos, y se presenta alto grado de deterioro por fisuras, pérdida de recubrimientos y acero a la vista, humedades y adición de cargas muertas que afectan el diseño original. No existe un plan de mantenimiento preventivo para evitar mayores daños en la edificación. En el templo, los elementos estructurales a la vista presentan buen estado de mantenimiento, sin perdidas de recubrimiento, ni presencia de humedades que generen patologías asociadas. El mantenimiento es riguroso y está bajo la dirección de los administradores del inmueble. Por estas condiciones, se otorga un valor bajo de 0.8 al edificio, y un valor medio de 1.0 para el templo. Con los valores obtenidos se calcula la vida útil esperada para los dos inmuebles patrimoniales, tomando como vida útil de referencia, 100 años, por tratarse de inmuebles patrimoniales en concreto reforzado.

3.2. Cálculo de vida útil esperada VUE

1. VUE del $edificio = 100 \times 1.2 \times 1 \times 1 \times 0.8 \times 0.8 \times 0.8 \times 0.8$
VUE del edificio $= 49.15$ años
2. VUE del $templo$ = 100 × 1.2 ×1 × 1 ×1 × 1× 1 × 1
VUE templo $= 120$ años

4. CONCLUSIONES

De acuerdo a los resultados obtenidos para la VUE de las dos edificaciones, se evidencia la importancia que representa contar con un buen nivel de diseños, calidad en los procesos constructivos y en los materiales de construcción, que, para el caso de edificaciones patrimoniales, son procesos que no se pueden controlar en el presente, pero que inciden en la vida útil esperada. En los dos casos analizados, de edificaciones en concreto reforzado de la época moderna, los factores diferenciadores que incrementaron la vida útil esperada, fueron las condiciones de uso, el nivel de mantenimiento y la prevención de daños, con lo cual el templo analizado tendría 70.85 años más de vida que el edificio de 13 pisos, y logra 20 años más, de su vida útil de diseño.

REFERENCIAS

[1] International Standards Organization (2008), ISO 15686- 8:2008, Buildings and constructed assets — Service-life planning — Part 8. https://www.iso.org/standard/39070.html

[2] NORMA CUBANA Edificios y bienes inmobiliarios construidos — planificación de la vida de servicio parte 1: principios generales y estructura (ISO 15686-1: 2011, IDT) (2015). Oficina Nacional de Normalización (NC). La Habana. Cuba.

[3] Hernández M, S. (2014) Planeación de la vida útil en proyectos arquitectónicos. Revista Temas de Ciencia y Tecnología vol. 18 número 53 mayo - agosto 2014 (pp. 54 – 56).

[4] Martínez, C. (2007). Responsabilidades y garantías de los agentes de la edificación. Editorial LexNova. 3era edición. Valladolid España. (pp. 38).

[5] García, F. (2006). Compendio de arquitectura legal derecho profesional y valoraciones inmobiliarias. Segunda edición. Editorial Reverté S.A. Barcelona. (pp. 181).

[6] Comite Euro internacional del hormigón (1995) Código modelo CEB- FIB para hormigón structural. Editorial Colegio de Ingenieros de Caminos, Canales y Puertos; 1ª ed.

[7] Instituto Geográfico Agustín Codazzi IGAC (2008). Resolución No. 620 del 23-09- 2008.Bogota. Col.

[8] Canadian Standards Association (2001), S478-95 (R2001), Guideline on Durability in Buildings, Toronto, CSA, pp. 9-17.

[9] Manrique, S. (2017). Metodologías y tecnologías para una construcción colaborativa. PlanBIM. Dirección general de obras públicas. Chile. https://www.mop.cl/papel/descargables/Sesion2BIM.pdf

[10] Merchan, P., & Santiago, S. (2018). Pasado, presente y futuro de los HBIM (Heritage/Historic Building Information Models). (pp. 1069-1077). Badajoz España: Universidad de Extremadura

[11] Villate, C., (2008). Edificios en altura. La carrera técnica por ganar en el Skyline, el caso colombiano: Doménico Parma. Dearq, (3), 61-65.

[12] Medina, J. (2003) Evaluación estructural del bloque C-2 de las residencias universitarias 10 de mayo. Departamento de ingeniería civil. Universidad Nacional de Colombia.

Characterization of lime-based grout enriched with nanoadditives.

Garduño, Carlos[1]; Cámara, Margarita[1]; Baeza, Juan Ramón[2]; Aguilar, Jaime[1]; Rodríguez, Rubén[1]; Compán, Víctor[1]

ABSTRACT

This research is centered around developing an injection grout for the structural repair of stone buildings by using lime-based grouts enriched with nanoadditives like multiwall carbon nanotubes or graphene oxide. The primary objective is to standardize these grouts in order to enhance their strength properties and effectively transforming them into piezoresistive materials. Upon injecting these grouts into stone pieces, they become sensitive to damage, breakage, or load variations, which are evident through changes in electrical conductivity when an electric current is applied. Various combinations of these compounds have been used to create diverse grout formulations.

An extensive testing campaign has been conducted on both the liquid grouts and the test pieces, encompassing assessments of flowability, uniaxial compression strength, and the attainment of piezoresistive properties, all in comparison to the original grout. Initial findings indicate an increased resistance in the test pieces and the successful achievement of electrical conductivity.

Keywords: *multiwall carbon nanotubes, graphene oxide, lime-based grout, tensile strength, piezoresistive properties*

1. RESEARCH DEVELOPMENT

There are certain types of stone, especially the calcarenite stone from southern Andalusia, which, in addition to having low resistant properties [1], have seen their physical, mechanical [2] and resistance properties deteriorated over time since they were extracted from the quarry until they reach our days as compositional pieces of the structure of a building. In this context, to repair and preserve buildings, as well as to improve the properties of structural stone, injection lime-based grouts have been used to fill fissures, cracks, etc. [3], provide cohesion and increase the mechanical properties of fillers in masonry walls.

What is intended to be done in this research is to elaborate and standardize a lime-based grout with nanoadditives such as carbon nanotubes [4] and/or graphene oxide. These additions are capable of improving the mechanical properties of the original grout [5], and therefore of the stone into which it is injected. It is also capable of helping to detect possible discontinuities, internal damage or wide intergranular spaces inside the stone elements, taking advantage of the piezoresistive/electrical properties provided by nanoadditives.

The ultimate goal of the research is to inject these grouts and fill the open capillary network that the calcarenite stone presents. However, the intermediate steps would be to make grouts, achieve suitable proportions and characterize their properties [4]. In the first instance, the grouts were elaborated using the Mapei Mape Antique I product, especially indicated for the injection of masonry elements. Up to 56 grouts of this product have been made, following different concentrations of carbon nanotubes (CNT) and graphene oxide (graphene). The types of mixtures have been:

[1]*Dep. de Estructuras de Edificación e Ingeniería del Terreno. Universidad de Sevilla (Spain). cgarduno@us.es* (corresponding author), *mcamara@us.es*, *jav@us.es* , *rrodriguezr@us.es, compan@us.es*

[2]*Dep. de Construcciones Arquitectónicas II. Universidad de Sevilla (Spain). jbaeza@us.es*

Table 1. Types of lime-based grouts mixtures executed

Mixed Grout Type Code	Value - % wt according to binder				
	Binder	%Distilled Water	%Fluidizer	%MWCNT	%Graphene
M_AD35	Mape Antique I	35	0	0	0
M_AD35_SP1_1,2	Mape Antique I	35	1,2	0	0
M_AD35_AQ_0,035_SP1_1,2	Mape Antique I	35	1,2	0,035	0
M_AD35_AQ_0,070_SP1_1,2	Mape Antique I	35	1,2	0,070	0
M_AD35_AQ_0,140_SP1_1,2	Mape Antique I	35	1,2	0,140	0
M_AD35_GP_0,035_SP1_1,2	Mape Antique I	35	1,2	0	0,035
M_AD35_GP_0,070_SP1_1,2	Mape Antique I	35	1,2	0	0,070
M_AD35_GP_0,140_SP1_1,2	Mape Antique I	35	1,2	0	0,140

Cubic 50x50x50mm grout test pieces and 160x40x40mm prismatic test pieces have been manufactured using steel molds to carry out the tests. Uniaxial compression has been tested according to the UNE 196-1 Determination of Resistance standard, as well as injectability according to the UNE-EN 445 standard, using a Marsh cone.

Figure 1. ***Left)*** *Filling of molds.* ***Right)*** *Cubic and prismatic lime-based grout test specimens.*

The proportions of nanoadditives represent less than 0.2% of the total weight of the binder in any combination. With this minimal addition, significant improvements are already achieved in the mechanical-resistant behavior of the grout and electrical conductive effects are achieved. The addition of the fluidizer is due to the fact that when the nanoadditives are added, the mixture loses fluidity and becomes thicker, a fundamental parameter to be able to perform injections into the stone. Even more for it to penetrate the free capillary network of the same. The minimum pore size in stone is 100µm, so the grouts used in the investigation must have a minimum particle width, smaller than said pore.

Table 2. Compressive Tensile Strength after setting (MPa).

	M_AD35	M_AD35 _SP1_1,2	M_AD35_A Q_0,140_SP 1_1,2	M_AD35_A Q_0,070_SP 1_1,2	M_AD35_AQ _0,035_SP1_ 1,2	M_AD35_G P_0,140_SP 1_1,2	M_AD35_G P_0,070_SP 1_1,2	M_AD35_ GP_0,035_ SP1_1,2
7	15,557	12,977	14,003	16,593	12,787	11,140	14,068	14,567
14	21,330	22,920	25,217	23,990	23,260	16,810	19,556	20,457
>=28	24,2	29,321	31,053	28,915	30,062	22,110	26,139	26,645

In general, the addition of the fluidizer also improves the uniaxial compressive strength of the specimens since it also improves the setting of the grout. However, the addition of carbon nanotubes further improves the increase in compressive strength of the specimens made with this grout. The increase in compressive tensile strength of the original grout increases from 24,2 MPa to 31,05 MPa of the one with the maximum concentration of MWCNT (0,14% wt). This represents an improvement of

128% at 28 days of setting. If we compare the original grout with fluidizer only and the one with more concentration of MWCNT, the improvement is 105% (from 29,31MPa to 31,05MPa). Other lime-based grouts products have been used to make test specimens and are being tested but their campaign is not finished yet, however they also show improvements in mechanical resistance without fluidizer.

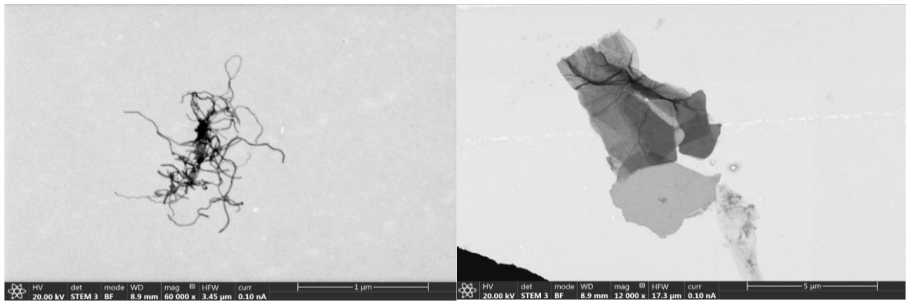

Figure 2. ***Left)*** *Multiwall Carbon Nanotube (MWCNT) Particles – Microscopy - STEM – CITIUS.* ***Right)*** *Graphene oxide plates – Microscopy - STEM – CITIUS*

Graphene oxide, on the other hand, does not represent a considerable improvement with respect to the original grout plus the fluidizer. The mixture sees the compressive strength diminished. Although it does demonstrate conductive behavior. This decrease in compressive strength may be due to the size of the graphene oxide molecules, which are much larger than those of MWCNT (diameter 0.001µm vs. 10µm). This fact could saturate the mixture and cause a deficiency in its cohesion. It can be seen in the values of the table that lower concentrations of graphene increase the breaking stress with respect to higher concentrations, so the proportion of this nanoadditive must be adjusted to incur a correct increase in mechanical properties.

A series of electric tests are being carried out to determine the gauge factor of the specimens. These tests consist on making flow a biphasic electric current (for preventing the polarization effect) through the specimen and measure changes in voltage-resistance while a strain is induced by load cycles [6]:

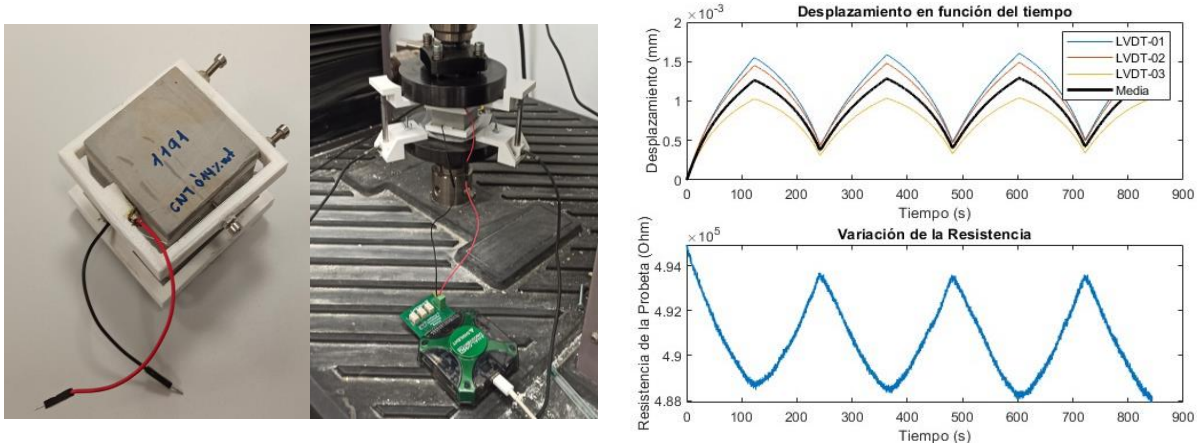

Figure 3. Left) *Electric measurement setup – Digillent Analog Discovery 2 + LVDTs.* ***Right)*** *Deformation (upper graph) and resistance lecture of a test specimen under load cycles (lower graph)*

2. CONCLUSIONS

In summary, the incorporation of nanoadditives into grouts offers significant improvements in compression resistance and has the potential to enhance traction, bending, and abrasion resistance as well.

Nanoadditives work by enhancing cohesion, filling gaps between grout particles, increasing density, and improving adhesion. This has widespread applications, including the restoration of stone structures by repairing cracks in masonry walls. However, there's ongoing research to determine the optimal proportions for enhancing grout properties when adding graphene oxide to the mixture. While it has achieved expected conductive properties, using the same weight ratio as nanotubes has not been effective, especially at higher concentrations. Establishing a percolation threshold for graphene proportion is advisable. Additionally, the electrical properties acquired in test specimens can be used to detect load changes, strain changes, and damages in the doped lime-based matrix of the grout. This monitoring principle can help prevent damage in stone structures filled with such grouts. However, further research is needed to inject the capillary network of stones with these grouts, and similar tests will have to be conducted on filled stones in the near future.

3. ACKNOWLEDGEMENTS

This work was supported by the "Secretaría General de Vivienda, Consejería de Fomento, Articulación del territorio y Vivienda of the Andalusian Regional Government (Spain)" under project US.22-05 (INYECT-NDT). The financial support is gratefully acknowledged.

4. REFERENCES

[1] Baeza, J., Compán, V., Cámara, M., Pachón, P., & Castillo, G. (2018). Identificación de las propiedades mecáni-cas de la piedra de San Cristóbal mediante técnicas no destructivas. En *REHABEN 2018, Euro-American Congress: Construction Pathology, Rehabilitation, Technology and Heritage Management*, 1098–1106.

[2] Baeza, J., Compán, V., Castillo, G., Cámara, M., & Pachón:, P. (2022) Determining static elastic modulus of weak sandstone in Andalusian historical constructions from non-destructive tests: San Cristóbal's stone. *Journal of Building Engineering, 57, 104864*.

[3] Gökyiğit-Arpaci, E.Y., Didem Oktay, N.Y., Serhan, U., & Dilek E.-A.(2019) *Performance evaluation of lime-based grout used for consolidation of brick masonry walls. Journal of Materials in Civil Engineering,* 31(6):04019059, 2019.

[4] D'Alessandro, A., Rallini, M., Ubertini, F., Materazzi, A.L., & Kenny, J.M. (2016). Investigations on scalable fabrication procedures for self-sensing carbon nanotube ce-ment-matrix composites for SHM applications. *Cement and Concrete Composites*, *65, 200–213*.

[5] Restuccia, L., Lopez, A., Ferro, G.A., Liberatore, D., & Tulliani, J.M. (2018). An investigation of the beneficial effects of adding carbon nanotubes to standard injection grout. *Fatigue & Fracture of Engineering Materials & Structures*, *41, 119–128*.

[6] Garcia-Macias, Enrique, Austin Downey, Antonella D'Alessandro, Rafael Castro-Triguero, Simon La-flamme y Filippo Ubertini: Enhanced lumped circuit model for smart nanocomposite cement-based sensors under dynamic compressive loading conditions. SENSORS AND ACTUATORS A-PHYSICAL, 260:45–57, JUN 15 2017, ISSN 0924-4247.

Consideration of the non-linear behavior materials in the structural analysis of the Church of Santa Ana in Sevilla by Finite Elements Method

Aguilar, Jaime[1]; Compán, Víctor[1]; Baeza, Juan Ramón[2]; Garduño, Carlos[1]; Rodríguez, Rubén[1]; Pachón, Pablo[1]

ABSTRACT

This research is centered in to bring the numerical models structural behavior closer to the real behavior of the Church of Santa Ana in Seville, through of high-definition geometric models that incorporate the non-linear materials' behavior.

This church is presented as an unique case study due to the geometric complexity of its vaults and the influence on the structural behavior of the constructive solution of its passable roof. The model has been developed “as it” and the result is a”high definition geometrical model”. To define the materials a dynamic identification campaign has been carried out using Operational Modal Analysis. A first linear analysis give us an approximation of the displacement levels and the stress state. With these results we decide to implement a constitutive model with nonlinear behavior using Concrete Damage Plasticity model in Abaqus Cae. The safety factor has been determinated increasing the gravity factor until the structural collapse.

Keywords: *masonry, vault, FEM, nonlinear behavior, high definition geometrical models.*

1. INTRODUCCIÓN

El objeto del presente trabajo es acercar el comportamiento estructural de los modelos numéricos de cálculo al comportamiento real de la Iglesia de Santa Ana de Sevilla, en Triana, mediante la elaboración de modelos geométricos de alta definición para su análisis por el MEF. Así mismo, se evaluará su estado tensional en aquellas zonas singulares que presentan valores por encima de los límites elásticos preestablecidos inicialmente [1] mediante la implementación de modelos constitutivos que caracteri-cen el comportamiento no lineal de los materiales [2]. El trabajo concluye con la determinación del nivel de seguridad que presenta el edificio aplicando incrementos del factor de gravedad hasta llevar el modelo numérico al colapso [3].

Para el análisis estructural de la Iglesia, se ha elaborado un modelo geométrico “as it”, adaptando las diversas soluciones constructivas a la realidad ejecutada, tomando de referencia el trazado geométrico teórico de sus bóvedas. De esta forma, se ha estimado necesario llevar a cabo ciertas simplificaciones entendiendo que no van a repercutir en el comportamiento estructural de forma representativa. Quizás la más significativa haya sido la de considerar el cuerpo de naves de forma modular estableciendo los tramos de bóvedas todos de la misma dimensión con planos de simetría transversales. Otro de los as-pectos considerados ha sido la de hacer coincidir los nervios longitudinales del espinazo en las tres

[1]*Dep. of Building Structures and Geotechnical Engineering. University of Seville (Spain). jav@us.es (Corresponding autor), compan@us.es ; cgarduno@us.es ; rrodriguezr@us.es ; ppachon@us.es*
[2]*Dep. of Architectural Construction II. University of Seville (Spain). jbaeza@us.es*

naves con las claves de los arcos. Respecto al arranque de nervios y el trazado de bóvedas, se ha procedido siguiendo el mismo criterio constructivo que pudieran haber empleado sus constructores. El resultado es un modelo de alta definición geométrica (Fig 1).

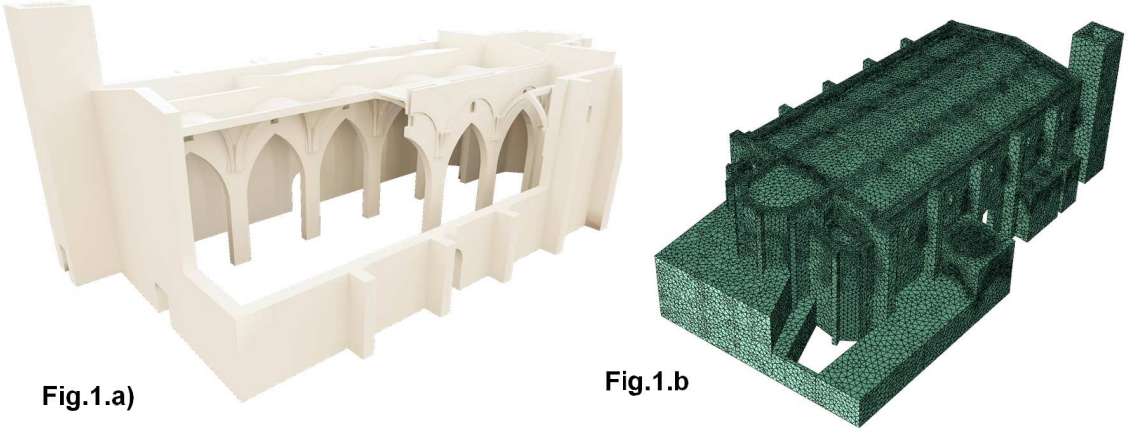

Figure 1. **a)** *Santa Ana. Representación del modelo geométrico con las simplificaciones adoptadas.* ***b)****. Modelo elaborado con la consideración del edificio en su totalidad (derecha).*

Para la caracterización de sus materiales se ha procedido mediante la realización de una campaña de identificación dinámica mediante OMA (Operational Modal Analysis) que nos ha permitido realizar un ajuste de las propiedades mecánicas de dichos materiales en los modelos numéricos hasta obtener un comportamiento dinámico en formas modales y frecuencias de vibración análogo al obtenido en la campaña de vibración ambiental (Tabla 1) [4].

Tabla 1. Propiedades mecánicas actualizadas tras la calibración del modelo numérico.

PROPIEDADES MECÁNICAS	**ρ** **Kg/m³**	**f_b** **MPa**	**f_m** **MPa**	**f_c** **MPa**	**f_t** **MPa**	**E** **MPa**	**ν**
MATERIAL COMPUESTO FÁBRICA DE PIEDRA	1.800	5,65	3	1,91	0,2	3.000	0,25
MATERIAL COMPUESTO FÁBRICA DE LADRILLO	1.800	13	3	1,5	0,15	1.800	0,25
MATERIAL COMPUESTO FÁBRICA DE LADRILLO EN PILARES	1.800	13	3	1,5	0,15	1.400	0,25
MATERIAL DE RELLENO	900	-	-	-	-	40	0,25
MATERIAL DE CUBIERTA	2.500					23.000	0,25

Un primer análisis en régimen lineal nos aporta una aproximación y un orden de magnitud tanto de los niveles de desplazamientos como del estado tensional localizándose zonas que superan los niveles de tensión admisibles de los materiales definidos. A la vista de estos resultados y analizando in situ los niveles de desplazamiento de un tramo del cuerpo de bóvedas mediante fotogrametría, se opta por implementar un modelo constitutivo que contemple el comportamiento en rango no lineal de estos

materiales. En este caso, un modelo en régimen elástico con la consideración de un comportamiento dañable plástico en rango no lineal distinguiendo tracciones y compresiones limitadas.

La metodología empleada para la realización de los modelos pasa por definir inicialmente su geometría mediante el software de generación de formas complejas Rhinosceros. Posteriormente se genera el mallado mediante métodos de generación adaptativa de malla con Ansys Icem y malla de tetraedros de 4 nodos de integración reducida (C3D4R). El análisis estructural se lleva a cabo con ABAQUS CAE. Respecto a las consideraciones de los materiales y para facilitar su estudio por el MEF, se establece la consideración del material como medio continuo e isótropo englobado en un único material ladrillo-mortero o piedra-mortero [5].

Desde el punto de vista tensional, los niveles de tracciones se han visto reducidos gracias a la redistribución de esfuerzos en las zonas más solicitadas, destacando las del cuerpo de bóvedas (**Fig.2.b**). Analizado este estado tensional y apreciándose el elevado nivel de solicitación en determinados elementos del conjunto (bóvedas, contrafuertes y pilares), se procede a realizar un nuevo cálculo que contemple un incremento del factor de gravedad hasta llevar la estructura al colapso numéricamente. De esta forma, se procede aumentando cuatro veces la gravedad obteniéndose como resultado un incremento de capacidad de carga de un 18% sobre el análisis anterior, arrojando un factor multiplicador de 1,72g. En relación a las patologías que se han podido detectar en la Iglesia, se analiza numéricamente la deformación plástica equivalente (PEQT) a las tensiones de tracción (tensile equivalente plastic strain $\varepsilon_t^{\sim pl}$) así como la evolución de la fisuración.

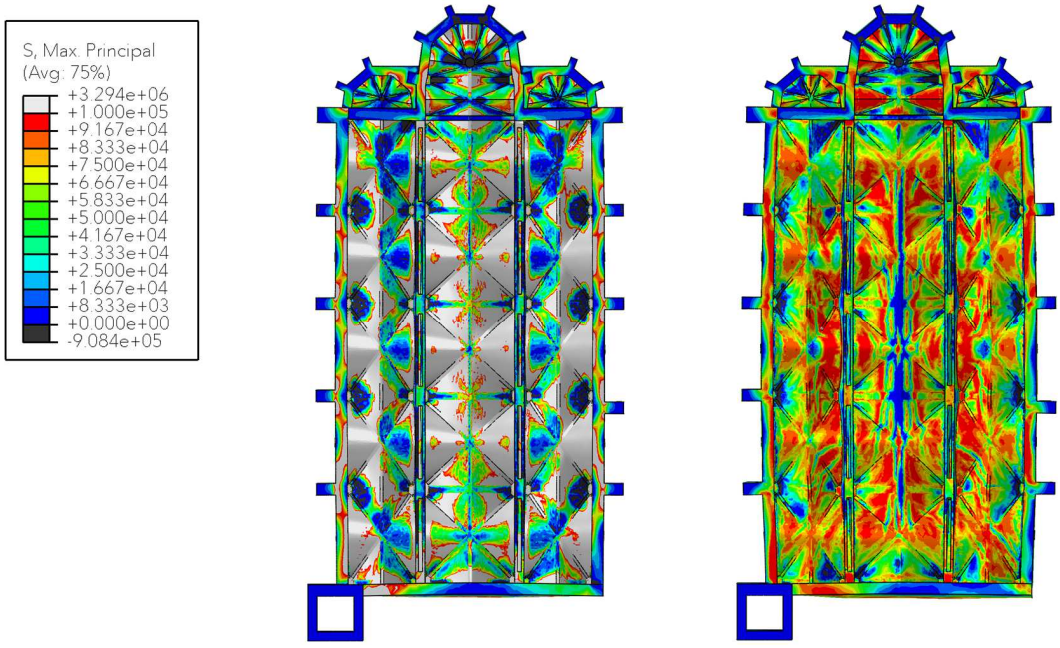

Fig.2.a **Fig.2.b**

Figure 2. a) Mapa de Tensiones Principales Máximas de Tracción en régimen de comportamiento lineal (Smax, N/m²). **b)** Mapa de Tensiones Principales Máximas de Tracción en régimen de comportamiento No lineal (Smax, N/m²).

2. CONCLUSIONES

La metodología empleada en la elaboración de modelos de alta definición geométrica mediante softwares de generación de formas complejas y su posterior análisis estructura mediante el MEF se presenta como una potente herramienta para la caracterización de edificios esta complejidad

La implementación del comportamiento no lineal de los materiales presenta unos resultados más adecuados al comportamiento real del edificio y de las patologías que éste presenta, consiguiéndose identificar con estos modelos la localización de las fisuras en zonas análogas a las identificadas en el edificio. La calibración de los modelos numéricos posibilita que se puedan estudiar actuaciones en edificios patrimoniales como el que nos ocupa sin la necesidad de realizar intervenciones de carácter destructivo.

Desde el punto de vista de comportamiento del conjunto, resulta destacable la rigidez que aportan la cabecera y los pies de la iglesia respecto del cuerpo de naves. Esto hace que tanto los pilares intermedios como los contrafuertes de los vanos centrales estén más solicitados.

Respecto al nivel de seguridad obtenido, preocupa considerablemente el alto nivel de fisuración que presenta debido fundamentalmente al gran peso que introduce el material de relleno sobre las bóvedas para conformar la cubierta transitable y el poco margen de seguridad analizado. Incluso ya desde la consideración del factor de gravedad de “1g”.

AGRADECIMIENTOS

Queremos agradecer todo el apoyo proporcionado a D. Francisco González de Canales, Arquitecto y Maestro Mayor de la Iglesia, y a Dña. Amparo Rodríguez Bavío por compartir sus conocimientos sobre la Iglesia. Del mismo modo, al Padre Eugenio (†) por habernos permitido deambular por el recinto y a todas las personas que ayudan a mantener, de una u otra forma, que la Iglesia de Santa Ana mantenga el aspecto que presenta hoy día. Y en estos últimos años, al Padre Antonio Rodríguez Bavío, Delegado Diocesano de Patrimonio de la Consejería de Cultura de la Junta de Andalucía.

REFERENCIAS

[1] Martínez, J.L., Martín-Caro, J.A., & León, J. (2001). Comportamiento Mecánico de la Obra de Fábrica. In Monografías sobre el análisis estructural de construcciones históricas de fábrica. Madrid: Departamento de Mecánica de los Medios Continuos y Teoría de Estructuras. ETS Ingenieros de Caminos, Canales y Puertos. UPM.

[2] Valseca, J.A. (2023). “Traza, geometría y estructura de la Iglesia de Santa Ana de Sevilla. Tesis Doctoral.” Sevilla: Universidad de Sevilla.

[3] Compán, V., Pachón, P., Cámara, M., Lourenço, P.B., & Sáez, A. (2017). Structural safety assessment of geometrically complex masonry vaults by non-linear analysis. The Chapel of the Würzburg Residence (Germany). *Engineering Structures, 140, 1–13*.

[4] Moreno, C., Amanda, E., García, P., Pérez, C., & Compán, V. (2017). Caracterización de propiedades dinámicas de edificios patrimoniales mediante análisis modal operacional. In ReUso. Granada 2017. Sobre una arquitectura hecha de tiempo. Volumen 1: Metodología, Técnica y Conservación. Granada: Editorial Universidad de Granada.

[5] López, J., Oller, S., & Oñate Ibáñez de Navarra, E. (1998). Cálculo del comportamiento de la mamposteria mediante elementos finitos. Monografía CIMNE M46. Barcelona: Centro

Damage assessment of cement-based thermal energy storage components

Ortiz-Vásquez, L.F.[1]; Roque, E.[1]; Endrino, J.L.[1]; Montero-Chacón, F.[1]

ABSTRACT

In this paper, we propose a computational framework for the design of cement-based thermal energy storage (CTES) components and the analysis of their structural integrity at high temperatures. For this purpose, we couple the fluid and solid mechanics problems strongly, including the heat transfer phenomena and the corresponding temperature-dependence of the material properties. The fracture problem is modeled by means of a phase-field fracture model based on the principal stress criterion to reproduce the material degradation. This approach allows the assessment of damage experienced by this type of components under operation conditions.

Keywords: thermal energy, energy storage, cement-based materials, finite elements

1. INTRODUCTION

Thermal Energy Storage (TES) systems are called to play an essential role in the following years. They can be combined with renewable energy harvesters to circumvent the grid issues associated with their dependency on natural resources. Heat storage in concrete stands out as an economic, flexible, and high energy density solution for energy storage [1]. However, high-temperature storage in concrete causes severe thermal loads, which may cause cracking and fatigue in the material, limiting the performance and durability of the system.[2]

In this work, we propose a finite element (FE) approach to assess the structural integrity of cement-based thermal energy storage (CTES) components. For this purpose, we include both the fluid and solid mechanics contributions in the formulation. The mass conservation, Navier-Stokes, and energy equations are used to describe the fluid motion, typically the so-called heat transfer fluid (HTF). Concrete behavior is modeled considering thermo-mechanical coupling with a phase-field fracture model.

2. MATERIALS AND METHODS

In our approach, we propose a strongly coupled fluid-mechanical model, including the heat transfer process, both in the solid and fluid domains. The mathematical description is presented below.

The thermal evolution in the solid domain can be described as Eq (1):

[1] *Materials and Sustainability Group, Department of Engineering, Universidad Loyola Andalucía, Avenida de las Universidades, s/n, 41704 Sevilla, Spain. lfortiz@uloyola.es, eroque@uloyola.es, jlendrino@uloyola.es, fpmontero@uloyola.es (Corresponding autor).*

$$\rho C_p \frac{\partial T}{\partial t} + \nabla \cdot \boldsymbol{q} = 0 \quad (1)$$

where ρ is the density, C_ρ the specific heat, T the temperature, t the time, and $\boldsymbol{q}$ the heat flow. Moreover, the heat flow $\boldsymbol{q}$, which depends on the thermal conductivity (k) and the temperature gradient, be obtained using the Fourier's law as Eq (2):

$$\boldsymbol{q} = -k\nabla T \quad (2)$$

On the other hand, the heat transfer in the fluid domain is given by:

$$\rho C_\rho \frac{\partial T}{\partial t} + \rho C_\rho v \cdot \nabla T + \nabla \cdot q = Q + Q_p + Q_{\mathrm{v}d} \quad (3)$$

where $\boldsymbol{v}$ is the fluid velocity, Q a source term, Q_p the pressure work, and $Q_{\mathrm{v}d}$ a viscous dissipation term. In the precious equation, $\boldsymbol{q}$ can be obtained using Eq. (3).[3].

The fluid motion is described using the Navier Stokes equations Eq. (4) and the conservation of mass Eq. (5). In this study, we consider laminar conditions for the fluid flow.

$$\rho \frac{\partial \boldsymbol{v}}{\partial t} + \rho(\boldsymbol{v} \cdot \nabla)\boldsymbol{v} = \nabla \cdot (-\mathrm{p}\mathbf{I} + \mu(\nabla \boldsymbol{v} + (\nabla \boldsymbol{v})^T) + \boldsymbol{F} \quad (4)$$

$$\rho \nabla \cdot \boldsymbol{v} = 0 \quad (5)$$

where p is the fluid pressure, μ the dynamic viscosity, and $\boldsymbol{F}$ the volume force vector.

Our work considers thermo-mechanical coupling, including the material damage through a phase-field fracture model. In the infinitesimal strain theory, the strain tensor ($\boldsymbol{\varepsilon}$) is given by the symmetric gradient of displacements ($\mathbf{u}$) as Eq. ((*6*):

$$\boldsymbol{\varepsilon} = \frac{1}{2}(\nabla \mathbf{u}^{\mathbf{T}} + \nabla \mathbf{u}) \quad (6)$$

Moreover, $\boldsymbol{\varepsilon}$ can be written as the sum of the elastic ($\boldsymbol{\varepsilon}^{\mathrm{el}}$) and the thermal ($\boldsymbol{\varepsilon}^{\mathrm{th}}$) strain tensors as Eq. (7):

$$\boldsymbol{\varepsilon} = \boldsymbol{\varepsilon}^{\mathrm{el}} + \boldsymbol{\varepsilon}^{\mathrm{th}} \quad (7)$$

In this case, the temperature effect in the mechanical contribution is modeled as an isotropic volume expansion, which depends on the thermal expansion coefficient (α), and the difference of the temperature in the solid with respect to a reference temperature as Eq. (8):

$$\boldsymbol{\varepsilon}^{\mathrm{th}} = \alpha\big(T - T_{ref}\big)\mathbf{I} \quad (8)$$

The stress tensor can be obtained using the constitutive law of the material as Eq. (9):

$$\sigma = ((1-d)^2 + k_n)\mathbf{C}\colon \boldsymbol{\varepsilon}^{\mathrm{el}} \quad (9)$$

where d es is the damage parameter, k_n a small numerical value to improve convergence, and $\mathbf{C}$ the stiffness tensor. Finally, the equilibrium can be written as Eq. (10):

$$\nabla \cdot \boldsymbol{\sigma} = 0 \tag{10}$$

We choose a phase-field fracture scheme to represent the cracking evolution in concrete. In this approach, damage varies in the range (0,1), representing 0 the pristine state, and 1 the broken material. The evolution of the damage parameter can be described as Eq. (11) [4]

$$\mathrm{d} - \mathrm{l}^2 \nabla^2 \mathrm{d} = 2(1 - \mathrm{d})\mathrm{D}_\mathrm{d} \tag{11}$$

Where l is the length-scale in the phase-field and D_d the cracking driven force. In this work, we follow the work of Miehe, and coworkers [4] and we include a principal stress-based driving force in the phase field equation, which can be written as Eq. (12)

$$D_d = \xi\left(\sum_{i=1}^{N}\left(\frac{\sigma_i}{\sigma_{max}}\right)^2 - 1\right) \tag{12}$$

where is the maximum principal stress, σ_{max} is the tensile strength, and ξ is a parameter that control the dissipation in the cracking process.

3. RESULTS AND DISCUSSION

For the simulations, we consider a cylindrical concrete heat exchanger with 1 m length, 25 cm outer diameter, and 5 cm inner diameter, as depicted in Figure 1. In the inner part, the HTF flows at 1 m/s and 500 K in the inlet.

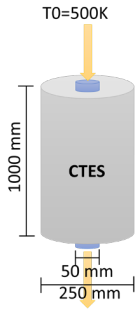

Figure 1. Geometry of the proposed Concrete Thermal Energy Storage component.

For the numerical implementation of the model, we use the multiphysics software Comsol. Two studies are carried out. In the first place, a transient analysis of the laminar flow (spf) and the heat transfer in solids and fluids (ht) are resolved considering a non-isothermal flow. Once the temperature field is obtained, the thermo-mechanical problem is solved at every time step.

Figure 2a. represents the heat transfer generated by the flow of the HTF into concrete. This heat transfer is dissipated radially along the solid medium. The pipe interface exhibits the highest temperature. On the other hand, Figure 2b represents the maximum principal stresses. The results obtained from this analysis are then surrogated into a refined scale analysis of the cross section of the CTES. Figure 2c shows the mechanical damage of concrete, which is seen through the radially emerging cracks. For this mesoscale analysis of concrete, large aggregates and their corresponding interfacial transition zone (ITZ) have been considered.

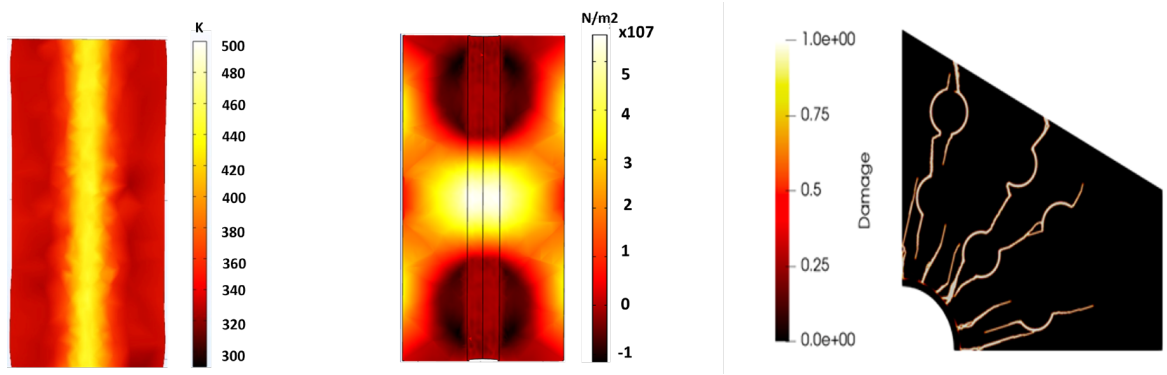

(a) (b) (c)

Figure 2. (a). Temperature profile across the CTES; (b) Principal stress field; (c) Cracking patterns.

4. CONCLUSIONS

This study proposes the use of the finite element method to analyze the thermal and mechanical behavior of concrete. We have implemented the mathematical model in Comsol multiphysics within the finite element approach. The results indicate that concrete presents mechanical damage at a certain time when it is subjected to temperature loads and discharges. However, this study gives us indications for future research that allow us to improve the mechanical properties of concrete to obtain long-lasting and sustainable thermal energy storage.

ACKNOWLEDGEMENTS

The authors would like to thank the Spain Ministry of Science and Innovation for the financial support of the project “Thermal Energy Storage and Materials Design for Solar-Driven Trigeneration”, grant number PID2021-128727OB-I00.

REFERENCES

[1] Reddy, K. S., Mudgal, V., & Mallick, T. K. (2018). Review of latent heat thermal energy storage for improved material stability and effective load management. *Journal of Energy Storage, 15, 205–227*.

[2] Bauer, T., Steinmann, W.-D., Laing, D., & Tamme, R. (2012). Thermal energy storage materials and systems. *Annual Review of Heat Transfer*, *15*, *131–177*.

[3] Giannuzzi, G.M., Liberatore, R., Mele, D., Mazzucco, G., Xotta, G., Salomoni, V.A., Majorana, C.E., & Di Maggio, R., (2017). Experimental campaign and numerical analyses of thermal storage concrete modules. *Solar Energy, 157, 596-602*.

[4] Miehe, C., Schänzel, L. M. & Ulmer, H. (2015). Phase field modeling of fracture in multi-physics problems. Part I. Balance of crack surface and failure criteria for brittle crack propagation in thermo-elastic solids. *Computer Methods in Applied Mechanics and Engineering, 294, 449-485.*

Design and characterization of an eddy current damper applied to vibration mitigation.

Iglesias-Pordomingo, Álvaro[1]; Magdaleno, Álvaro[1]; Lorenzana, Antolín[1]

ABSTRACT

Structural vibration phenomena are a key issue in the assessment of slender structures under dynamic loading. In order to dissipate energy from the structure movement, damping devices are used to meet the acceleration requirements. In this paper, an experimental method is developed to study the effects of a passive Eddy current damper. The new method approaches damping characterization from frequency domain to estimate the physical damping value, by using an electrodynamic shaker and a data acquisition system. Modal analysis techniques are applied to obtain the transfer functions, and an identification algorithm is used to estimate damping. The results are validated with experimental data from time domain techniques and with data from a tuned mass damper prototype.

Keywords: tuned mass damper, Eddy current, damping, experimental modal analysis.

1. INTRODUCTION

Vibration problem is a common issue in the design and performance of slender structures made of flexible materials. Tuned mass dampers (TMD) are some of the most used devices to mitigate vibration. A TMD consists of a single degree of freedom (SDOF) system that involves mass, stiffness and damping. In this paper, TMD design is studied by focusing on the characterization of magnetic damping.

Eddy current dampers (ECD) have been widely used as passive damping devices. Their interest relies on the non-contact property of magnetic damping, avoiding non-linear effects, such as friction, in the relative motion of the TMD. Eddy currents are generated by the relative movement of permanent magnets with respect to a close non-ferromagnetic conductive material. A magnetic force arises to oppose the movement and leads to energy dissipation. This force has been deeply studied by several authors, so that different configurations of ECDs have been analyzed [1], and the parameters which affect to magnetic damping [2].

This work continues the one presented by Fernández et al. [3], in which magnetic damping is identified from temporal domain data. The objective of this work is to develop and validate a novel methodology of damping identification in the frequency domain, so that the global effects of damping are characterized. The results are validated in a real TMD prototype.

[1] *ITAP. University of Valladolid (SPAIN). alvaro.iglesias@uva.es (Corresponding author), alvaro.magdaleno@uva.es, ali@eii.uva.es*

2. EXPERIMENT DESIGN

In this study a small TMD configuration is developed (Fig. 1). The design consists of an "extruded flexible quadrangle", in which two of the faces are the fixed and moving masses respectively, and the edges between them are flexible thin beams, which provide the necessary stiffness together with an additional traction spring. In both sides of the TMD there is a copper plate which is aligned with the moving mass, where the magnets are placed (Fig. 1). The magnets are embedded in a plastic magnet holder. Two steel angular plates allow to control the gap between the magnets and the copper plate.

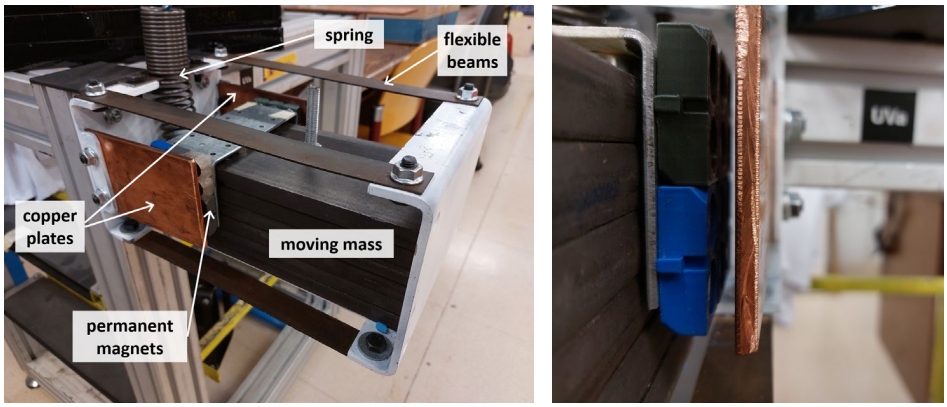

Figure 1. *TMD design (left) and detail of the gap between copper and magnets (right).*

Before analysing the performance of the TMD, this study is aimed at predicting the magnitude of damping associated to the number of magnets that are placed. Previous studies show that the best arrangement of magnetic polarities is the one named as "bands" [3], in which the pole-change-limit is perpendicular to the movement (Fig. 2). This layout is applied in this paper, so that the parameter of study is the number of pairs of magnets (the cases are shown in Fig. 2).

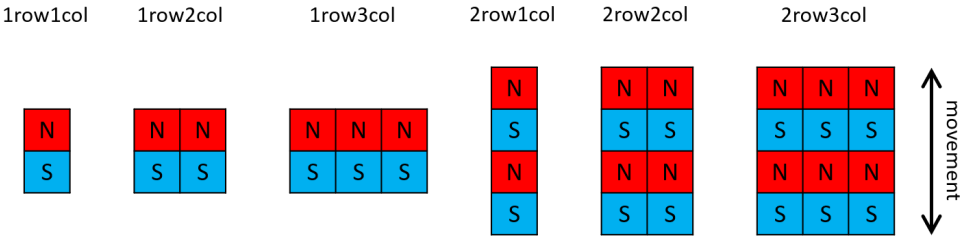

Figure 2. *Different magnet arrangements in the experiment.*

To determine the damping, a frequency analysis is conducted. The experimental setup is similar to the previous study that was conducted by focusing in the time domain: the LEGO® car prototype that was designed and used in [3], that runs along a copper plate with the magnets behind the chassis separated from the copper with a gap of 1.5 mm. The magnet holder is also the one used in the mentioned study, so that magnets are placed by pairs of north-south.

The experiment design is shown in Fig. 3: the car is placed over the copper plate and linked to an electrodynamic shaker through a rigid stick. The copper plate is put in horizontal position, and the dynamic shaker applies an alternative sine movement. The magnet array moves over the copper plate generating Eddy currents.

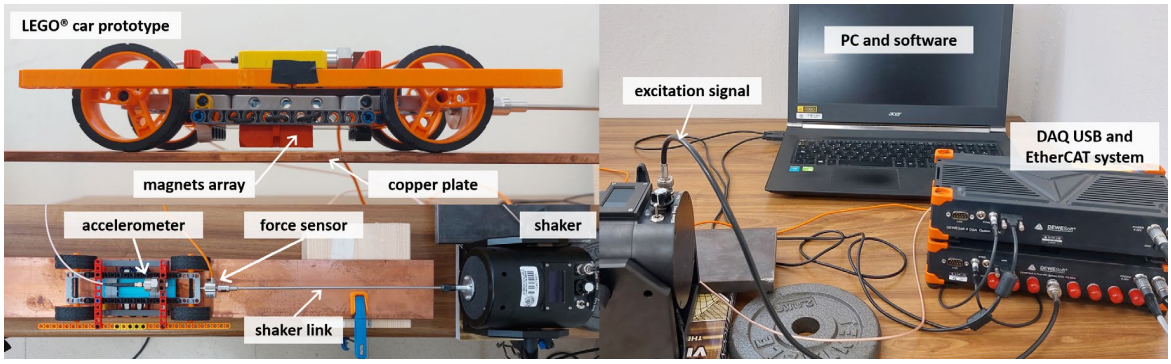

Figure 3. *Experimental layout and measurement chain.*

3. METHODOLOGY

The method to estimate damping is inspired by the experimental modal analysis technique (EMA); the acceleration of the magnets is measured with an accelerometer on the car, and the magnetic force is measured with a force sensor between the stick and the car (Fig. 3). The shaker applies a sine sweep to excite a wide range of frequencies. Both signals are led to a data acquisition system commanded by DewesoftX, where the frequency response functions (FRF) are calculated.

The FRF represents the transfer function of a system and models its dynamic behavior. In this case, the accelerance [m/Ns^2] is calculated (relationship between acceleration and force). Although the experiment with the LEGO® car seems to involve only mass and damping, there are some unavoidable effects that lead to consider the effects of the stiffness in the experimental setup. This behavior can be related to a SDOF system with mass, damping and stiffness (m-c-k). Eq. (1) shows the accelerance expression for SDOF systems in terms of physical properties, where ω is the frequency in [rad/s], m stands for the mass [kg], c for the damping [Ns/m] and k for the stiffness [N/m].

$$h(\omega) = \frac{-\omega^2}{-m\omega^2 + ic\omega + k} \tag{1}$$

Once the experimental results are processed, the values of m, c and k that best fit the calculated FRFs are found. To do so, a least squares method is applied to minimize the error between the experimental and the analytical FRF calculated with the expression of Eq. (1). The damping value of the car without magnets is also considered and subtracted. Table 1 shows the results of the fitting process (New method), and Fig. 4 shows the overlapping between experimental and analytical FRFs.

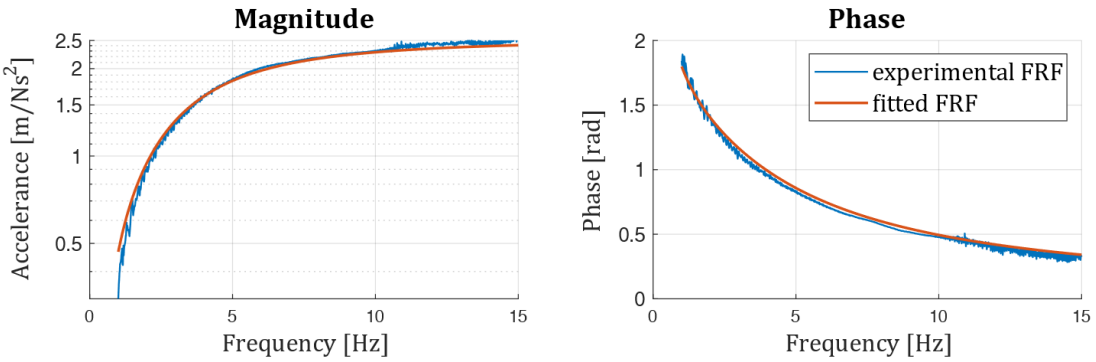

Figure 4. *Example of FRF fitting associated to the case 2 rows – 3 columns (Fig.2).*

4. VALIDATION

4.1. Comparison with temporal results

The same magnet arrangement cases where previously studied through a temporal domain technique developed in [3], using the same experimental layout and obtaining a matrix of damping values analogous to the calculated with the new method, according to Fig. 2. Table 1 shows the results of the comparison and the relative error.

4.2. Comparison with TMD results

As the final objective is to implement the magnetic damping in the TMD prototype that was described before, a set of experiments are performed to identify the damping value at the TMD off-board (this means attached to a fixed platform). An experimental modal analysis (EMA) is conducted by means of an impact hammer. The FRFs corresponding to each of the cases are fitted to the SDOF expression at Eq. (1) to identify the m, c and k of the TMD. The final damping value is divided by 2, because of the hypothesis that 2 magnet arrays side by side of the TMD duplicate the value of damping. Table 1 shows the results of the comparison and relative error between all the damping values.

Table 1. Summary of damping results and relative errors

	DAMPING VALUES [Ns/m]									**RELATIVE ERROR**					
Number	**New method**			**Temporal results**			**TMD (EMA)**			**Temporal results**			**TMD (EMA)**		
of rows	**1 col.**	**2 col.**	**3 col.**	**1 col.**	**2 col.**	**3 col.**	**1 col.**	**2 col.**	**3 col.**	**1 col.**	**2 col.**	**3 col.**	**1 col.**	**2 col.**	**3 col.**
1	**2.91**	**5.66**	**10.47**	2.40	6.14	9.90	2.90	6.06	9.64	21.3%	7.8%	5.8%	0.3%	6.6%	8.6%
2	**4.54**	**12.58**	**21.90**	5.03	13.96	22.70	4.95	11.47	15.19	9.7%	9.9%	3.5%	5.03%	9.7%	44.1%

5. CONCLUSIONS

Eddy current dampers are effective passive devices, as damping reaches significative values; the highest damping value has been 21.90 Ns/m. The hypothesis of linear damping is met because it has been possible to fit FRFs (which constitute a linear model) to an analytical expression of a linear SDOF system. In the temporal comparison, none of the error values exceed 10%, except for the less damping scenario, in which the temporal result might be less accurate because the LEGO® car might not have reached a terminal velocity during the experiment. In the validation with the TMD results, the error does not exceed 10% but for the higher damping value, due to the effects of the interaction with the elements of the TMD, which should be further investigated.

ACKNOWLEDGEMENTS

The authors wish to acknowledge to the AEI, Spanish Government (10.13039/501100011033), and to "ERDF A way of making Europe", for the partial support through the grant PID2022-140117NB-I00.

REFERENCES

[1] Shan, J., Liu, J., Loong, C.N., Wu, W. (2021). Design and analysis of plate-type eddy-current damper with high energy-dissipation capability. *Smart Structures and Systems, 27 (5), 769-781.*

[2] Zhong, T., Feng, X., Zhang, Y., Zhou, J. (2022). Experimental study on the effect of EC-TMD on the vibration control of plant structure of PSPPs. *Smart Structures and Systems, 29 (3), 457-473.*

[3] Fernández, G., Iglesias-Pordomingo, Á., Cacho-Pérez, Lorenzana, A. Quantifying the damping performance of magnet arrays using kinematic methods. In 7th International Conference on Mechanical Models in Structural Engineering CMMoST 2023. Málaga. Universidad de Málaga.

Performance of an inertial controller for an FRP footbridge considering a crowd-structure interaction load model

Díaz, Iván M.[1]; Gallegos-Calderón, Christian[1]; Naranjo-Pérez, Javier[2]; Barrera-Vargas, Christian A.[1]

ABSTRACT

Crowd-structure interaction (CSI) has proven to play an important role on the dynamic response of Fibre-Reinforced Polymer (FRP) footbridges due to the lightweight nature of composite materials. Thus, the consideration of this phenomenon is essential to avoid over dimensioning both, the structure itself and the integrated vibration control devices, such as Tuned Mass Dampers). This paper presents the performance of a passive inertial controller that mitigates vertical human-induced vibrations on a 10m long FRP pedestrian structure, accounting for a transfer function of the coupled crowd-structure-controlled system. Predictions about the acceleration response of the footbridge with the passive device subjected to a crowd-induced loads are compared with experimental results. Additionally, a sensitivity analysis considering the damping ratio of the human body is carried out to assess the prediction accuracy of the CSI load model.

Keywords: footbridge vibrations, human-structure interaction, crowd-structure system, TMD

1. CROWD-STRUCTURE-TMD SYSTEM

Existing guidelines [1] define non-interacting load models to represent human-induced actions in the assessment of lightweight pedestrian structures at Vibration Serviceability Limit State (VSLS). In Fibre Reinforced Polymer (FRP) footbridges, unreal response predictions may be obtained using these load models since human-structure interaction (HSI) is neglected. Additionally, due to the lightweight of composite materials, these structures exhibit lively responses due to pedestrian actions, even when the footbridge natural frequencies lie above 5 Hz [2]. Well-established devices, such as Tuned Mass Dampers (TMDs), can be useful for controlling the excessive human-induced vibrations without adding mass or modifying the stiffness of FRP pedestrian structures.

This paper presents the performance of a TMD installed on an FRP structure while accounting for Crowd-Structure Interaction (CSI). For this purpose, a distributed Mass-Spring-Damper-Actuator (MSDA) system, representing the crowd, that includes an inertial controller (Fig. 1) is employed.

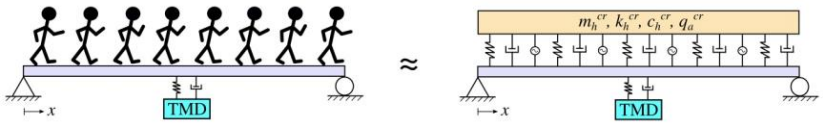

Figure 1. *Crowd-structure system including a TMD.*

[1] *E.T.S.I. Caminos, Canales y Puertos. Universidad Politécnica de Madrid (SPAIN). ivan.munoz@upm.es (Corresponding author). christian.gallegos@upm.es. christian.barrera@upm.es.*

[2] *E.T.S. Ingeniería. Universidad de Sevilla (Spain). naranjo3@us.es.*

The dynamic problem shown in Fig. 1 can be addressed though the block diagram shown in Fig. 2. The transfer function (TF) associated to the crowd-structure-controller system between the footbridge acceleration at midspan ($\ddot{y}_s$) and the crowd driving force (F_a^{cr}) is denoted herein as GT_{CL}. For the case of a simply supported structure, this TF is defined as follows

$$GT_{CL}(s) = \frac{2/\pi \cdot G_H^{cr}(s) \cdot G_S(s)}{1 - [(2/\pi)^2 \cdot G_{HSI}^{cr}(s) \cdot G_S(s) + G_T(s) \cdot G_s(s)]} \tag{1}$$

where $s = j\omega$ is the Laplace variable, ω is the angular frequency in rad/s, $G_S(s)$ is the TF of the structural system, $G_H^{cr}(s)$ is the TF between the crowd driving force and the contact force of the pedestrians with the structure, $G_{HSI}^{cr}(s)$ is the TF related to HSI, and $G_T(s)$ is the TF associated to the passive inertial controller.

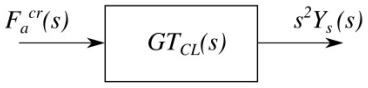

Figure 2. *Block diagram of the closed-loop TF of the crowd-structure-controller system.*

Considering the modal parameters of the first vertical vibration mode of a simply supported structure, the TF between the structure acceleration at midspan and the external force in the Laplace domain is

$$G_S(s) = \frac{s^2}{m_s\, s^2 + c_s\, s + k_s} \tag{2}$$

where m_s (kg) is the mass, $k_s = \omega_s^2 m_s$ (N/m) is the stiffness, $c_s = 2\omega_s m_s \zeta_s$ (Ns/m) is the viscous damping of the fundamental vibration mode, and ζ_s (Hz) is the damping ratio of this mode.

The TF between the force generated by the crowd without including the force transmitted to them due to the structure movement, and the driving force from the flow of pedestrians is

$$G_H^{cr}(s) = \frac{m_h^{cr}\, s^2}{m_h^{cr}\, s^2 + c_h^{cr}\, s + k_h^{cr}} \tag{3}$$

being m_h^{cr} the mass of the crowd, and k_h^{cr} and c_h^{cr} the stiffness and viscous damping of the flow of pedestrians, respectively. These parameters are obtained as follows

$$m_h^{cr} = \sum_{i=1}^{n} m_{hi},\ k_h^{cr} = \sum_{i=1}^{n} k_{hi},\ c_h^{cr} = \sum_{i=1}^{n} c_{hi} \tag{4}$$

with $i = 1, 2, \cdots, n$, where n is the number of individuals within the crowd, $k_h = \omega_h^2 m_h$ (N/m) is the person stiffness, $\omega_h = 2\pi f_h$ (rad/s) is the angular natural frequency of the human, $c_h = 2\omega_h m_h \zeta_h$ (Ns/m) is the viscous damping of the pedestrian body and ζ_h is the damping ratio of the human.

The crowd driving force applied at midspan of a simply supported structure is

$$F_a^{cr} = W_h \cdot GLF_r \cdot cos(2\pi f_{as}) \cdot n' \cdot S \tag{5}$$

where

$$n' = \frac{10.8\sqrt{\zeta_s \cdot n}}{S} \tag{6}$$

being S the area of the deck, $W_h = m_h \cdot g$ (N) the weight of a person, GLF_r the generalised load factor of the *r*th harmonic of the walking action.

The TF between the crowd interacting force, which is the force transmitted due to the structure movement, and the structure acceleration is

$$G_{HSI}^{cr}(s) = \frac{m_h^{cr}(c_h^{cr}\, s + k_h^{cr})}{m_h^{cr}\, s^2 + c_h^{cr}\, s + k_h^{cr}} \tag{7}$$

Finally, the TF between the control force and the structure acceleration is

$$G_T(s) = \frac{m_t(c_t\, s + k_t)}{m_t\, s^2 + c_t\, s + k_t} \tag{8}$$

where m_t (kg) is the inertial mass, $k_t = \omega_t^2 m_t$ (N/m) is the stiffness of the device, $c_t = 2\omega_t m_t \zeta_t$ (Ns/m) is the viscous damping, and ζ_t (Hz) is the damping ratio of the TMD.

2. CONTROLLED FRP FOOTBRIDGE

The FRP footbridge shown in Fig. 3a is employed herein to apply the previously described methodology. The 10m long structure is formed by pultruded FRP elements, and it presents a width of 1.5 m. The structure has been designed to meet all the requirements at Ultimate Limit State and Deflection SLS. Through the installation of a passive TMD, verifications at VSLS have also been achieved. The device mitigates the vertical vibrations related to the fundamental vibration mode of the structure, whose modal parameters are: m_s=405 kg, f_s=7.56 Hz, and ζ_s=1.40%. Whilst the parameters of the TMD are: m_t=25 kg, f_t=7.47 Hz, and ζ_t=14% [3].

Prior the numerical response prediction, the experimental response of the structure was obtained. Two traffic classes (TCs) accounting for 3 and 8 pedestrians walking for 5 minutes on the bridge were considered to represent different crowd scenarios. Thus, the bridge was subjected to a weak TC (Fig. 3b) and a dense TC (Fig. 3c). Both tests were carried out before and after the installation of the TMD, and the response of the structure was measured at midspan using an accelerometer. The experimental results are presented in Table 1.

Figure 3. *Experimental campaign: (a) FRP footbridge, (b) Weak TC, and (c) Dense TC.*

3. RESULTS AND DISCUSSION

Employing the procedure described in Ref. [4], the numerical prediction of the uncontrolled bridge under the crowd action is firstly computed. Secondly, the result of the FRP bridge that includes the

TMD is calculated using the methodology presented in Section 1. The results of the analyses are presented in Table 1, where it is seen that the experimental and numerical Maximum Transient Vibration Values (MTVVs) for the four studied cases agree. This demonstrates the importance of representing pedestrians as dynamic systems in the analysis of FRP footbridges at VSLS.

Table 1. Comparison of MTVVs (m/s^2)

Traffic class	Uncontrolled FRP footbridge		Controlled FRP footbridge	
	Experiment	**Prediction**	**Experiment**	**Prediction**
Weak	1,22	1,20	0,48	0,42
Dense	1,20	1,10	0,59	0,50

In Fig. 4, a sensitivity analysis considering the damping ratio of the human body is presented for the weak TC TC. In these graphs, it is seen that the employed HSI model of the crowd leads to a significant variation of the result when the FRP bridge is uncontrolled. On the other hand, when the structure includes the TMD, the MTVV does not change substantially.

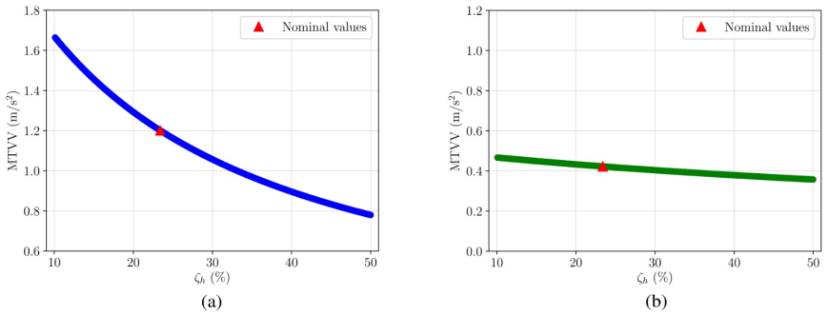

Figure 4. *Sensitivity analysis considering ζ_h for the weak TC (a) Uncontrolled structure, and (b) Controlled bridge.*

ACKNOWLEDGEMENTS

The authors acknowledge the grant PDI2021-127627OB-I00, funded by Ministerio de Ciencia e Innovación, Agencia Estatal de Investigación and 10.13039/ 501100011033 FEDER, European Union. Gallegos-Calderón thanks SENESCYT-Ecuador for the financial support. Naranjo-Pérez thanks Ministerio de Universidades for the Margarita Salas grant funded through the program 'European Union - NextGenerationEU'. Barrera-Vargas thanks the Spanish Minister for the FPI PRE2019-087494 predoctoral grant.

REFERENCES

[1] Butz C, Heinemeyer C, Keil A, Schlaich M, Goldack A, Trometer S, et al: HIVOSS Design of footbridges guideline. Joint Research Center (2008).

[2] Gallegos-Calderón, C., Naranjo-Pérez, J., Díaz, I.M., Goicolea, J.M.: Identification of a human-structure interaction model on an ultra-lightweight FRP footbridge. Applied Sciences 11(14), 6654 (2021).

[3] Gallegos-Calderón, C., Naranjo-Pérez, J., García-Palacios, J.H., Díaz, I. M.: Design and performance of a tuned vibration absorber for a full-scale lightweight FRP pedestrian structure. Journal of Composites for Construction, 26(6) (2022).

[4] Gallegos-Calderón, C., Naranjo-Pérez, Renedo, C.M.C., Díaz, I. M.: A frequency-domain approach to model vertical crowd-structure interaction in lightweight footbridges. Journal of Sound and Vibration, 557, 117750 (2023).

Discussion on shear strength models for RC beams with apparent contradictory initial hypotheses through Digital Image Correlation

Cladera, Antoni[1]; Montoya-Coronado, Luis[1]; Ruiz-Pinilla, Joaquín[1]; Ribas, Carlos[1]

ABSTRACT

One of the focal points of discussion over the past decade has been the conceptual disparity between design models for predicting the shear strength in RC beams based on shear friction or on the shear transferred by the un-cracked compressed concrete. In a recently published work, we conducted experimental tests on RC beams without stirrups that demonstrated, thanks to Digital Image Correlation, that a significant redistribution of shear-transfer actions occurs between the final 2% and 10% of the shear strength. This redistribution implies that models based on the compression chord transfer action and those considering shear friction as the primary shear transfer action are not contradictory but instead represent two closely related states before and after the observed redistribution. In this research, we re-examine and compare the test results with two previously published shear strength models for RC beams without stirrups.

Keywords: Shear strength; Concrete beam; Mechanical model; Photogrammetry; Aggregate interlock.

1. INTRODUCTION

Discussions on different shear strength models are common within the academic structural engineering community. Since the 1970s, it has been widely acknowledged that approximately 20 variables influence shear and torsional strengths. However, simpler design models often face the challenge of omitting secondary factors.

To address this issue, accurate measurements of the progressive failure process, particularly the formation of critical cracks, have become crucial. Among the various techniques available, Digital Image Correlation (DIC) is a highly suitable tool for tracking crack kinematics throughout experiments [1, 2, 3]. This enables the evaluation of different shear transfer actions, including the contribution of aggregate interlock, at any given instant during beam loading.

This paper presents results from six reinforced concrete (RC) beams without stirrups. Detailed DIC measurements were recorded to track the kinematics of the critical crack. Furthermore, these test results will be compared with two previously published shear strength models for RC beams without stirrups: the Compression Chord Capacity Model (CCCM) [4] and the model included in Model Code 2010 (MC-2010) [5], which is based on shear friction.

[1]*Industrial and Construction Engineering Dpt. University of Balearic Islands (SPAIN). antoni.cladera@uib.es (Corresponding author). luisal12@gmail.com. joaquin.ruiz@uib.es. carlos.ribas@uib.es*

2. EXPERIMENTAL CAMPAIGN

The six RC beam specimens had dimensions of 100 mm in width (*b*), 200 mm in depth (*h*), and a total length of 1600 mm (*L*). A concrete cover (cc) of 25 mm was specified for all specimens. The beams were subjected to a simple supported 3-point bending test with an externally symmetrical configuration. However, one shear span was internally reinforced with stirrups to ensure failure occurred in the shear span without stirrups (Fig. 1). The specimens were tested with a total free span of 1250 mm (resulting in *a/d* ratio approximately equaling 3.70 for all specimens). Table 1 illustrates the three different ratios of longitudinal reinforcement used. At the time of testing, the mean compressive strength (f_{cm}) was 42.2 MPa, and the splitting strength (f_{sp}) was 3.5 MPa. All reinforcements consisted of standard B500SD ribbed bars. See [6] for more detailed information.

Table 1. Beam specimens' main characteristics, results and predictions

Beam specimen	Tensile reinforcement	V_{test} [kN]	δ_{test} at V_{test} [mm]	Failure mode	V_{CCCM} [kN]	V_{test}/V_{CCCM}	V_{MC2010} [kN]	V_{test}/V_{MC2010}
V1-1-Φ16	Φ16	29.4	3.04	Shear	27	1.11	22	1,31
V1-2-Φ16	Φ16	27.9	2.89	Shear	27	1.05	22	1,24
V2-1-Φ12	Φ12	24.4	3.55	Shear	22	1.11	19	1,31
V2-2-Φ12	Φ12	26.5	4.68	Shear	22	1.20	19	1,42
V3-1-Φ10	Φ10	24.4	12.53	Shear-Flexure*	20	1.24	16	1,49
V3-2-Φ10	Φ10	23.1	4.57	Shear-Flexure*	20	1.18	16	1,41
* Shear failure after yielding of tensile longitudinal reinforcement.						1.15	Average	1.37
V_{test}: shear strength; $V_{CCCM/MC2010}$: predicted shear strengths; δ_{test} : mid-span deflection.						6.23	CoV(%)	6.85

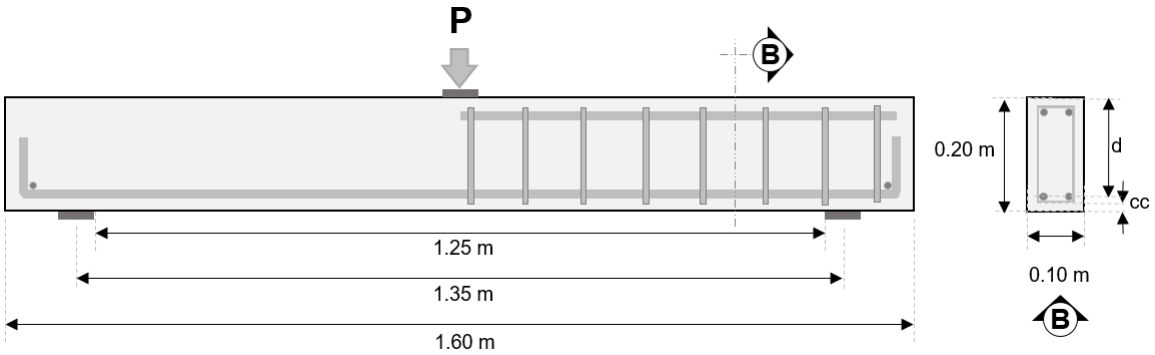

Figure 1. *Experimental test configuration [6].*

3. AGGREGATE INTERLOCK ANALYSIS AND RESULTS

The critical crack was discretized as shown in Fig. 2. The original Walraven's model [7] was used to evaluate the aggregate interlock contribution by associating the relative displacements between the crack surfaces (opening *w* and sliding *Δ*) with the transferred normal and tangential stresses. By the integration of these stresses along the crack surface, the relation between the stresses in a crack and the displacement components allows the calculation of the shear and normal forces acting along the crack. An example of the reported results is presented in Fig. 3, where *State I.a* stands for the instant when the first branch of the critical crack (Fig. 2) is fully developed, and *State II.a* corresponds to the development of the second branch. The same procedure was applied to the remaining five tests, which corresponded to RC members with identical cross-sections and test set-up configurations but with variations in the longitudinal reinforcement (see Table 1).

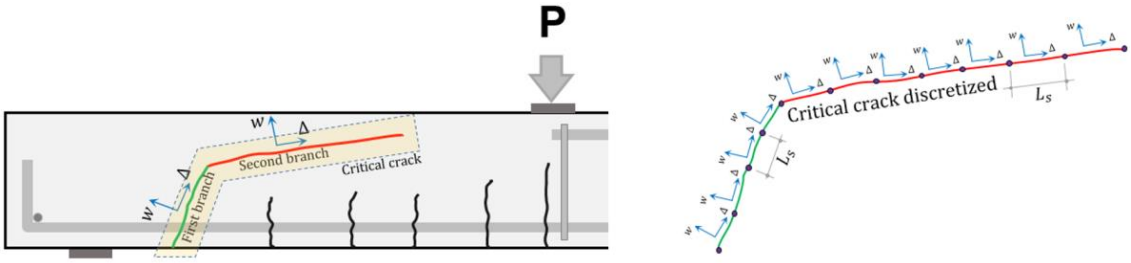

Figure 2. *Idealization of the aggregate interlock contribution calculation (adapted from [6]).*

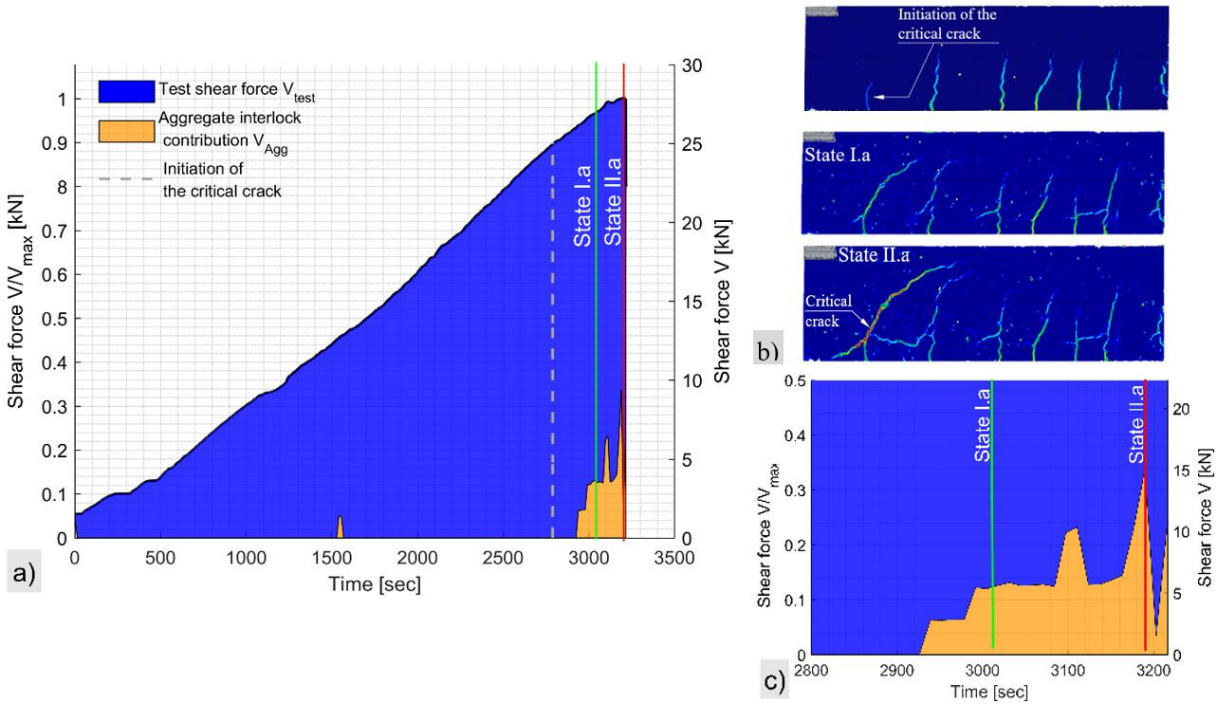

Figure 3. *Specimen V1-2-ϕ16: a) aggregate interlock contribution throughout the test; b) specimen cracks pattern; c) aggregate interlock contribution in the final time steps [6].*

In beams that exhibited shear-governed failure, the aggregate interlock contribution in *State I.a* ranged from 7.7% to 16%, while the shear force varied from 90% to 98% of the total shear strength. However, within the same beams, the aggregate interlock contribution increased significantly in State II.a, ranging from 32.9% to 85% of the total shear force. This crucial finding clarifies that mechanical models based on equilibrium in *State I.a*, where shear stresses across the compression zone are assumed to be the primary transfer action, and models emphasizing aggregate interlock as the main shear-transfer action in *State II.a* are not contradictory. Instead, both models are suitable for shear strength design. Moreover, these models are complementary, denoting two closely related states before and after the significant redistribution of shear-transfer actions observed near failure.

For example, Table 1 provides the predictions made by the CCCM (compression zone model) and by the Level II of approximation of MC-2010 (aggregate interlock model) for these six tests. Despite the MC-2010 displaying a higher safety level with V_{test}/V_{pred} = 1.37 (more conservative model), both models exhibit a similar Coefficient of Variation. Furthermore, it is important to note that the CCCM is most accurate but slightly conservative, with V_{test}/V_{pred} = 1.15, indicating that the predicted shear strength for this set of beams is 87% of the experimentally measured shear strength. According to the Digital Image Correlation (DIC) analysis conducted at this load level, the contribution of aggregate interlock to the

total shear strength is markedly low. This observation substantiates the primary hypothesis of the CCCM, i.e., the main shear transfer action is the shear transferred through the compression zone.

4. CONCLUSIONS

The analysis of these RC elements without stirrups reveals that the critical shear crack (CSC) undergoes an initial widening, rotating around its tip near the neutral axis without significant sliding. As a result, the contribution of aggregate interlock to shear strength remains negligible until shear forces approach 90% to 98% of the total shear strength. However, as the beam reaches failure, the formation of a secondary branch of the CSC, accompanied by substantial sliding, significantly enhances the aggregate interlock's contribution to shear strength. This contribution varies from 31.9% to 85% at failure. Notably, this pronounced redistribution of shear-transfer actions, occurring between the final 2% and 10% of the applied load, suggests that models based on equilibrium when stresses trigger the second branch of the CSC, such as the Compression Chord Capacity Model, and models that prioritize aggregate interlock as the primary shear-transfer action, such as the Model Code, are not contradictory. Instead, they depict two closely associated states before and after the observed redistribution.

ACKNOWLEDGEMENTS

Research projects PID2021-123701OB-C22 and RTI2018-099091-B-C22 funded by MCIN/AEI/10.13039/501100011033 and by "ERDF A way of making Europe" and TED2021-130272B-C22 funded also by MCIN/AEI and by the "European Union NextGenerationEU/PRTR".

REFERENCES

[1] Cavagnis, F., Fernández Ruiz, M., & Muttoni, A. (2015). Shear failures in reinforced concrete members without transverse reinforcement: An analysis of the critical shear crack development on the basis of test results. *Engineering Structures,* 103, 157-173.

[2] Huber, T., Huber, P., & Kollegger, J. (2019). Influence of aggregate interlock on the shear resistance of reinforced concrete beams without stirrups. *Engineering Structures*, 186, 26-42

[3] Monserrat López, A., Fernández Ruiz, M., & Miguel Sosa, P. (2021). The influence of transverse reinforcement and yielding of flexural reinforcement on the shear-transfer actions of RC members. *Engineering Structures*, 234, 111949

[4] Cladera, A., Marí, A., Bairán, J.M., Ribas, C, Oller, E. & Duarte, N. (2016). The compression chord capacity model for the shear design and assessment of reinforced and prestressed concrete beams. *Structural Concrete*, 17(6), 1017-1032

[5] International Federation for Structural Concrete (2013). Fib Model Code for Concrete Structures 2010. Berlin: Verlag Ernst & Sohn.

[6] Montoya-Coronado, L. A., Ribas, C., Ruiz-Pinilla, J. G., & Cladera, A. (2023). Time-history analysis of aggregate interlock in reinforced concrete beams without stirrups. *Engineering Structures*, 283, 115912.

[7] Walraven, J.C. (1980). Aggregate Interlock: A Theoretical and Experimental Analysis. Delft University of Technology.

Dynamic characterization of a timber footbridge by means of wearable devices.

Magdaleno, Alvaro[1]; Iglesias-Pordomingo, Alvaro[1]; Abazeed, Amgad S.[2]; Jarak, Tomislav[1]

ABSTRACT

Performing an accurate modal analysis is a challenging task that usually requires gathering synchronized data at high sampling rates. To do so, high-end systems composed of high-sensitivity sensors and powerful data-loggers are assumed to be necessary to obtain such data. However, low-cost devices have recently experienced a boost in their characteristics, enabling the recording of medium-to-high quality data at a very reduced cost. In this work, a pair of instrumented insoles and a set of wearable IMUs originally designed to capture the motion of human limbs are used to gather some data from a slender structure. The data is used to estimate the modal properties of the structure, which are compared with the ones obtained by means of a high-end system to show the goodness of the low-cost devices.

Keywords: low-cost devices; modal analysis; timber footbridge

1. INTRODUCTION

High quality data are often required to perform accurate and reliable modal analysis. In order to success, carefully synchronized force and response data needs to be registered at high sampling frequencies, something that typically requires high-end systems composed of high-sensitivity sensors and powerful dataloggers [1]. This kind of systems, however, tend to be expensive and they are not affordable for a number of research groups. Low-cost devices have recently emerged as an alternative to high-end systems thanks to a boost of their characteristics and performance without their price being increased. Among the low-cost devices, wearable devices, such as instrumented insoles and inertial measurement units (IMUs), have gained a special attention thanks to their applications in biomechanics and their ease of use [2,3].

In this work, wearable sensors are used as an alternative to a high-end system to register the necessary signals to perform a modal analysis of a timber footbridge. The results are compared to the ones obtained by a high-end system in order to quantify the success of the proposed methodology.

2. METHODOLOGY

This section is devoted to describing the methodology to perform the modal analysis with both the wearable devices and the high-end ones. Both systems are aimed at obtaining a set of frequency response functions (FRF) of the structure under study from which the modal properties are estimated. The structure is an arched timber footbridge located in Peñafiel (Valladolid, Spain), shown in Fig. 1a. It consists of two spans, being the one under study 50 m long and 3 m width. In order to perform the

[1] *ITAP. Universidad de Valladolid (SPAIN). alvaro.magdaleno@uva.es (Corresponding author); alvaro.iglesias@uva.es; tomislav.jarak@uva.es*
[2] *Dept. of Construction and Building Eng., Arab Academy for Science, Technology and Maritime Transport (EGYPT)*

analysis, it is divided into 8 sections with the same length as shown in Fig. 1b. For simplicity, only sections from 2 to 8 are monitored and sections 1 and 9 are assumed to be rigidly supported.

(a)

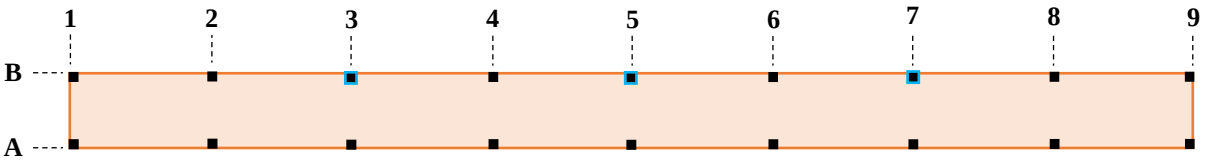

(b)

Figure 1. *(a) Picture and (b) schema of the main span of the timber footbridge.*

2.1. Wearable devices

As mentioned, a pair of instrumented insoles (Novel Loadsol®) is used to measure the force that a standing person applies on the ground, acting as a shaker; and a set of wearable IMUs (Movella DOT®), originally designed to capture the movement of human limbs, are used to measure the structural vertical acceleration instead of conventional accelerometers. Both sensors are wirelessly controlled by means of a smartphone, to which they are connected via Bluetooth and require different apps to work, so the data cannot be synchronously stored. Moreover, the insoles data are recorded at 100 S/s, while the IMUs are recorded at 120 S/s.

The measurement procedure is as follows: the person wearing the insoles and the smartphone is placed at a point such as B3 and four IMUs are located at four different points, such as A2, B2, A3 and B3 (due to the Bluetooth connection, the IMUs cannot be placed too far away from the smartphone); then, the recording starts and the person starts to randomly bounce to apply some force on the structure during 6-8 min. During this time, both apps are storing their corresponding data. Once the recording is done, sensors A2 and B2 are moved to A4 and B4 and the whole procedure is repeated with the person bouncing close to B3. Then, the person moves to B5, and sensors placed on A3 and B3 are also moved to section 5. This is subsequently repeated until all points have been measured.

It is important to note several aspects of this strategy. First, several points are measured twice. This is helpful in the case of one IMU not recording properly during a test or for comparison purposes. Second, contrary to the traditional approaches of roving sensors (the force stays while the accelerometer moves from one point to another; or vice versa), here both the input force and the IMUs move along the footbridge because the set of sensors must remain as close as possible to the smartphone. This will require special care when processing the data, as explained in section 2.3. Finally, as stated before, force and acceleration data are not recorded synchronously. As a consequence, before performing the processing described in section 2.3, both signals must be resampled to the same sampling frequency and the force signal needs to be synchronized with the acceleration ones (the four IMUs do register synchronously). In this work, this is done manually by checking the phase diagram of a FRF computed between the force signal and the closest acceleration

signal (B3, B5 or B7), which theoretically has a bounded phase diagram. As can be in Fig. 2, if both signals are not synchronized (blue or yellow), the phase diagram has a linear tendency. Then, for each test, the optimal delay is sought so the resulting phase diagram is as horizontal as possible (red).

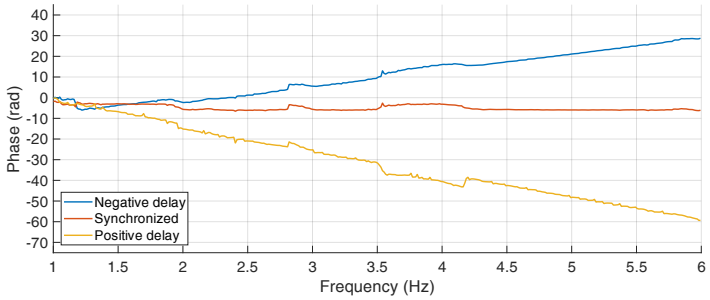

Figure 2. *Example of phase diagrams between signals with different time delays (dt)*

2.2. High-end system

For comparison purposes, a high-end system composed of 8 uniaxial accelerometers and an electrodynamic shaker are used. The shaker is placed near B3, and the accelerometers are placed in the first 8 positions, between A2 and B5, only covering half of the footbridge. The inertial force induced by the shaker is estimated by means of another accelerometer whose signal multiplied by 13.2 kg of moving mass provides with the applied force, which is continuous random during 6-8 min. The nine signals are synchronously recorded with a SIRIUS® (Dewesoft) datalogger and directly stored in the computer, ready for the next processing steps.

2.3. Modal parameters estimation

As explained, the synchronized data is composed of a force signal and several acceleration signals. If they have been registered by means of the wearable sensors, a previous synchronization procedure must be performed as stated in section 2.1. Several frequency response functions are computed correlating every acceleration with the force signal (wearable and high-end system separately). Fig. 3 shows the auto-FRF, i.e., the one that correlates acceleration of point B3 with the force applied in the same point obtained with both systems. As can be seen, high similarities exist between both FRFs.

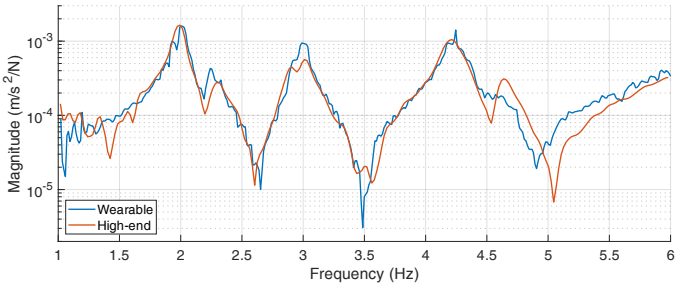

Figure 3. *Magnitude of the FRF of point B3 obtained with both systems*

The resulting FRFs are fitted to the conventional accelerance expression, which enables to obtain an estimation of the natural frequencies (ω_r), damping ratios (ζ_r) and mode shapes (ϕ_r). The eight FRFs associated to the high-end system are processed simultaneously because they have the same reference; however, the FRFs associated to the wearable system are processed in three batches, one per reference or point where the force is applied. This has an impact on how to estimate the mode shapes because the auto-FRF changes from one batch to another, but the natural frequencies and

mode shapes remain the same thanks to the mass of the person who applies the force being negligible with respect to the structural mass. Table 1 shows a comparison between the first three natural frequencies and damping ratios and Fig. 4 plots the associated mode shapes. Please note that the mode shapes associated to the high-end system have been extrapolated to the not measured half of the structure by symmetry.

Table 1. Summary of the estimated modal properties

Mode	Wearable		High-end	
	ω_r [Hz]	ζ_r (%)	ω_r [Hz]	ζ_r (%)
1	1.95	1.71	1.99	1.81
2	2.90	1.20	2.91	1.48
3	4.13	1.46	4.21	1.33

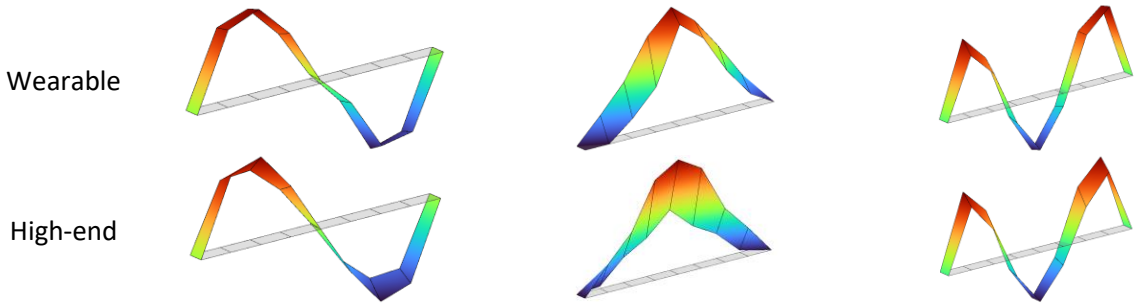

Figure 4. *First three identified mode shapes (1, 2 and 3 from left to right)*

3. CONCLUSIONS

As can be seen from the presented results, the wearable devices permit to gather data which, after a proper conditioning, can be used to perform a modal analysis of the structure. The most critical aspect is the synchronization of both kind of sensors, which are managed by different apps and have different sampling rates. Once this issue is overcome, a conventional modal analysis technique can be applied, like the curve-fitting method used in this work. As a result, some of the first modes have been identified by means of the wearable sensors, including the scaled mode shapes. Some differences can be appreciated between both sets of modal properties, but the results are acceptable considering that the wearable system is around 10 times cheaper than the high-end one.

ACKNOWLEDGEMENTS

The authors wish to acknowledge to the AEI, Spanish Government (10.13039/501100011033), and to "ERDF A way of making Europe", for the partial support through the grant PID2022-140117NB-I00.

REFERENCES

[1] Maia, N.M.M. & Silva, J.M.M. (1997). Theoretical and experimental modal analysis, chapter 3. Hertfordshire: Research Studies Press, LTD.

[2] Rana, M. & Mittal, V. (2021). Wearable sensors for real-time kinematics analysis in sports: a review. *IEEE Sensors Journal, 21(2), 1187-1207*

[3] Liu, S.Q., Zhang, J.C., Zhang, Y.Z. & Zhu, R. (2020). A wearable motion capture device able to detect dynamic motion of human limbs. *Nature Communications, 11(1), 5615*

Elimination of temperature effects on the modal properties on external post-tensioning tendons. A case of study

Chillitupa-Palomino, Luis[1]; Soria, Jose M. [1]; Diaz, Ivan M.[1]; Garcia-Palacios, Jaime H. [1]; Naranjo-Perez, Javier[2]

ABSTRACT

The precise estimation of modal properties is of paramount importance in Structural Health Monitoring, as any notable variations may indicate loss of structural mass or stiffness. Consequently, it is important to eliminate or reduce the influence of external factors that could obscure such damage-related changes in modal properties. In case of post-tensioning external tendons, modal properties are used as performance indicators and for the indirect estimation of tension forces. Thus, the elimination of temperature effects on several post-tensioning tendons which are continuously monitored in a railway bridge is undertaken in this work. Two unsupervised cascade clustering procedures based on gaussian mixture model were used for that purpose. The first to detect trends within the estimated frequency dataset and selects a group of data that fits the expected behavior. The second to filter the outlier values still found within the dataset. Finally, a regression analysis is done to the classified data.

Keywords: Structural Health Monitoring, Gaussian Mixture Model Clustering, Temperature effects, post-tensioning tendons

1. INTRODUCCTION

In vibration-based structural health monitoring, modal frequencies play an important role in evaluating structural integrity [1]. A substantial shift in these frequencies can serve as a performance indicator of structural elements losing mass or stiffness, signifying potential damage. However, beyond the influence of operational loads, environmental factors such as temperature and humidity can exert an impact on modal frequencies, potentially concealing signs of structural damage [2]. This interference can lead to inaccurate assessments, causing significant structural issues to go unnoticed. In the specific context of post-tensioned cables, temperature fluctuations emerge as a prominent factor contributing to frequency variations, emphasizing the critical need to mitigate this source of modal variability. Additionally, modal properties can be used to estimate tension forces. In this case, the removal of temperature effects is crucial for the accuracy of the estimation.

To address this challenge, unsupervised learning techniques, including clustering using Gaussian Mixture Models, were employed to filter the data. This process aids in isolating and identifying significant patterns within the noisy dataset. The application of regression models to classified data obtained from one-year monitoring of several external post-tensioning allows to achieve frequency variation with respect to temperature. This relationship serves as a fundamental step toward enhancing

[1]*E.T.S.I. Caminos Canales y Puertos. Universidad Politécnica de Madrid (Spain). luis.cpalomino@upm.es (Corresponding author), jm.soria@upm.es, ivan.munoz@upm.es, jaime.garcia.palacios@upm.es.*
[2]*E.T.S. Ingeniería. Universidad de Sevilla (Spain). jnaranjo3@us.es*

structural health assessments and mitigating the masking effect of environmental factors on damage detection.

2. MONITORING SYSTEM

The monitoring system is sketched on Figure 1. The system comprises a total of 12 sensors: 8 accelerometers, 6 of which are situated individually on the horizontal part of the tendon (one for each tendon) all of them placed at 1/8 of span from the middle, 2 accelerometers positioned on the box girder's floor and 2 Linear Variable Differential Transformers (LVDT) placed to measure the cable sag at midspan. Additionally, the ambient temperature and humidity are measured inside the box girder.

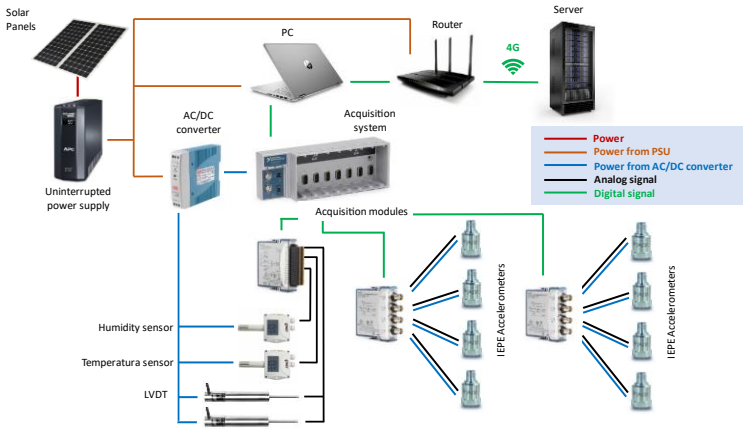

Figure 1. *Monitoring system.*

The acquisition system supports two acquisition loops: one at 0.5 Hz for static measurements (cable sag, temperature, and humidity) and another, much faster loop at 1651 Hz for dynamic measurements (accelerometers). Additionally, the train passing is automatically detected, and data is then categorized into two groups: forced and ambient. Forced data are stored when a train is crossing the bridge (and a few seconds later) whereas ambient data is stored any other time. From the later data, the first seven natural frequencies are extracted.

3. MODAL PROPERTIES AND TEMPERATURE EFFECT REMOVAL

Figure 2 displays the first modal frequency derived from the postprocessing of accelerometer data and temperature recordings over one-year time span. Note that there are general stops due to bridge rehabilitation works and minor technical problems. As can be observed in Figure 2.a, no patterns are explicitly presented.

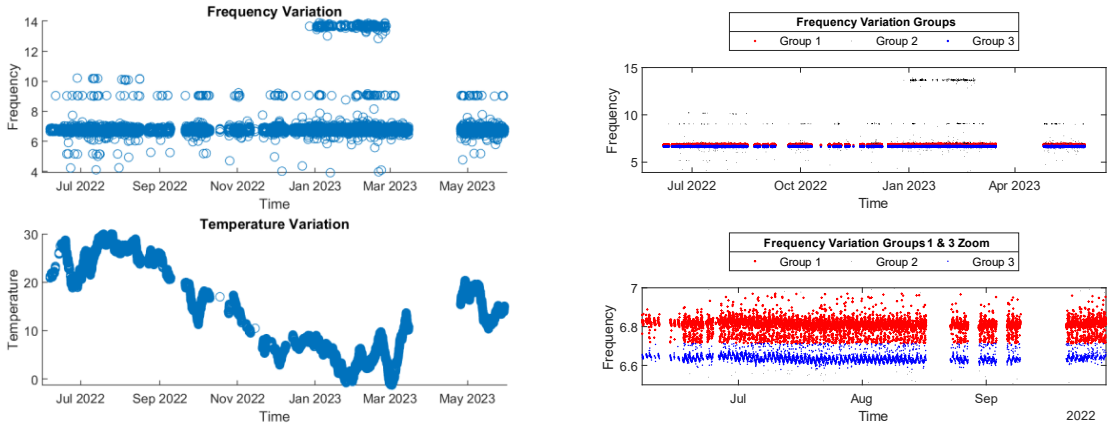

a. Unclassified data *b. Classified data*

Figure 2. *Data analysis, 1 year (First Classification).*

To carry out the classification problem, an unsupervised learning technique, was employed to group similar data. Specifically, the Gaussian Mixture Model (GMM), a probabilistic clustering method known for uncovering intricate data patterns, was utilized. The training process involved the random selection of 10% of the total data points, with the model configured to classify the data into three distinct groups. The outcomes of this clustering process are depicted in Figure 2.b.

In this case, Group 3 (blue) is the selected choice for analysis due to its distinct and sustained trend throughout the entire study period. Although data from Group 1 (red) could also be considered it, however, lacks the consistency observed in the data from Group 3 notably, at some time intervals, the group 1 data points exhibit greater dispersion, whereas Group 3 exhibits a more clearly defined and consistent evolution over time. The frequency vs temperature of the filtered dataset, containing only Group 3 data, still shows too many outliers, thus, a second classification problem is solved the same way as the previous one using a GMM-based clustering, Figure 3 shows Group 3 dataset classified into 3 new groups, being Groups 1 and 3 data of interest and Group 2 composed of outliers.

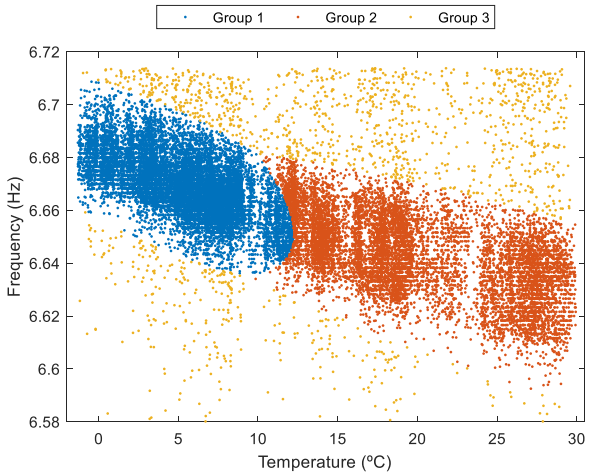

Figure 3. *Group 3's Frequency vs Temperature, unfiltered & classified (Second Classification).*

Upon the exclusion of data from Group 2, a substantially cleaner dataset is derived, as illustrated in Figure 4.a. The temporal evolution of both frequency and frequency variation can be observed in Figure 4.b.

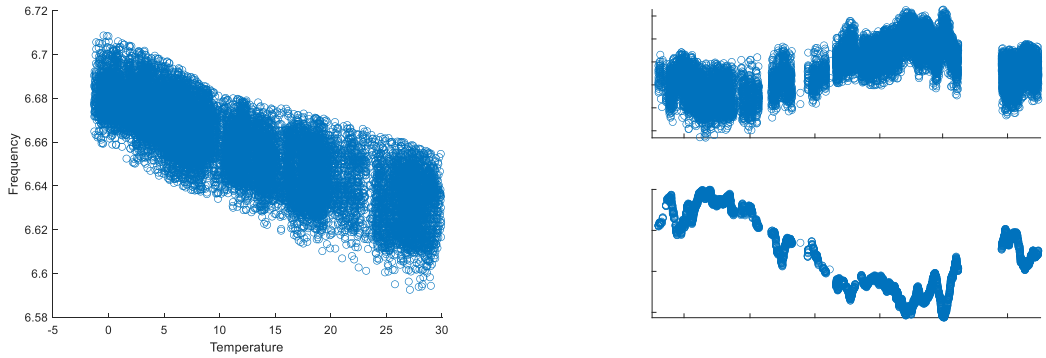

a. Frequency vs Temperature b. Frequency and temperature over time

Figure 4. *Group 3's Filtered data.*

Finally, a preliminary regression analysis is carried out, a stepwise linear regression analysis was conducted utilizing temperature (T), humidity (H) as input variables, while the fundamental natural frequency (F) served as the output variable. The resulting regression expressions are detailed in Table 1 and are applicable for temperatures between -1ºC and 30ºC.

Table 1. Stepwise Linear Regression Results

Independent Variables	**Expression**	**R squared**
T	$F = 6.678 - 0.002 \cdot T$	0.681
T, 1/H	$F = 6.678 - 0.002 \cdot T + 0.378 \cdot 1/H$	0.703
T, 1/H, T^3	$F = 6.678 - 0.002 \cdot T + 0.378 \cdot 1/H + 3.315 \cdot 10^{-7} \cdot T^3$	0.705

The preliminary regression model explains up to 70% of frequency variation. Future works will consider the application of other clustering algorithms and the application if time series models for forecasting such as ARMA and ARIMA models.

ACKNOWLEDGEMENTS

Research project PID2021-127627OB-I00 funded by MCIN/ AEI / 10.13039/501100011033 / FEDER, EU.

REFERENCES

[1] Luo, J., Huang, M., & Lei, Y. (2022) Temperature Effect on Vibration Properties and Vibration-Based Damage Identification of Bridge Structures: A Literature Review. Buildings. MDPI. https://doi.org/10.3390/buildings12081209

[2] Wang, Z., Yang, D.H., Yi, T.H., Zhang, G.H., & Han, J.G. (2022) Eliminating environmental and operational effects on structural modal frequency: A comprehensive review. Structural Control Health Monitoring. John Wiley and Sons Ltd. https://doi.org/10.1002/stc.3073

Evaluation of impact severity reduction in a bi-material demonstrator based on recycled tires.

González Vega, Joaquín[1]; Castillo López, Germán[1]; López Medina, Pablo[1]; García Sánchez, Felipe[1]

ABSTRACT

In the contemporary context, the substantial accumulation of non-biodegradable end-of-life tire residues poses a significant environmental concern. Annually, thousands of tons of these residues, highly flammable and constituting a severe fire hazard, are generated. This study proposes a novel application for these residues: incorporation into guardrails to create a hybrid-material system capable of dissipating higher levels of impact energy. This innovation aims to enhance the safety of guardrails. To achieve this objective, a numerical model will be employed to quantify the impact mitigation achieved through the introduction of a viscoelastic material derived from end-of-life tires. A downscaled model is used to establish a robust numerical-experimental correlation. Once satisfactory results are obtained from the numerical model, the virtual analysis of a full-scale model will be possible, without the need for physical tests, which are very expensive.

Keywords: End of life tires, Recycling, Impact severity reduction, numerical experimental correlation.

1. INTRODUCCIÓN Y OBJETIVOS

Actualmente, el elevado uso al que se ven sometidos los vehículos, unido a su importante volumen como producto de consumo, supone un gran problema medioambiental, ya que anualmente, entre otras cosas, se generan millones de toneladas de residuos provenientes de los neumáticos que cumplen su vida útil, también llamados neumáticos fuera de uso, NFU en adelante.

Una de las formas de mitigar este problema es darle un nuevo uso a este material. En este contexto, se creó la presente línea de investigación, enfocada a evaluar el efecto que la adición de un aglomerado, formado por pellets procedentes de NFU y poliuretano, a los actuales sistemas de protección vial, pueden tener sobre la severidad del impacto contra ellos.

En una primera fase, [1], se estudiaron las propiedades de los pellets, que forman el aglomerado, sometidos a cargas de impacto de compresión. Este análisis sirvió para el diseño del dispositivo experimental, así como para confirmar la idoneidad del modelo numérico elegido para este material.

El presente trabajo muestra resultados preliminares, a escala de laboratorio, comparando resultados experimentales sobre un elemento metálico, construido ad hoc Fig. 1 (izquierda), con los resultados obtenidos sobre el mismo elemento al que se ha añadido el aglomerado. Considerando que las conclusiones definitivas de esta línea de investigación habrían de obtenerse de ensayos a escala real, que no son económicamente viables, se desarrolla, en este trabajo, un modelo numérico, Fig. 1 (derecha), cuya

[1]*Dpto. Ingeniería Civil, de Materiales y Fabricación, Universidad de Málaga. España. e-mail: jogonve@uma.es "(Corresponding author)"; gcastillo@uma.es; 0619988177@uma.es; fgsanchez@uma.es.*

fiabilidad se evalúa en base a su comparación con los resultados experimentales. Un modelo numérico fiable aportaría una potente herramienta de diseño de sistemas de protección vial bimaterial, incluyendo el aglomerado, así como para reducir el número de ensayos, a escala real. En consecuencia, los objetivos de este trabajo son la comprobación de la disminución de la severidad del impacto por la presencia del material reciclado, así como el desarrollo de un modelo numérico que permita valorar esta disminución sin acudir a ensayos reales.

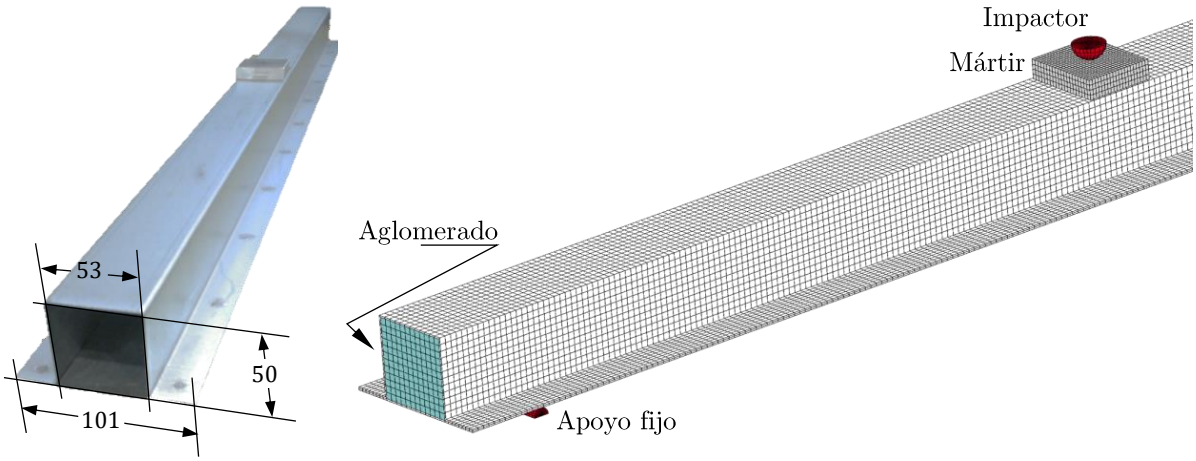

Figura 1. *Espécimen de viga sin relleno, cotas en mm (izda.). Detalle del modelo numérico (dcha.)*

La severidad del impacto ha sido medida mediante los dos parámetros tradicionalmente utilizados para este fin, la fuerza máxima y el criterio de lesión encefálica (HIC, por sus siglas en inglés, de aquí en adelante).

En la idea de que el daño que sufre el cerebro, durante un impacto, no es sólo función de las aceleraciones a que está sometido, sino del tiempo que está sometido a esas aceleraciones, el HIC valora la probabilidad de daño cerebral en proporción a una integral, en el tiempo, de las aceleraciones que sufre el cerebro, su definición puede consultarse, por ejemplo, en [2]. Como la duración de los impactos para los que se define el HIC es superior a la de los impactos realizados en este trabajo, aquí se ha considerado un parámetro ligeramente diferente que denominaremos $\overline{\mathrm{HIC}}$ y que se define en la Eq. (1), donde $g(t)$ es la aceleración en g y t_i es el tiempo de impacto.

$$\overline{\mathrm{HIC}} = t_i \left[\frac{1}{t_i} \int_{t_i} g(t)dt \right]^{2.5} \tag{1}$$

2. ESTUDIO EXPERIMENTAL

El estudio experimental ha consistido en una campaña de ensayos en los que se aplica una carga puntual de impacto en el centro de una viga, de chapa de acero, apoyada en sus extremos, véase Fig. 1. La luz entre apoyos ha sido de $900\ \mathrm{mm}$ y la chapa empleada ha sido de 1 mm de espesor. Los ensayos se han realizado mediante una máquina de caída de dardo CEAST 9350 de INSTRON®. Para este estudio preliminar y con la intención de no sobrepasar el régimen elástico de los especímenes, se trabajó con una masa total de impacto de $5.3\ \mathrm{kg}$ y una velocidad de impacto de $2\ \mathrm{m/s}$. Para evitar efectos locales se interpuso un mártir entre la viga de acero y el impactor.

Se realizaron seis ensayos: tres sobre la viga hueca de acero y tres sobre la viga de acero más aglomerado; obteniendo una alta repetibilidad de los resultados como se puede ver en la Fig. 2.

3. ESTUDIO NUMÉRICO

El análisis numérico se ha realizado mediante dinámica explícita haciendo uso del software *LS Dyna®*. En la elección de este software ha influido de forma decisiva que implementa el modelo de comportamiento de Bergstöm-Boyce [3], que se ha utilizado para el aglomerado teniendo en consideración que este modelo incorpora altas velocidades de deformación y grandes deformaciones que, si bien no se consideran en este trabajo preliminar, se considerarán en la siguiente fase del trabajo.

Las propiedades del aglomerado y el acero se han determinado respectivamente, de forma experimental, en [4] y [5].

4. CORRELACIÓN NUMÉRICO-EXPERIMENTAL Y ANÁLISIS DE RESULTADOS.

La Fig. 2 muestra el buen ajuste que tienen los resultados del modelo numérico en relación a los resultados experimentales. En esta situación estamos en condiciones de valorar los resultados marcados en los objetivos: (i) la aportación del aglomerado en la disminución de la severidad del impacto (con el acero en régimen lineal) y (ii) lo adecuado del modelo numérico para el mismo fin.

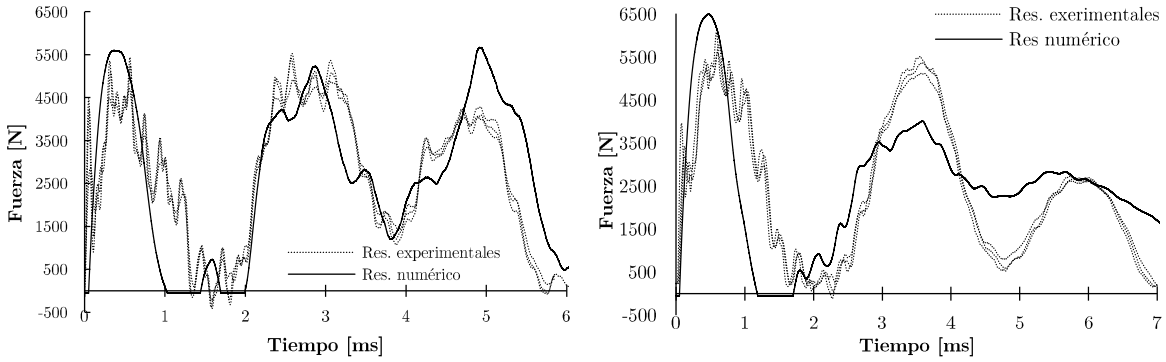

Figura 2. *Resultados experimentales vs. numérico. Viga hueca (Izda.) y viga con aglomerado (Dcha.)*

Respecto a los resultados experimentales, véase Tabla 1, se observa que la fuerza máxima media aumenta aproximadamente un 13.4% por la presencia del aglomerado, lo que es esperable al tratarse de un espécimen un 68.7 % más pesado que el espécimen hueco y, por lo tanto, con mayor inercia ante el impacto, sin embargo, el $\overline{\mathrm{HIC}}$ disminuye un 12.7%. En el caso numérico, el incremento de la fuerza máxima es del 14.4 %, muy similar a los resultados reales, mientras que el decremento del $\overline{\mathrm{HIC}}$ resulta menor que el real: un 4.2 %.

Tabla 1. Resultados del análisis de severidad del impacto.

Viga	Parámetro	Experimental	Numérico
Acero [2.30 kg]	$\overline{\mathrm{HIC}}$ [s]	117.23 ± 2.55	118.07
	$\mathrm{F_{max}}$ [N]	5124.66 ± 307.48	5670.26
Acero + Aglomerado [3.88 kg]	$\overline{\mathrm{HIC}}$ [s]	102.35 ± 1.06	113.09
	$\mathrm{F_{max}}$ [N]	5812.68 ± 238.90	6486.22

Comparando los valores numéricos y experimentales, tenemos una diferencia del $0.7\ \%$ para el $\overline{\mathrm{HIC}}$ y del $10.6\ \%$ para $\mathrm{F_{max}}$ en el caso de la viga hueca. Para la viga con aglomerado se observan diferencias del $10.5\ \%$ para el $\overline{\mathrm{HIC}}$ y del $11.6\ \%$ para $\mathrm{F_{max}}$.

5. CONCLUSIONES

Se ha fabricado un demostrador bimaterial acero-aglomerado de caucho reciclado, para valorar como la presencia del último reduce de la severidad ante cargas de impacto.

Los ensayos de laboratorio muestran una alta repetitividad en los resultados. Los resultados numéricos y experimentales presentan un alto grado de correlación.

La adición del aglomerado de NFU supone una mejora del $\overline{\mathrm{HIC}}$ del sistema, lo que supone una disminución de la probabilidad de sufrir lesiones craneoencefálicas como consecuencia de un impacto lo que, a falta de estudios más avanzados que incluyan comportamiento elastoplástico y dimensiones reales, apunta en la dirección de una posible mejora en los sistemas actuales de retención de vehículos.

El modelo desarrollado permite el estudio de casos a escala real para evaluar la efectividad de futuros diseños sin necesidad de realizar ensayos, de coste muy elevado, o, al menos, reduciendo su número.

Esta investigación tiene una derivada medioambiental indiscutible: el uso del aglomerado de caucho, a partir de neumáticos reciclados, en los millones de kilómetros de vías alrededor del mundo puede suponer una contribución decisiva en la gestión de un tipo de residuo que, actualmente, supone un problema medioambiental de primer orden.

6. AGRADECIMIENTOS

Este trabajo ha sido financiado por la Consejería de Transformación Económica, Industria, Conocimiento y Universidades, dentro de los Proyectos I+D+i en el marco del Programa Operativo FEDER, a través del proyecto “Absorción de Energía de Impacto a Partir de Neumáticos Fuera de Uso -NFU- Reciclados. Aplicación a Sistemas de Contención de Vehículos” de referencia UMA20-FEDERJA-028.

7. REFERENCIAS

[1] González-Vega, J., Castillo-López, G., Galindo-Moreno, J.M., Guerrero-Porras, S., García-Sánchez, F., 2022. Experimental viscoelastic properties evaluation, under impact loads and large strain conditions, of coated & uncoated rubber from end-of-life tires. Polymer Testing 107, 107468.

[2] Henn, H. W. (1998). Crash tests and the head injury criterion. Teaching mathematics and its applications, 17(4), 162-170.

[3] Bergström, J., 2015. Mechanics of Solid Polymers: Theory and Computational Modeling. doi:10.1016/C2013-0-15493-1.

[4] Guerrero-Porras, S. (2023). Determinación experimental de las propiedades viscoelásticas homogeneizadas de un aglomerado realizado a partir de neumáticos reciclados. Trabajo Fin de Máster. Universidad de Málaga

[5] López-Medina, P. (2023). Diseño y ensayo de un demostrador de laboratorio para la evaluación numérica y experimental de la disipación de la energía de impacto en un sistema multimaterial basado en neumáticos reciclados. Trabajo Fin de Grado. Universidad de Málaga

Experimental study on fire resistance of glulam-lightweight concrete composite slabs with inclined crossing screws

Álvarez Rabanal, Felipe Pedro[1]; Lozano Martínez-Luengas, Alfonso[1] ; Alonso Martínez, Mar[1] ; del Coz Díaz, Juan José[1] ; Martínez Martínez, Juan Enrique[1]

ABSTRACT

Composite slabs made of lightweight concrete and glulam (TLCC) are sustainable and structurally efficient construction elements, since they combine the compressive strength of concrete with the flexural resistance of glulam. However, there is a lack of information in standards and codes about its behavior in fire conditions. The study of its fire resistance represents an innovative contribution that will increase its use in the construction sector. An experimental study following UNE-EN 1363-1:2021 standard was carried out to determine the fire resistance of TLCCs, made with local and northern European woods, joined with inclined crossing screws. During the tests, all the slabs met the integrity and insulation criteria indicated in the standard, bearing capacity being the one that determined their completion. In all cases, test stopped when the deflection speed limit indicated in the standard was exceeded. Once the results were analyzed, it was determined that only TLCC made with Chestnut offers R30 fire protection.

Keywords: Glulam-concrete composite slab, Lightweight concrete, Fire resistance, Local wood, Sustainable construction.

1. INTRODUCCIÓN

En la actualidad, las emisiones de gases de efecto invernadero debidas a materiales estructurales utilizados en construcción son una de las principales preocupaciones mundiales. Los materiales primarios más utilizados, acero y hormigón, requieren de enormes cantidades de energía para su producción y son responsables de altas emisiones de carbono [1]. Por ello, gobiernos e instituciones de todo el mundo han puesto en marcha políticas para fomentar el uso de materiales alternativos que supongan un menor impacto ambiental. Entre estos materiales alternativos, la madera aparece como un material natural y renovable, que requiere de muy poca energía para su producción, capaz de producirse localmente, totalmente reutilizable y que puede almacenar CO_2 a lo largo de toda su vida útil [2].

Los forjados mixtos fabricados con elementos de madera y hormigón (TCC), son una solución constructiva en crecimiento en edificaciones realizadas en todo el mundo. Suelen ser construcciones livianas, estructuralmente muy eficientes, en las que el hormigón aporta la rigidez al conjunto y la madera la resistencia sin necesidad de aumentar su peso. Las principales desventajas para su desarrollo son la escasa información acerca de sus propiedades mecánico-resistentes y aislantes en diferentes condiciones de servicio, y que en la normativa actual el comportamiento frente al fuego de los TCCs solamente está contemplado en alguno de los supuestos de cálculo para aquellos fabricados con coníferas (abeto),

[1] *Departamento de Construcción e Ingeniería de Fabricación. Universidad de Oviedo (ESPAÑA). alvarezfelipe@uniovi.es (Corresponding author), alozano@uniovi.es, mar@constru.uniovi.es, juanjo@constru.uniovi.es, quique@constru.uniovi.es.*

no para maderas locales (castaño, roble, eucalipto, pino). En el ámbito internacional, destacan diversas investigaciones realizadas sobre el comportamiento mecánico-estructural de los TCCs con hormigones normales y maderas laminadas de coníferas en condiciones de incendio [3,4].

El principal objetivo de este trabajo es avanzar científica y tecnológicamente en el conocimiento de los TCCs para fomentar su aplicación en construcción industrializada. Se propone estudiar la resistencia frente al fuego de TLCCs elaborados con diferentes tipos de vigas de madera laminada encolada (glulam) y hormigón ligero estructural (LWC), unidas con conectores metálicos cruzados. En estudios previos realizados sobre este tipo de forjados [5,6], se llevaron a cabo ensayos de resistencia al deslizamiento, resistencia a flexión y transmitancia térmica. Los resultados obtenidos de los módulos de deslizamiento mostraron un incremento de la resistencia a cortante de los forjados fabricados con maderas locales (pino y castaño) del 43,7% y 28% respectivamente respecto a los fabricados con madera de abeto importada del norte de Europa. En los ensayos de flexión, las losas fabricadas con maderas locales presentaron mayores valores de resistencia a flexión que las de abeto, produciéndose en todas ellas un modo de fallo a cortante en la zona de los conectores de unión mediante la aparición de fisuras longitudinales. Los ensayos de transmitancia térmica sirvieron para demostrar que los conectores metálicos tienen una gran influencia en la variación de la transferencia térmica en la zona de conexión del forjado, por lo que deben tenerse en cuenta en procesos en los que exista transferencia de calor.

2. MATERIALES Y MÉTODOS

Se diseñaron y fabricaron 6 especímenes de TLCCs (2 por cada tipo de madera: abeto, castaño y pino) de 2.340 mm de longitud entre apoyos y 1.100 mm de ancho. Se utilizaron conectores metálicos cruzados 45° (240 mm, Ø9 mm) uniendo las vigas de glulam (200x100x2.600 mm) y las losas de LWC (60 mm de espesor). Previamente al hormigonado de las losas, se sensorizó la unión mediante la colocación de cables de termopar tipo K sobre la superficie de las vigas y los conectores metálicos (Fig. 1, izquierda).

Figura 1. *Colocación de los conectores y sensorización mediante termopares de las vigas de glulam (izquierda), vista del montaje de probeta en horno de resistencia al fuego (centro) y sección carbonizada de las vigas de glulam después del ensayo de resistencia al fuego (derecha).*

Los ensayos de resistencia al fuego se realizaron sobre las 6 probetas colocadas en la parte superior de un horno de resistencia al fuego según UNE-EN 1363-1 (ver Fig. 1, centro). Durante el ensayo se sometió a las losas a una curva de fuego normalizada ISO-834 y se aplicó una carga constante sobre la parte central de la losa (40% de la carga de rotura obtenida en ensayos de flexión a temperatura ambiente).

3. RESULTADOS Y DISCUSIÓN

Durante los ensayos, todas las losas cumplieron con los criterios de integridad y aislamiento indicados en la norma, siendo la capacidad portante la que determinó su terminación. En todos los casos, la prueba se detuvo cuando se superó el límite de velocidad de deflexión indicado en la norma para las dimensiones de las losas ensayadas (2,34 mm/min). En el gráfico de la izquierda de la Fig. 2, se puede observar la evolución de la deformación vertical (Flecha) y de la velocidad de deflexión durante los ensayos realizados sobre cada una de las losas. En la imagen de la derecha de la Fig. 2, se puede comprobar en la vista cenital de uno de los forjados ensayados las líneas de fisuración que generan los esfuerzos cortantes y los gradientes térmicos en la parte superior de las losas de hormigón durante los ensayos. En la imagen de la derecha de la Fig. 1, se puede comprobar la pérdida de sección que se produce en una de las vigas de glulam ensayadas, siendo esta la principal causa que genera el modo de fallo a flexión de este tipo de forjados en condiciones de incendio.

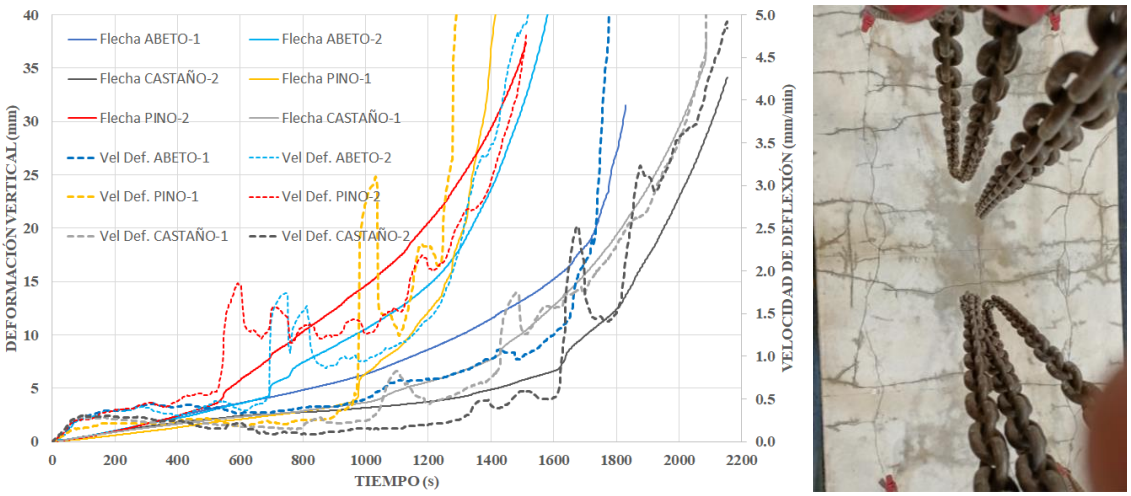

Figura 2. *Curvas tiempo-temperatura de los TLCCs durante el ensayo de Resistencia al fuego (izquierda) y fisuración en la parte superior de la losa después del ensayo (derecha).*

Como se muestra en la *Tabla 1*, los resultados obtenidos revelaron que los tiempos de resistencia al fuego de los forjados fabricados con madera de pino y abeto (21 y 25 minutos de valor promedio respectivamente) no superaron el valor mínimo R30 que según la normativa se requiere para este tipo de estructuras. Los fabricados con madera laminada encolada de castaño fueron los únicos en los que se superaron los 30 minutos de resistencia al fuego.

Tabla 1. Valores del tiempo de resistencia al fuego de las muestras ensayadas

Muestra	TIEMPO
ABETO-1	28,81 min
ABETO-2	21,74 min
PINO-1	20,77 min
PINO-2	21,23 min
CASTAÑO-1	30,12 min
CASTAÑO-2	30,63 min

4. CONCLUSIONES

Los ensayos de resistencia al fuego de este trabajo suponen un avance en el conocimiento, ya que son comúnmente realizados sobre forjados mixtos fabricados con madera de coníferas y hormigones normales, pero nunca antes se habían llevado a cabo sobre forjados fabricados con maderas locales combinadas con LWC. Los resultados obtenidos indican un mejor comportamiento frente al fuego de los forjados fabricados con la madera local de castaño frente a las importadas, lo que permitirá fomentar el aprovechamiento de recursos autóctonos y estimular la demanda de estos productos, reduciendo así el coste de transporte con la utilización de productos locales (ahorro energético en la logística).

Este estudio supone un avance significativo en la comprensión del comportamiento de este tipo de solución constructiva en condiciones de incendio y pueden servir como base para la mejora de la normativa con la inclusión en los DBs de SI-E y SE-M del comportamiento de los TCCs en condiciones de incendio, que actualmente no se contemplan. En general, el sector de la construcción es el que sufre un mayor impacto con los resultados, lo que puede servir para impulsar su uso por parte de los diferentes actores que lo conforman (arquitectos, ingenieros, empresas constructoras, fabricantes, administraciones o usuarios finales). Otros impactos a tener en cuenta es que el fomento del uso de forjados fabricados con materiales reutilizables y reciclables supone una mejora importante en el ciclo de vida del producto, y que el menor coste estructural debido a su menor peso respecto a otros tipos de forjados convencionales implica un ahorro energético importante en la construcción de edificios.

AGRADECIMIENTOS

Los autores agradecen a la Fundación para el Fomento en Asturias de la Investigación Científica Aplicada y la Tecnología (FICYT) y al Ministerio de Ciencia, Innovación y Universidades del gobierno de España las ayudas recibidas a través de los proyectos AYUD/2021/51328 y PGC2018-098459-B-I00, ambos financiados con fondos FEDER. También agradecen a las empresas Weber Saint-Gobain y Rothoblass su asesoramiento técnico y la aportación de los materiales necesarios para poder realizar este estudio.

REFERENCIAS

[1] CEI-Bois. (2014). Tackle Climate Change: build with wood, p. 48. Brussel: The European Confederation of woodworking industries.

[2] Sathre, R., & O'Connor, J. (2010). A synthesis of research on wood products & Greenhouse gas impacts 2nd Edition, p. 117. Vancouver, BC: FPInnovations (Technical report TR-19R).

[3] Klippel, M., & Frangi, A. (2017). Experimental and analytical investigation on fire resistance of glulam-concrete composite beams. *Journal of Structural Engineering, 143(7), 04017052*.

[4] Hao, D., Xiamin, H., Zhong, X., & Yanfei, M. (2021). Fire safety of glued-laminated timber beams in bending. *Journal of Building Engineering, 44, 103244*.

[5] Martínez-Martínez, J.E., Alvarez Rabanal, F.P., Alonso-Martínez, M., del Coz Díaz, J.J. Comparative analysis of the shear behaviour of glulam timber. In VII International Conference on Technological Innovation in Building (CITE 2022). Madrid: Universidad Politécnica de Madrid.

[6] Martínez-Martínez, J.E., Alvarez Rabanal, F.P., del Coz Díaz, J.J., Alonso-Martínez, M. Comparative structural behaviour among timber and steel deck- lightweight concrete composite slabs. In International Conference on Civil, Structural and Environmental Engineering (ICCSEE 2022). Barcelona.

Experimental test of asymmetric haunched joint with threaded bars

Loureiro, Alfonso[1]; López, Manuel[1]; Gutiérrez, Ruth[1]; Reinosa, José Manuel[1]

ABSTRACT

End plate joints using single bolts are widely used in steel structures. This type of connection has low rigidity and resistance, and so, it is usual to use horizontal welded plates both in the traction and compression zones, and an inclined one in the shear column web panel. This type of joint is expensive, and difficult of execution, especially in existing structures that need to reinforce the joints. In order to stiffen and reinforce the end plate bolted joints, in a more economical and easy way to execute, even in existing structures, the use of threaded bars is proposed, using double nut, both in the traction and compression zones.

This paper shows the experimental results of an asymmetric haunched joint using threaded bars, observing a substantial improvement, with respect to the use of single bolts, both in resistance and rigidity.

Keywords: Asymmetrical haunched steel joints, Threaded bars, End plate joints.

1. INTRODUCCIÓN

Las uniones atornilladas con chapa de testa se utilizan ampliamente en estructuras de acero. Se trata de uniones cuyo comportamiento semirrígido ha sido analizado por autores como Azizinamini et al [1], y Yee y Melchers [2]. El análisis de este tipo de uniones se puede realizar mediante el método de componentes indicado en el EC3 [3]. Uno de los componentes más influyentes es el T-stub formado por las alas de la columna y la placa frontal, el cual ha sido analizado por autores como Loureiro et al. [4] y Girao et al. [5]. Es habitual rigidizar este tipo de uniones mediante chapas soldadas, aumentando el coste de la unión. La opción propuesta en este trabajo consiste en la utilización de barras roscadas, tanto en la zona de tracción como en la de compresión, con doble tuerca. El estudio realizado por Nip y Surtees [6] muestra que el uso de barras roscadas para la zona de compresión, en uniones trabajando a flexión, da buenos resultados. Bayo et al. [7], López et al. [8] y Loureiro et al. [9] han realizado estudios sobre uniones soldadas asimétricas. Sin embargo, el presente estudio se centra en las uniones atornilladas asimétricas con cartabón y chapa de testa, mostrando los resultados comparativos de dos ensayos similares, uno de ellos con la configuración habitual de tornillos simples, y el otro utilizando barras roscadas con doble tuerca.

2. ENSAYOS A ESCALA REAL

2.1. Descripción de los ensayos: tipología e instrumentación

[1] *University of A Coruña (SPAIN). a.loureiro@udc.es (Corresponding author), manuel.lopez.lopez@udc.es, j.reinosa@udc.es, ruth.gutierrez@udc.es*

Este trabajo se centra en el estudio experimental comparativo de dos uniones similares asimétricas con cartabón y chapa de testa. Una de ellas con tornillos simples y la otra con barras roscadas. En ambos casos la columna es un HEA200, y las vigas son IPE200 e IPE300, utilizando una chapa de testa de 12 mm de espesor. Los tornillos y las barras roscadas son M20, de calidad 10.9. Las propiedades reales de los materiales se muestran en la *Tabla 1*.

Tabla 1. Propiedades de los materiales

Elemento	Value	
	E (MPa)	fy (MPa)
HEA200	210547	381
IPE200	209784	351
IPE300	210874	342

La instrumentación utilizada consiste en células de carga, sensores de desplazamiento, inclinómetros para medir las rotaciones de la viga fuerte, la viga débil y el centro de la unión, con el fin de captar la rotación de sólido rígido. La Fig. 1 y la Fig. 2 muestran imágenes de ambas pruebas.

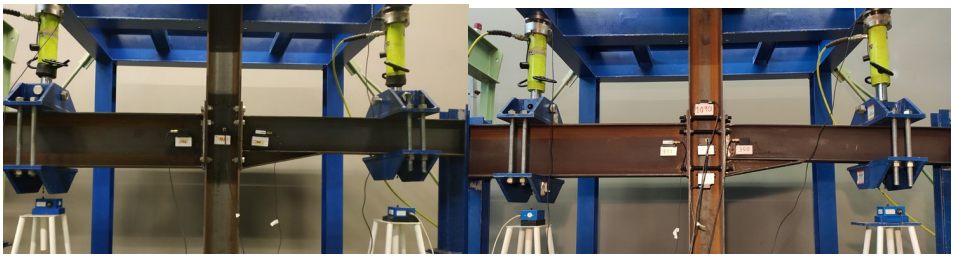

(a) (b)

Figura 1. *Vistas de los ensayos a escala real: (a) con tornillos simples y (b) con barras roscadas.*

(a) (b)

Figura 2. *Vistas de detalle de los nudos tras los ensayos: (a) con tornillos simples y (b) con barras roscadas.*

2.2. Desarrollo de los ensayos y análisis de resultados

Se ha aplicado carga simétrica en ambas vigas, y se ha estudiado el comportamiento de la viga débil, que es el elemento que caracteriza la rigidez y resistencia de la unión, observándose un notable incremento, tanto de la rigidez como de la resistencia de la unión, cuando se utilizan barras roscadas. En la unión con tornillos simples aparecen importantes deformaciones por flexión en las alas del pilar y en la chapa de testa, en la zona de tracción. También se observa un ligero pandeo local en el alma del pilar en compresión. En cambio, la unión con barras roscadas muestra un comportamiento mucho más estable, de forma que la fluencia se inicia con una carga mucho mayor, permaneciendo la columna sin daño observable a simple vista. La Fig. 2 muestra el estado final de deformación de las uniones en ambos ensayos.

Las gráficas momento-rotación correspondientes al comportamiento de la viga débil se muestran en la Fig. 3 y se resumen en la *Tabla 2*. Se observa que el uso de barras roscadas conduce a un aumento en la resistencia de un 55.8 %, y un aumento de la rigidez del 64.3 %, respecto a la unión con tornillos simples. Adicionalmente, se puede observar que la unión con tornillos simples y la de barras roscadas permanecen en la zona elástica hasta alcanzar los 35 KNm y 62 KNm, respectivamente, lo que representa un incremento del 77.1 %.

Tabla 2. Resultados de los ensayos para la viga débil (IPE200)

Ensayo	Rigidez inicial (KNm/mrad)	Resistencia (KNm)	Componente más débil
Ensayo 1	26.94	129.5	Alas del pilar a flexión y alma del pilar a compresión
Ensayo 2	43.74	83.1	Chapa de testa

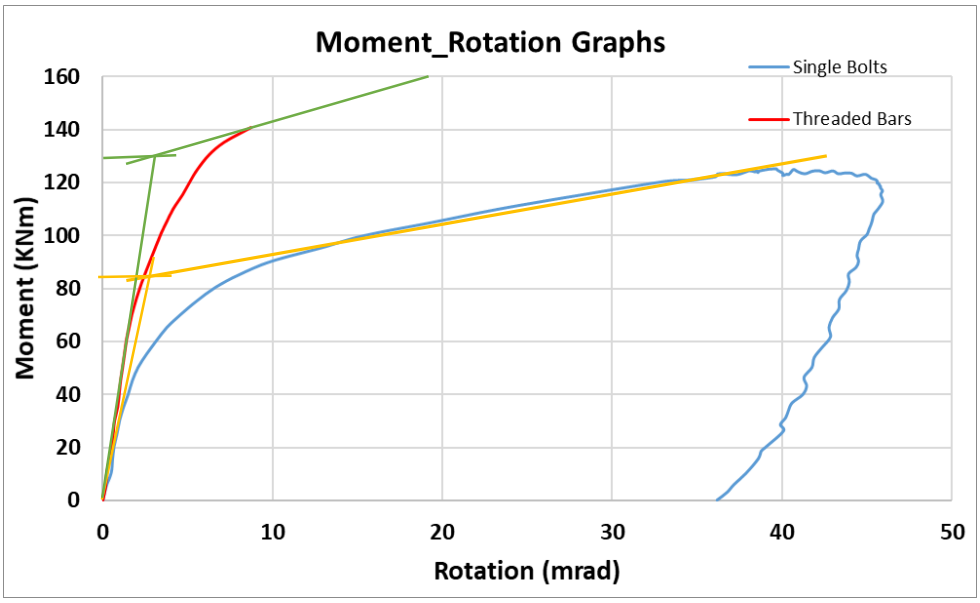

Figura 3. *Resultados comparativos*

3. CONCLUSIONES

El trabajo realizado muestra que, en el caso de la unión con tornillos simples, el fallo se produce por flexión de las alas de la columna, seguido del alma de la columna en compresión, mientras que, en la unión con barras roscadas no se aprecia fallo en ningún elemento de la columna, siendo la chapa de testa la que inicia la plastificación.

El análisis de los datos ha arrojado un notable mejor comportamiento de la unión con barras roscadas, con una ganancia del 64.3 % en rigidez y del 55,8 % en resistencia, y un importante incremento del 77.1 % en el rango elástico de la unión, con respecto al uso de tornillos simples.

Teniendo en cuenta que el cambio de pernos simples por barras roscadas es realmente sencillo y económico, este tipo de unión presenta una clara alternativa al uso de rigidizadores soldados, siendo especialmente interesante en el caso de estructuras ya construidas que necesitan ser reforzadas.

AGRADECIMIENTOS

Se agradece el financiamiento obtenido a través del Proyecto PID2020-113895GB-C31, financiado por el MCIN /AEI /10.13039/ 501100011033.

REFERENCIAS

[1] Azizinamini A., Bradburn J.H., Radziminski J.B. (1987) Initial stiffness of semi-rigid steel beam-to-column connections. Journal of Constructional Steel Research, 8 pp. 71–90.

[2] Yee YL; Melchers R.E. (1986) Moment–rotation curves for bolted connections. Journal of Structural Engineering, 112 pp. 615–635.

[3] Eurocode 3 (2005). Design of steel structures, Part 1–8: Design of joints. CEN.

[4] Loureiro, A.; Gutierrez, R.; Reinosa J.M.; Moreno A. (2010). Axial stiffness prediction of non-preloaded T-stubs. Journal of Constructional Steel Research, 66(12), pp. 1516-1522.

[5] Girao A.M.; Bijlaard F.; Gresnigt N., Simoes L. (2004) Experimental assessment of the behaviour of bolted T-stub connections made up of welded plates. Journal of Constructional Steel Research, 60(2) pp. 269–311.

[6] Nip T.F, Surtees J.O. (1999), Threaded bar compression stiffening for moment connections, Proceeding of the 2nd International Conference on Advances in Steel Structures, Pergamon Pr, Hong Kong, 15-17 december/1999, pp. 283-290.

[7] Bayo E., Loureiro A., Lopez M. (2015), Shear behaviour of trapezoidal column panels. I: Experiments and finite element modelling, Journal of Constructional Steel Research, 108 pp. 60-69.

[8] Lopez M., Loureiro A., Bayo E. (2015), Shear behaviour of trapezoidal column panels. II: Parametric study and cruciform element, Journal of Constructional Steel Research, 108 pp. 70-81.

[9] Loureiro A., Lopez M., Bayo E. (2016), Shear behaviour of stiffened double rectangular column panels: Characterization and cruciform element, Journal of Constructional Steel Research, 117 pp. 126-138.

Fatigue crack growth rate base-curve involving thickness and stress ratio in 2024-T3 &T351 aluminium alloys.

Rodríguez, I.[1], Ortega, N.[1], Lunas, J.[1], Pedraza, C.[1], Martín, A.[1]

ABSTRACT

The availability of reliable fatigue crack growth (FCG) prediction tools is essential to the design of structures subjected to fatigue loading. Constant amplitude (CA) test provides Δk vs. da/dN data, but CA test data applicability is limited because of the strong influence of stress ratio (R) and thickness on the FCG.

To develop crack growth rate base-curves involving thickness and R, available CA test data from literature have been analysed according to PIFCC fundamentals and considering the transition from plane strain state to plane stress state at the crack tip. This tool is able to estimate Δk vs. da/dN data under CA loading for thicknesses and stress ratios of which there is no information available, especially for thin components (1 to 5 mm) in which the stress state transitions hinder the estimations. Applied to 2024 and 7075 aluminium alloys it provides an expression of FCG rate along 4 decades.

Keywords: Fatigue, C.A. behaviour, AA2024, AA7075.

1. INTRODUCCIÓN.

La herramienta básica de predicción de crecimiento de grietas de fatiga son los ensayos CA, que pueden proporcionar datos Δk (o $k_{Máx}$) vs. da/dN desde valores de crecimiento próximos al umbral hasta la rotura. Introducido el cierre de grieta desde criterios plásticos (PIFCC), la definición de Δk_{ef} como variable directora del crecimiento agrupó las curvas de crecimiento para cualquier R en la zona de comportamiento de Paris, como muestra la Fig.1. También desde conceptos PIFCC, los primeros modelos de crecimiento bidimensionales Strip-Yield introducen un factor de constricción promedio "α" que les permite afrontar problemas triaxiales adaptando la tensión de fluencia a tracción al estado tensional del frente de grieta. La elección de los valores de "α" han sido empleadas frecuentemente como parámetros de ajuste del modelo y por facilitar la convergencia en valores efectivos.

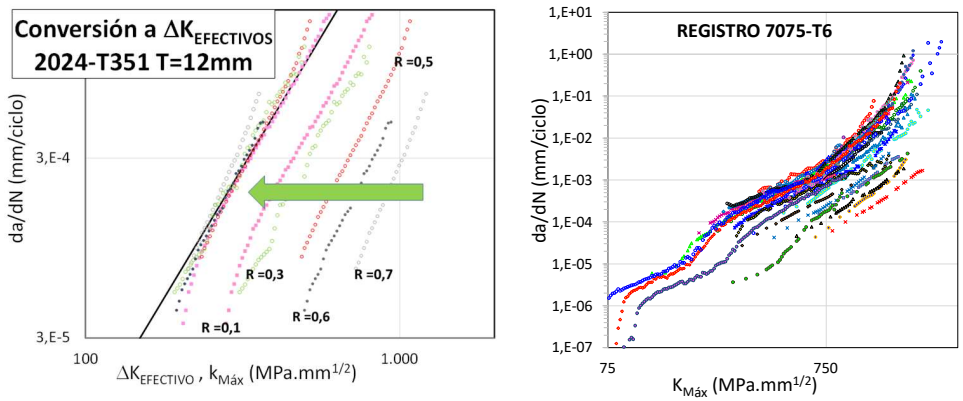

Figura 1. *Conversión a valores efectivos desde $k_{Máx.}$ (izda.), Registros empleados en aleación 7075-T6 (dcha.)*

[1] *Departamento de Ingeniería Civil, de Materiales y Fabricación. Universidad de Málaga. (España).*

irene.rodriguez.calero@gmail.com, noemioregasuarez@uma.es, 06198747964@uma.es, cpedraza@uma.es,

La transición entre estados tensionales ha sido relacionada con valores de da/dN, Δk_{ef} o la relación entre radio plástico y espesor del elemento. Junto a esto, cambios en el crecimiento a espesores bajos (3-6 mm) y notables a espesores de 1 a 3 mm, han limitado los modelos y ecuaciones de crecimiento que incluyen espesor y R. En este trabajo se desarrolla el método de puntos singulares aplicado por Martín [1] a AA2024 y por Zúñiga [2] a AA7075 y se aplica a AA7050-T7451. La capacidad del modelo para estimar la senda de crecimiento en espesores muy reducidos se ha extendido hasta espesores de 1 mm.

2. MÉTODO DE PUNTOS SINGULARES PARA ESTIMACIÓN DE CRECIMIENTO DE GRIETAS BAJO C.A.

En las aleaciones de estudio la senda de crecimiento exhibe diferencias que dificultan su análisis. La Fig.1. incluye los registros empleados en la aleación AA7075-T6 obtenidos del programa NASGRO o recopiladas de publicaciones. En la Fig.2. se muestra el perfil genérico de crecimiento para estas aleaciones, el perfil sinuoso en zonas de crecimiento umbral no es explicable desde planteamientos PIFCC, y sugiere la existencia de otros mecanismos de crecimiento. El estudio de Wanhill [3] sobre esta etapa de crecimiento destaca los cambios en la topografía de fractura hasta alcanzar el punto marcado como 3 en la Fig.2. donde, desde caras corrugadas de topografía rugosa va incorporando las comunes estrías homogéneas de fatiga, disminuyendo la rugosidad y la deflexión en la grieta hasta iniciar en punto 4 el crecimiento estable, con los puntos 2,3 y 5 presentándose a da/dN similares.

La pendiente de Paris del material se obtiene desde ensayos de espesor medios y R baja, aplicándola a cada registro para identificar el "C" propio. El inicio de transición lo define el espesor y se da en todo R a una misma da/dN. En la Fig.2. (dcha.) se aprecia cómo para dos R, dos espesores comparten tramo lineal de Paris en deformación plana (DP) y, a una misma da/dN los registros de menor espesor se bifurcan en transición hacia Paris en tensión plana (TP). En ambas imágenes de la Fig.2. se ha representado la transición con una pendiente común a todos los R y espesores del material, y su valor es obtenido del conjunto de registros que presentan esta etapa. En la zona inicial de crecimiento, estas aleaciones ofrecen un punto singular de crecimiento en el que es posible su posicionamiento en da/dN, $k_{Máx}$ y la pendiente con la que transita. En el punto "3" de la Fig.2. se produce la inflexión que refleja cambios en el mecanismo de crecimiento; es identificado para la aleación AA7075-T6 en la Fig.3. y se indica su valor de $K_{Máx}$. La Fig.3. (dcha.) muestra los datos de da/dN de AA2024 en los que comienza la transición. La inclusión de espesores de 1 mm ha sido posible en la aleación AA7075-T6 prolongando la pendiente de la inflexión hasta confluir con la transición trazada desde el punto de inicio de Paris en TP.

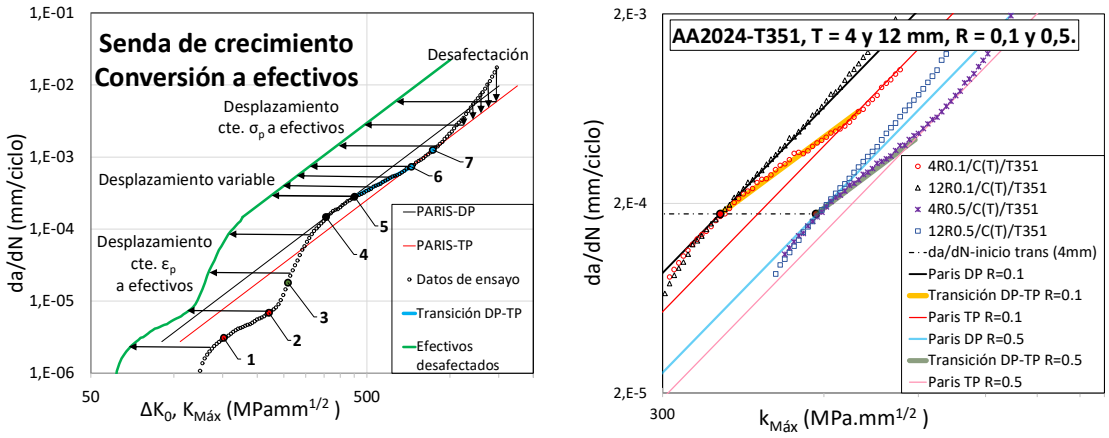

Figura 2. *Senda de crecimiento genérica en AA2024, puntos singulares empleados y conversión a valores efectivos (izda.). Puntos de inicio de transición y tramos de Paris en DP y TP en 2024-T351 (dcha.).*

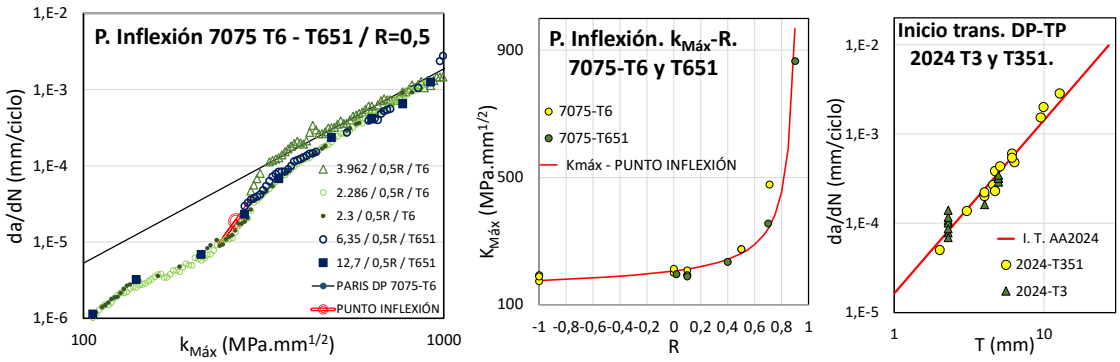

Figura 3. *Confluencia de sendas de crecimiento de diferentes registros y calidades para un mismo R en el Punto de Inflexión (izda.). Valores de* $K_{Máx}$ *en función de R del Punto de Inflexión para 7075-T6 y T651 (centro). Estimación de da/dN de comienzo de transición de DP a TP para la aleación 2024-T3 y T351 (dcha.).*

En cada registro se valora la aceleración presente en valores de $k_{Máx}$ superiores al de inicio de efectos de k_c. La Fig.4. (izda.) muestra funciones de ponderación en función de la relación $k_{Máx}/k_c$. Como indica la Fig.2. (izda.) la desafectación de los registros se proyecta sobre la senda de crecimiento. Para la conversión a valores efectivos según las ecuaciones de Newman [4] se toman valores de "α" 1.73 para DP y, para TP, 1.10 (AA7075) y 1.15 (AA 7075 y AA2024). Los valores efectivos son corregidos mediante el método 2π de Paris-Donald [5] obteniendo los valores respecto a la variable directora Δk_0. La conversión a valores Δk_0 agrupa el conjunto de ensayos como se aprecia en la Fig.4. (dcha.) para la aleación AA7075-T6 con geometrías, espesores y condiciones de ensayo muy diferentes. Los valores de "α" reducen la dispersión, haciendo más representativa la recta base. La recta inferior es definida en esta etapa en valores Δk_0 como una envolvente superior de los tramos rectos exhibidos por los distintos ensayos.

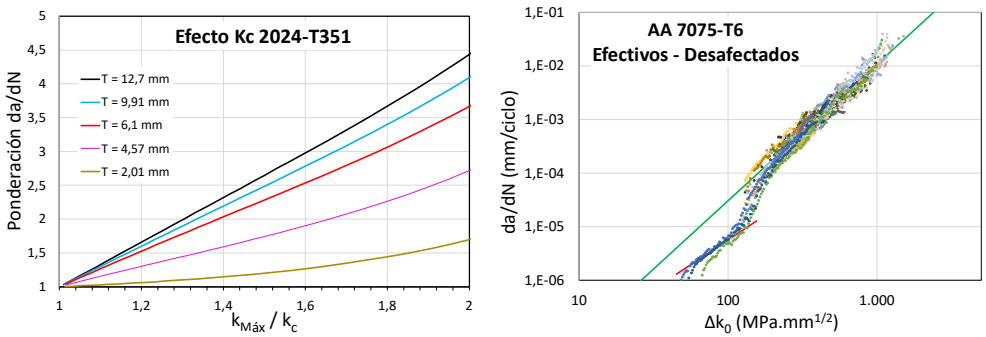

Figura 4. *Funciones de ponderación del efecto* K_c *la aleación 2024T-351 (izda.). Convergencia en valores efectivos de los datos de crecimiento para los registros 7075-T6 y Recta base del material en valores efectivos (dcha.).*

Para la generación de los registros CA se desharán las transformaciones. En la Fig.5. (izda.), partiendo de las rectas efectivas e inferior del material en valores Δk_0 se convierten a nominales de $k_{Máx}$. En la Fig.5. (centro), se fija el punto de inflexión y su pendiente se prolonga a las rectas inferior y de Paris DP. Desde el punto de Paris DP con velocidad de inicio de transición se lanza la transición hasta alcanzar a Paris TP. Como expone la Fig.5. (izda.), la senda seguirá este curso hasta inicio de efectos aceleradores en k_c. Desde ese valor en adelante los datos de velocidad serán ponderados según la relación $k_{Máx}/k_c$. Aplicaciones de este procedimiento se muestran en la Fig.6. (izda.), sobre AA7075-T6 con R=0 y espesor que no desarrolla Paris de DP, y en la Fig.6. (dcha.) sobre AA2024-T351 y dos casos: R=0.1 y R=0.7.

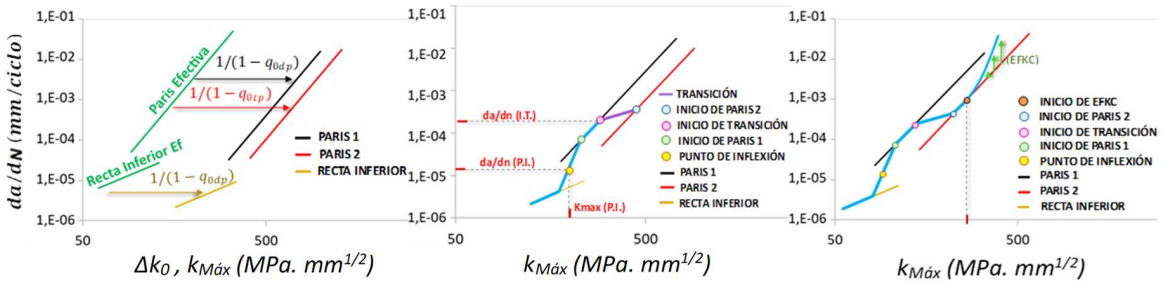

Figura 5. *Etapas en el procedimiento de generación de registros de CA desde la recta base del material. Conversión a $k_{Máx}$ (izda), aplicación de puntos singulares y transición (centro) y afectación por k_c (dcha.).*

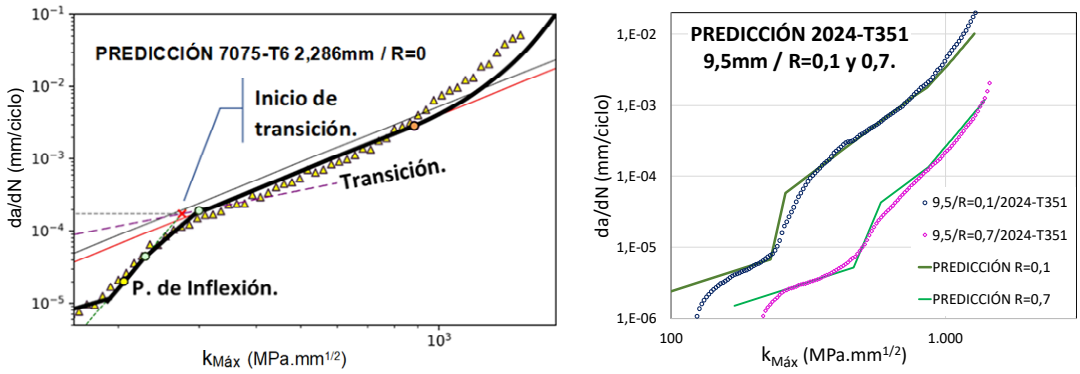

Figura 6. *Ejemplos de aplicación del generador de registros a varias aleaciones, R y espesores.*

3. CONCLUSIONES

Se ha incluido también la aplicación del método a AA7050. Las modificaciones incluidas han ampliado las posibilidades de generación de registros a espesores inferiores a los planteados inicialmente. Adaptar los "α" a cada aleación, respecto a los teóricos de partida (1.73 para DP y 1.0 para TP) ha mejorado el agrupamiento de test en valores efectivos Δk_0 y la representatividad de la curva base.

REFERENCIAS

[1] Martín, A., (2016). Análisis comparativo de modelos strip-yield en crecimiento de grietas por fatiga aleatoria (PhD. Tesis). Málaga: Universidad de Málaga.

[2] Zúñiga, R., Martín, A., Moreno, B., López-Crespo, P., Pedraza, C. (2018). Estimación del crecimiento de grietas desde valores efectivos de Δk: procedimiento de los puntos singulares aplicado a Al 2024 y Al 7075. Anales de Mecánica de Fractura, 35, 358-363.

[3] Wanhill, R.J.H. (1988). Low Stress Intensity Fatigue Crack Growth in 2024-T3 and T351. Engineering Fracture Mechanics, 30, 233-260.

[4] Newman Jr J.C. (1984). A crack-opening stress equation for fatigue crack growth. International Journal of Fracture, 24, 131-135.

[5] Donald, J.K., Paris, P.C. (1999). An evaluation of ΔKeff estimation procedures on 6061-T6 and 2024-T3 aluminium alloys. International Journal of Fatigue, 19, 47-57.

Fatigue strain fields comparison between Synchrotron X-Ray Diffraction and 3D Numerical computation in a bainitic steel

Aguilera, Jose A.[1]; M. Cerezo, Pablo[1]; Garcia-Gonzalez, Antonio[1]; Lopez-Crespo, Pablo[1]

ABSTRACT

Engineers prioritize resource preservation when designing lightweight materials, but fatigue can pose challenges. Although various experimental methods exist for studying fatigue cracks, some are only effective for transparent materials. For example, transmission photo-elasticity is limited in application, and post-failure metallography and micro-indentation cannot be adopted during mechanical testing. However, Synchrotron X-ray diffraction experiments can obtain valuable data from the bulk of metallic materials. A study was done on a 12mm thick Compact Tension bainitic steel sample (used in civil engineering and Wind offshore industry). A fatigue test was conducted by applying 51,000 loading cycles at a frequency of 10 Hz, ΔP=14.9KN (0.5kN to 15.4kN), followed by a 24.5 kN load. We analyzed the strain fields along the crack growth direction (εxx) and loading direction (εyy). Both experimental and Finite Element Methods data showed promising results with similar strain field shapes and values, showing as well consistency with mode I loading.

Keywords: bainitic steel, S-XRD diffraction, Finite Element Analysis, fatigue

1. OBJECTIVES

Engineers nowadays are greatly concerned with preserving resources, which makes the use of lightweight designs a popular and efficient solution. However, lightweight designs are prone to fatigue, so studying how fatigue cracks develop and spread during cyclic loading is crucial.

Several methods can be used to collect experimental data. However, most of them are only eligible to obtain data from the surface [1]–[4], being not precise enough to understand the behaviour in the bulk of the specimens during different tests [5]. Synchrotron X-ray diffraction (S-XRD) allows for obtaining data from the interior of the material, which makes it an innovative solution for understanding the strain fields inside the bulk [6]. The use of experimental data allows for the validation of 3D Finite Element Analysis in both the interior, with the S-XRD technique, and surface areas, with former techniques [7].

A Finite Element Methods (FEM) model was generated to simulate the behaviour of different fatigue states in a Compact Tension (CT) specimen. XRD data has also been used to validate a FEM with interior data; once the FEM is fitted, it has been taken mainly to determine strain and stress fields and other fracture and fatigue parameters [8], [9]. In this study, the size and geometry of the strain fields in the midplane of the specimen were determined using S-XRD in comparison with an entire 3D specimen FEM analysis. This validation will support the future use of the FEM model for more complex problems that are hard to test experimentally.

[1] *Department of Civil and Materials Engineering. University of Malaga (SPAIN). j.a.aguilera.garcia@uma.es (Corresponding author), pm@uma.es, tolin@uma.es, plc@uma.es*

2. APPROACH

2.1. Fatigue test and S-XRD configuration

A CT specimen W=50 mm and B=12mm manufactured from bainitic steel is subjected to pre-cracking by 51,000 cycles at 10 Hz with a ΔK = 28 MPa$\sqrt{m}$, from Pmin = 0.5 kN and Pmax = 15.4 kN. This results in a total crack length of 22 mm. After this pre-cracking step, a load of 24.5 kN is applied, the time when the S-XRD measurement is done.

An elastic strain experiment was performed on the ID15 beamline at the European Synchrotron Radiation Facility (ESRF) in Grenoble, France, using synchrotron X-ray diffraction. Data is collected in two directions; the strain information in the crack growth direction and in the crack opening direction. A 2D map of measurements is taken from the CT specimen, resulting in around 500 measurements, in the mid-plane, like in Fig. 1 b) with a gauge volume like Fig. 1 a), with dimensions of 1.4 mm long and 60 µm x60 µm wide and high. Due to the thickness of the sample (B=12 mm), this volume is considered representative of the material bulk.

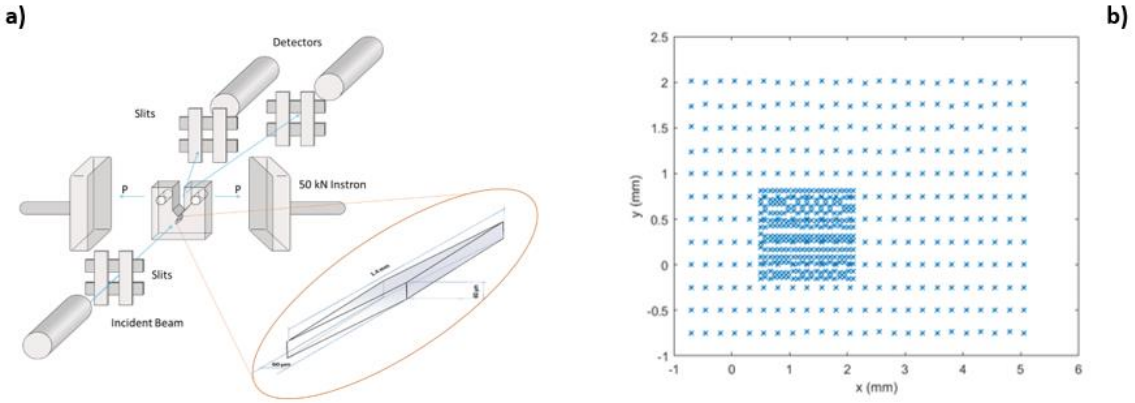

Figure 1. *a) s-XRD experiment set-up. b) 2D Map for point measured in the experiment.*

2.2. Finite Elements Model

A Finite Element Model (FEM) was created and compared to experimental S-XRD results for accuracy. ANSYS was used for programming and optimisation. The mesh has an 8 µm element size at the crack tip and is gradually increased to 3 mm, the shape transition is inspired by previous works [10]. This FE mesh allows a precise stress and strain gradient evaluation at the crack tip. A complete experimental fatigue test was developed into two steps; a) A pre-cracking 51,000 cycles (f=10 Hz) with a variable force of 15,400-500 N (R=0.03). The crack length was approximately 22 mm, b) Furthermore, a new load of 24.5 kN was applied to the specimen.

The interior conditions of the CT were measured using Synchrotron X-ray diffraction during experimental tests. Both simulation steps were carried out with complex non-linear equations and elastoplastic material behaviour: young modulus, E = 220 GPa; yield strength, σy = 699 MPa; tangent modulus, ET = 2,06 GPa. To balance the computational cost, a similar strategy validated in previous work [10] has been applied. The FE Model is B=1 mm thick; the external forces were divided proportional to this thick reduction and plane strain boundary conditions were assumed (as the

specimen is B=12 mm thick, this hypothesis is suitable). The parameter used to control the Fatigue Crack Growth Rate (FCGR) was the Accumulated Plastic Strain (APS=0.8) measured around the crack tip nodes, at the two Gauss points.

3. RESULTS

The strain field results obtained along the crack growing direction ε_{xx} and loading direction ε_{yy} are presented in Fig. 2. Fig. 2 a) and b) represent experimental data from S-XRD; therefore, the FEM data are shown in Fig. 2 c) and d), all for the fatigue step with P = 15.4 kN. The shape obtained from the FEM analysis is like the XRD experimental data, with a relatively identical contour line value of 2000 for the ε_{yy} strain map, indicated in yellow in Fig. 2 b) and d).

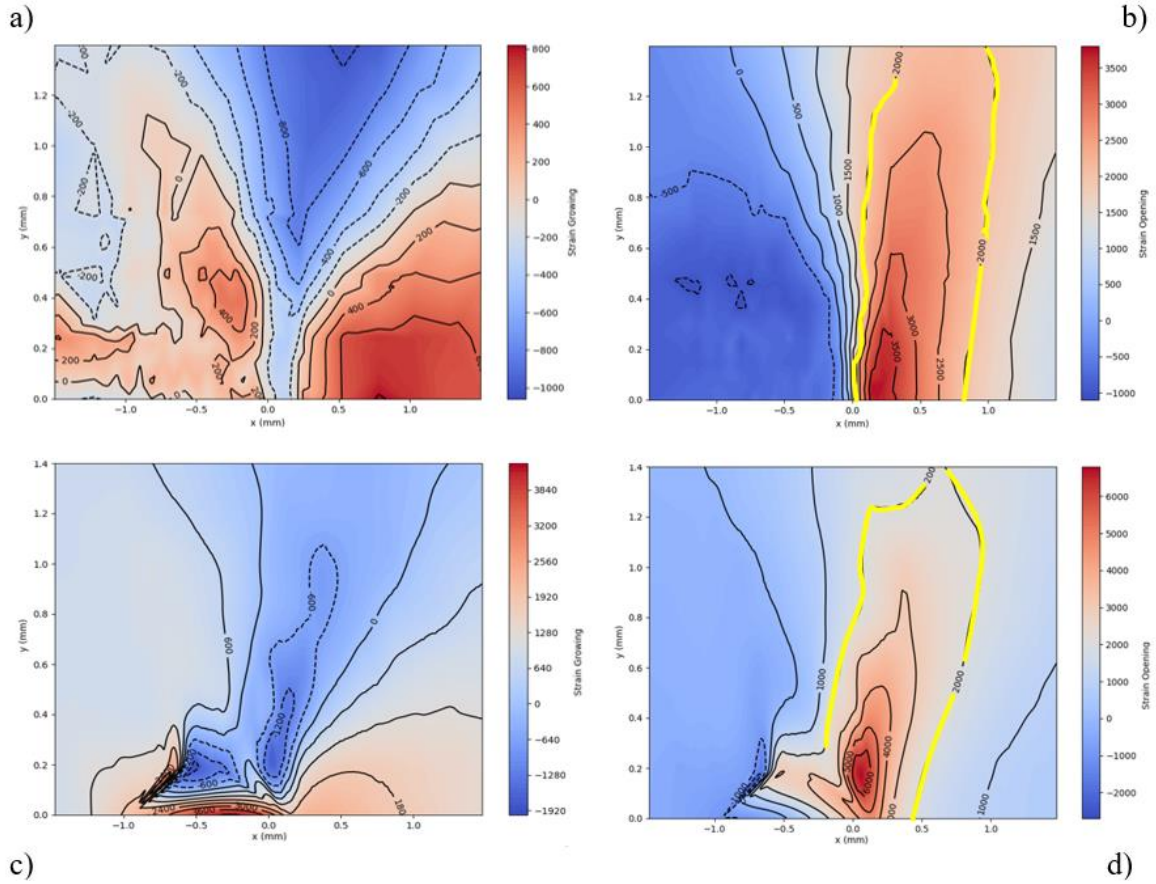

Figure 2: *Strain maps for εxx obtained from a) experimental XRD and b) FEM. Strain maps for εyy from c) experimental XRD and d) FEM. All figures for the fatigue state at P = 15.4kN.*

4. CONCLUSIONS

To describe the strain fields on the surface and bulk of the specimen, a 3D FEM model was developed. A comprehensive examination of the strain fields in ε_{xx} and ε_{yy} has been undertaken, and the findings are highly encouraging. The curves derived from experimental and numerical data closely match shape and value. In regions with higher strain gradients (specifically, the crack-tip zone), coincidences are decreasing. The Map obtained shows a consistent presence of numerical strain fields with historical

strains in the crack growth direction, indicating the Elasto-Plastic numerical analysis in the pre-cracking cycle. To accurately predict crack growth rate, Elasto-Plastic models should be used near the crack tip with strong gradients of stresses and strains. Meshing size near the crack tip is also critical.

ACKNOWLEDGEMENTS

Authors are grateful for the beam time granted by the ESRF (MA1483). Authors would also like to acknowledge the financial support of Programa Operativo FEDER (Junta de Andalucia, Spain) through grant reference UMA18-FEDERJA-250. This work was also supported by the Henry Royce Institute for Advanced Materials, funded through EPSRC grants EP/R00661X/1, EP/S019367/1, EP/P025021/1, and EP/P025498/1 and the European Social Found, through the Youth Employment Initiative, grant reference UMAJI84. The authors are especially thankful to Manuel Carrera for his help in the early stages of this study. We would also acknowledge funding for open access charge: Universidad de Malaga / CBUA.

REFERENCES

[1] Hooper, C. G., Khusnutdinova, K. R., Huntley, J. M., & Ruiz, P. D. (2022). Theoretical estimates of the parameters of longitudinal undular bores in polymethylmethacrylate bars based on their measured initial speeds. Proceedings of the Royal Society A: Mathematical, Physical and Engineering Sciences, 478(2266).

[2] Nowell, D., Paynter, R. J. H., & De Matos, P. F. P. (2010). Optical methods for measurement of fatigue crack closure: moiré interferometry and digital image correlation. Fatigue Fract Eng Mater Struct, 33(12), 778–790.

[3] Dehnavi, M. Y., Khaleghian, S., Emami, A., Tehrani, M., & Soltani, N. (2014). Utilizing digital image correlation to determine stress intensity factors. Polym Test, 37.

[4] Díaz, F. A., Yates, J. R., & Patterson, E. A. (2004). Some improvements in the analysis of fatigue cracks using thermoelasticity. Int J Fatigue, 26(4).

[5] Bellett, D., Taylor, D., Marco, S., Mazzeo, E., Guillois, J., & Pircher, T. (2005). The fatigue behaviour of three-dimensional stress concentrations. Int J Fatigue, 27(3).

[6] Robertson, S. W., Mehta, A., Pelton, A. R., & Ritchie, R. O. (2007). Evolution of crack-tip transformation zones in superelastic Nitinol subjected to in situ fatigue: A fracture mechanics and synchrotron X-ray microdiffraction analysis. Acta Mater, 55(18).

[7] Simpson, C. A., Tonge, S., Connolley, T., Reinhard, C., Marrow, T. J., & Mostafavi, M. (2019). Validating 3D two-parameter fracture mechanics models for structural integrity assessments. Theoretical and Applied Fracture Mechanics, 103, 102281.

[8] Lorenzino, P., & Navarro, A. (2015). Growth of very long ‘“short cracks”’’ initiated at holes. Int J Fatigue, 71, 64–74.

[9] De Pannemaecker, A., Buffiere, J. Y., Fouvry, S., & Graton, O. (2017). In situ fretting fatigue crack propagation analysis using synchrotron X-ray radiography. Int J Fatigue, 97.

[10] Borges, M. F., Neto, D. M., & Antunes, F. V. (2020). Numerical simulation of fatigue crack growth based on accumulated plastic strain. Theoretical and Applied Fracture Mechanics, 108

Finite element model for the proposal of a simplified temperature field in SR-CFST columns subjected to fire.

Medall, David[1]; Ibáñez, Carmen[1]; Albero, Vicente[2]; Lapuebla-Ferri, Andrés[3]; Espinós, Ana[1]; Romero, Manuel L.[1]

ABSTRACT

Former works by the authors highlighted the limitations of concrete-filled steel tubular (CFST) columns when exposed to fire conditions. One solution is to embed an open steel section within the concrete core of the CFST section, generating the so-called steel-reinforced concrete-filled steel tubular (SR-CFST) column. This work describes the development of a finite element model to evaluate the thermal behaviour of SR-CFST stub columns under a fire situation. The numerical model is validated with experimental campaigns and used to carry out a parametric study to examine the influence of several parameters over the thermal response of the columns. Afterwards, a simplified temperature distribution proposal is developed to predict the representative temperatures of each column component under exposure to a standard fire. With this tool, the axial capacity of a SR-CFST stub column at a given fire resistance time can be quickly evaluated.

Keywords: steel-reinforced concrete-filled steel tubular columns, fire resistance, finite element model, thermal analysis, simplified temperature proposal.

1. INTRODUCTION

Previous investigations by the authors showed that concrete-filled steel tubular (CFST) columns fail prematurely under fire exposure, which led to the development of new solutions to improve the fire behaviour of these columns [1]: the so-called Steel-Reinforced CFST (SR-CFST) columns. The experimental investigations regarding this typology of sections exposed to elevated temperatures are scarce [2-3]. Some authors have studied its performance under fire conditions through numerical simulation, validating their models against existing experiments [4]. After conducting a literature review, it becomes clear that no method for analyzing the thermal behaviour of this type of section exists in the international design codes. Therefore, this paper develops a numerical model to conduct extensive parametric studies from which design equations are derived.

2. DEVELOPMENT OF THE FINITE ELEMENT MODEL

A sectional model was developed using the finite element analysis software ABAQUS to characterize the thermal behaviour of SR-CFST columns exposed to fire. A nonlinear heat transfer analysis was

[1]*ICITECH, Universitat Politècnica de València (SPAIN). damemar@doctor.upv.es (Corresponding author), caribus@upv.es, aespinos@mes.upv.es, mromero@mes.upv.es*
[2]*Department of Mechanical Engineering and Construction, Universitat Jaume I (SPAIN). valbero@uji.es*
[3]*Department of Continuum Mechanics and Theory of Structures, Universitat Politècnica de València (SPAIN).*

conducted to obtain the temperature field of the studied sections under exposure to ISO-834 standard fire. The main characteristics of the finite element model are presented in Fig. 1.

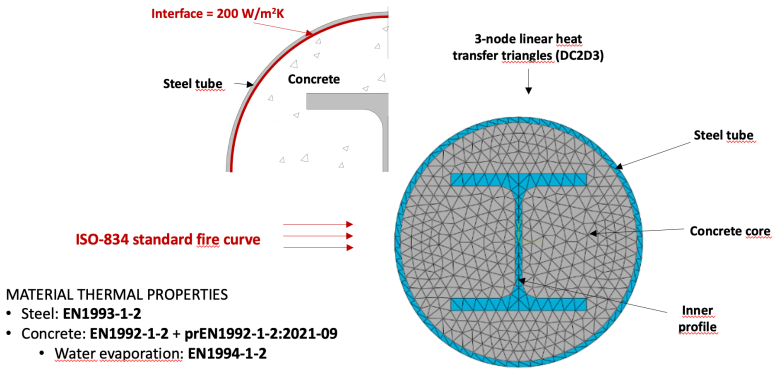

Figure 1. *Schematic view of the main characteristics of the developed FE model.*

3. VALIDATION OF THE THERMAL MODEL

Fig. 2 (a) shows a comparison between the predicted and measured temperatures in an experimental test performed by Chu et al. [5] and Fig. 2 (b) summarizes the predictions of all the cases used for the thermal model validation.

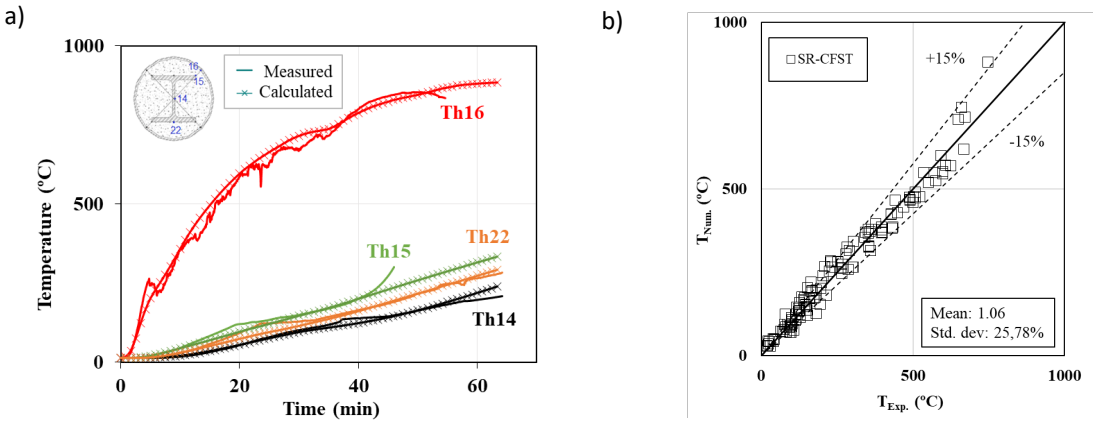

Figure 2. *a) Comparison between measured and computed temperature-time curves for the case specimens tested by Chu et al. [5] b) Numerically predicted temperatures versus experimental temperatures.*

4. PARAMETRIC STUDIES

Once the thermal model was validated, a parametric study was conducted in which several geometric parameters of the SR-CFST section were varied: the cross-section shape (circular or square), the outer steel tube dimensions, the steel tube wall thickness, and the inner steel profile dimensions.

By using the coordinates (z_i, y_i), area (A_i) and temperature (θ_i) of the centroid of each finite element of the mesh and adding all of them by sectional integration, one can obtain the cross-sectional plastic resistance and flexural stiffness of the SR-CFST column at a given standard fire time (see Fig. 4). The

reduction factors corresponding to the temperature of each finite element are obtained according to EN1994-1-2 [6].

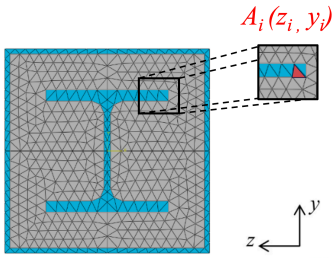

Figure 3. *Sectional integration to compute the mechanical capacity of the SR-CFST column at a specific standard fire time.*

5. SIMPLIFIED TEMPERATURE DISTRIBUTION PROPOSAL FOR SR-CFST SECTIONS

A multivariant nonlinear regression analysis is performed with the temperature database arising from the parametric study. By processing the results, design equations for predicting the equivalent temperature representative of each part of the cross-section are deduced: the outer steel tube ($\theta_{a,eq}$), the concrete infill ($\theta_{c,eq}$) and the web and flanges of the steel profile ($\theta_{w,eq}$ and $\theta_{f,eq}$), see Fig 4.

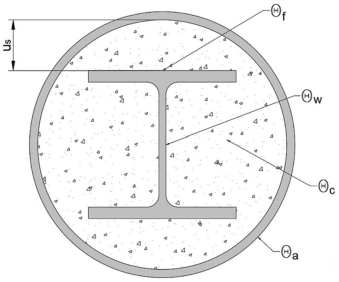

$$\theta_{f,eq} = a_1 + b_1 R + b_2 R^2 + c_1 (A_m/V) + c_2 (A_m/V)^2 + d_1 R (A_m/V) + e_1 R^{f1} (A_m/V)^{f2} + g_1 u_s$$

$$\theta_{w,eq} = a_1 + b_1 R + b_2 R^2 + c_1 (A_m/V) + c_2 (A_m/V)^2 + d_1 R (A_m/V) + e_1 R^{f1} (A_m/V)^{f2} + g_1 (A_{sp}/A_c) + g_2 (A_{sp}/A_c)^2$$

$$\theta_{c,eq} = a_1 + b_1 R + b_2 R^2 + c_1 (A_m/V) + c_2 (A_m/V)^2 + d_1 R (A_m/V) + e_1 R^{f1} (A_m/V)^{f2} + g_1 R (A_p/A_c)$$

$$\theta_{a,eq} = a_1 + b_1 R + b_2 R^2 + c_1 (A_m/V) + e_1 R^{f1} (A_m/V)^{f2}$$

Figure 4. *Equivalent temperatures for the different parts of the SR-CFST section.*

By means of the proposed equations, a value of the equivalent temperatures of the four cross-section parts can be obtained, through which it is possible to easily compute the cross-sectional plastic resistance and flexural stiffness of a SR-CFST column at a specific fire exposure time by direct addition of the reduced mechanical capacity of each of the four parts. Fig. 5 illustrates the application of the method to a SR-CFST specimen, leading to conservative results as compared to the ones obtained by numerical simulation.

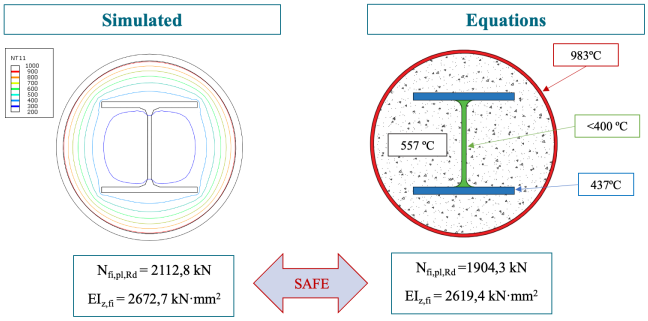

Figure 5. *Comparison of the results obtained by FE analysis with those obtained by applying the equivalent temperature equations to a circular SR-CFST column at a given standard fire exposure time (R60).*

6. CONCLUSIONS

A two-dimensional FE model for the thermal behaviour of SR-CFST columns exposed to fire was developed and tested against the existing experimental campaigns in the literature. A parametric study was performed in which different geometries were subjected to a heat transfer analysis before a numerical integration procedure was applied to obtain the cross-sectional plastic resistance and flexural stiffness at standard fire exposure time. The influence of numerous parameters on the thermal behaviour of SR-CFST columns exposed to fire was studied, such as the section shape (circular or square), the outer steel tube diameter and wall thickness or the dimensions of the inner steel profile.

By means of the parametric studies results, the authors developed a set of equivalent temperature equations that allow practitioners to calculate a simplified temperature field for SR-CFST columns exposed to ISO-834 standard fire. The proposed design method covers a current limitation in EN1994-1-2 [6] for the fire design of this type of composite columns.

ACKNOWLEDGEMENTS

The authors would like to express their sincere gratitude for the help provided through Grant PID2019-105908RB-I00 and for the first author's pre-doctoral contract through Grant PRE2020-093106 funded by MCIN/AEI/ 10.13039/501100011033 and by "ESF Investing in your future".

REFERENCES

[1] Albero V., Espinos A., Romero M.L., Hospitaler A., Bihina G. & Renaud C. (2016). Proposal of a new method in EN1994-1-2 for the fire design of concrete-filled steel tubular columns. *Engineering Structures, 128, 237–255.*

[2] Tan Q-H., Gardner L., Han L-H. & Song T-Y. (2019). Fire performance of steel reinforced concrete-filled stainless steel tubular (CFSST) columns with square cross-sections. *Thin-Walled Structures, 143, 106197.*

[3] Espinos A., Romero M.L. & Lam D. (2016). Fire performance of innovative steel-concrete composite columns using high strength steels. *Thin-Walled Structures, 106, 113–128.*

[4] Mao W-J., Wang W-D. & Xian W. (2020). Numerical analysis on fire performance of steel-reinforced concrete-filled steel tubular columns with square cross-section. *Structures, 28, 1–16.*

[5] Chu T.B., Gernay T., Dotreppe J.C. & Franssen J.M. (2016). Steel hollow columns with an internal profile filled with self-compacting concrete under fire conditions. *Proceedings of the Romanian Academy, 17(2), 152-159.*

[6] EN 1994-1-2 (2005). Eurocode 4: Design of composite steel and concrete structures. Part 1.2: General rules - Structural fire design.

Forensic analysis taken after the collapse of a raised steel wine tank

Salvador Ivorra[1], Benjamín Torres[1], Luis Estevan[1], José Manuel Piqueras[2]

ABSTRACT

This paper describes an analysis of the collapse of a 106 m^3 steel raised wine tank that suddenly collapsed at 03:45 am, fortunately without serious injuries but causing considerable material damage to the company´s facilities. The collapse generated the progressive failure of the other steel tanks attached to the one that originally failed. After several field visits to assess the collapse "in situ", a diagnosis was made about the causes of the accident. The collapse mechanism of the system was found to be due to cyclic horizontal loads and the results allowed us to conclude that this type of structure is highly vulnerable to horizontal loads.

Keywords: Collapse; steel structure; structural robustness; cyclic loading; forensic engineering

1. INTRODUCTION.

Raised liquid storage tanks have been the subject of a large number of publications over the last decades. This singular type of structure consists of a steel tank supported on steel or concrete columns and used to store liquids. Their main characteristic pathologies range from small cracks to the complete collapse of the supporting elements [1]. In most cases, the tanks have been designed by outdated standards and thus hazards like seismically-induced fires and seismically-induced tsunamis were completely ignored [2-4]. These types of structures are generally correctly dimensioned for gravity loads, but have a very low capacity to activate ALPs, and frequently become seriously damaged or, in most cases, suffer complete collapse when horizontal loads act on them.

The aim of this work is to analyse the sudden collapse of a wine storage tank. The accident took place at 3:45 a.m. on October 4th, 2020, and luckily caused no injuries, although the material damage was considerable and the repairs were assessed at several thousand euros. An initial total collapse in one tank led to the progressive failure of many of the neighbouring tanks. To identify the causes of the initial collapse, a forensic engineering study was carried.

2. DESCRIPTION OF THE RAISED STEEL WINE TANK.

The structure under study consisted of a raised stainless-steel tank used to ferment the must. The tank geometry is given in Fig. 1.a. The columns were joined to the tank by a continuously welded steel plate and were connected to each other at a height of 1400 mm from the floor by horizontal steel ties. Since wine fermentation is an aerobic process, the must has to be provided with oxygen to avoid its turning into vinegar. This was done by an automatic process of pumping air under pressure into the base of the tank to form bubbles that rise to the top to carry out the recovery cycle (Fig. 1.b). The air is injected

[1] *Department of Civil Engineering, University of Alicante, P.O. Box 99, 03080 Alicante (Spain). sivorra@ua.es (corresponding author). benjamin.torres@ua.es. luis.estevan@ua.es*
[2] *Piqueras Ingenieros SL, Britania Street, 03540 Alicante (Spain). administracion@piquerasingenieros.es.*

under 9 bar pressure into the tank in a continuous automatic process (for no more than 10 seconds) for as long as it takes for the correct fermentation.

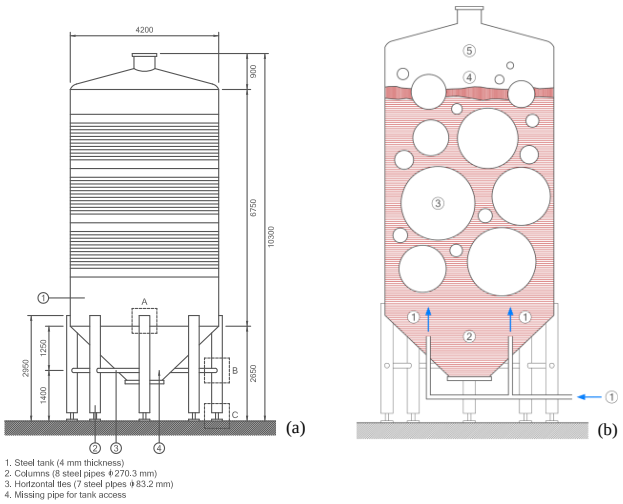

Figure 1. *(a)- General geometry of the raised tank. (b)- Scheme of pressurized air injection.*

3. DESCRIPTION OF THE FAILURE.

On October 4th, 2020, at 3:45 a.m. one of the tanks full to 85% of its capacity collapsed and started a series of collapses of other nearby tanks. A total of 18 units were seriously damaged, either because they collapsed completely or because they suffered significant deformations caused by the impacts of neighbors (Fig. 2.a). Fig. 2.b shows the buckled upper section of the tank where it was joined to the columns and Fig. 2.c shows the broked welding lines on the plates that joined the columns to the tank.

(a) (b) (c)

Figure 2. *Damage caused by tank collapse: (a)-general view. (b)- Buckled upper column section. (c)- Broken welding on the column-tank joint*

4. EXPERIMENTAL TESTS.

Five test sets (geometry identification, tensile tests, penetrant liquids, scanning electron micro-scope and hardness test) were conducted to evaluate the mechanical and chemical properties of the material extracted from parts of the tanks not affected by the accident. The results obtained from the experimental tests did not show any signs that the cause of the collapse could be attributed either to the poor mechanical properties of the steel used in the structures or to deficient welds.

5. NONLINEAR STATIC PUSHOVER ANALYSIS.

The numerical study was carried out on SAP2000 software [5]. For material properties, a conventional steel was used with a Young´s modulus of 210000 MPa, a Poisson´s ratio of 0.3 and a mass density of 7.8 ·10-9 N/mm3. The yield stress obtained in the experimental tests was used in each element. Each of the frame elements is assigned a possibility of developing plastic hinges at their ends. Default hinge properties are provided based on FEMA 365 [6]. Fig. 3 shows the evolution of the formation of plastic hinges in columns and ties. The results are given in the form of a graphic scale of colours that refers hinge formation to the performance levels laid down in [6, 7]. The successive formation of hinges involves activating mechanisms for the collapse of the structure.

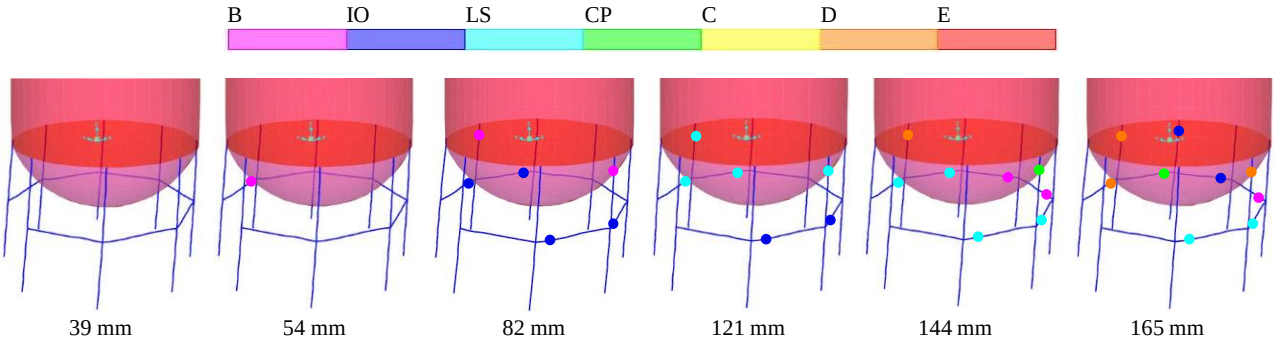

Figure 3. *Evolution of hinge formation in columns and ties (pushover analysis).*

At a displacement of 121 mm, the hinges in ties and heads of columns involves loss of strength and stiffness in the system against lateral loads. In adition, Fig. 4 shows the first vibration modes associated with each of the frequencies obtained. After reviewing the images from the security camera, it was clearly seen that the tank collapsed due to a combination of the first two modal shapes (Fig. 4).

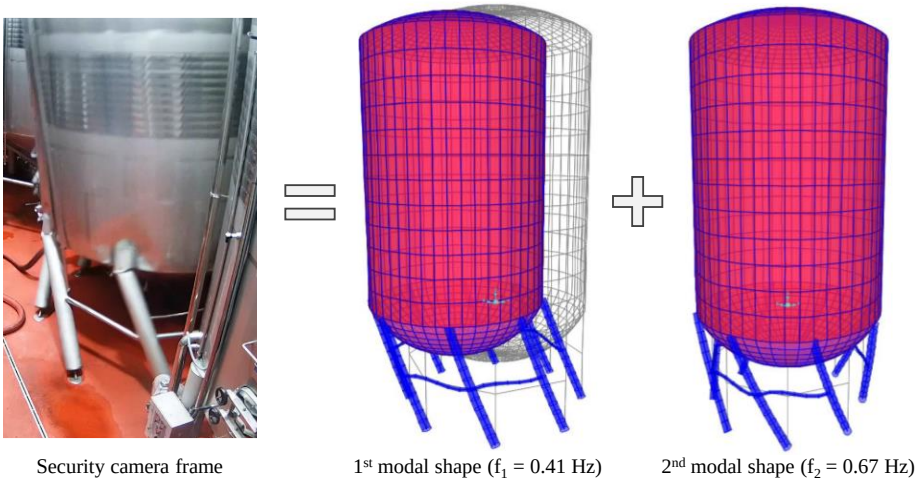

Figure 4. *Instant of collapse obtained from security camera, as a combination of the first two modal shapes.*

6. CONCLUSIONS.

This paper describes and analyses the sudden collapse of a 106 m3 capacity raised wine storage tank in the early morning of October 4th, 2020. Everything indicated that the collapse occurred due to horizontal loads caused by an air injection system installed in the tanks to improve the wine fermentation. A nonlinear static pushover test was also carried out to study the structural behavior up to the point of collapse after various elements had reached their yield stress. The results showed that the formation of plastic hinges implies the generation of collapse mechanisms, so that at a certain level of horizontal displacement the structure is unable to bear higher loads. In view of the results obtained, the air injection system involves a serious risk to the stability of the tanks.

REFERENCES

[1] H. Sezen, A.S. Whittaker, Seismic performance of industrial facilities affected by the 1999 Turkey earthquake, J. Perform. Constr. Facil. 20 (1) (2006) 28-36. https://doi.org/10.1061/(ASCE)0887-3828(2006)20:1(28)

[2] H.N. Phan, F. Paolacci, O.S. Bursi, N. Tondini, Seismic fragility analysis of elevated steel storage tanks supported by reinforced concrete columns, J. Loss Prev. Process Ind. 47 (2017) 57-65. https://doi.org/10.1016/j.jlp.2017.02.017

[3] K. Hatayama, Tsunami damage to oil storage tanks in the MW90 2011 Tohoku Japan earthquake, In: Proc. Of ASME 2015 Pressure Vessels and Piping Conference (Boston, Massachusetts, USA) (2015).

[4] Y. Itoh, Y. Waki, K. Kasuya, Material tests and analysis for pressure vessels rupture study under fire in plant, In: Proc. Of ASME 2015 Pressure Vessels and Piping Conference (Boston, Massachusetts, USA) (2015).

[5] SAP2000. Integrated Solution for Structural Analysis & Design Version 17. CSI Analysis Reference Manual, Computers & Structures, INC.

[6] Prestandard and commentary for the seismic rehabilitation of buildings. Federal Emergency Management Agency FEMA 365. American Society of Civil Engineers (2000).

[7] Seismic evaluation and retrofit of existing buildings. American Society of Civil Engineers. Structural Engineering Institute. ASCE STANDARD 41-13 (2014).

GreenDAC: An educational software on Design for Deconstruction

Reinosa, J.M.[1]; Loureiro, A.[1]; Gutiérrez, R.[1]; López, M.[1]

ABSTRACT

GreenDAC® is an educational software developed at the Structural Analysis Lab from the University of A Coruña (Spain). The program was conceived to explore the benefits of Design for Deconstruction (DfD) in steel structures assembled with semi-rigid connections. This program allows the students to examine how DfD affects embodied carbon of different structural bay types through a quantification of embodied carbon savings. The life span of the building is considered so the elements suitable for reuse may have more than one life cycle, and the structure's environmental impact is reduced. The Inventory of Carbon and Energy (ICE) was used as the main data set for the embodied carbon calculations. The objective of this paper is to show the possibilities of the software in education and to describe the use of the different options by means of a representative case.

Keywords: design for deconstruction; semi-rigid connections; educational software

1. INTRODUCTION

New construction, maintenance and renovation of buildings account for 40% of the world's material flows [1] and for more than one third of total energy use. In particular, the structure may represents 24 % of the total initial embodied energy of buildings [2]. When buildings reach the end of their useful life, they are typically demolished and hauled to landfills. Nevertheless, the stream of materials generated when a building is dismantled could be reused for a new construction. In fact, reuse is definitely better than recycling, since no reprocessing energy is required and the component is simply moved from one location to another. Deconstruction is usually described as a process that systematically takes apart structural and non-structural components trying not to damage them, with the particular intention of reusing the components after recovery [3]. The best strategy in design for deconstruction (DfD) is to include deconstruction in the design of the building [4] and, therefore, the connection technology between elements becomes important. Bolted connections in steel frameworks have substantial economical and practical advantages [5-9]. One of the most popular semi-rigid bolted typologies in the North American market is the top and seat angle connection with double web angle (TSDW). The knowledge of the actual connection behaviour allows us to obtain a least-weight design of semi-rigid beams by means of the application of theorems for an optimal design [10]. This beam weight optimisation, combined with an application to easy measure the CO2 savings, will permit to reduce emissions and quantify this reduction, providing another interesting tool to improve the DfD. In this sense, *GreenDAC* program implements the PAS2050 [11] philosophy of action, relying on the ICE database [12] with a specific focus on the building sector. *GreenDAC* is a tool conceived to quantify the CO2e reduction with the premise of using semi-rigid angle connections and common standard shapes, minimizing the number of different member sizes. The program mainly consists of two charts: the Data chart and the Results chart. The Data chart contains many predefined configurations related to some different possible module combinations. Hot rolled steel profiles can be selected from the respective

[1]*Departamento de Ingeniería Naval e Industrial. Universidade da Coruña (SPAIN). j.reinosa@udc.es (Corresponding author). a.loureiro@udc.es. rutgut@udc.es. manuel.lopez.lopez@udc.es.*

menus for each structural element. Additionally, it is possible to choose the bolt class, bracing and a flooring made up of precast hollow-core planks. The number of life cycles must be included.

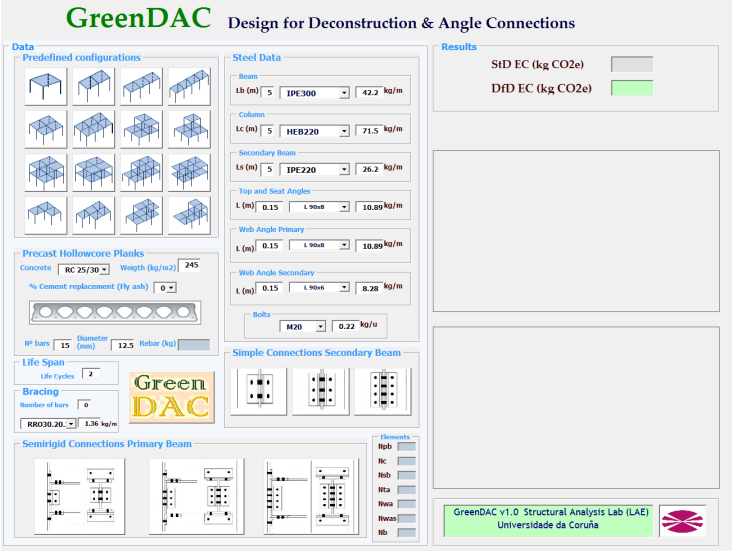

Figure 1. *Predefined configurations and typical set of steel data.*

In the Results chart, the embodied carbon can be checked related both to DfD and for an approximate Standard Design with simple connections. Besides, the embodied carbon per square meter is represented as well as the percentages of contribution from the different elements.

2. BENCHMARK

A steel-framed structural bay analyzed by Densley [4] to examine how DfD affects embodied carbon of different structural bay types will be used to check *GreenDAC*. The life span was assumed fifty years in a one hundred year period. The ICE was used as the data set for the embodied carbon calculations. The bay size is 6x6 metres, constructed from two primary beams, two perimeter beams and four columns. Flooring is made up of reusable precast hollow-core planks. A variable office loading of 2.5 kN/m2 plus 1 kN/m2 for partitions was assumed. Wind loading was not considered and substructure and roof structure were not included. Densley compared three different typologies of structural bays. The third bay, whose elements are independent, will serve to display *GreenDAC*® performance.

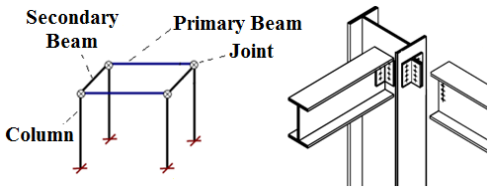

Figure 2. *Densley's benchmark structural bay and connection detail*

Once the connection characteristics and steel sections were defined regarding an optimal semi-rigid design, the structure was calculated by means *RSTAB*® package [13], introducing the rotational stiffness and considering a maximum vertical displacement *Uz* = L / 300 = 20 mm. The connection was configured using L150.75.12 for top and seat angles and L100.12 for the web angles, with two bolt rows in the web

angle. In this case, a valid solution that meets both ELS and ULS requirements was found with European profiles IPE220, IPE200 and HEA180 for primary beams, secondary beams and columns respectively. Once an optimal design has been obtained, the data was introduced in *GreenDAC®*.

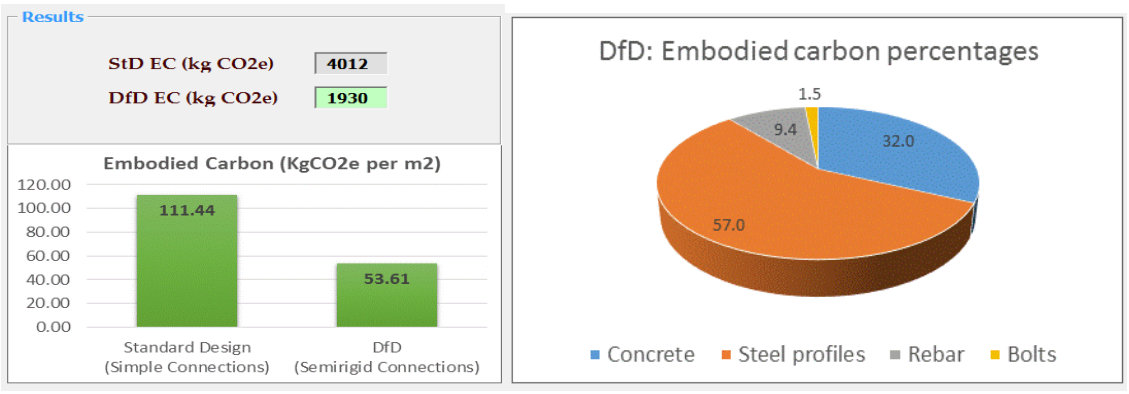

Figure 3. *GreenDAC results for the semi-rigid frame.*

3. CONCLUSIONS

Table 1 includes the semi-rigid model described in this paper and the calculation of Densley's simple frame for non-composite bay, both of them computed with *GreenDAC®*. The first bay has a composite floor that acts in unison with all the beams. In the second, only the secondary beams act compositely. Finally, the third bay has a steel frame with precast planks, which act non-compositely. When DfD is considered in combination with optimized semi-rigid connections, the non-composite bay embodies the least carbon. The decrease in the embodied carbon if DfD is about 22 % when semi-rigid connections are used, in comparison with the simple connection design of Densley's benchmark. However, this percentage is larger if the comparison is established between a composite bay Standard Design and DfD with semi-rigid connections, reaching a decrease in the embodied carbon of about 60%. The results from this benchmark show the significant benefit derived from the use of DfD when it is combined with semi-rigid structural design, due to the maximum amount of optimized steel sections, which were designed for reuse. This comparison suggest that, if the bays are designed for deconstruction and these design benefits are accounted for, then the non-composite semi-rigid bay is the most sustainable choice in terms of embodied carbon and future reuse.

Table 1. Summary table showing the embodied carbon of each bay type, Kg $CO2e/m^2$

Bay Type	*Composite*	*Partially Composite*	*Non-Composite*	
Connection type	*Simple*	*Simple*	*Simple*	*Semi-rigid*
Standard Design	134	164	**136**	**112**
DfD Design	103	102	**69**	**54**

4. ACKNOWLEDGEMENTS

The financial support provided through grant PID2020-113895GB-C31 funded by MCIN/AEI/10.13039/501100011033 is gratefully acknowledged.

REFERENCES

[1] Roodman D.M., Lenssen N. (1995) A Building Revolution: How Ecology and Health Concerns are Transforming Construction*, Paper 124*, Worldwatch Institute, Washington, D.C., p. 5.

[2] *Cole*, R.J. and P.C. Kernan. (1996) Life-Cycle Energy Use in Office. Buildings. *Building and Environmen*t *31: (4)*

[3] Hobbs, G. and J. Hurley (2001) Deconstruction and the Reuse of Construction Materials, CIB World Building Congress-Deconstruction Meeting-, Wellington, New Zealand, p.98-124

[4] Densley Tingley, D. (2012) Design for Deconstruction: An Appraisal. PhD Thesis. The University of Sheffield.

[5] Loureiro,A., Gutiérrez, R., Reinosa, J.M., Moreno, A. (2010) Axial stiffness prediction of non-preloaded T-stubs: An analytical frame approach. *Journal of Constructional Steel Research*, *Volume 66, Issue 12, Pages 1516-1522*

[6] Loureiro,A., Reinosa, J.M., Gutiérrez, R., Moreno, A. (2011) New proposals on the calculation of the flexural resistance in angle connections. *Journal of Constructional Steel Research*, *Volume 67, Issue 4, Pages 613-622*

[7] Reinosa, J.M., Loureiro,A., Gutiérrez, R., López, M. (2013) Analytical frame approach for the axial stiffness prediction of preloaded T-stubs. *Journal of Constructional Steel Research*, *Volume 90, Pages 156-163*

[8] Reinosa, J.M., Loureiro,A., Gutiérrez, R., López, M. (2015) Analytical frame approach for the rotational stiffness prediction of beam-to-column angle connections. *Journal of Constructional Steel Research*, *Volume 106, , Pages 67-76*

[9] Reinosa, J.M., Loureiro,A., Gutiérrez, R., López, M. (2015) Analytical plate approach for the axial stiffness prediction of stiffened angle cleats. *Journal of Constructional Steel Research*, *Volume 106, Pages 77-88*

[10] Xu, L. (2001) On the minimum–maximum bending moment and the least-weight design of semi-rigid beams. *Journal of the International Society for Structural and Multidisciplinary Optimization*, *21, pp. 316–321*

[11] PAS 2050. Guide to PAS 2050 (2008), How to assess the carbon footprint of goods and services. British Standards Institution.

[12] Hammond, G., Jones, C. (2011) Inventory of Carbon & Energy (ICE) version 2.0

[13] RSTAB8 Program Description (2013). Ing.-Software Dlubal.

Implementation of the BIM Methodology for the diagnosis and pathology activities of construction in CEMOSA

Troyano Moreno, Miguel[1]; Jiménez Redondo, Noemi[2]; García Villena, Francisco Antonio[2]; Hernández Villalobos, Eusebio[3]; Sevilla Hurtado, Lorenzo[1]

ABSTRACT

The BIM methodology has been established as the most efficient way to design, build and operate a certain asset in the AEC-FM industry (Architecture, Engineering, Construction, and Facility Management). However, there are still activities within this industry where their implementation is not sufficiently mature, as occurs in diagnosis and pathology studies, due to the lack of a standard to store damage information and the lack of computer applications to properly generate the corresponding information models. This communication describes the developments carried out by the company CEMOSA to address these activities through the BIM methodology, focusing on the description of the processes, data models and the functionality of the applications that allow collect information and generate information models.

Keywords: Inspection, Damage, Building Information Modeling (BIM), Damage Information Modeling (DIM), Industry Foundation Classes (IFC).

1. INTRODUCCIÓN

BIM (Building Information Modeling) se ha establecido como la metodología más eficiente para abordar los procesos de diseño, construcción y mantenimiento de construcciones [1]. Se basa en la obtención e intercambio de modelos digitales que contienen la información relativa a la construcción que se está diseñando (Projetc BIM), construyendo (As-Built BIM) o manteniendo (As-Is BIM), compuestos, a su vez, de otros modelos que contienen la información agrupada por disciplinas o dominios (arquitectura, estructura, instalaciones, etc.).

Durante la fase de mantenimiento, una actividad importante son los estudios de diagnosis y patología de la construcción, donde se realizan inspecciones para la detección de daños que puedan comprometer las condiciones de seguridad, durabilidad y funcionalidad de la construcción. Para integrar en estos estudios la metodología BIM y, con ello, aprovechar los beneficios que con ella se obtienen, es necesario poder integrar la información de los daños en el modelo BIM mediante un modelo BIM de daños o DIM (Damage Information Model). Se están desarrollando tecnologías que permiten detectar y representar los daños en modelos BIM [2,3], pero no están suficientemente maduras para su uso cotidiano en la realización de inspecciones, como las inspecciones principales de puentes de ferrocarril [4] y obras de paso [5], ni abarcan todos los tipos de daños que se pueden presentar.

[1] *Dep. Ingeniería Civil de Materiales y Fabricación. Universidad de Málaga (ESPAÑA). mtroyano@uma.es (Corresponding author). lsevilla@uma.es*
[2] *Dep. Investigación e Innovación. CEMOSA (ESPAÑA). noemi.jimenez@cemosa.es. fantonio.garcia@cemosa.es*
[3] *Dep. Desarrollo. CEMOSA (ESPAÑA). eusebio.hernandez@cemosa.es*

En esta ponencia se describe la metodología implementada en CEMOSA para obtener los modelos DIM y poder utilizar la metodología BIM en las actividades de diagnosis y patología de la construcción.

2. DIAGRAMA DE PROCESOS

El diagrama de procesos es el que se muestra en la Fig. 1, describiéndose en los siguientes apartados los aspectos más relevantes.

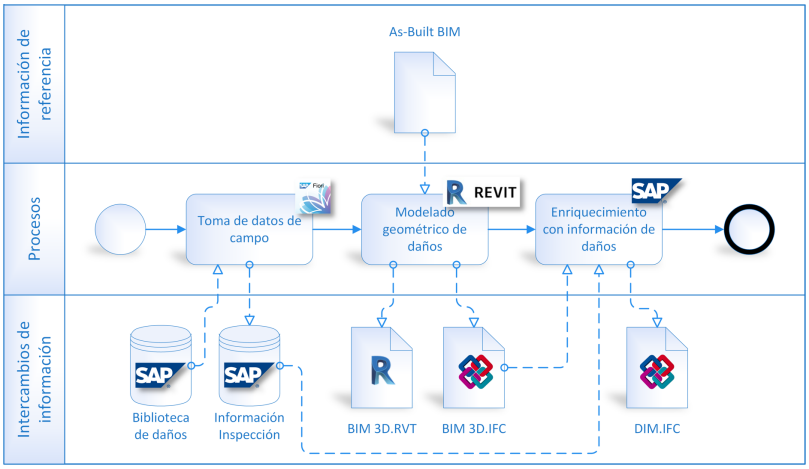

Figura 1. *Diagrama de Procesos*

2.1. Biblioteca de daños

Se ha implementado, sobre el ERP SAP® de CEMOSA, una biblioteca de daños basada en las guías de ADIF, del Ministerio de Fomento y de la Fundación MUSSAT [4-6], así como en la experiencia acumulada en el departamento de diagnosis y patología de CEMOSA. De forma esquemática, la estructura de esta biblioteca se muestra en la Fig. 2a). En ella se clasifican los distintos tipos de elementos constructivos (1) y los tipos de daños (2), se definen los criterios de valoración (3) y sus posibles intensidades (4), se asignan los tipos de daños que se pueden presentar en cada tipo de elemento constructivo (5) y, para estos, se establecen sus criterios de valoración (6). Por último, para cada tipo de elemento, tipo de daño, criterio de valoración e intensidad se define el correspondiente índice de gravedad (7).

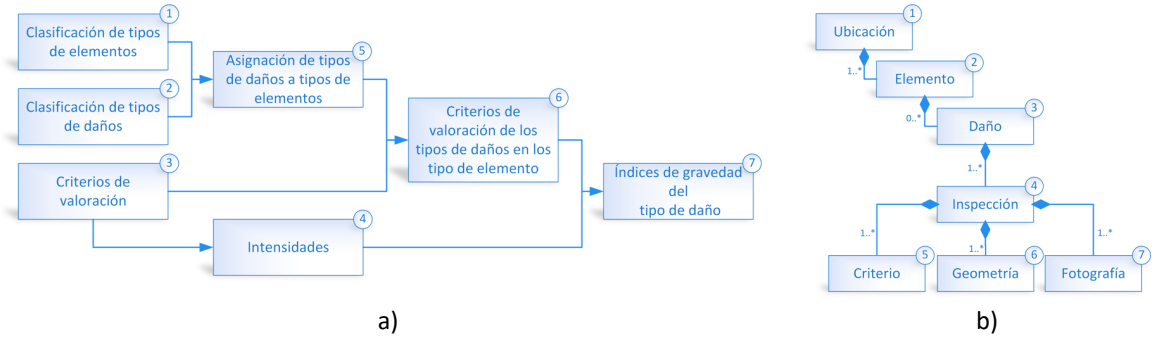

Figura 2. *Esquema a) de la estructura de la biblioteca de daños y b) de clases del modelo de datos de daños*

2.2. Toma de datos de campo

Para la toma de datos de campo se ha desarrollado, sobre el ERP SAP® de CEMOSA, una aplicación móvil, denominada *Visitas*, utilizando como *front-end* SAP Fiori®. Esta aplicación permite registrar, entre

otra información, la relativa a la visita de inspección y a los daños detectados en el activo durante las inspecciones, según la biblioteca de daños descrita anteriormente. En la Fig. 2b) se representa el esquema de clases del modelo de datos de daños. Este modelo permite descomponer una construcción en distintas ubicaciones (1) a inspeccionar, que se componen de distintos elementos constructivos (2). Cada elemento constructivo puede contener varios daños (3) y cada daño puede contener la información de sucesivas inspecciones (4). Finalmente, la información del daño en cada inspección se compone de distintos criterios de valoración (5), distintos objetos geométricos (6) que representan los daños en el momento de la inspección y las correspondientes fotografías (7). Al asignar el técnico inspector la intensidad del daño para cada criterio de valoración según la biblioteca de daños, se determina automáticamente el índice de gravedad del daño.

2.3. Modelado geométrico de daños

Una vez realizada la inspección, utilizando la aplicación Autodesk Revit®, se genera el modelado geométrico de los daños para obtener un modelo BIM geométrico de daños que contiene únicamente la geometría de éstos (además de la información asociada a dicha geometría). Esos daños se representan sobre el modelo BIM del activo (As-built BIM), que se vincula al modelo BIM de daños. A efectos de esta ponencia, el modelo BIM del activo se considera un dato de partida.

Se han creado distintas familias de daños en Revit para poder representar sus tipologías en la biblioteca de daños. Para los que admiten una representación lineal (por ejemplo *fisuras*) o superficial (por ejemplo *oxidación superficial / deterioro de la protección*), estas familias permiten visualizar las formas de dichos daños; para los desplazamientos (por ejemplo *desplazamientos excesivos / desplomes*) o giros (por ejemplo *movimiento / giro del encofrado*) estas familias permiten visualizar la magnitud del daño; mientras que para el resto daños (por ejemplo *pérdida de tornillos / roblones*) las familias visualizan un tótem que indica su posición.

El resultado de este proceso es el modelo geométrico de daños en formato nativo de Revit (BIM 3D.rvt), que permite actualizar estos daños con los resultados obtenidos en futuras inspecciones, y en formato estándar Ifc (BIM 3D.ifc), que, tras un proceso de enriquecimiento con la información de los daños contenida en SAP, tal como se describe en el punto siguiente, dará lugar al definitivo modelo BIM de daños (DIM.ifc) para el instante en el que se realizó la inspección.

2.4. Enriquecimiento información de daños

Se ha desarrollado una aplicación sobre el ERP SAP® de CEMOSA que permite enriquecer automáticamente el modelo BIM geométrico de daños (BIM 3D.ifc), generado en el proceso anterior, con toda la información de los daños almacenada en el ERP SAP®, y que obtiene finalmente el modelo BIM de daños de la construcción (DIM.IFC), para un instante determinado de su vida útil (cuando se realizó su inspección). Este modelo incluye la geometría actual de los daños, junto con la evolución histórica de la información de los daños.

En la Fig. 3 se muestra el modelo DIM de un puente ferroviario, en el que se aprecia la geometría de los daños y, para uno de los daños (fisuras en la pila del puente), su información asociada.

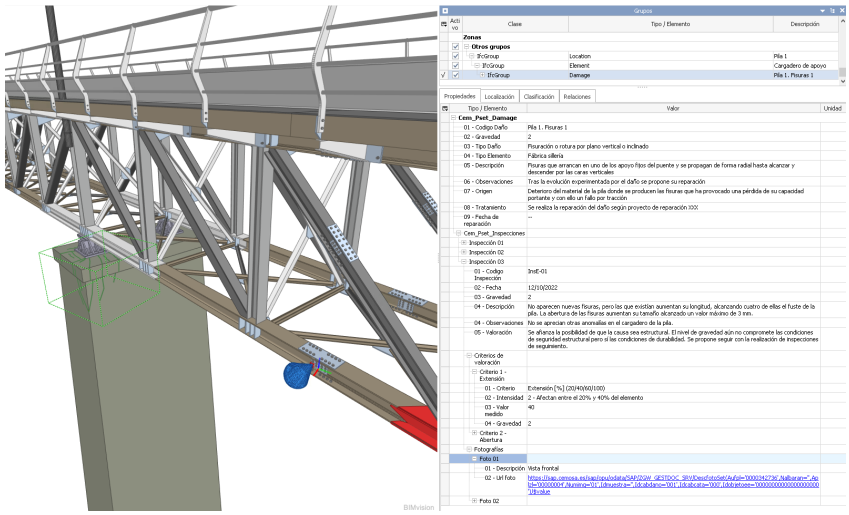

Figura 3. *Modelo DIM: geometría daños lineales (fisuras), superficiales (oxidación) y tótem (pérdida de tornillos)*

3. CONCLUSIONES

Se han desarrollado los procesos, modelos de datos y herramientas informáticas necesarias para implantar la metodología BIM en las actividades de diagnosis y patología de la construcción. El resultado final es la generación automática del modelo DIM que contiene toda la información de los daños existentes en la construcción y, como beneficio adicional, la determinación automática de los índices de gravedad de los daños detectados en las inspecciones a partir de la biblioteca de daños. Además, estos desarrollos han servido de partida para proyectos ya iniciados por CEMOSA, cuyos objetivos son obtener gemelos digitales de cara a la gestión y mantenimiento de infraestructuras.

AGRADECIMIENTOS

Este trabajo se ha realizado dentro del proyecto RESILTRACK (IDI-20171007), financiado por el programa CIEN-CDTI, y del proyecto DREAM (ITC-20181133) cofinanciado con fondos FEDER a través del Programa FEDER INTERCONECTA del CDTI, Ministerio de Ciencia e Innovación de España. Los autores expresan su agradecimiento a la Universidad de Málaga-Campus de Excelencia Internacional Andalucía Tech, por el soporte prestado en el desarrollo de este trabajo.

REFERENCIAS

[1] R. Sacks, et al., (2018). BIM Handbook: A Guide to Building Information Modeling for Owners, Designers, Engineers, Contractors, and Facility Managers, 3rd Edition. Wiley, Hoboken, NJ, USA.

[2] M. Artus, M.S.H. Alabassy, C. Koch, (2022). A BIM Based Framework for Damage Segmentation, Modeling, and Visualization Using IFC. Applied Sciences, 12, 2772

[3] R. Sacks, et al., (2018). SeeBridge as next generation bridge inspection: Overview, Information Delivery Manual and Model View Definition. Automation in Construction. 90 134–145.

[4] ADIF. (2023). NAP 2-4-1.0 Inspección principal de puentes de ferrocarril, 2a Ed.

[5] Ministerio de Fomento. (2012) Guía para la realización de inspecciones principales de obras de paso en la Red de Carreteras del Estado.

[6] Fundación MUSSAT. (2009) Análisis estadístico nacional sobre patologías en la edificación (III).

Influence of Parameter Estimation on the Fragility Curves of the Monastery of San Jerónimo (Granada)

Hernández-Montes,Enrique[1]; Gil-Martín, Luisa María[1]

ABSTRACT

The parameter estimation approach has an influence on the obtained fragility function. To demonstrate this, fragility functions for a cultural heritage construction in Granada were calculated using two statistical inferences. The fragility curves are based on nonlinear dynamic analyses of both the original and degraded geometries using finite element (FE) models. Macro-modelling was used in the FE models, which were subjected to ground motions specific to the city of Granada selected using the Probabilistic Seismic Hazard Analysis (PSHA) methodology.

Keywords: fragility curve; FE modelling; log-normal distribution

1. ASSESSING OF THE STRUCTURAL VULNERABILITY. HAZARD ANALYSIS, DISAGGREGATION AND RECORD SELECTION.

Fragility curves are effective tools for assessing structural vulnerability. These curves describe the conditional probability of reaching or exceeding a certain damage state caused by seismic event of a given severity, corresponding to a certain ground motion intensity measure (IM). In this study, seismic ground motions of different intensities or IM levels which were considered, specifically 10 average pseudo-acceleration levels ranging from 0.026 g to 0.587 g. The accelerograms were obtained through a Probabilistic seismic hazard analysis (PSHA) for the site of Granada. All sources within 200 km from the sites were considered, with V_{s30}=400 m/s. For each IM level, several pairs (N-S, E-W) of records were selected based on the geometric mean of the two horizontal components using the correlation model of Baker and Jayaram [1]. The scaling factor was limited to 6.0 to get the best match.

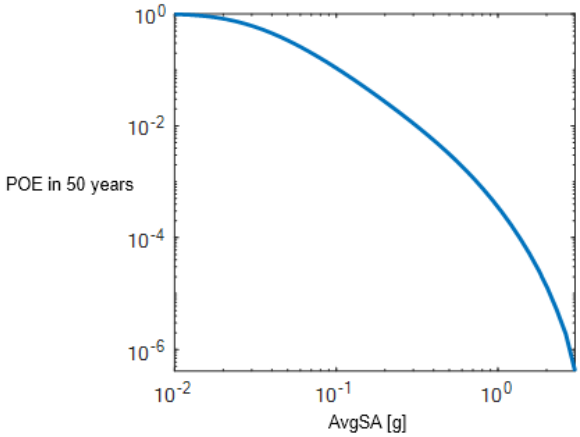

Figure 1. *Hazard curves at Granada site in terms of AvgSA.*

[1] *Structural Mechanics Department. University of Granada (SPAIN). emontes@ugr.es, mlgil@ugr.es (Corresponding author).*

The records were selected from the NGA-West database [2]. The hazard analysis was performed for AvgSA (defined as the geometric mean of spectral accelerations) within the period range of [0.2, 2.0] s, with an increment of 0.1s. The resulting hazard curve is depicted in Figure 1. For more detailed information refer to [3].

2. PROBABILISTIC DISTRIBUTION OF STATISTICAL DATA USED IN DEVELOPING FRAGILITY CURVES

Uncertainties in the seismic analysis of structures make statistical and probabilistical approaches the most reasonable methods for obtaining Fragility Functions (FF). A fragility function, typically modeled as a lognormal cumulative distribution function, allows determine the probability that the damage state of a structure (DS) reaches or exceeds a given reference damage state (d_{ref}), conditioned on the value of an certain value of intensity measure (IM), that in this case is adopted equal to AvgSA. In statistic terms, fragility functions (FC) are expressed as:

$$FC = P\left[DS \geq d_{ref} \middle| IM = AvgSA_i \right] \quad (1)$$

The value of d_{ref} depends on the considered damage mechanisms, which in the study case refers to the compressive strength of the stone. In this fragility analysis, the commonly used IM-based approach is considered and so, the probability of exceeding the limit response is determined for various earthquake intensity levels, resulting in a statistical population. The Fragility Curves (FC) of the San Jerónimo Monastery (in Granada) are obtained by performing non-linear FE analysis of both degraded and non-degraded structures when subjected to seismic ground motions of different intensities, Figure 1. The mechanical characterization of the material was made by laboratory tests [4,5] while the degradation patterns of the façades was measured using 3D photogrammetry [6,7]. The FE model was restrained at ground level and, after being subjected to the action of their own weight, accelerations in two perpendicular directions induced by the accelerograms selected ad-hoc for Granada were applied to the nodes at the ground level. Sets of hazards consistent accelerograms, in N-S and W-E directions, denoted as a(t), were used to assess the structural response at different seismic intensity level. To obtain the FC, the compressive strength corresponding to the 95th percentile (data from experimental test [5]) was adopted as the reference value (6.8 MPa) corresponding to failure or damage state of interest. The FCs were obtained for both the non-deteriorated monastery and with a degradation level corresponding to 500 years (assuming a uniform degradation velocity) [6].

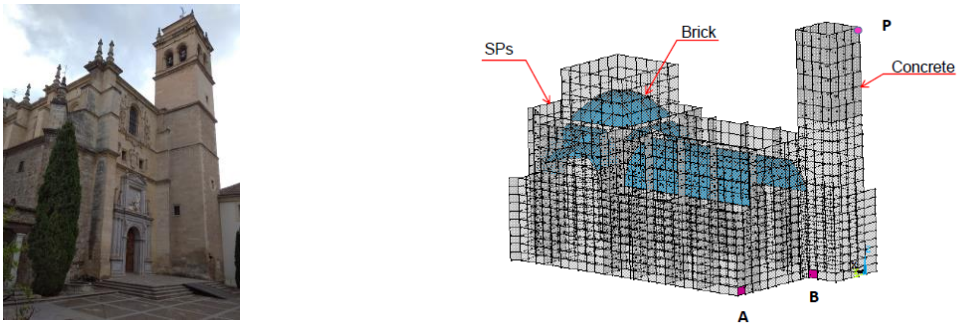

Figure 2. a) The Church of San Jerónimo monastery of Granada and b) numerical model. *Adapted from* [3]

The Monastery of San Jerónimo is modeled with shell elements (Figure 1b). The materials of the monastery are Santa Pudia stone [5] for walls, concrete for the upper part of the tower (depicted in dark grey in Figure 1b), and brick fabric for the domes (in blue in Figure 1b).

In this piece of work, the Fragility Functions (FF) of the San Jerónimo Monastery (in Granada) are obtained by estimating the parameters (i.e., median and standard deviation) from using two different approaches, as described below.

1.1. Method 1

Method 1 employs a simple two-stripe approximation procedure. For each value of IM (a total of 10 values of AvgSA has been considered), the number of collapses n_{fail} and the number of cases analyzed n_{anal} are quantified. The fraction causing collapse is then calculated as the Probability of Exceedance (PoE) = n_{fail}/ n_{anal}. To construct the FCs, the median (μ) and the standard deviation (σ) of the log-normal distribution are required. In this case, two stripes separated enough to guarantee accuracy [8] are considered, labeled 1 and 2. The two equations summarizing this approach are presented in Eq.(2).

$$\left.\begin{array}{l} CDF\left[LogNormalDistrib\left[\mu,\sigma\right],AvgSA_1\right]=PoE_1 \\ CDF\left[LogNormalDistrib\left[\mu,\sigma\right],AvgSA_2\right]=PoE_2 \end{array}\right\} \rightarrow \mu \text{ and } \sigma \quad (2)$$

Once μ and σ are known from Eq.(2), the FC can be obtained as:

$$FF = CDF\left[LogNormalDistrib\left[\mu,\sigma\right],x\right] \quad (3)$$

with CDF as the cumulative distribution function for the log-normal distribution evaluated at *x, being x =AvgSA*.

The FCs for the Monastery of San Jerónimo and for the two ages studied obtained from this method are represented in Figure 3a [3].

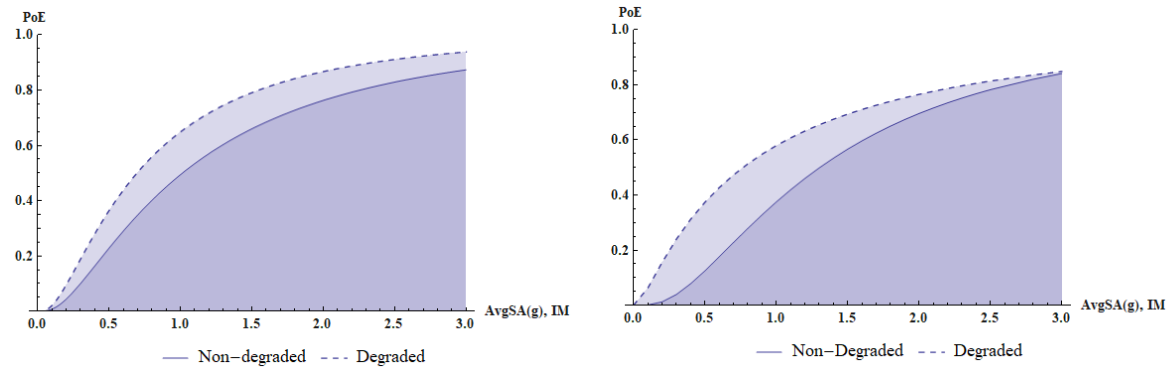

a) *b)*

Figure 3. *Fragility curves of San Jerónimo. a) Method 1 (Adapted from* [3]*). b) Method 2.*

1.2. Method 2

In this method, based on FEMA P-58 [9], the FF can be formulated in statistical terms as:

$$FF_i = CDF\left[NormalDistrib\left[ln\left(AvgSA_i\right),ln\left(\mu\right),\hat{\sigma}\right]\right] \quad with \quad \hat{\sigma}=ln\left(\sigma\right) \quad (4)$$

with *ln* as the natural logarithm. The values of μ and $\hat{\sigma}$ are adjusted (using tools such as Solver of Excel) by maximizing the sum of natural logarithms of the likelihood (note that *ln*(likelihood) is negative), as indicated in Eq.(5) [10]:

$$\mu,\hat{\sigma} = Max \sum_{i=1}^{n} ln\left(BinomDistrib\left[n_{fail,i}, n_{anal,i}, FF_i \right] \right) \quad (5)$$

with *BinomDistrib* referring to the Binomial distribution. Once μ and $\hat{\sigma}$ are known, the FF is completely defined by Eq.(4). The FCs for the Monastery of San Jerónimo obtained from Method 2 are represented in Figure 3b. Comparison of both figures in Figure 3 shows that Method 2 predicts lower probabilities of collapse at low IM levels.

4. CONCLUSIONS

A log-normal probability distribution has been considered for the development of fragility curves. The calibration of the FF requires estimating the values of the media and standard deviation from structural analysis, in this case, carried out using FE. The values of the parameters are been obtained using two approaches. Based on the results obtained in this study, it can be concluded that fragility functions obtained for the Monasterio of San Jerónimo are sensitive to the method used for obtaining the statistical parameters, mainly in the range of lower IM levels.

REFERENCES

1. Baker, J.W., Jayaram, N. (2008). Correlation of Spectral Acceleration Values from NGA Ground Motion Models. *Earthquake Spectra*, *24*, 299–317.
2. Ancheta, T.D., Eeri, M., Darragh, R.B., Eeri, M.,Stewart, J.P., Eeri, M., Seyhan, E., Eeri, M., Silva, W.J., Eeri, M., et al. (2014). NGA-West2 Database, *30*, 989–1005.
3. Gil-Martín, L.M., Hdz, L., Kohrangi, M., Menéndez, E., Hernández-Montes, E.(2022). Fragility Curves for Historical Structures with Degradation Factors Obtained from 3D Photogrammetry. *Heritage*, 3260–3279.
4. Gil-Martin, L.M., Fernández-Ruíz, M.A., Hernández-Montes, E. (2022). Mechanical characterization and Elastic Stiffness Degradation of Unstabilized Rammed Earth. *Journal of Building Engineering*, *56*, (104805).
5. Gil-Martín, L.M., Fernández-Ruíz, M.A., Hernández-Montes, E. (2022). Mechanical Characterization and Creep Behavior of a Stone Heritage Material Used in Granada (Spain): Santa Pudia Calcarenite. *Rock Mechanicks and Rock Engineering*, *55(9), 5659-5669*.
6. Jalón, M.L., Chiachío, J., Gil-Martín, L.M., Hernández-Montes, E. (2021). Probabilistic Identification of Surface Recession Patterns in Heritage Buildings Based on Digital Photogrammetry. *Journal of Building Engineering*, *34*, *101922*.
7. Menéndez, E., Gil-Martín, L.M., Salem, L., Jalón, L., Hernández-Montes, E., Alonso, M.C. (2022). Bayesian Assessment of Surface Recession Patterns in Brick Buildings with Critical Factors Identification. *Boletín la Sociedad Española Cerámica y Vidrio.*
8. Aschheim, M., Hernández-Montes, E., Vamvatsikos, D. (2019). Design of Reinforced Concrete Buildings for Seismic Performance: Practical Deterministic and Probabilistic Approaches. Boca Raton: CRC Press. Taylor & Francis.
9. FEMA P-58 (2012). Seismic Performance Assessment of Buildings. Washington.
10. Baker, J.W. (2015). Efficient Analytical Fragility Function Fitting Using Dynamic Structural Analysis. *Earthquake Spectra*, *31*, 579–599.

Influence of modal shape residual criterion on the MLM FEMU of civil engineering structures

Ereiz, Suzana[1]; Jiménez-Alonso, Javier Fernando[2]; Naranjo-Pérez, Javier[2]; Gallegos - Calderón, Christian[3] ; Duvnjak, Ivan[1]; Limongelli, Maria Pina[4]

ABSTRACT

This paper describes the impact of different mode shape comparison criteria on the finite element model updating (FEMU) results under the maximum likelihood model updating method. FEMU is used to update numerical models according to the real structural behaviour. Under the maximum likelihood method, FEMU is formulated as the optimization problem combining the bi-objective optimization and decision-making problem. The bi-objective function is defined as the differences between the actual structural behavior and that predicted by the numerical model, usually comparing the natural frequencies and mode shapes through the formulation of the residuals. The mode shape residual is mostly defined using the Modal Assurance Criterion which has a great difference between the value of two mentioned, natural frequency and mode shape, residual. To overcome this limitation, this paper analyzes four different comparison criteria: modal assurance criterion, root mean square error, mean absolute error. Pareto optimal front and knee point have been considered as comparison criteria.

Keywords: mode shapes, finite element model updating (FEMU), maximum likelihood method (MLM), multi-objective optimization.

1. INTRODUCTION

Due to different assumptions and predictions introduced during modelling the obtained numerical model may not reflect the real structural behaviour [1]. To cope with this problem the results obtained as a part of experimental investigation are used for the FEMU process. This process can be performed using different methods, while for practical engineering application MLM [2] is mostly used to calibrate the value of the most relevant physical parameters of the structure, θ. According to this approach, the FEMU problem can be formulated as the combination of two sub-problems: a bi-objective optimization – Eq.(1)- and a decision-making sub-problem. The bi-objective function is generally defined in terms of the residuals between the numerical and experimental modal properties (natural frequencies and mode shapes) of the structure. The natural frequency residual, $r_t^f(\theta)$, is mostly defined as the relative difference between the experimental and numerical ones. On the other hand, the mode shapes residual, $r_t^m(\theta)$, can be defined according to different criteria [4] in terms of

[1] *Faculty of Civil Engineering, University of Zagreb (Croatia). (Corresponding author). suzana.ereiz@grad.unizg.hr*

[2] *Higher Technical School of Engineering, University of Seville (Spain) jfjimenez@us.es, jnaranjo3@us.es*

[3] *Department of Continuum Mechanics and Theory of Structure, Polytechnic University of Madrid (Spain) christian.gallegos@upm.es*

[4] *Department of Architecture, Construction Engineering and Built Environment, Polytechnic University of Milano (Italy) mariagiuseppina.limongelli@polimi.it*

the experimental, ϕ_t^{exp}, and numerical mode shapes, ϕ_t^{num}. The criteria tested herein are shown in Table 1.

$$\min f(\theta) = (f_1(\theta) \quad f_2(\theta)) = \min\left(\sum_{t=1}^{m_f} r_t^f(\theta)^2 \quad \sum_{t=1}^{m_m} r_t^m(\theta)^2\right) \tag{1}$$

As a solution of this optimization problem, a set of the possible optimal solutions is obtained, the so-called Pareto optimal front [3]. Subsequently, the decision-making sub-problem consists of the selection of the best solution, the so-called "knee" point, among the different elements of the Pareto front.

Table 1. Mode shapes comparison criteria.

Comparison criteria			
$MAC(\phi_t^{exp}, \phi_t^{num})$	$RMSE_t$	MAE_t	$MSF(\phi_t^{exp}, \phi_t^{num})$
$\frac{\left\lvert\lvert\phi_t^{exp}\rvert^T \lvert\phi_t^{num}\rvert\right\rvert^2}{\lvert\phi_t^{num}\rvert^T \lvert\phi_t^{exp}\rvert}$	$\sqrt{\frac{1}{K}\sum_{k=1}^{K}(\phi_{k,t}^{exp} - \phi_{k,t}^{num})^2}$	$\frac{1}{K}\sum_{k=1}^{K}\lvert\phi_{k,t}^{exp} - \phi_{k,t}^{num}\rvert$	$\frac{\lvert\phi_t^{exp}\rvert^T \lvert\phi_t^{num}\rvert}{\lvert\phi_t^{num}\rvert^T \lvert\phi_t^{num}\rvert}$
Mode shapes residual			
$\sqrt{\left(\frac{\left(1-\sqrt{MAC_t(\theta)}\right)^2}{MAC_t(\theta)}\right)}$	$\frac{RMSE_t}{\left(1-\sqrt{(RMSE_t)^2}\right)^2}$	$\frac{MAE_t}{\left(1-\sqrt{(MAE_t)^2}\right)^2}$	$\frac{\left(1-\sqrt{(MSF_t)^2}\right)^2}{{MSF_t}^2}$

2. FEMU OF A LABORATORY FOOTBRIDGE

To test the abovementioned comparison criteria, as a case study, an ultra-light-weight fiber reinforced polymer laboratory bridge was considered (Fig. 1.).

(a) (b) (c)

Fig. 1. *Ultra-lightweight FRP laboratory footbridge a) assembling of superstructure b) bridge walking surface c) ambient vibration test.*

The initial numerical model was developed using the commercial FE package Ansys [5]. The FE model is realized using SHELL 181 elements considering both isotropic and orthotropic behavior, 3D linear beam elements BEAM 188, 3D solid elements (SOLID185) defined by eight nodes having three degrees of freedom at each node and COMBIN 14 elements to model the support in longitudinal and transversal direction. Based on this numerical model, a modal analysis was performed to obtain numerically each *t* natural frequency and associated mode shape (Fig. 2).

The characterization of the real structural behavior is performed through the static and dynamic test. The static test is performed by measuring deflection in the middle of span (Fig. 1.c.). The maximum measured deflection was 12.8 mm. The modal properties (natural frequencies and mode shapes)

were experimentally identified using operational modal analysis under ambient conditions. The 18 sensors were arranged in two lines with 9 measuring points in each in the vertical direction (Fig. 3).

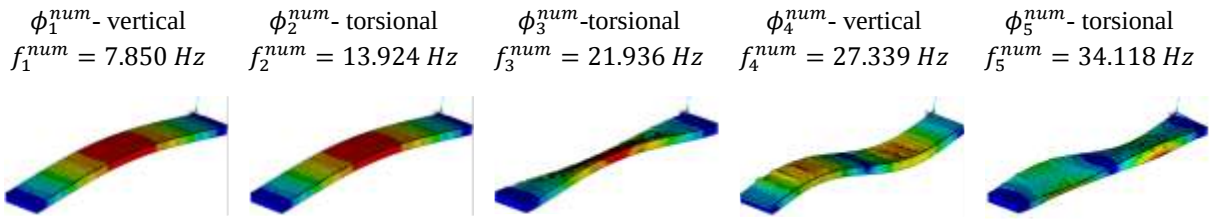

Fig. 2. *Numerical natural frequencies (f_t^{num}) and mode shapes (ϕ_t^{num}) obtained from the initial FEM of the laboratory footbridge for t=1, …,5.*

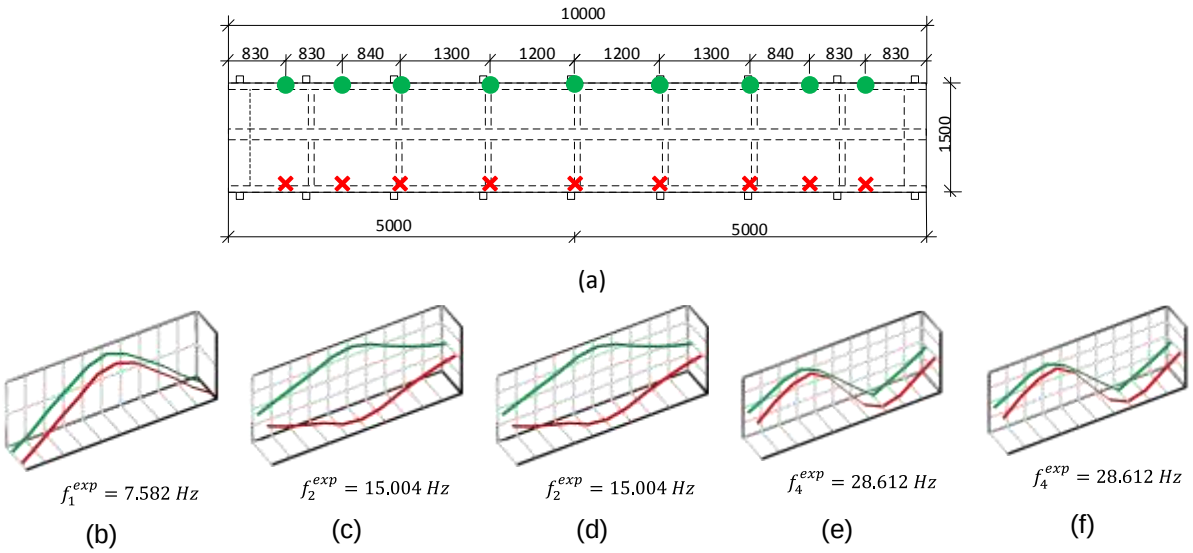

Fig. 3. *Experimental identification during ambient vibration test: a) arrangement of the measurement points b) – f) characteristic mode shape (ϕ_t^{exp}) for each corresponding natural frequency (f_t^{exp}).*

To perform the FEMU, the most relevant updating parameters, θ, were selected according a sensitivity analysis. This analysis was based on the ratio between the modal strain energy associated with the considered physical parameters and the overall modal strain energy of the structure. As result, eight updating parameters were selected. The updating of the numerical model was performed using an implementation of the Harmony Search nature inspired optimization algorithm [6] in Matlab software [7]. Different mode shapes residual criteria were considered. Fig. 4 shows the normalized Pareto front of the two terms of the bi-objective function for the different considered criteria.

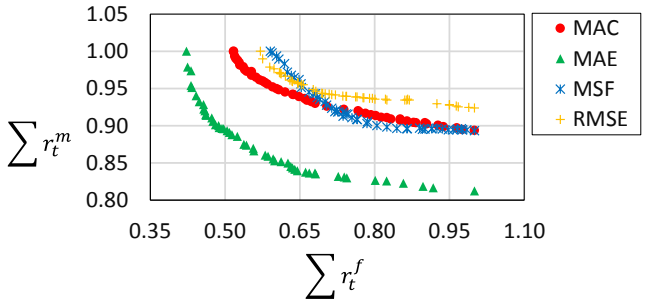

Fig. 4 *Comparison of the normalized Pareto optimal front obtained based on the different formulations of the mode shape residuals.*

3. DISCUSSION

For a more detailed comparison of the obtained results, a static test performed experimentally was

replicated numerically. Values of the deflection obtained on the numerical updated model, using different mode shape residual criteria, are shown in Table 2.

Table 2 Comparison of the deflection in the middle of span numerically predicted by four different optimal numerical model.

	Deflection [mm]	
Mode Shape Residual	**Numerical**	**Experimental**
MAC (Modal Assurance Criterion)	12.96	12.80
MAE (Mean Absolute Error)	12.72	
MSF (Modal Scale Factor)	12.95	
RMSE (Root Mean Squared Error)	13.01	

According to these results, the solutions obtained vary from 0.63% to 1.64% due to the different formulation of the criteria used to update numerical model. It can be remarked that the solution provided by the MAE criteria is better than the remaining criteria as it results in a numerical model whose deflection in the middle of span the best corresponds to the experimentally determined one.

4. CONCLUSION

Using different mode shape comparison criteria to perform the FEMU results in different optimal numerical models. The MAE comparison criterion provides a numerical model whose sum of observed natural frequencies error is the lowest than the one obtained using the comparison criteria such as MAC, MSF, and RMSE. If the static performance is observed, it can be concluded that the numerical model updated based on the MAE comparison criteria provides results that best correspond to experimentally obtained ones. To sum up, it can be remarked that the MAE comparison criterion has shown the best performance when it is implemented to solve the multi-objective FEMU problem of civil engineering structures. Further studies are needed to compare the dynamic response (acceleration) of the updated numerical models obtained using different comparison criteria with the experimentally obtained one.

REFERENCES

[1] Ereiz, S.; Duvnjak, I.; Jiménez J. F. A. (2022) Review of finite element model updating methods for structural applications, Structures, vol. 41, pp. 684–723

[2] Marwala, T. (2010). Finite-element-model updating using computational intelligence techniques: Applications to structural dynamics, 1st edition. London, England: Springer-Verlag London

[3] Cuate, O; Schütze O. (2020) Pareto explorer for finding the knee for many objective optimization problems. Mathematics, 8:6–15.

[4] Ewins, D. J. (2000) Model validation: Correlation for updating, Sādhanā, 25,3, 221-234.

[5] Jiménez-Alonso, JF; Naranjo-Perez J; Pavic A; Sáez A. (2020) Maximum Likelihood Finite-Element Model Updating of Civil Engineering Structures Using Nature-Inspired Computational Algorithms. Structural Engineering International, 1–13.

[6] Ansys, Engineering Simulation Software. (n.d.) Retrieved September 19, 2022, from https://www.ansys.com/.

[7] Matlab 2022. https://uk.mathworks.com/.

Investigating the effects of semi-cyclic loads on recovery stresses of Iron-Based Shape-Memory Alloy

Mir, Antoni[1]; del Río-Bonnín, Sandra[1] Ribas, Carlos[1]; Montoya-Coronado, Luis A. [1]; Ruiz-Pinilla, Joaquín G. [1]; Ortiz, Galo[2]; Oller, Eva[2]; Cladera, Antoni[1]

ABSTRACT

Shape-memory alloys (SMAs) have gained significant attention in the field of civil engineering due to their unique thermomechanical properties, allowing them to recover from large deformations and regain their original shape through the shape memory effect (SME). This SME can be used with the objective to use SMAs as prestressing reinforcement, as they generate recovery stresses upon activation (heating and subsequent cooling) when deformation is constrained. This paper presents an analysis of the behaviour of iron-based SMA (Fe-SMA) strips and re-bars under semi-cyclic loads after activation as recent studies have revealed that Fe-SMA re-bars experience losses in recovery stresses when subjected to semi-cyclic loads. To assess these losses, various strip and bar typologies were consecutively activated and subjected to semi-cyclic tensile tests. The results demonstrate some distinct aspects of the behaviour depending on the Fe-SMA reinforcement typology.

Keywords: Iron-based Shape Memory Alloys (Fe-SMA), Shape Memory Effect (SME), martensitic transformation, recovery stresses, semi-cyclic loads.

1. INTRODUCTION

Concrete structures can suffer various forms of decay, impacting their performance. Over time, these structures often face increased demands, sometimes exceeding their intended capacity. To address this, various methods for reinforcing concrete elements have emerged. Shape-memory alloys (SMAs) have gained attention in the field of civil engineering due to their capacity to recover from deformation and return to their initial shape [1].

The main properties of SMAs, which are the shape memory effect (SME), super-elasticity, and a substantial dumping capacity, are all due to the martensitic transformation[2]. Fe-SMAs can be used for prestressing RC structures thanks to the generation of recovery stresses during the activation process. This process involves heating and subsequent cooling, provided it is accompanied by a restriction in the shape-recovery capacity (constrained strains) [2], [3].

This paper presents the characterization of Fe-SMA strips and bars intending to assess whether there are any losses in recovery stresses when subjecting the material to semi-cyclic loads. This study was

[1] *Industrial Engineering and Construction . Universitat de les Illes Balears (Spain). antoni.mir@uib.es (Corresponding author), s.del-rio@uib.es, carlos.ribas@uib.es,luis.montoyaib.es, joaquin.ruiz@uib.es, antoni.cladera@uib.es*

[2] *Civil and environmental engineering. Universitat Politècnica de Catalunya (Spain). eva.oller@upc.edu, galo.ortiz@upc.edu*

motivated by recent research indicating that the advantages of reinforcing with Fe-SMA could significantly decrease under the influence of semi-cyclic loads [4].

2. DESCRIPTION OF THE EXPERIMENTAL CAMPAIGN

Fe-SMA strips and bars were characterized to evaluate the potential losses in recovery stresses when semi-cyclical loads are applied. A Z100 Zwick universal tensile machine equipped with a 100 kN load cell was used to perform the described tests.

2.1 Fe-SMA strips characterization

The recovery stress tests consisted of 3 steps (Figure 1). Initially, it was necessary to subject the strips to a pre-strain, which was performed at ambient temperature to induce martensite formation within them. Following this, the prestrained sample was subjected to an initial preload of approximately 50 MPa to prevent the thermal expansion effect derived from heating the sample. In the third step, the strip was heated using a heat gun until it reached approximately 160 °C, followed by cooling. Throughout the heating and cooling processes, deformation was prevented at the ends of the sample. As the sample underwent reverse martensitic transformation during the heating phase, recovery stresses were induced.

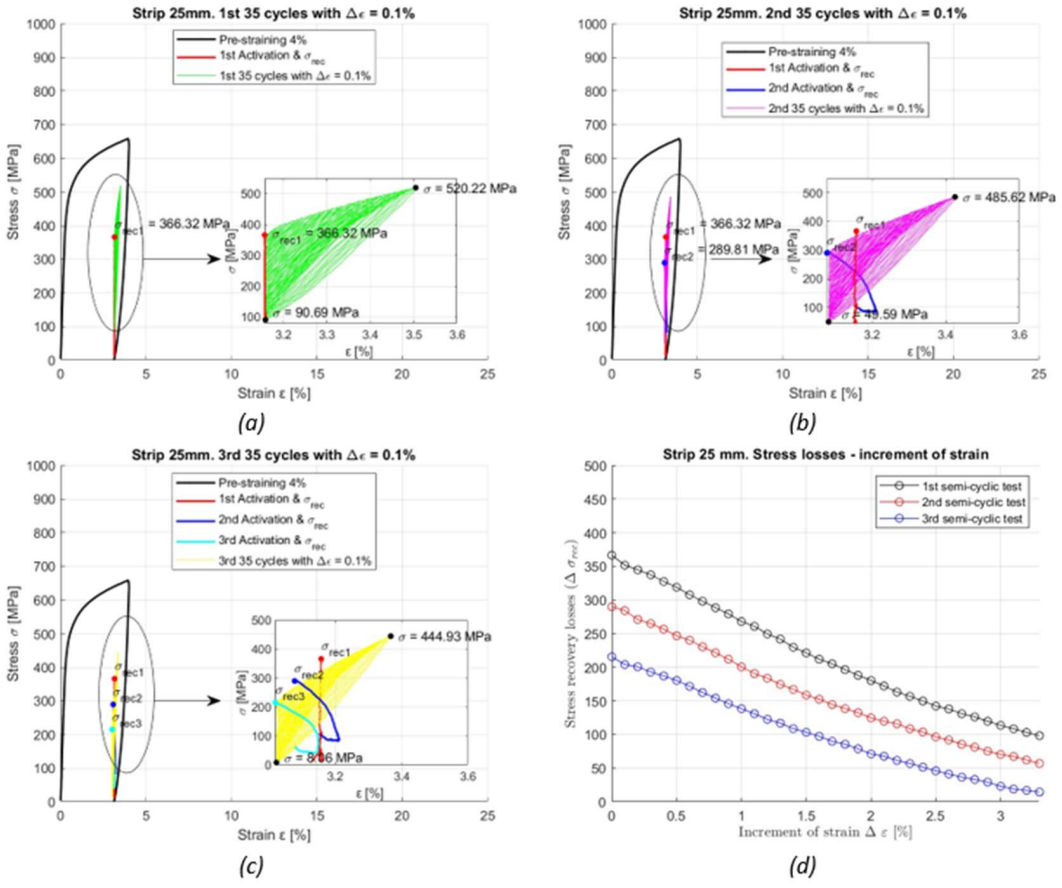

Figure 1 . *(a)(b)(c) Consecutive activations and semi-cyclical tests (d) Recovery stress losses in Fe-SMA strips.*

Subsequently, semi-cyclical load tests were conducted to evaluate the loss of recovery stresses following the application of these types of loads. The activation procedure, followed by semi-cyclic loads was repeated consecutively to evaluate the capability to generate recovery stresses after exposure to semi-cyclic loads, as shown in Figure 1.

The findings reveal a linear reduction decrease in recovery stress upon the application of semi-cyclic loads. The entirety of the recovery stress generated during activation is lost in the 3rd semi-cyclic test. Additionally, the recovery stress decreases by approximately 20% after each semi-cyclic test and subsequent activation.

3.2 Fe-SMA bars characterization

The tested Fe-SMA bars had a diameter of 11 mm and were already pre-strained by the provider. The main goal of this test was to find a correlation between the activation temperature and the attainment of recovery stress, as well as to assess the loss of recovery stress after applying semi-cyclical loads.

First, the bar was activated at 200°C using a heat gun and then allowed to cool to room temperature. Subsequently, five load and unloading semi-cycles were applied to the sample, with an increment (Δε) in strain per cycle equal to 0.1%, reaching a strain level of 0.5% (Figure 2). Next, the bar was activated again up to 200°C, was left to cool, and finally, semi-cycles were applied again. Thus, the performed test included five SMA activations, with five corresponding consecutive cycles. This process was replicated with different bars, activating them at 250°C and finally at 160°C.

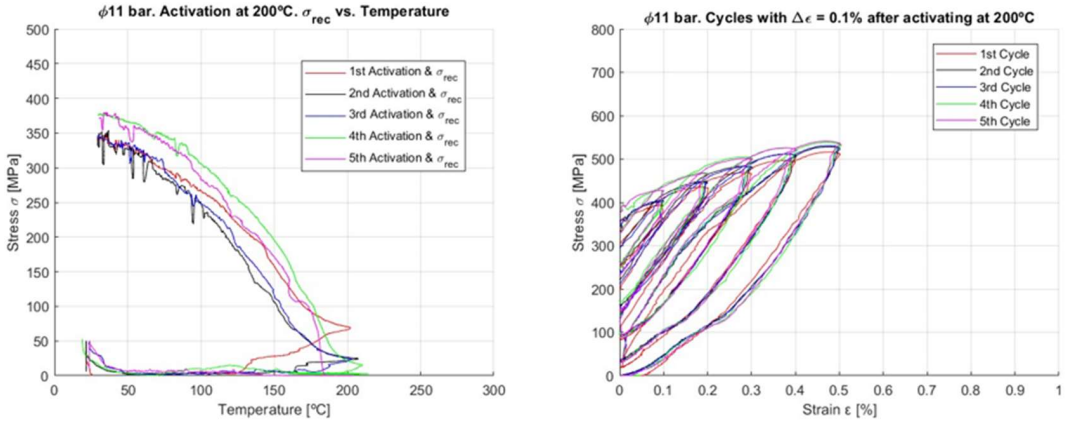

(a) *(b)*

Figure 2. *(a) Recovery stresses of ϕ11-bar at 200°C (b) Semi-cyclic tests applied after each activation of the Fe-SMA bar.*

The results indicate that the recovery stresses generated by activating the Fe-SMA bars are lost when subjecting the bar to semi-cyclic loads. By applying 5 cycles with 0.1% strain increments per cycle, and reaching a final strain level of 0.5%, the bars lose all previously generated recovery stress. However, this stress can be fully recovered again if the bar is reactivated, as shown in Table 1 and Figure 3. From these results, it can also be deduced that there is a linear increase in the recovery stress with the activation temperature, exhibiting roughly a 20-25% stress increases for every 40-50°C increment.

Table 1. Fe-SMA bars characterization results

Recovery stresses	Activation temperature		
	250ºC	**200ºC**	**160ºC**
1st σ_{rec} (MPa)	432.40	347.57	270.81
2nd σ_{rec} (MPa)	435.09	353.79	286.31
3rd σ_{rec} (MPa)	450.11	346.46	294.18
4th σ_{rec} (MPa)	444.61	378.04	289.88
5th σ_{rec} (MPa)	440.87	379.96	259.75
Mean	440.62	361.16	280.19

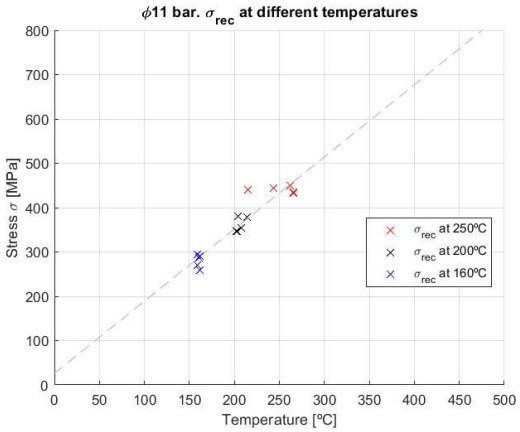

Figure 3 . *Recovery stresses of ϕ11-bar at different temperatures*.

3. CONCLUSIONS

An experimental campaign was conducted to evaluate the loss of recovery stress in Fe-SMA strips and bars under semi-cyclic loads. The findings showed contrasting behaviour between strips and bars in terms of generating recovery stresses. Strips saw a 25% reduction in recovery stress after each semi-cyclic test, while bars maintained consistent recovery stresses through 5 activations and a correlation was found between activation temperature and recovery stress in the re-bars. Further research is necessary to fully understand the reasons behind this differential behaviour.

ACKNOWLEDGEMENTS

This research was conducted as a part of projects CICLO, funded by the Tourist Stay Tax Law No. ITS 2017-006 (No. PRD2020/39) provided by Comunitat Autònoma de les Illes Balears through the Conselleria de Fons Europeus, Universitat I Cultura and the Direcció General de Política Universitària i Recerca, and PID2021-123701OB-C22 funded by MCIN/AEI/10.13039/501100011033 and by "ERDF A way of making Europe". We also acknowledge the "SOIB/Conselleria de Fons Europeus, Universitat i Cultura" and "European Union NextGenerationEU" for the grant awarded to the first author.

REFERENCES

[1] M. R. Izadi, E. Ghafoori, M. Shahverdi, M. Motavalli, and S. Maalek (2018). Development of an iron-based shape memory alloy (Fe-SMA) strengthening system for steel plates. Eng Struct, vol. 174, pp. 433–446, doi: 10.1016/j.engstruct.2018.07.073.

[2] A. Cladera, B. Weber, C. Leinenbach, C. Czaderski, M. Shahverdi, and M. Motavalli (2014). Iron-based shape memory alloys for civil engineering structures: An overview," Construction and Building Materials, vol. 63. Elsevier Ltd, pp. 281–293, doi: 10.1016/j.conbuildmat.2014.04.032.

[3] L. A. Montoya-Coronado, J. G. Ruiz-Pinilla, C. Ribas, and A. Cladera (2019) Experimental study on shear strengthening of shear critical RC beams using iron-based shape memory alloy strips," Eng Struct, vol. 200, doi: 10.1016/j.engstruct.2019.109680.

[4] B. Schranz, C. Czaderski, M. Shahverdi, J. Michels, T. Vogel, and M. Motavalli (2019). Ribbed iron-based shape memory alloy bars for pre-stressed strengthening applications. IABSE Symposium 2019 Guimarães.

Joint practices in third year subjects of the Mechanical Engineering Degree. Design, manufacture and testing of composite materials

Capel-García, Isabel [1]; López-Martínez, Javier[1]; Ariza-Camacho, María Jesús[2]; Garzón-Garzón, Eduardo[1]

ABSTRACT

This work presents a series of joint practices to be carried out in the subjects of Strength of Materials, Materials Technology, and Machines Design I, in the third year of the Degree in Mechanical Engineering at the University of Almería. The objective of this project is to increase the student motivation and interest in these subjects, as well as to promote an active and participatory role in the learning process. To achieve this objective, a set of five joint practices have been planned in three different subjects. With the purpose of manufacturing a mechanical element that can resist certain loading conditions, the tasks to be carried out by the students during the practices include the fabrication of plastic and fiber-reinforced plastic composite specimens and the experimental determination of their bending properties, and the design of mechanical elements and FEM simulation.

Keywords: joint practices, multi-course, flexure test, composite materials, mechanical design.

1. INTRODUCCIÓN

El conocimiento de la estructura interna de los materiales industriales y de su comportamiento mecánico es fundamental en la formación del graduado en ingeniería mecánica. Dichos conocimientos son abordados en profundidad en las asignaturas de Elasticidad y Resistencia de Materiales (ERM), Materiales Industriales (MI), y Cálculo y Diseño de Máquinas I (CDM), todas ellas impartidas en el tercer curso del Grado en Ingeniería Mecánica de la Universidad de Almería. El alto grado de relación entre los contenidos de estas tres asignaturas es una motivación para el desarrollo de actividades formativas que integren, de alguna manera, a dichas asignaturas de forma conjunta. En los últimos años, entre las actividades formativas que se vienen realizando en estas asignaturas, se incluyen una serie de prácticas de laboratorio relacionadas con la determinación experimental de las propiedades mecánicas de plásticos (ERM), la fabricación de compuestos plásticos reforzados con fibra (MI), la determinación experimental de las propiedades a flexión de los materiales (MI), y el diseño mediante ordenador de elementos mecánicos atendiendo a los propiedades mecánicas de los mismos (CDM). En este trabajo se propone la modificación de dichas prácticas, relacionándolas entre sí, donde los conocimientos adquiridos y los resultados obtenidos en una primera práctica sean necesarios para la realización de las prácticas posteriores. Con estas prácticas concatenadas [1], y multi-asignatura [2], se espera conseguir una mayor motivación e interés del alumnado, así como favorecer el papel activo y participativo en el proceso de aprendizaje.

[1] *Departamento de Ingeniería. Universidad de Almería (España). Dirección e-mail: isabelcapelgarcia@gmail.com; javier.lopez@ual.es (Corresponding author); egarzon@ual.es*

[2] *Departamento de Química y Física. Universidad de Almería (España). Dirección e-mail: mjariza@ual.es*

2. DESCRIPCION DE LAS PRÁCTICAS

En esta sección se describen las prácticas propuestas. Además, se muestran resultados obtenidos en el Trabajo Fin de Grado (TFG) realizado por Capel-García [3], en el cual se llevó a cabo el diseño y fabricación de una maneta de freno de bicicleta en fibra de carbono, y en el que se realizaron tareas similares a las que se proponen para estas prácticas. Los buenos resultados alcanzados en dicho TFG han supuesto también una motivación para impulsar el presente trabajo.

El conjunto de prácticas tiene como punto final el diseño y fabricación con plástico reforzado con fibra de un elemento mecánico sencillo. La meta y motivación desde el punto de vista del alumno es conseguir el mejor diseño, que soporte las condiciones de carga requeridas, con el menor peso posible. Además, para ello, deberá aprender y poner en práctica el proceso de fabricación necesario. Se han planificado las siguientes prácticas concatenadas:

- Práctica 1 (ERM, 1er semestre). Ensayo de flexión - Determinación de las propiedades de flexión de plásticos.
- Práctica 2 (MI, 2^{o} semestre). Fabricación de material plástico reforzado con fibra.
- Práctica 3 (MI, 2^{o} semestre). Determinación de las propiedades de flexión de material plástico reforzado con fibra.
- Práctica 4 (CDM, 2^{o} semestre). Diseño y simulación de un elemento mecánico frente a carga estática.
- Práctica 5 (CDM, 2^{o} semestre). Fabricación y ensayo de resistencia de un elemento mecánico.

2.1. Práctica 1 (ERM). Ensayo de flexión - Determinación de las propiedades de flexión de plásticos

El ensayo de flexión permite obtener de forma sencilla valores de propiedades mecánicas importantes. En esta primera práctica se le pide al alumno que determine las propiedades de resistencia a la flexión y módulo de elasticidad en flexión de distintos plásticos. Para ello, estará disponible el siguiente material: probetas de distintos materiales, una máquina de ensayos universal y la normativa de referencia UNE-EN ISO 178 para la determinación de las propiedades de flexión de plásticos. Los objetivos de aprendizaje de la práctica son: la comprensión y aplicación de normativa de carácter técnico; el manejo de una máquina de ensayos universal; y el aprendizaje de las curvas tensión-deformación de materiales plásticos y obtención de las propiedades características.

Los conocimientos que habrán adquirido los alumnos en esta práctica, y que serán necesarios para el desarrollo de las siguientes, son: cómo determinar las propiedades de flexión de materiales, el uso de la normativa asociada, y el manejo de una máquina multifunción. Como resultados prácticos obtenidos por los alumnos, que serán necesarios emplear posteriormente, son los valores de la resistencia a la flexión y del módulo de elasticidad en flexión de un plástico PLA en impresión 3D.

2.2. Práctica 2 (MI). Fabricación de material plástico reforzado con fibra

Los objetivos docentes de esta práctica son el aprendizaje del tipo de materias primas y el proceso necesario para la fabricación de materiales compuestos fibra-matriz. El objetivo del trabajo práctico de los alumnos es la fabricación de probetas de ensayo realizadas en compuesto resina epoxi - fibra de carbono con distinta fracción de fibra. Las dimensiones de las probetas deberán ser conforme a la norma UNE-EN ISO 14125 para la determinación de las propiedades de flexión de plásticos reforzados

con fibra. Igualmente, se fabricarán al menos cinco probetas de cada composición para tener una muestra representativa mínima (según UNE-EN ISO 14125).

2.3. Práctica 3 (MI). Determinación de las propiedades de flexión de material plástico reforzado con fibra

Esta práctica tiene como objetivo determinar las propiedades de flexión de los materiales compuestos fabricados en la Práctica 2 mediante el correspondiente ensayo destructivo (UNE-EN ISO 14125), así como evaluar la ejecución del proceso de fabricación de las probetas. Para ello, el primer paso será el desmoldeo de las probetas, su preparación y toma de medidas haciendo uso de la instrumentación necesaria. Una vez preparadas las probetas, se realizarán los ensayos de flexión en la máquina de ensayos universal. Finalmente, se obtendrán a partir de las curvas tensión-deformación los valores de la resistencia a la flexión y del módulo de elasticidad en flexión para cada una de las composiciones fibra-matriz fabricadas. La Fig. 1 es un ejemplo de las curvas obtenidas para tres composiciones distintas [3]. Las curvas tensión-deformación registradas, así como el aspecto de la rotura de las probetas permitirán además identificar deficiencias en la fabricación. Los resultados concretos de esta práctica será la selección de la mejor composición fibra-matriz y la identificación de sus propiedades mecánicas. Estos resultados serán empleados en la fase de diseño mecánico que se aborda en la siguiente práctica.

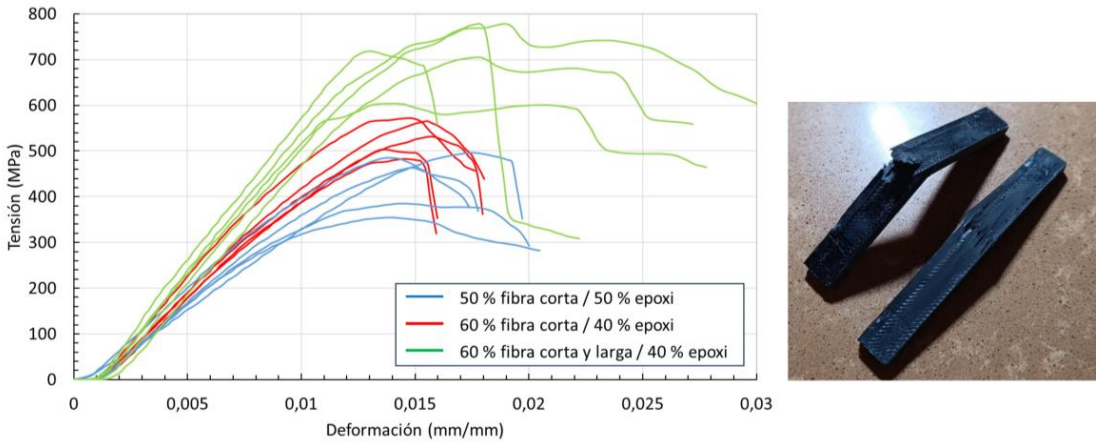

Figura 1. *Curvas tensión-deformación para distintos porcentajes en peso de fibra de carbono/matriz epoxi (izquierda) y ejemplo del aspecto de la fractura de las probetas (derecha) [3].*

2.4. Práctica 4 (CDM). Diseño y simulación de un elemento mecánico frente a carga estática

En esta práctica se propone realizar el diseño de un elemento mecánico sencillo sometido a un estado de cargas conocido. Los objetivos docentes son el aprendizaje del proceso de simulación mediante elementos finitos, y el dimensionado de un elemento mecánico sometido a un estado de cargas estático. Los datos de partida son las dimensiones generales del elemento, el estado de cargas (directo o mediante interpretación de normativa) y los valores de resistencia a la flexión y módulo de elasticidad obtenidos en la práctica anterior. El alumno deberá actuar sobre algunas dimensiones del elemento (definidas por el profesor) para optimizar el peso del elemento. Para ello hará uso de un software de simulación mediante elementos finitos. En las modificaciones de las dimensiones o geometría del elemento, el alumno deberá tener presente las posibilidades del proceso de fabricación posterior. El resultado de esta práctica será el diseño optimizado del elemento mecánico, el cual será empleado en la quinta y última práctica.

2.5. Práctica 5 (CDM). Fabricación y ensayo de resistencia de un elemento mecánico

En esta última práctica se lleva a cabo la fabricación y ensayo del elemento diseñado en la Práctica 4. Se prevé la posibilidad de dos métodos de fabricación dependiendo de la complicación geométrica de la pieza. En primera instancia se buscará la elección de un elemento mecánico sencillo que permita su fabricación en material compuesto. En caso de que la geometría o dimensiones de la pieza no hagan factible su fabricación, ésta se llevará a cabo mediante impresión 3D con el PLA caracterizado en la Práctica 1. En cualquier caso, la fabricación del elemento mecánico se llevará a cabo previamente a la sesión de prácticas. La Fig. 2 es un ejemplo de elemento mecánico complejo realizado con fibra de carbono [3]. Durante la sesión de prácticas los grupos harán una breve exposición y defensa del diseño realizado, y se llevarán a cabo los ensayos de carga sobre los prototipos.

Figura 2. *Maneta de freno de bicicleta de montaña fabricada con matriz epoxi-fibra de carbono [3].*

3. CONCLUSIONES

Se han preparado un conjunto de cinco prácticas concatenadas para tres asignaturas obligatorias de tercer curso del Grado en Ingeniería Mecánica de la Universidad de Almería, estando prevista su realización durante el curso 2023-2024. El resultado final de las prácticas es un elemento mecánico diseñado y fabricado por el alumno/a. Durante las prácticas el alumno/a deberá: manejar normativa técnica, fabricar piezas en materiales compuestos y realizar ensayos de flexión para la caracterización de dichos materiales, aprender las claves para la selección de materiales y la mejora del diseño de elementos mecánicos o estructurales en base a su resistencia estática, y realizar ensayos de resistencia en el elemento final fabricado. Con la concatenación de las prácticas se espera conseguir una mayor motivación e interés del alumno/a, lo que se espera que repercuta favorablemente en su proceso de aprendizaje.

REFERENCIAS

[1] Carretero-Ayuso, M.J. Experiencia docente con el alumnado del ámbito de la edificación: valoración de los trabajos concatenados en las actividades de la evaluación continua. I Jornadas de Innovación Docente en la Ingeniería (pp. 31-37). Cáceres: Quirós Rosado, E. (Ed.).

[2] Elkorobarrutia, X., Pérez, J.M., Sagardui, G., Etxeberria, L. Coordinación en PBL integrando múltiples asignaturas: una experiencia integrada. Actas del Simposio-Taller XXIII Jenui (pp. 19-25). Cáceres: Universidad de Extremadura (Ed.).

[3] Capel-García, I. (2023). Diseño y fabricación de una maneta de freno para bicicleta MTB (Trabajo Fin de Grado). Almería: Universidad de Almería.

Library of digital models and constructive simulations of structural elements

Sánchez Berrocal, Juan[1]; Troyano Moreno, Miguel.[1]

ABSTRACT

The aim of this communication is to describe the use of new technologies to obtain a library of digital models of structural elements and construction simulations to improve learning processes in the sujects of concrete structures and foundations. To this end, the Autodesk BIM tools Revit and Navisworks are used to obtain the 3D geometric model of the structural elements, which includes both the shapes and the reinforcement and formwork, the Autodesk 3DS Max tool to create the animations that represent the construction simulations, the Sketchfab web platform to visualise the digital models and the YouTube platform to visualise the costruction simulations. These web platforms allow not only to visualise the elements of the library but also to embed these components in other web platforms, such as the Moodle learning platform, and in the UMA CV.

Keywords: BIM, Digital model, Reinforced concrete, Construction simulation, Teaching reinforced concrete.

1. INTRODUCCIÓN

La enseñanza de las asignaturas de estructuras, como la de estructuras de hormigón y cimentaciones, requieren transmitir los conocimientos relativos a la disposición de armados y los procesos constructivos de los elementos estructurales que constituyen las estructuras (zapatas, pilotes, muros, vigas, forjados,…). Para describir la disposición de armados, tradicionalmente, las herramientas docentes que se suelen utilizar son representaciones gráficas, en forma de esquemas o vistas de armados, junto con fotografías tomadas directamente en la obra. Estas herramientas son representaciones estáticas de los armados, que no permiten la interacción del alumno para poder cambiar el punto de vista o focalizar una parte determinada del armado para obtener un mayor nivel de detalle. Con respecto a los procesos constructivos, de nuevo, se utilizan representaciones gráficas y fotografías, junto con videos de obra tomados durante la construcción de los elementos estructurales. Estos videos aportan claramente un gran valor docente, pero son difíciles de obtener videos que recojan el proceso completo y con el suficiente nivel de detalle, y, en algunas ocasiones, pueden mostrar malas prácticas e incluso defectos de ejecución que pueden transmitir una mala enseñanza al alumno.

Por otro lado, los avances tecnológicos, en especial el surgimiento de la metodología BIM [1], ha permitido la digitalización del sector AEC (Architecture, Engineering and Construction), y con ello la obtención de modelos BIM de la construcción, y en especial de los elementos estructurales, con muy alto nivel de detalle, que reflejan de forma fidedigna las características de lo que se quiere construir, en especial sus características geométricas. Estos modelos BIM, tras un proceso de conversión a un formato 3D estándar, pueden almacenarse y visualizarse en plataformas web que permiten a sus usuarios

[1] *Dep. Ingeniería Civil, de Materiales y Fabricación. Universidad de Málaga (ESPAÑA). jsanchezb@uma.es (corresponding author). mtroyano@uma.es*

interactuar con dichos modelos, y pueden ser utilizados en programas de animación para obtener videos con la simulación de sus procesos constructivos, que, a su vez, pueden ser almacenados en plataformas web, como YouTube, para que sus usuarios puedan visualizarlos a demanda. Estos modelos digitales y simulaciones constructivas pueden ser utilizados como herramientas docentes para mejorar los procesos de aprendizajes en las asignaturas de las materias relacionadas.

En esta ponencia se describe como se puede generar una biblioteca de modelos digitales y simulaciones constructivas de elementos estructurales que permitan mejorar la docencia de las asignaturas de Estructuras de Hormigón y Cimentaciones de la Escuela de Ingenierías Industriales de la UMA.

2. PROCESOS

El diagrama de procesos para la obtención de la biblioteca de modelos digitales y simulaciones constructivas se muestran en la figura 1 y se describe a continuación.

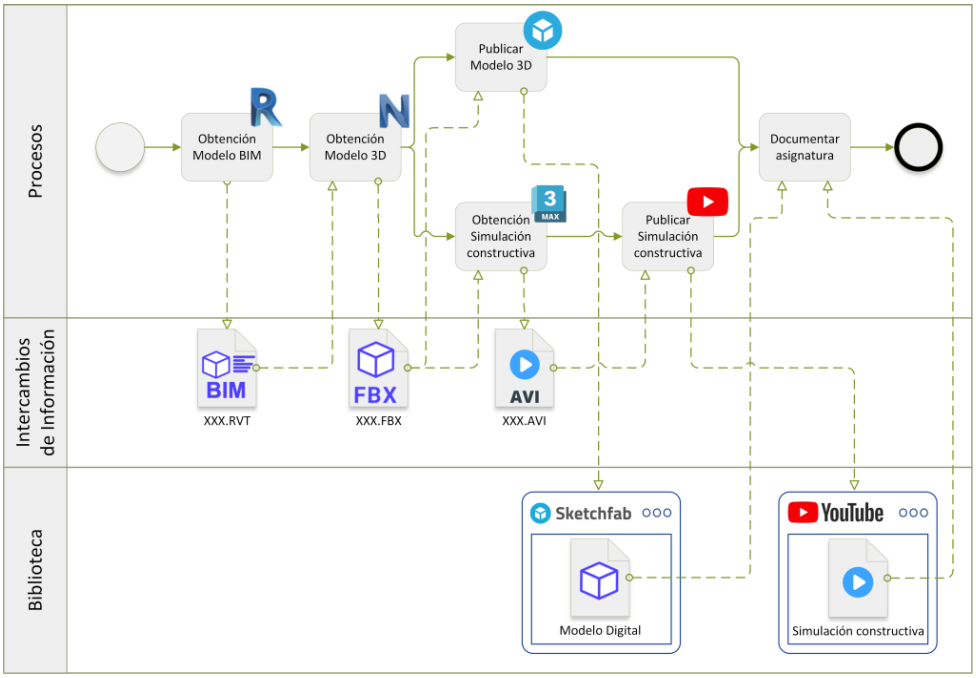

Figura 1. *Diagrama de procesos*

2.1. Obtención del Modelo BIM

En primer lugar, se obtiene el modelo BIM del elemento estructural utilizando la aplicación Autodesk Revit. Esta es la aplicación de modelado BIM más extendida en España, y permite la obtención de una geometría precisa y de alto grado de definición, tanto de las formas del elemento, como de sus armados y elementos auxiliares (separadores, conectores…). La ventaja que presenta Revit frente a otros modeladores, para este propósito, es su capacidad para obtener los armados de los elementos estructurales, al permitir trazar cualquier geometría de armadura y restringir su posición a los paramentos del elemento o a otras armaduras de forma paramétrica, lo cual permite un alto grado de precisión y automatización, y la eliminación de colisiones entre armados.

El resultado de este proceso es un fichero nativo de Revit, en formato RVT.

2.2. Obtención del Modelo 3D

Para poder publicar la geometría del elemento estructural en la plataforma web Sketchfab se requiere un formato de archivo 3D compatible, siendo uno de los recomendados el formato FBX. Aunque Revit permite la exportación a este formato, el fichero FBX obtenido presenta dificultades para su tratamiento en Sketchfab. Es por ello, por lo que la generación del fichero FBX se realiza desde la aplicación Autodesk Navisworks Manage, que permite leer el fichero generado por Revit en formato nativo RVT y generar el fichero FBX. Este fichero ya es adecuado para su tratamiento posterior en Sketchfab.

2.3. Publicar Modelo 3D

Una vez obtenido el modelo 3D en formato FBX se publica este en la plataforma web Sketchfab, y se editan algunas de sus propiedades para orientar correctamente el modelo y transparentar las formas de hormigón para poder visualizar los armados.

Esta plataforma permite a cualquier usuario la visualización y manipulación del modelo 3D, realizando rotaciones y zoom para poder apreciar con todo detalle sus características.

El resultado de este proceso es la obtención de una colección de modelos 3D de elementos estructurales en la plataforma web Sketchfab que es lo que denominamos de esta ponencia biblioteca de modelos digitales [2,3].

Figura 2. *Vista de algunos de los modelos digitales en la plataforma web Skechfab*

2.4. Obtención de la simulación constructiva

La simulación del proceso constructivo del elemento estructural se realiza con Autodesk 3DS Max.

Esta aplicación permite importar el fichero FBX para obtener la geometría de la simulación. En esta aplicación se aplican texturas para una representación lo más realista posible, se define la escala de tiempos, y para una serie de fotogramas clave se establece la posición de cada componente del elemento estructural y la posición de la cámara.

El resultado final de este proceso es un video en formato AVI con la simulación de la construcción del elemento estructural.

2.5. Publicar simulación constructiva

Para que los videos con la simulación constructiva estén a disposición de los alumnos en cualquier momento, y siguiendo las recomendaciones del Servicio Central de Informática de la UMA para no colapsar los recursos del Campus Virtual, se comparten a través de la plataforma YouTube.

El resultado de este proceso es la obtención de una colección de videos de simulaciones constructivas de elementos estructurales en la plataforma YouTube, que es lo que denominamos en esta ponencia biblioteca de simulaciones constructivas [4].

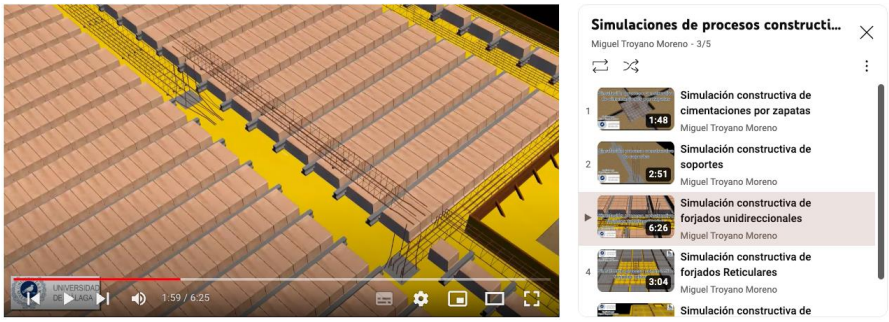

Figura 3. *Vista de la lista de distribución de YouTube con los videos de las simulaciones constructivas*

2.6. Documentar asignatura.

Los modelos digitales y los videos de las simulaciones constructivas pueden ser utilizados para documentar la asignatura a través de los links a las páginas donde se encuentran dichas herramientas. Además, ambas plataformas admiten la compartición mediante frame, lo que permite incrustar directamente esos modelos digitales y videos en otras plataformas web, como la plataforma de aprendizaje Moodle con la que se ha diseñado el Campus Virtual de la Universidad de Málaga.

3. CONCLUSIONES

El uso las aplicaciones Revit, Naviswork y 3DS Max de Autodesk, y las plataformas web Sketchfab y YouTube han permitido desarrollar una biblioteca de modelos digitales y simulaciones constructivas de los elementos estructurales más representativos de las estructuras de hormigón y cimentaciones, que permiten una mejora sustancial del proceso de enseñanza de estas materias. El procedimiento seguido puede aplicarse para otras materias de la ingeniería.

AGRADECIMIENTOS

Los autores expresan su agradecimiento a la Universidad de Málaga-Campus de Excelencia Internacional Andalucía Tech, por el soporte prestado en el desarrollo de este trabajo.

REFERENCIAS

[1] R. Sacks, et al. (2018) BIM Handbook: A Guide to Building Information Modeling for Owners, Designers, Engineers, Contractors, and Facility Ma-nagers, 3rd Edition, Wiley, Hoboken, NJ, USA.

[2] M. Troyano Moreno, Biblioteca de modelos digitales de elementos estructúrales, https://sketchfab.com/mtroyano/models (accessed September 6, 2023).

[3] J. Sánchez Berrocal, Biblioteca de modelos digitales de elementos estructúrales, https://sketchfab.com/JSBUMA/models (accessed September 9, 2023).

[4] M. Troyano Moreno, Simulaciones constructivas de elementos estructurales, https://www.youtube.com/playlist?list=PL4zeyXXRdoGHU49vd5KmkaDzkUqlzWY6Z (accessed September 6, 2023).

Meta-modelling for fast prediction of the effective elastic properties of cement mortar doped with CNT

Rodríguez Romero, Rubén[1]; Pachón, Pablo[2]; Aguilar, Jaime[2]; Baeza Álvarez, Juan Ramón[2]; Garduño, Carlos[2]; Sáez, Andrés[1]

ABSTRACT

This article presents an innovative metamodeling approach for predicting the effective elastic properties of cement grouts containing carbon nanotubes (CNTs), for the purpose of structural rehabilitation. The study addresses the homogenization of nano- and micro- scales through a representative volume element (RVE). The numerical model consists of a cement matrix doped with randomly oriented CNTs, yet the computational load associated with this model poses a significant processing limitation. To overcome this challenge, a metamodeling approach based on a Kriging surrogate model is proposed. This approach provides a fast and accurate alternative to bypass the time-consuming numerical homogenization process. The surrogate model establishes a connection between the microstructural characteristics of CNTs, cement, and the effective elastic properties of the composite grouts. The accuracy and efficiency of the proposed metamodel are demonstrated through detailed analyses.

Keywords: historical heritage preservation, masonry structures, structural rehabilitation, CNT-enriched cement, surrogate models.

1. INTRODUCCIÓN

Las construcciones de fábrica son vitales en el patrimonio arquitectónico europeo debido a su relevancia económica y social. Dada su importancia y su vulnerabilidad frente a amenazas como terremotos y el deterioro gradual de los materiales, la conservación anticipada se ha vuelto prioritaria en la agenda política de Europa. Esto ha motivado que se investiguen técnicas de rehabilitación estructural enfocadas en preservar los valores arquitectónicos mediante técnicas de mínima intervención [1]. La nanotecnología y la ciencia de materiales posibilitan crear materiales innovadores que permitan aplicar técnicas de rehabilitación menos invasiva. La investigación se enfoca en fortalecer estructuras de mampostería mediante morteros de inyección. El interés se debe a su potencial innovador para mejorar las propiedades mecánicas de la piedra [1].

El objetivo principal es utilizar CNTs en morteros de alto rendimiento para rehabilitar piedra porosa débil mediante inyecciones. Para lograr esto, se ha desarrollado un método que predice de manera rápida y precisa las propiedades elásticas de materiales compuestos utilizando modelos sustitutos. Se emplea homogeneización para analizar propiedades elásticas efectivas a través de modelos de

[1] *Departamento de Mecánica de Medios Continuos y Teoría de Estructuras. Universidad de Sevilla (ESPAÑA). rrodriguezr@us.es (Corresponding author)*

[2] *Departamento de Estructuras de Edificación e Ingeniería del Terreno. Universidad de Sevilla (ESPAÑA). ppachon@us.es, jav@us.es, jbaeza@us.es, cgarduno@us.es, andres@us.es*

elementos finitos en 3D. Debido a la carga computacional, se propone un modelo de Kriging universal para relacionar las propiedades de los CNTs y el cemento con las propiedades elásticas del mortero compuesto.

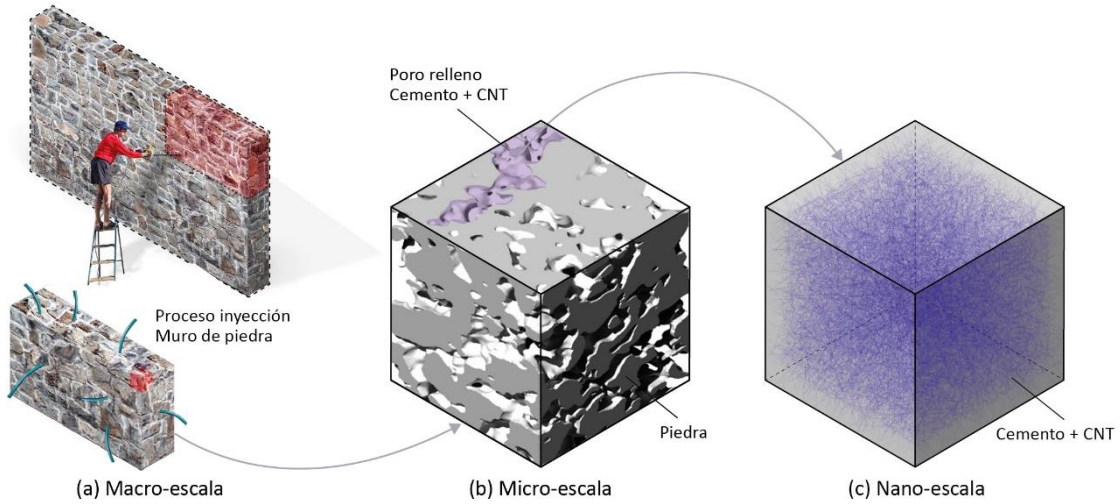

Figura 1. *Flowchart del metamodelado propuesto: (a) Macro-escala, (b) Micro-escala, tomografía de piedra porosa, y (c) Nano-escala CNT/cemento.*

2. MARCO TEÓRICO

La homogeneización mecánica numérica se emplea mediante un enfoque clásico, como es la condición de Hill-Mandel, para estimar las propiedades efectivas de materiales heterogéneos. El objetivo es aplicar un enfoque de modelado sub-escala basado en el concepto de RVE [2]. Modelamos matriz y CNTs con propiedades isotrópicas, simplificando (véase [3]). Para abordar la complejidad de modelar grandes volúmenes de CNTs al azar (relación de aspecto ≈ 1000), utilizamos un algoritmo RSA modificado [4]. Esto permite usar elementos de viga para las inclusiones tipo fibra, mientras que la matriz se modela con una malla regular no conforme.

Estimar propiedades efectivas a través de RVEs numéricos es computacionalmente intenso, limitando su aplicación para estructuras a gran escala. Se propone usar modelos sustitutos más livianos, entrenados mediante simulaciones FEM directas con un enfoque de Monte Carlo (MCS). La construcción de un modelo sustituto involucra: (a) muestreo del espacio de diseño y generación de una población de entrenamiento mediante simulaciones MCS; y (b) construcción de una superficie de predicción (Fig. 2).

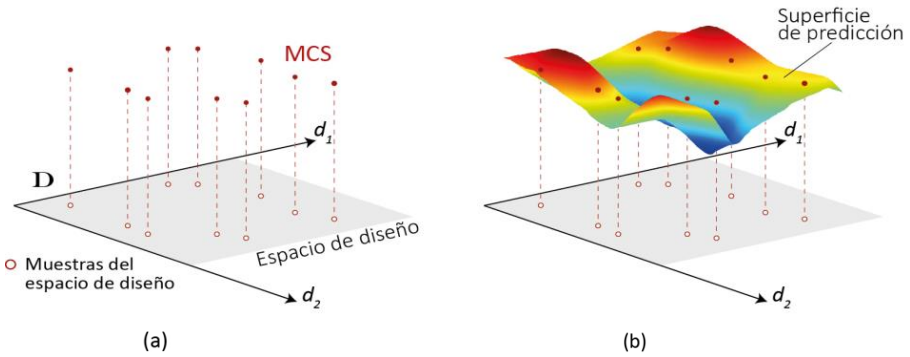

Figura 2. *La interpolación de Kriging unidimensional.*

La creación del modelo sustituto implica realizar análisis de convergencia de las propiedades elásticas efectivas para determinar tamaño y densidad de malla del RVE. En técnicas de homogeneización, estos aspectos se determinan estadísticamente. Los parámetros de material empleados para análisis posteriores se detallan en la Tabla 1, abarcando un rango común en inyecciones de lechada (módulo de elasticidad de 2 a 10 GPa y relaciones de Poisson de 0.05 a 0.3).

Tabla 1. Propiedades constitutivas de las fases consideradas para investigar materiales compuestos CNT/cemento

	Material	
	MWCNTs	**Mortero de cemento**
Módulo de Young	0.23-1.22 TPa[a]	2-10 GPa[c]
Coeficiente de Poisson [-]	0.1-0.28[b]	0.05-0.3[d]
Diámetro [nm]	1.8	-
Longitud [μm]	0.41	-
Fracción de volumen [%]	0.01-1.2	-
Porosidad [%]	-	-

Fuentes: [a][5]; [b][6]; [c][7]; [d][7]

3. ANÁLISIS DE VALIDACIÓN

La precisión del RVE se analiza comparando las predicciones de homogeneización computacional con el método clásico de Eshelby-Mori-Tanaka (MT) y datos experimentales de un compuesto de policarbonato (PC) reforzado con nanotubos de carbono de pared única (SWCNT) ($Lcnt$ = 1.3 μm, $Dcnt$ = 1.8 nm) reportado por Talò y coautores [8].

4. MODELADO SUSTITUTO

El modelo sustituto considera cinco variables de entrada: fracción de volumen de CNT, módulo elástico y Poisson de CNT, y módulo elástico y coeficiente de Poisson de la matriz de cemento. Los rangos se basan en la Tabla 1. La precisión de un modelo sustituto depende en gran medida de la calidad de los datos de entrada, que deben estar uniformemente distribuidos en todo el dominio de interés. En este estudio, se emplea el muestreo de hipercubo latino para lograr esta distribución uniforme. Se realizan análisis de convergencia con poblaciones de entrenamiento de 32 a 512 individuos y un conjunto de validación de 1024 muestras. La convergencia se alcanza para poblaciones de 128 individuos, con RMSE cercano a cero y coeficientes R2 cercanos a uno, asegurando la precisión del modelo sustituto. La Fig. 3 muestra la comparación entre las predicciones del RVE directo y el modelo sustituto resultante, se observa como resultado una fuerte evidencia de que el modelo sustituto está entrenados con alta precisión.

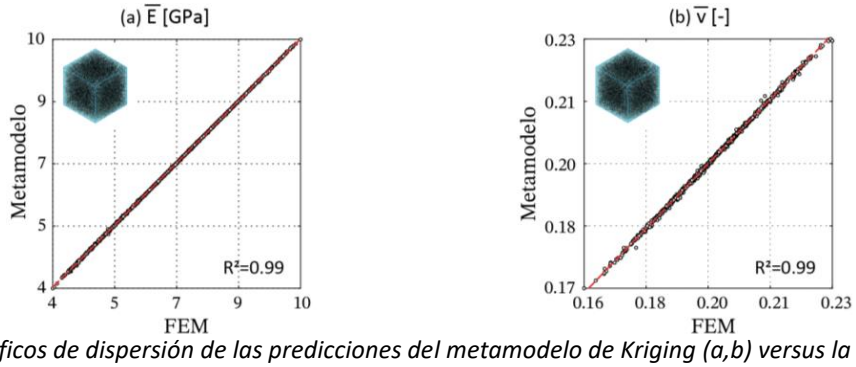

Figura 3. *Gráficos de dispersión de las predicciones del metamodelo de Kriging (a,b) versus la evaluación de los RVE FEM para los VS de 1024 muestras.*

El meta-modelo también presenta una carga computacional baja, con tiempos promedio de evaluación de 0.18 segundos. Estos reducidos tiempos de evaluación hacen que los meta-modelos sean una solución eficiente para realizar análisis paramétricos intensivos, optimización iterativa, así como el análisis de elementos estructurales a gran escala.

5. CONCLUSIONES

En este trabajo se ha presentado un enfoque de meta-modelado para la predicción rápida de las propiedades elásticas efectivas de lechadas de CNT/cemento. La metodología desarrollada utiliza meta-modelos Kriging para evitar la homogeneización numérica del compuesto. El meta-modelo se entrena de manera no intrusiva a través de simulaciones directas de Monte Carlo de la homogeneización numérica de los RVE. El meta-modelo, considera como variables independientes la fracción de volumen de CNT, así como los módulos de Young y los coeficientes de Poisson de la matriz y los CNT (5 variables). La dimensión y densidad de malla de los RVE, así como los tamaños de las poblaciones de entrenamiento para los modelos sustitutos, se seleccionan a través de análisis de convergencia y estadísticos. El meta-modelo demostró una alta precisión y una demanda computacional muy baja, con tiempos de evaluación de 0.18 segundos. Para mejoras futuras, se debe considerar características microestructurales como la ondulación y aglomeración de los CNTs además de analizar la permeabilidad de las inyecciones en la piedra. También sugerimos explorar el meta-modelado jerárquico para una predicción aún más rápida de propiedades elásticas efectivas de la piedra inyectada.

6. REFERENCIAS

[1] Comisión Europea, Dirección General de Deporte para Educación, Juventud y Cultura. Marco europeo de acción para el patrimonio cultural.

[2] Buda, A., Gori, V., de Place Hansen, E. J., Polo López, C. S., Marincioni, V., Giancola, E., Vernimme, N., Egusquiza, A., Haas, F., & Herrera-Avellanosa, D. (2022). Existing tools enabling the implementation of EN 16883:2017 Standard to integrate conservation-compatible retrofit solutions in historic buildings. *Journal of Cultural Heritage, 57, 34–52.*

[3] Ostoja-Starzewski, M. (2002). Microstructural randomness versus representative volume element in thermomechanics. *Journal of Applied Mechanics, 69(1), 25–35.*

[4] Georgantzinos, S. K., Antoniou, P., Markolefas, S., & Giannopoulos, G. Finite element predictions on vibrations of laminated composite plates incorporating the random orientation, agglomeration, and waviness of carbon nanotubes. (2022). *Acta Mechanica, 233 (5), 2031-2059.*

[5] Iorga, L., Pan, Y., & Pelegri, A. (2008). Numerical characterization of material elastic properties for random fiber composites. *Journal of Mechanics of Materials and Structures, 3(7), 1279-1298.*

[6] El Moumen, A., Tarfaoui, M., & Lafdi, K. (2018). Computational homogenization of mechanical properties for laminate composites reinforced with thin film made of carbon nanotubes. *Applied Composite Materials, 25, 569-588.*

[7] Zhao, P., & Shi, G. (2011). Study of Poisson ratios of single-walled carbon nanotubes based on an improved molecular structural mechanics model. *Computers Materials and Continua, 22(2), 147.*

[8] Talò M., Krause B., Pionteck J., Lanzara G., Lacarbonara W. (2017). An updated micromechanical model based on morphological characterization of carbon nanotube nanocomposites. *Composites B, 115, 70-78.*

Mobile phone-based structural dynamic analysis for teaching experimental testing

Daniel Sánchez-Muñoz[1]; José M. Soria[2]; Iván M. Díaz[2]; Jaime H. García-Palacios[3]

ABSTRACT

The paper shows the potential of mobile phones as versatile and cost-effective educational tools to acquire structural dynamic data, and to be used for teaching/learning experimental dynamics. As an example, dynamic measurements are performed on a two-storey laboratory-scale building model. To record its structural response (acceleration responses and spectra), the "MATLAB Mobile" application is used with the mobile's triaxial MEMS accelerometer. At high sampling frequencies, the sensor shows non-uniform time steps, requiring post-processing corrections. MATLAB Drive (cloud storage) and MATLAB Online (online service for MATLAB allowing the execution of Live Scripts without local installation) are used for this purpose. In addition, to explore the accuracy of different mobile applications in recording accelerations and to determine the influence of the type of mobile device, other mobile applications are evaluated.

Keywords: MATLAB Mobile, educational innovation, structural dynamics, experimental testing.

1. INTRODUCTION

The paper arises from a teaching project of ETSI Caminos of Technical University of Madrid. The aim is to develop affordable tools for master level students of Experimental Analysis of Structures and Dynamic and Seismic Analysis of Structures, following the steps of other related projects [1],[2]. Considering that standard accelerometers are expensive, smart mobile phones offer hands-on training for all students in an affordable way, even at home. Versatile, portable, popular and equipped with multiple MEMS sensors (MicroElectroMechanical Systems, increasingly present in the field of Structural Health Monitoring [3]), mobile phones allow quick and easy data acquisition in real-time, with storage capacities. Therefore, they can be used to collect data in structural models or lively structures and, through the appropriate post-processing, to obtain the results to be interpreted by the students.

The paper continues by comparing several available mobile applications. A description of the model used and the experimental dynamic tests carried out are shown in Section 3. Section 4 presents the results. Finally, some conclusions are given in Section 5.

[1] *E.T.S.I. Caminos, Canales y Puertos - UPM (SPAIN). daniel.smunoz@alumnos.upm.es (Corresponding author).*
[2] *Department of Mechanics of Continuous Media and Theory of Structures. E.T.S.I. Caminos, Canales y Puertos – UPM (SPAIN). jm.soria@upm.es. ivan.munoz@upm.es.*
[3] *Department of Civil Engineering: Hydraulics, Energy and Environment. E.T.S.I. Caminos, Canales y Puertos - UPM (SPAIN). jaime.garcia.palacios@upm.es*

2. COMPARISON OF MOBILE APPLICATIONS

Five mobile phone applications have been used for data acquisition: MATLAB Mobile (1), Myshake (2), Phyphox (3), Physics Toolbox Suite (4) and Sensor Sense (5).

Only MATLAB Mobile presents the option of modifying the sampling frequency (0 - 100 Hz), the other applications have a default sampling frequency (approximately 12 Hz in (2), 200 Hz in (3), 400 Hz in (4) and 5 Hz in (5)). Therefore, given the impossibility of making a comparison under the same frequency conditions, MATLAB Mobile has been chosen because of its wide range of MATLAB products (such as MATLAB Drive and MATLAB Online) that facilitate data acquisition and processing.

3. LABORATORY MODEL AND DYNAMIC EXPERIMENTAL TEST

The experimental dynamic analysis was carried out on a two-storey laboratory model as shown in Figure 1, where the accelerations of the model were measured using a mobile phone. Furthermore, an additional concentrated mass in the form of a weight disc was used to analyse the new behaviour.

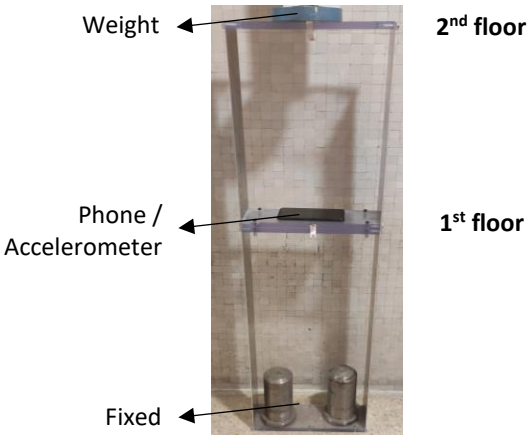

Fig. 1. *Model of a two-storey building and elements used.*

The two vibration modes were intentionally excited:

- First mode: a displacement was applied to the 2nd floor.
- Second mode: a displacement was applied to the 2nd floor and the same, but opposite, displacement to the 1st floor.

To analyse these two cases, the position of the mobile (M) and the weight (W) were varied equally in both cases, as shown in Table 1.

Table 1. Combinations of mobile (M) and weight (W) studied.

Case	Without weight		With weight			
Combination	1	2	3	4	5	6
2nd floor	M		M		M , W	W
1st floor		M	W	M , W		M

MATLAB Mobile was used to collect the data, which are stored in the cloud with MATLAB Drive and processed using MATLAB code. In addition, it is possible to run this code without downloading the program using a MATLAB Online Live Script.

4. RESULTS

The results obtained comprise the accelerations of the structure after the excitation and the frequency spectra to derive the natural frequencies. Measurements are taken at a sampling frequency of 100 Hz. An example, corresponding to the case without the weight and with the mobile on the 2nd floor, is shown in Figure 2.

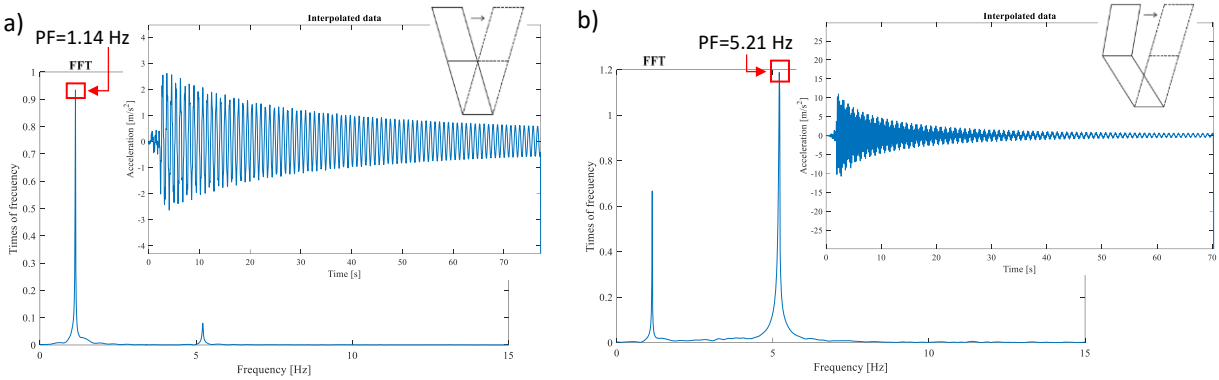

Fig. 2. *Frequency spectra with their maximum (Peak Frequency) and accelerations in the scenario without weight and mobile on the 2nd floor, corresponding to: a) first mode, showing only one type of deformation; b) second mode, showing over time the deformation of the first mode.*

By adding the weight, it can be seen (as illustrated in Table 2) that the frequency is lower since, keeping the stiffness (K) constant, the mass (M) increases.

Table 2. Values of the frequencies in each case and the variation they undergo when a weight is placed.

	Without weight		
	Combination	1	2
1st mode	**Frecuency (Hz)**	1.139	1.141
2nd mode	**Frecuency (Hz)**	5.206	5.178

	With weight				
	Combination	3	4	5	6
	Variation from combination	1	2	1	2
1st mode	**Frecuency (Hz)**	0.860	0.864	0.834	0.833
	Variation (%)	-24.5	-24.3	-26.8	-27.0
2nd mode	**Frecuency (Hz)**	4.265	4.393	4.502	4.339
	Variation (%)	-18.1	-15.2	-13.5	-16.2

In addition, the variation of the frecuency spectrum after reducing the sampling frequency to 10 Hz has been studied. The maximum recordable frequency (Nyquist frequency) is half the sampling frequency; therefore, it would be unable to accurately record frecuency values above 10/2 Hz and consequently to perceive the second mode in the frecuency spectrum.

Additionally, after performing the acceleration measurements, it can be observed in the data processing that the measured time interval is not homogeneous. This phenomenon has been corrected with a spline interpolation.

5. CONCLUSIONS

As it can be seen, mobile phones can be used as a teaching tool in experimental dynamics, since:

- They allow to acquire real measurements easily.
- Although they are less accurate than standard accelerometers, their sensitivity and precision are sufficient for teaching purposes and analysing lively structures.
- Practice-based learning (suitably combined with theoretical matters) can be carried out with the student allowing a self-learning approach.
- Important and difficult-to-understand aspects of experimental dynamics can be learnt easily.

In this way, students can learn basic concepts of dynamics:

- Behaviour in response to variations in the mass or stiffness of the structure.
- Visualisation of vibration modes and interpretation of frequency spectra.
- The importance of the Nyquist frequency and the coding data processing.
- The importance of a constant time step, among other aspects of experimental dynamics.

The next step is to study synchronisation matters between several mobile phones in order to obtain the mode shapes [4].

ACKNOWLEDGEMENTS

The authors would like to thank the Technical University of Madrid for the financial support that made this innovative education project “Structural monitoring: multidisciplinary and new challenges for future professionals in the sector” (in ETSICCP with code IE23.0406) possible.

REFERENCES

[1] Muñoz Díaz, I., García Palacios, J., Soria Herrera, J.M., de la Concha Renedo, C.M. (January-April 2019). A Mobile Tool for Teaching Advanced Dynamic Analysis. *ABE/IEE, Vol. 3 Nº3, 72-82*.

[2] A García Palacios, J., Muñoz Díaz, I., Mosquera Feijoo, J.C., Soria Herrera, J.M., Tirado Andrés, F. (June 2018). Learning Dynamic Analysis of Structures Using Handy and Affordable Equipment on the Way of Smart Structures. In IV International Conference on Structural Engineering Education, Structural Engineering Education Without Borders (p.p. 1-6). Madrid.

[3] Komarizadehasl, S., Turmo Coderque, J., Lozano Galant, J.A. (October 2022). Operational and Analytical Modal Analysis of a Bridge Using Low-Cost Wireless Arduino-Based Accelerometers (published by Universitat Politècnica de Catalunya). Barcelona: Universitat Politècnica de Catalunya.

[4] Martinelli, L., Valdivieso, D. (August 2029). Synchronization Issues in Data Acquisition on Android Phones for Acceleration Recordings. EVACES 2023 (p.p. 305-313). Milan: Springer.

Model for considering soil-structure interaction and its implementation in the optimal design of RC frame structures

Negrin, Iván[1]; Kripka, Moacir[2]; Yepes, Víctor[1]

ABSTRACT

This paper proposes a methodology to simulate the soil-structure interaction (SSI) in structural optimization processes. The aim is to create a scenario more aligned with reality, which is not reflected in the traditional methods of considering perfectly rigid or articulated supports. A Winkler-type model is proposed where a hyperbolic equation that relates the pressure p with the settlement S is used to calculate the stiffness coefficient k. This coefficient simulates the interaction that causes additional deformation of the superstructure during the loading process, increasing internal forces. Several reinforced concrete frame structures with traditional rigid supports and the proposed SSI model are optimized to demonstrate the influence of this phenomenon. The results show that using traditional supports, as is commonly done, leads to inefficient superstructure design. Therefore, the proposed methodology is conducive to creating more realistic models that allow for more efficient and durable sustainable designs.

Keywords: soil-structure interaction; reinforced concrete; frame structure; optimization; Winkler model.

1. INTRODUCTION

One of the most debated aspects today by structural engineers is the need to minimize construction costs, material consumption, and the environmental footprint of the construction industry. This can be achieved through a more efficient use of building materials due to design optimization [1].

Reinforced concrete (RC) frame building structures are essential to the construction sector, so their environmental impact is quite significant. Although many studies have been carried out on how to improve the sustainability indexes of this type of structure, there are still some drawbacks. The first is the limited consideration of case studies. Most of them are simple elements or plane structures. Few authors have optimized the design of 3D RC frame structures with a realistic approach [2]. Besides, the few studies performed on more complex systems have the weakness of the supports considered. Authors usually assume structures with idealized supports (e.g., fixed), even when the soil and foundation assembly is not perfectly rigid. Support displacements (settlements) exist and influence the superstructure behavior, which is not the case with classical supports. This idealization leads to an inefficient design of the superstructure. Therefore, it will suffer accelerated deterioration with the

[1] *Institute of Concrete Science and Technology (ICITECH). Universitat Politècnica de València (46022 Valencia, Spain). ianegdia@doctor.upv.es (Corresponding author). vyepesp@cst.upv.es.*
[2] *Graduate Program in Civil and Environmental Engineering, University of Passo Fundo (Km 292, BR 285, Passo Fundo 99052-900, RS, Brazil). mkripka@upf.br*

consequent need for additional maintenance during its life cycle. It makes the design optimization lose all its validity [3].

This study proposes a model to consider the soil-structure interaction (SSI), mainly focused on its use in structural optimization of 3D RC frame building structures. The optimization objective is to minimize CO_2 emissions. The SSI model has a Winkler-type approach, in which a hyperbolic equation that relates the pressure *p* to the settlement *S* is used to calculate the stiffness coefficient *k*. The use of this type of equation to model soil stiffness has been validated by several authors on different types of soils [4]. Therefore, the results aim to compare optimized designs of structures (1) with classical supports and (2) considering the SSI using the proposed model.

2. METHODOLOGY

Fig. 1a shows the three case studies used. In case 2, the length of the spans is increased to 8 and 6 m (direction of the "x" and "y" axis, respectively), and case 3 is similar in plan to case 1, but with an additional level.

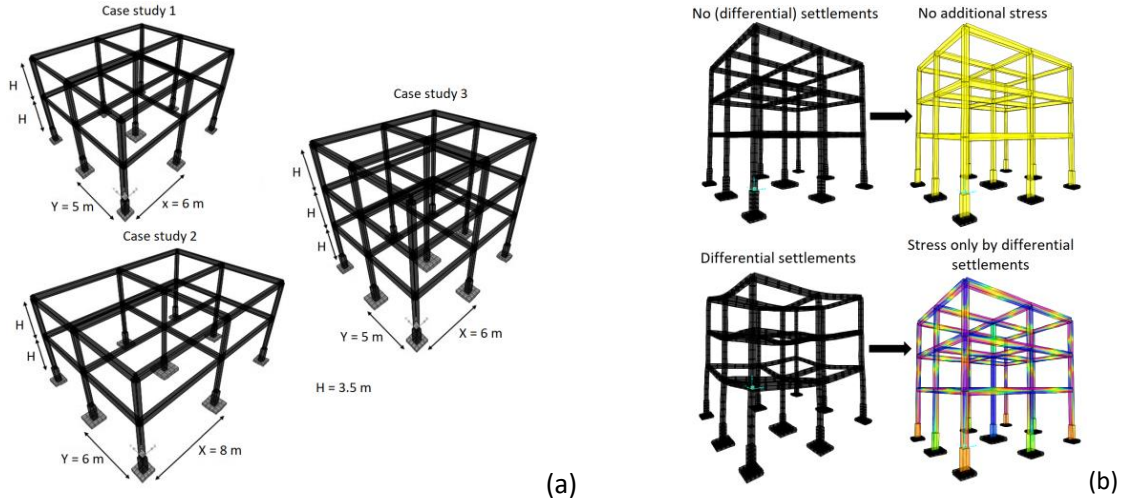

Figure 1. *Some aspects of the methodology: (a) three case studies, and (b) representation of the additional stress produced by differential settlements.*

When considering soil-structure interaction, the soil beneath the foundations is considered to deform during the loading-unloading process. Presumably, these settlements are not equal in all supports since, even if the soil is the same (as in this study), the forces reaching each group of foundations are different. These differential settlements, even in the permissible range, cause the superstructure to deform and additional stresses to appear (see Fig. 1b). This phenomenon does not occur in models with rigid supports.

$$k = \tan\alpha = \frac{p}{S} = \frac{q^{*}_{br\_II} - p}{\bar{S} \cdot \left[\left(\frac{q^{*}_{br\_II}}{R'^{*}} \right) - 1 \right]} \quad (1)$$

Eq. 1, proposed by [5], is used to obtain the soil stiffness coefficient *k*. Here, *p* and *S* are the foundation's acting pressure and settlement respectively. $\bar{S}$ is the base settlement for an acting pressure equal to the soil base linearity limit stress *R'**, and $q^{*}_{br\_II}$ is the base bearing capacity pressure

based on expressions from the theory of plasticity. This coefficient *k* is applied to the nodes formed by discretizing the foundation base.

Another point highlighted in the study is how different soil types behave and how it is reflected in the proposed model. For this purpose, two different soil types are considered, one predominantly cohesive (FI = 8º, C = 60 kPa, E = 12 MPa, $\gamma = 19$ kN/m³, $\mu = 0.40$) and one predominantly frictional (FI = 32º, C = 10 kPa, E = 15 MPa, $\gamma = 17.5$ kN/m³, $\mu = 0.30$). The hypothesis is that, although cohesive soils are more deformable than frictional, differential settlements are more significant in the latter. It is because the behavior is generally nonlinear in this type of soil, while in the former, it is usually linear [1].

The algorithm considering the SSI in the optimization process starts with a model with classical supports. After performing the analysis of this model, a pre-design of the foundations is made, and the stiffness coefficient *k* is calculated for each foundation. Both the foundations and the springs of stiffness *k* are included in the initial model. Lastly, the ultimate design is made with the internal forces of this model with SSI, and the final outputs of the structure are calculated (CO_2 emissions in this case).

The optimization problem is formulated with 16 discrete variables that regulate the dimensions of the cross sections of the frame elements, the foundations base's rectangularity, and the concrete's quality in the three groups of structural elements (beams, columns, and foundations). The objective is to minimize the CO_2 emissions produced both by the manufacture of building materials and by construction activities on site. The constraints ensure that the designs meet the requirements of the structural codes. The Biogeography-Based Optimization (BBO) [6] heuristic is used as the optimization algorithm. For more information on the methodology in general, refer to [1 ,2, 3].

3. RESULTS AND DISCUSSION

The fundamental hypothesis of the study is that the superstructure of models that consider SSI is more stressed than models with classical supports. A direct way to verify this approach is by optimizing the design of each model and comparing the outputs. Fig. 2 shows that optimized designs of models with SSI lead to more emissions than traditional models (no SSI). It does not mean that not considering the interaction is more beneficial, but quite the opposite. Structures with rigid supports require less material in the superstructure since they are less stressed. However, the supports are not rigid, and differential settlements exist in practice. Therefore, by optimizing the design of a structure with idealized supports, a considerable percentage less construction material is used than is actually needed (see differences in percentages in Fig. 2 at the top of the bar charts).

The columns are the elements that change the most from one model to another (red arrows in Fig. 2). It is because the increase in bending resulting from differential settlements affects columns more than beams since the latter are more prepared to resist bending stresses. On the contrary, columns work mainly under axial load, so the increase in bending affects their design more. Another point is that frictional soils are more prone to differential settlements. The graph also shows the differences between the models with SSI and those with classic supports (*). The most significant differences are for case study 3. It obeys that the axial load reaching the foundations is higher by having an additional level. Therefore, the phenomenon of differential settlement becomes more acute.

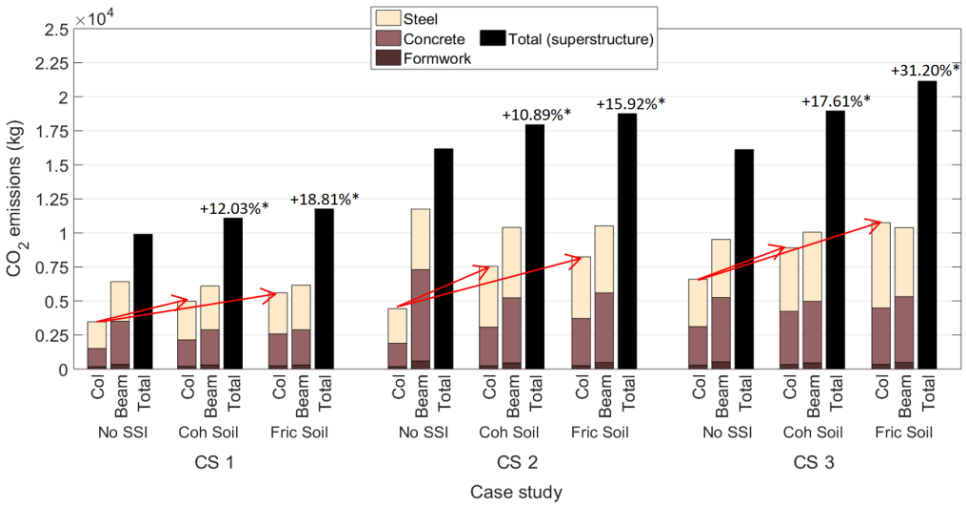

Figure 2. *Emissions for each optimal solution broken down by columns, beams and total of the superstructure. * Compared to models with idealized supports (No SSI)*

4. CONCLUSIONS

This study proposes a model for considering soil-structure interaction in optimizing reinforced concrete frame buildings. The results indicate that the common practice of assigning idealized supports provides inefficient designs. Therefore, the proposed methodology is highly beneficial for obtaining durable and sustainable structures.

ACKNOWLEDGEMENTS

This work was supported by the grant PID2020-117056RB-I00, which was funded by MCIN/AEI/10.13039/501100011033 and by "ERDF A way of making Europe". Grant PRE2021-097197 funded by MCIN/AEI/10.13039/501100011033 and by FSE+.

REFERENCES

[1] Negrin, I., Kripka, M., & Yepes, V. (2023). Metamodel-assisted meta-heuristic design optimization of reinforced concrete frame structures considering soil-structure interaction. *Engineering Structures, 293, 116657*.

[2] Negrin, I., & Chagoyén, E. (2022). Economic and environmental design optimisation of reinforced concrete frame buildings: A comparative study. *Structures, 38, 64-75*.

[3] Negrin, I., Roose, D., Chagoyén, E., & Lombaert, G. (2021). Biogeography-Based Optimization of RC structures including static soil structure interaction. *Structural Engineering and Mechanics, 80(3), 285-300*.

[4] Bao, T., & Lui, Z. (2019). Evaluation of Winkler Model and Pasternak Model for Dynamic Soil-Structure Interaction Analysis of Structures Partially Embedded in Soils. *International Journal of Geomechanics, Vol. 20, No. 2*.

[5] Klepikov, S.N., Tregub, A.S., & Matveev, I.V. (1987). Calculation of buildings and works on collapsible soils. Kiev: Budivielnik.

[6] Simon, D. (2008). Biogeography-Based Optimization. *IEEE Transactions on evolutionary computation, 12(6), 702-13*.

Model selection techniques for supervised damage identification using deterministic finite element model updating

Hernández-González, Israel Alejandro[1]; García-Macías, Enrique[1]

ABSTRACT

The widespread deployment of Structural Health Monitoring systems globally has advanced unsupervised damage assessment methods. These techniques utilize monitoring data to detect damage, primarily focusing on identifying whether a structure is damaged or undamaged (Level I). However, determining the location and severity of damage (Levels II and III) remains challenging. Achieving higher identification levels often requires a theoretical model of the asset being monitored. Selecting appropriate model parameters is not straightforward, and classical sensitivity-based approaches may overlook potential failure mechanisms. To address this, the paper introduces a model selection method that entails constructing various numerical models to represent potential failure mechanisms within the structure. The particle swarm global optimization algorithm is employed to calibrate these models simultaneously. Bayesian Information Criterion is used to compare the models' fits with experimental data, enabling the selection of the most likely model. Consequently, this approach enables comprehensive damage identification, including identifying failure mechanisms, localization, and quantification.

Keywords: Bayesian Criterion Information, Model Selection, Model Updating, Operational Modal Analysis, Supervised Damage Identification.

1. MODEL UPDATING

Finite element model updating refers to the process of calibrating certain model parameters x_i, $i = 1,\dots,m$, (organized in a vector of parameters $\boldsymbol{x} = [x_1, x_2, \dots, x_m]^{\mathrm{T}}$) with the aim of minimizing the mistach between experimental and the theoretical predictions. Note that numerical models of large-scale structures generally contain a significant amount of uncertainty stemming from different assumptions, like idealization and discretization. To minimize such uncertainties, it is necessary to define the objective function $J(\boldsymbol{x})$, which explains the relative differences between experimentally determined vibrational modes and their theoretical counterparts [1]:

$$J(\boldsymbol{x}) = \sum_{i=1}^{l} [\alpha \varepsilon_i(\boldsymbol{x}) + \beta \delta_i(\boldsymbol{x})] + \eta \sum_{i=1}^{m} (1 - x_i)^2, \tag{1}$$

with

[1] *Department of Structural Mechanics and Hydraulic Engineering. University of Granada (SPAIN). israela42@correo.ugr.es (Corresponding author), enriquegm@ugr.es*

$$\varepsilon_i(\boldsymbol{x}) = \frac{\left|f_{exp}^i - f_{model}^i\right|}{f_{exp}^i}, \qquad \delta_i(\boldsymbol{x}) = 1 - MAC_i(\boldsymbol{x}), \tag{2}$$

where α, β and η denote weighting coefficients. The terms f_{exp}^i and f_{model}^i denote the i-th experimental and numerical resonant frequency, respectively. Finally, the term MAC_i stands for the Modal Assurance Criterion (MAC) value between the i-th experimental and numerical mode shapes, respectively. On this basis, the procedure is given by the following constrained non-linear minimization problem where $\overline{\boldsymbol{x}} = \mathrm{argmin}_{\boldsymbol{x}\in D}\, \boldsymbol{J}(\boldsymbol{x})$.

2. MODEL SELECTION BY BAYESIAN INFORMATION CRITERION

The optimization problem outlined above is critically determined by the fitting parameters in $\boldsymbol{x}$. Nonetheless, the selection of these parameters represents a formidable problem. There is not a general procedure for making such a selection, and this should be conducted considering the potential failure mechanisms the structure may experience. There is therefore no general model that can reproduce all the different pathologies a structure may present, but instead specific models should be created for specific failure mechanisms. On this basis, a proper model selection approach needs to be adopted to identify the most plausible model class. In this paper, the use of Bayesian Information Criterion (BIC) is proposed as a simple but effective approach, allowing to compare and select models by simultaneously testing several specific hypotheses [2]. Under the assumption that the model errors are independent and identically distributed according to a normal distribution, the BIC for the i-th model class can be expressed as:

$$\boldsymbol{BIC_i} = n\ln\left(\frac{RSS}{n}\right) + m\ln(n), \text{with RSS} = \sum_{i-1}^{n}(y_i - \hat{y}_i)^2, \tag{3}$$

where $\hat{L}_i$ is the maximized value of the likelihood function of the model MC_i, i.e. $\hat{L} = p(y \mid \hat{\boldsymbol{x}}, MC_i)$, $\hat{\boldsymbol{x}}$ are the parameter values that maximize the likelihood function, y is the observed data (resonant frequencies and mode shapes) and n is the number of observations.

3. CASE STUDY: TRUSS STRUCTURE

The investigated 31-bar planar truss structure (Fig. 1) is a benchmark case study for model updating and optimization investigations utilized by several researchers in the literature (e.g. [3], [4]). The FE of the structure is defined using planar 2-nodes truss elements implemented in Python. The mass density and the modulus of elasticity of the material are defined as 2770 kg/m^3 and 70 GPa, respectively. All the elements of the structure are defined with a cross-section area of 4.83 cm^2.

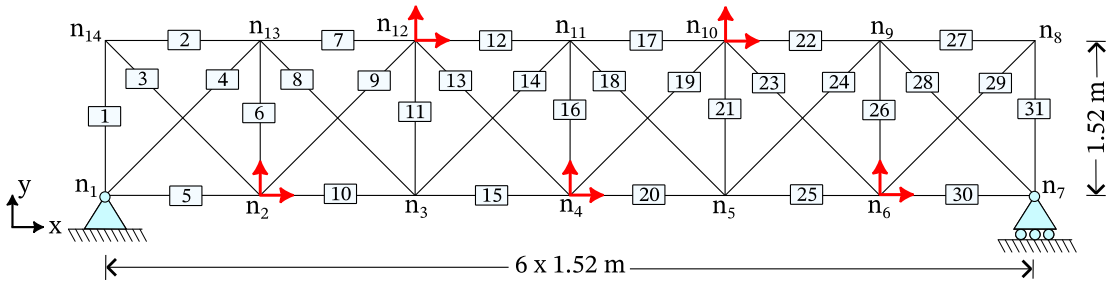

Figure 1. *Case Study: Truss structure with a total of 28 degrees of freedom.*

To discretize the mode shapes, five sensors monitoring "x" and "y" directions are defined at nodes n_2, n_4, n_6, n_{10}, and n_{12} as indicated with red arrows in Fig. 1. The first eight frequencies and mode shapes are considered in the subsequent analyses. To evaluate the robustness of the proposed approach to the presence of noise in the measurements, the modal displacements ϕ_{ij} are contaminated with a random zero-mean normally distributed with standard deviation $\sigma = 0.01$, 0.05 and 0.01. To assess the effectiveness of the proposed model selection approach, four classes of competitive models have been defined as reported in Fig. 2. Specifically, the fitting parameters of the model classes are defined as stiffness multipliers k_i of the bars highlighted in blue. Note that the defined classes represent nested models, in which a subset of the parameters are always contained in the previous class following Occam's razor principle [5]. In the FE model calibration in Eq. (1), the range of variation of the stiffness multipliers k_i is set to [0.7, 1.1], and the weighting factors α, β and η have been set to 1, 1 and 2, respectively, after manual tuning.

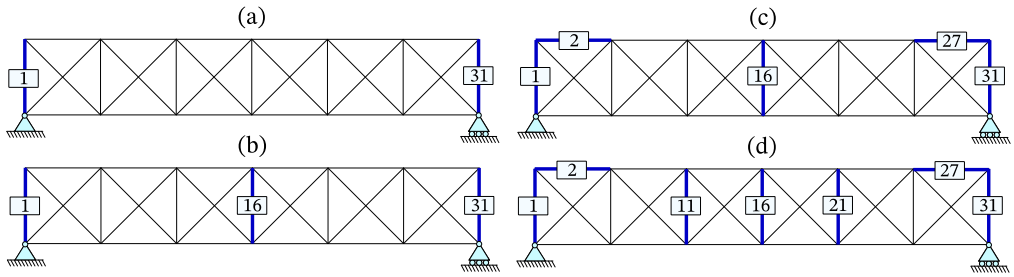

Figure 2. *Model classes MC_1 through MC_4 correspond to (a) through (d) for Case Study: Truss structure.*

A dense set of synthetic experimental data has been generated to assess the effectiveness of the proposed approach. To do so, in every iteration, one of the four model classes is randomly selected, affecting the corresponding bars with reductions uniformly distributed in the range of 0 to 20% ($k_i \in [0.8,1.0]$). On this basis, the proposed model selection approach is applied to all the simulated tests, extracting in every analysis the most plausible model explaining the simulated scenarios. Then, to determine whether the calibration indicates the appearance of damage, a simple two-class damage classification model (damaged or non-damaged) is proposed. Considering that the healthy condition of the truss structure is represented by the configuration of all the multipliers equal 1, the classification model considers the structure to be damaged if any of the bars experiences a reduction in stiffness larger than a certain threshold d. Finally, the effectiveness of the damage identification is assessed in terms of receiver operating characteristic curves (ROC) as shown in Fig. 3. Note in most cases, the ROC curves are way above the diagonal line dividing the ROC space (non-discrimination line), which highlights the accuracy of the proposed model selection approach. For all the studied noise levels, it can be observed that the classification results consistently improve as the number of

parameters decreases. This is ascribed to the circumstance that the BIC penalizes the complexity of the model, which becomes dominant over the prediction error.

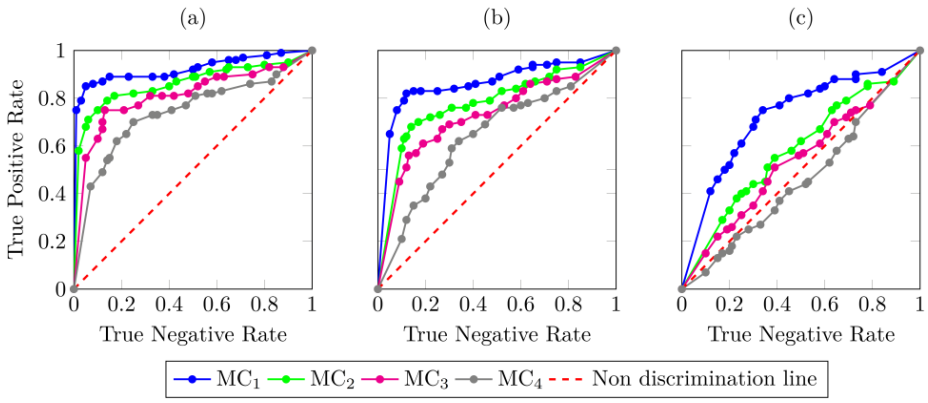

Figure 3. *ROC Curves: Noise Level 1 (a), Noise Level 2 (b) and Noise Level 3 (c) for Case Study: Truss structure.*

4. CONCLUSIONS

In this study, a novel supervised damage identification approach has been introduced. It simultaneously calibrates several models that replicate various damage scenarios. Subsequently, a straightforward model selection method, which analyzes the BIC values from the calibrations, is employed to identify the most plausible model that explains the observed damage condition. The presented numerical results and discussion have evidenced that potential of the proposed methodology for conducting full damage identification (detection of damage pathology, localization, and quantification).

ACKNOWLEDGEMENTS

This work has been supported by the Spanish Ministry of Science and Innovation through the research project ''BRIDGEXT - Life-extension of ageing bridges: Towards a long-term sustainable Structural Health Monitoring'' (Ref. PID2020-116644RB-I00).

REFERENCES

[1] E. García-Macías, I. A. Hernández-González, E. Puertas, R. Gallego, R. Castro-Triguero, and F. Ubertini. (2022). “Meta-Model Assisted Continuous Vibration-Based Damage Identification of a Historical Rammed Earth Tower in the Alhambra Complex,” *International Journal of Architectural Heritage*, pp. 1–27.

[2] M. J. Bayarri, J. O. Berger, W. Jang, S. Ray, L. R. Pericchi, and I. Visser. (2019). “Prior-based Bayesian information criterion,” *Stat Theory Relat Fields*, vol. 3, no. 1, pp. 2–13.

[3] M. Nobahari and S. M. Seyedpoor. (2013). “An efficient method for structural damage localization based on the concepts of flexibility matrix and strain energy of a structure,” *Structural Engineering and Mechanics*, vol. 46, no. 2, pp. 231–244.

[4] S. Seyedpoor. (2012). “A two stage method for structural damage detection using a modal strain energy-based index and particle swarm optimization,” *Int J Non Linear Mech*, vol. 47, no. 1, pp. 1–8.

[5] C. Mari and E. Mari. (2023). “Occam’s razor, machine learning and stochastic modeling of complex systems: the case of the Italian energy market,” *Qual Quant*, pp. 1–19.

Modeling of clay domes made by 3D printing

Pedraza Rodríguez, Consolación[1]; Vergara Bello, Francisca[2] ; Muñoz González, Carmen María[2], Martín Romero, José Alberto[1]

ABSTRACT

Additive manufacturing, widely used in the industry, has also gained great popularity in construction, presenting the same advantages: the material can be reduced with the use of different patterns without leaving waste. Therefore, construction using 3D printing can be considered a sustainable construction, furthermore, in this case, because of the use of a clearly ecological material such as clay. In fact, this work arises from the idea of building a university recreational complex starting from the earth towards the earth. This excavation process rises forming the dome, this having been chosen for aesthetics and because this shape is very suitable for 3D printing. For the structural analysis of the dome, a previous topological optimization study is carried out. To get the different densities the deposition trajectory is modified and the mechanical properties are determined by a homogenization process released by finite elements.

Keywords: Topologic Optimization, homogenization, 3D printing, earth construction

1. INTRODUCCIÓN

La fabricación aditiva es una tecnología ampliamente aplicada en la industria, se adapta fácilmente a las necesidades de diseño y no genera residuos. Esta técnica también se aplica en el ámbito de la construcción [1]. La impresión 3D permite una gran adaptación al diseño, favoreciendo el desarrollo de complejos patrones. En este campo se utiliza, sobre todo hormigón, aunque, como en el presente trabajo, se pueden utilizar otros materiales, en concreto la arcilla. La construcción con tierra surge en los primeros asentamientos permanentes con el desarrollo de la agricultura y la ganadería, lo que facilitó la aparición de las primeras poblaciones y ha resurgido durante las primeras décadas del siglo XXI, debido a sus propiedades sostenibles [2]. Desde entonces la evolución que ha seguido la metodología de estas construcciones no ha sufrido un cambio tan espectacular como el desarrollo de la robótica ha permitido con la impresión 3D.

2. MARCO TEÓRICO

2.1. Optimización topológica

El peso de los materiales tiene un gran impacto en la construcción, no sólo por el coste de la producción sino también por el comportamiento del conjunto durante su vida útil. La optimización topológica es una herramienta matemática que permite la determinación de esta reducción durante la etapa de

[1] *Área de Medios Continuos y Teoría de Estructuras. Universidad de Málaga (España). cpedraza@uma.es (Corresponding author), jamartinr@uma.es*
[2] *Área de Construcciones Arquitectónicas. Universidad de Málaga (España).* paqui_vb96@hotmail.com*, carmengonzalez@uma.es*

diseño. Para ello se determina una función objetivo, así como unas restricciones deseadas. La herramienta intentará optimizar la distribución del material al mismo tiempo que se cumplan las condiciones de diseño. El resultado de la optimización puede incluir un modelo con una distribución de densidades intermedias que se distribuyen a lo largo del modelo, por lo que puede ser necesario revisar la topología optimizada [3].

La fabricación aditiva permite construir piezas con geometrías complejas, por lo que resulta una tecnología idónea para el uso de la optimización topológica.

En este trabajo se ha minimizado la energía del sistema, y como restricción se ha tenido en cuenta que la suma de densidades específicas sea menor que la densidad global. También se ha acotado las tracciones máximas al tratarse de un material, la arcilla, con una resistencia a tracción mucho menor que a compresión, Eq. (1) [4].

$$mínS = \sum_{i=1}^{Ne} \frac{1}{2} \boldsymbol{u}^{eT} \boldsymbol{k}_e \boldsymbol{u}^e \quad \text{s.a.} \sum_{i=1}^{N_e} \rho_i v_i < \rho; \sigma_I \leq \sigma_t \tag{1}$$

Donde S es la energía de deformación, $\boldsymbol{u}^e$ es el desplazamiento en los nodos, $\boldsymbol{k}_e$ es la rigidez de cada elemento, N_e es el número de elementos, ρ_i es la densidad de cada elemento, v_i es el volumen específico de cada elemento, ρ es la densidad global, σ_I , la tensión principal máxima y σ_t , la resistencia a tracción.

2.2. Teoría de homogenización

En ingeniería se pueden encontrar estructuras en las que un elemento se repite en una o varias direcciones. Estos elementos están constituidos por uno o más materiales, es un hecho presente en gran parte de los materiales compuestos, constituidos por dos o más materiales; aunque en el presente trabajo está realizado de un solo material. El proceso de homogenización consiste en sustituir el material heterogéneo original por un material homogéneo imaginario que simplifique el análisis de los resultados.

Existen muchos métodos analítico-numéricos basados en la teoría de homogenización: homogenización asintótica, método de la celda generalizada, elementos finitos, transformada de Fourier, y homogenización del campo medio. En el presente trabajo se utiliza un programa de elementos finitos específico para problemas de homogenización, Digimat-FE (Hexagon). En éstos se define un volumen representativo (RVE, por su abreviatura en inglés) que puede ser definido como “un volumen de material que es estadísticamente representativo de la vecindad infinitesimal del material en ese punto”[5].

3. RESULTADOS Y DISCUSIONES

El presente trabajo se ha centrado en una cúpula que forma parte de un conjunto de cúpulas, Fig. 1, cuyo fin es un centro lúdico de la Universidad de Málaga sito en la zona de Teatinos entre el Bulevar Louis Pasteur y la calle Jiménez Fraud.

Figura 1. *Conjunto arquitectónico sobre el que se encuentra la cúpula.*

3.1. Geometría, material, cargas y modelo de elementos finitos

El modelo que se ha estudiado es una cúpula semiesférica de $20.6m$ de diámetro exterior, con una altura de $9.4m$ y un espesor variable, siendo su espesor máximo de $0.46m$. El modelo de elementos finitos consta de 206800 elementos, la mayoría hexaédricos de 8 nodos, y 386100 nodos, Fig. 2.

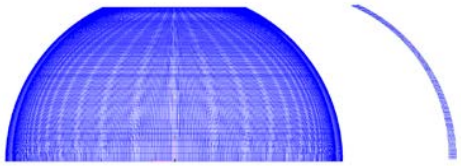

Figura 2. *Modelo de elementos finitos de la cúpula y sección de la misma*

Las condiciones de contorno son de empotramiento en el suelo y unos contrafuertes hasta $2.9m$ de altura en gran parte del contorno que serían fabricados con super-adobe. Las acciones consideradas son las que marca la normativa [6] en la zona: peso propio, peso de un lucernario, sismo, viento y nieve. El material considerado es arcilla de $1700Kgm^{-3}$ de densidad, un módulo de Young de $E = 102.65MPa$, coeficiente de Poisson $\nu = 0.4$ y resistencia a tracción a $\sigma_t = 0.3MPa$

3.2. Resultados de la optimización topológica

La optimización topológica se ha realizado con el programa de elementos finitos PATRAN-NASTRAN (Hexagon), se ha limitado la tensión principal máxima a $0.3MPa$. Hay que indicar que la geometría venía dada, es evidente que puede lograrse una optimización de la forma, pero se tenían que cumplir ciertas condiciones de diseño. La distribución de densidades se puede ver en la Fig 3.

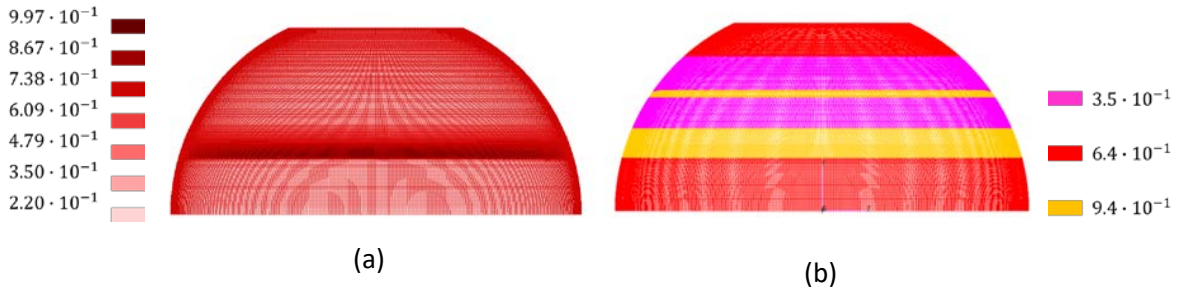

Figura 3. *Distribución de densidades como resultado del proceso de optimización topológica (a) disposición elegida(b).*

En la Fig. 3.a se observa la variación de densidades que da el sistema (distribución continua) y en la 3.b la disposición adoptada (distribución discreta).

3.3. Resultados de la homogenización. Volumen representativo

Las propiedades homogeneizadas se han determinado con el programa de elementos finitos DIGIMAT-FE. Aunque se parte de un material isótropo, las propiedades homogéneas resultantes corresponden a un material ortótropo.

Se ha elegido el volumen mostrado en la Fig. 4.a, ya discretizado, es un paralelepípedo de $0.43m \times 0.46m \times 0.45m$, y se han ido variando los espesores de los diferentes cordones para obtener las densidades deseadas, en la Fig. 4.b se pueden ver algunos ejemplos.

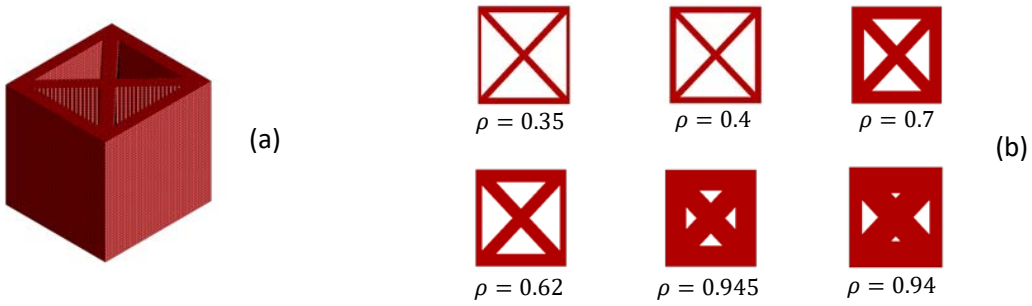

Figura 4. *RVE discretizado (a) y algunas variaciones de éste con sus densidades (b).*

3.4. Resultados

En la Fig. 5.a se representan las tensiones máximas en la cúpula no optimizada, en blanco las tensiones mayores de $0.3MPa$ y en la Fig. 5.b, las optimizadas. En esta última se representa en negro las tensiones mayores de $0.105MPa = 0.35 * 0.3MPa$ que sería la tensión máxima admisible correspondiente a la densidad de $\rho = 0.35$ si se aplica la regla de las mezclas, pues ésta es la densidad menor aplicada. Las zonas en negro corresponden a densidades mayores, siempre cumpliéndose que la tracción máxima es menor de $0.3MPa * \rho$.

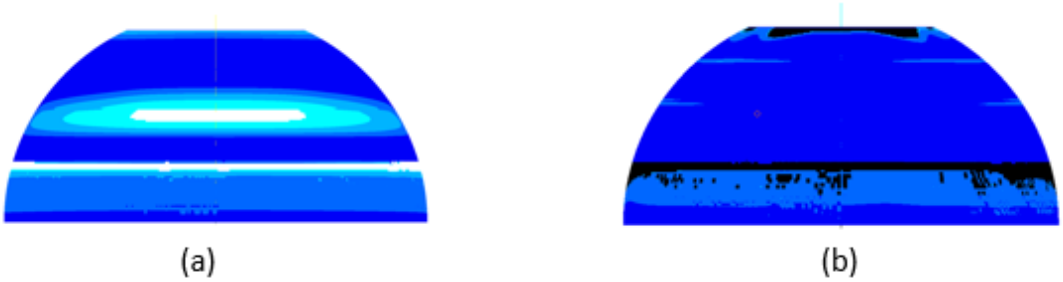

Figura 5. *Tensión máxima con el material in optimizar (a) y optimizado(b).*

4. CONCLUSIONES

La optimización topológica es una herramienta que en combinación con el método de homogenización resulta útil para el diseño de construcciones realizadas con impresión 3D. Cambiando los patrones de impresión se puede lograr mejores propiedades homogeneizadas.

5. REFERENCIAS

[1] Bici, A., Yunitsyna, A. (2023). Analysis of 3D printing techniques for building construction: a review, *Construction Robotics*, 7(2), 107-123.

[2] Bestraten, S., Hormías, E., Altemir A. (2023). Construcción con tierra en el siglo XXI. *Informes de la construcción,* 63, 5-20

[3] Rezaie, R., Badrossamay, M., Ghaeai, A., Moosavi, H. (2013). Topology optimization for fused deposition modeling process*, Procedia CIRP*, 6, 521-526

[4] Nastran 2021 Documentation: *MSC-Software*

[5] Rodriguez, J.F., P-Thomas, J., Renaud, J.E. (2003). Mechanical behavior of acrylonitrile butadiene styrene fuse depositon materials modeling, *Rapid Prototyping Journal, 9,* 219-230.

[6] DB-SE_AE, 2009, *Ministerio de fomento*

Modelling of Fatigue Fracture by Phase-Field Methods

Jarak, Tomislav[1,2]; Jukić, Krešimir[2]; Tonković, Zdenko[1]; José María García-Terán[2], Antolín Lorenzana Ibán[2]

ABSTRACT

In this contribution two approaches used to model fatigue by the Phase-Field (PF) method are explained. To this end, two models for High Cycling Fatigue (HCF), both implemented in FEM, are used and briefly explained. The first one is based on the degradation of fracture toughness, i.e., crack resistance force, and the other on defining additional the crack driving force, accounting for fatigue. The behavior of presented models is demonstrated by simple illustrative problems, revealing their ability to reproduce S_N curves and crack growth laws. Calibration of both models is commented in order to assess their applicability for predicting fatigue in realistic materials.

Keywords: fatigue, phase-field, S-N curves, Paris law.

1. INTRODUCTION

In recent years, the Phase-Field (PF) method has gained much attention in simulating fatigue fracture [1] due to its ability to predict complex crack initiation and propagation processes without additional ad hoc conditions. Besides, its implementation in existing numerical methods, such as the Finite element Method (FEM) is relatively simple. The method is based on the variational formulation of Griffith's theory, according to which the entire fracture process is governed solely by the minimization of the total energy functional Ψ_{total}, which can be defined as

$$\Psi_{\text{total}} = \Psi_{\text{int}} + \Psi_f - \Psi_{\text{ext}}, \tag{1}$$

where Ψ_{ext} is the potential of external forces. In the PF models for brittle fracture, used to develop the models for HCF, the internal energy Ψ_{int} is defined by decomposing elastic energy ψ_e in two parts and degrading only the part that contributes to the crack evolution (the positive deformation energy) as

$$\Psi_{\text{int}} = \int_\Omega \psi_e \mathrm{d}V, \; \psi_e = g\psi_0^+ + \psi_0^-. \tag{2}$$

ψ_0^+ and ψ_0^- denote the effective positive and negative deformation energy. In this work, the standard quadratic energy degradation function $g = (1-\phi)^2$ is used. The scalar phase field $\phi \in [0,1]$ divides the undamaged healthy material ($\phi = 0$) and the totally damaged material ($\phi = 1$) in a smooth

[1] *Faculty of Mechanical Engineering and Naval Architecture, University of Zagreb (CROATIA). tomislav.jarak@fsb.hr (Corresponding author). kresimir.jukic@fsb.hr, zdenko.tonkovic@fsb.hr .*

[2] *ITAP, School of Industrial Engineering, University of Valladolid (SPAIN). tomislav.jarak@uva.es (Corresponding author). josemaria.gteran@uva.es, ali@eii.uva.es.*

continuous manner. Various approaches for decomposing the deformation energy have so far been proposed, and finding physically the completely correct decomposition is still an unresolved issue.

2. FATIGUE MODELLING

In fatigue modelling, in general case the dissipated fracture energy Ψ_f can be extended as

$$\Psi_f = \Psi_{f.r} + \Psi_{f.d} = \int_\Omega \int_0^t G_c F\left(\bar{\psi}_{\text{his.r}}\right) \dot{\gamma}\, d\tau\, \mathrm{d}V + \Psi_{f.d}\left(\bar{\psi}_{\text{his.d}}\right),\ \gamma = \left(\alpha(\phi)/l + l(\nabla\phi)^2\right)/2, \tag{3}$$

where $\Psi_{f.r}$ represents the energy term defining material resistance to fracture, while $\Psi_{f.d}$ is the energy term resulting in additional crack driving forces related exclusively to fatigue fracture. The so-called crack surface density function γ regularizes the crack geometry, and *l* denotes the length-scale parameter, defined here as a dependent material parameter. The function $F\left(\bar{\psi}_{\text{his.r}}\right)$ is often called the fatigue degradation function, as it serves to describe the degradation of the fracture toughness due to the impact of cyclic loads, i.e., describes the reduction of resistance to fracture due fatigue. It is described by one or more variables $\bar{\psi}_{\text{his.r}}$ dependent on loading history. Analogously, $\Psi_{f.d}$ describes how the crack driving forces increase due to the impact of cyclic loads and are dependent on a set of load history variables $\bar{\psi}_{\text{his.d}}$. The history variables should be monotonously increasing functions with respect to the number of loading cycles, and should not affect the response of material to the proportional (monotonous) loading. The choice of these variables is not unique, and various different formulations have been proposed. All models are phenomenological, and both F and $\Psi_{f.d}$ introduce one or more new material fatigue parameters, which should be calibrated from appropriate experimental data. Although many existing models can reproduce some important fatigue phenomena, they usually have only one or two fatigue material parameters. Therefore, the question arises whether they can accurately reproduce both S-N and crack growth curves simultaneously by only one set of parameters. To illustrate this issue, here two different models are considered.

2.1. Model 1 – degradation of fracture toughness

This model uses $\gamma = 3/8\sqrt{2}\left(2\phi/l + l(\nabla\phi)^2\right)$. Fatigue is modelled by choosing

$$F = \xi\left(1 - \bar{\psi}_\infty / \psi_{\text{his.r}}\right)^2,\ \psi_{\text{his.r}}(t) = \int_0^t \psi_e(\tau) H(-\dot{\psi}_e)\, \mathrm{d}\tau,\ \ \Psi_{f.d} \equiv 0, \tag{4}$$

where ξ and $\bar{\psi}_\infty$ are model fatigue parameters and $\psi_{\text{his.r}}$ is the loading history variable defined in terms of deformation energy. More details about this model can be found in [2]. As can be seen, here no extension of crack driving forces is assumed, and the model belongs to the group of often-used models based on the degradation of fracture toughness, where this degradation is described by some *ad hoc* assumed functions, typically without firm physical background.

2.2. Model 2 – extension of crack driving forces

The model considered here is based on the classical AT2 model for brittle fracture, employing $\gamma = 1/2\left(\phi^2/l + l(\nabla\phi)^2\right)$. The model is developed by assuming two additional crack driving forces, taking into account crack initiation and crack propagation due to the impact of cyclic forces as

$$F \equiv 1,\ \Psi_{f.d} = \int_\Omega \int_0^t \dot{g}\, G_c\, \bar{\psi}_{\text{his.d}}\, d\tau\, \mathrm{d}V,\ \bar{\psi}_{\text{his.d}} = \bar{\psi}_{\text{his.init}} + \bar{\psi}_{\text{his.prop}},\ \bar{\psi}_{\text{his.init}} = \psi_{\text{crit}}^{1-k_1} \int_0^t k_3\, \psi_{\text{e.init}}(\tau) H\left(-\dot{\psi}_{\text{e.init}}\right) \mathrm{d}\tau,$$
$$\psi_{\text{e.init}} = \left(g^f \psi_0^+\right)^{k_1},\ \bar{\psi}_{\text{his.prop}} = \psi_{\text{crit}}^{1-k_2} \int_0^t k_4\, \psi_{\text{e.prop}}(\tau) H\left(-\dot{\psi}_{\text{e.prop}}\right) \mathrm{d}\tau,\ \psi_{\text{e.prop}} = \left(g^f \psi_0^+\right)^{k_4}. \quad (5)$$

Here, no fracture toughness degradation is introduced, and additional crack driving forces $\bar{\psi}_{\text{his.init}}$ and $\bar{\psi}_{\text{his.prop}}$ result from crack initiation and crack propagation due to fatigue, respectively. The formulation of these forces is here motivated by the exponential structure of the Paris law and Basquin equation used to describe S-N curves. This model has been presented and studied in detail in [3].

3. RESULTS AND DISCUSSION

First, we consider the compact tension (CT) specimen, shown in Fig. 1, loaded by cyclic loading defined with load ratio $R = F_{\min} / F_{\max} = 0$ to investigate behavior of Model 1. The material parameters are $E = 210$ GPa, $\nu = 0.3$, $G_c = 5$ kN/mm, $l = 0.5$ mm, and geometry is defined by $a_0 = 7{,}5$mm, $b = 1$mm, $c = 0{,}08$mm, $W = 30$mm, while thickness is 15mm. The influence of model fatigue parameters on S-N and crack growth curves is shown in Fig. 1. $\bar{\psi}_\infty$ strongly influences both curves, which aggravates the model calibration. The solution could be found in designing a fatigue degradation function with more fatigue parameters, but designing such physically meaningful function could be far from trivial.

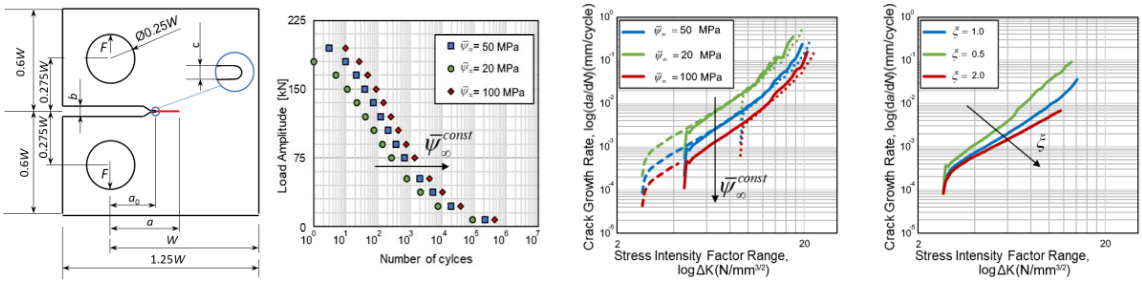

Figure 1. *From left to right: CT specimen, influence of $\bar{\psi}_\infty$ on S-N curves and crack growth curves, influence of ξ on crack growth curves (for $\bar{\psi}_\infty = 50$ MPa).*

Next, the potential of the Model 2 is demonstrated by considering a similar CT specimen with parameters $a_0 = 11$mm, $b = 3{,}125$mm, $c = 0{,}2$mm, $W = 50$mm and thickness 1mm. The following material parameters are applied, unless stated otherwise: $R = 0$, $E = 116$ GPa, $\nu = 0.33$, $G_c = 35$ MPa mm, $\sigma_{\text{crit}} = 907$MPa, $l = 0.4582$mm, $k_1 = 2$, $k_2 = 1$, $k_3 = 0.001$, $k_4 = 1$, $\phi_{\text{thres}} = 0.4$. The results shown in Fig. 2 indicate that we can relate each of the parameters k_i almost exclusively to only one of the parameters of S-N or Paris curves, which allows for a relatively easy calibration of this model.

4. CONCLUSIONS

The fatigue modelling by numerical PF method is explained, based either on the degradation of fracture toughness or on designing additional crack driving forces. The problem of calibration of resulting models is illustrated by simple problems. The results indicate that PF models have to be equipped by a sufficient number of material fatigue parameters in order to successfully reproduce important fatigue phenomena of realistic engineering materials, including the S-N and crack growth curves.

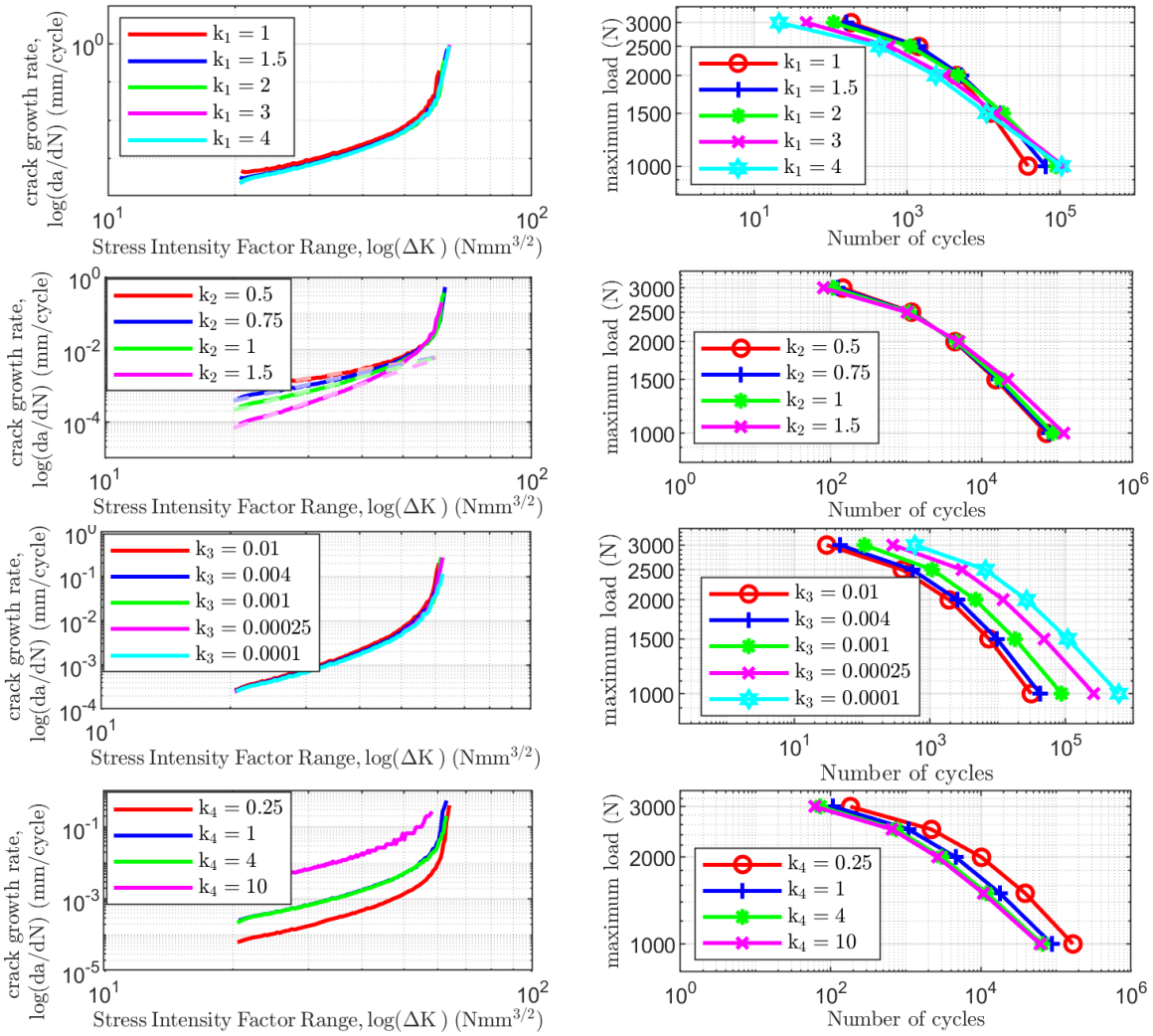

Figure 2. *Influence on fatigue parameters of Model 2 on crack growth curves (left) and total fatigue life curves (right).*

ACKNOWLEDGEMENTS

The authors wish to acknowledge to the AEI, Spanish Government (10.13039/501100011033), and to "ERDF A way of making Europe", for the partial support through the grant PID2022-140117NB-I00.

REFERENCES

[1] Kalina, M., Schneider, T., & Brummund, J., Kästner, M. (2023). Overview of phase-field models for fatigue fracture in a unified framework. *Engineering Fracture Mechanics, 288, 109318. https://doi.org/10.1016/j.engfracmech.2023.109318*

[2] Seleš K., Aldakheel F., Tonković Z., Sorić J., Wriggers P. (2021). A general phase-field model for fatigue failure in brittle and ductile solids. *Comput Mech.* ,67(5), 1431–52. https://doi.org/10.1007/s00466-021-01996-5

[3] Jukić, K., Ambati, M., Jarak, T., Kästner, M., Tonković, Z. (2023). Calibration of phase-field brittle fatigue model by purposeful design of crack driving forces. *Engineering Fracture Mechanics, 289, 109341. https://doi.org/10.1016/j.engfracmech.2023.109341*

Modelling of spalling in reinforced concrete columns subjected to fire

Ibáñez, Carmen[1]; Peña, David L.[2]; Albero, Vicente[3]; Hospitaler, Antonio[1]; Lapuebla-Ferri, Andrés[4]; Saura, Héctor[1]

ABSTRACT

Spalling is a stochastic phenomenon that usually occurs within the first 30 minutes of fire exposure and can affect any area of an exposed reinforced concrete element, which makes its occurrence difficult to be predicted. Although some models focus on that, the work described herein does not deal with modelling the mechanism of the occurrence of spalling; it is assumed that spalling occurs, and its effects on the behavior of the columns are analysed. To that end, an advanced numerical model, validated against experiments for the fire behaviour of slender reinforced concrete columns under bending, is developed in SAFIR. The influence of several parameters is investigated. In general, mid-length spalling and surface spalling are more damaging. For columns with lower slenderness, e.g. columns in dwellings, the effect considered is more notable than for columns with higher slenderness.

Keywords: reinforced concrete columns; spalling; fire resistance; numerical model; SAFIR.

1. INTRODUCTION

Due to water evaporation, the increase in the internal pore pressure of reinforced concrete (RC) elements exposed to fire can result in the phenomenon of spalling, causing a loss of concrete and a subsequent loss of resistance of the cross-section. Parameters affecting the occurrence of spalling can be material, geometrical, or environmental [1]. Conclusions about the possibility of spalling and the reasons producing it are generally circumstantial mostly due to the lack of instrumentation and consistent data results. Despite spalling being a stochastic phenomenon, the range of time occurrence seems to be reasonably well set for the worst case scenarios in which the reduction of the effective cross-section can have serious consequences on the fire resistance of RC elements ([1], [2]). The worst case scenario tends to be when spalling results in the complete loss of concrete cover, directly exposing the reinforcement to the heat source. Some models focus on predicting the occurrence of spalling but given the stochastic nature of the phenomenon it is complicated to draw solid conclusions.

In contrast, the investigation presented in this paper does not deal with modelling the mechanism of occurrence of spalling. It is implicit that spalling occurs, and its effects on the performance of the columns are analysed after its occurrence. Therefore, an advanced numerical model is developed and experimental data for the behaviour of slender RC columns under bending subjected to fire are used

[1] *ICITECH. Universitat Politècnica de València (SPAIN). caribus@upv.es (Corresponding author); ahospitaler@cst.upv.es; hsaura@cst.upv.es.*
[2] *Civil Engineering Institute. Austral University of Chile (CHILE). david.pena@uach.cl*
[3] *Dpt. of Mechanical Engineering and Construction. Universitat Jaume I (SPAIN). valbero@uji.es*
[4] *Dpt. of Continuum Mechanics and Theory of Structures. Universitat Politècnica de València (SPAIN). anlafer0@mes.upv.es*

for its validation. Spalling can affect either the corner of the cross-section or one of the sides. In this work both types of spalling are covered to investigate the effect of a number of parameters, including the column slenderness, the location of spalling over the column length or the damage dimension.

2. MODEL DESCRIPTION AND VALIDATION

2.1. Description

An advanced numerical model for simulating the fire behaviour of slender RC columns was developed employing the computer program SAFIR [3] for the analysis of structures, which enables modelling of the behavior of structures at the accidental case of fire. The main parameters were the column length, the cross-section dimensions, the load level and eccentricity, the end conditions and the thermal and mechanical material properties. It consisted of two parts: the concrete cross-section and the reinforcing bars. For both materials the thermal mechanical properties given by EN 1992-1-2 [4] were used.

A sequentially coupled thermal-stress analysis is conducted: first, a thermal analysis is carried out and then a mechanical problem is solved. For conducting the thermal analysis, the standard time-temperature curve ISO 834 is applied to the exposed surface through the convection and radiation heat transfer mechanisms. For validation, the actual furnace time-temperature curve reported in the literature was used. The cross-section is discretised (Fig. 1) and each fiber is characterized by its position, temperature and corresponding material properties. Nodal temperatures are stored as a function of time and then read into the mechanical analysis from an input file.

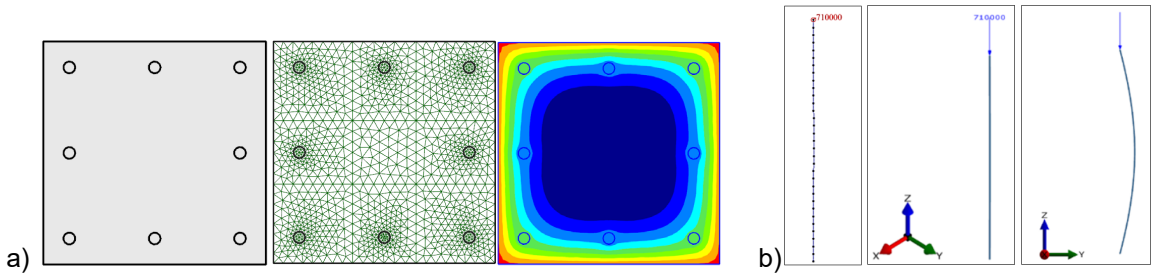

Figure 1. *a) RC cross-section definition, mesh and temperature field after 60 min; b) RC column modelling*

The length of each column is discretised in several beam-column elements (Fig. 1b). The axial load is applied to the top node of the column. The initial imperfection of the column is considered by means of the first buckling mode shape of a pinned–pinned column which exhibits a sinusoidal shape. The mid-height maximum deflection was L/1000. In Fig. 1b one of the columns modelled is shown as example.

2.2. Thermo-mechanical validation

The model was validated by comparing their predictions with data from fire tests available in the literature. In total, 74 slender RC columns were used according to the compilation by Gernay [5]. In each test, a loaded slender RC column was exposed to a standard time-temperature curve on its four sides. Some parameters varied between the tests: end conditions, length of the column, cross-section geometry, reinforcement ratio, material strengths, and magnitude and eccentricity of the load. Fig. 2a shows the good agreement that exists between tests and predicted results in terms of fire resistance rating (FRR) for the 74 cases used in validation, with most of them lying on the safe side.

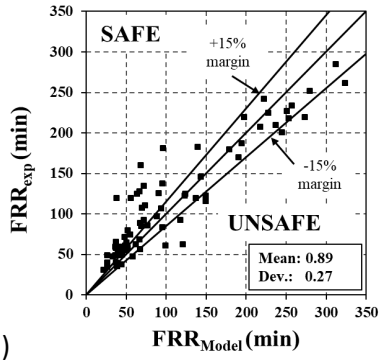

a)

Column	FRR_{Exp} (min)	FRR_{Model} (min)	FRR_{Mod} / FRR_{Exp}
300x300 mm, 4ϕ25, HR=74%, f_c=34.8 MPa, f_s=444 MPa, u=48 mm, N=1778 kN (Series I column 8 [5])	146	143	0.98

b)

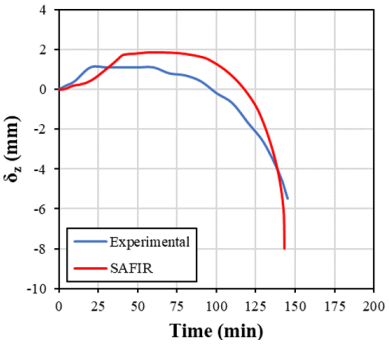

Figure 2. *a) Model vs. experimental results; b) Axial displacement-time curves for one of the columns modelled*

In Fig. 2b the fire response of a slender RC column in terms of axial displacement-time is shown to illustrate the validation process (pinned–pinned column). It was found that the overall response predicted by the model reproduced with high precision the real behavior of the slender RC columns.

3. APPLICACION FOR THE EVALUATION OF SPALLING EFFECTS

The model was applied to evaluate the effects of spalling in slender RC columns. Both corner and surface spalling were modelled (Fig. 3a) with times of occurrence of 30 and 10 min after heating respectively. The most severe scenario with the reinforcement exposed to the heat source was modelled. A cross-section measuring 300x300mm with 8ϕ16 reinforcing bars and a concrete cover of 35 mm is taken as reference to show the results obtained. Grades C30 and B500S are used for concrete and steel respectively. The column is 4-sided exposed to the standard curve ISO 834. First, the thermal analysis is conducted and when spalling occurs the fibres of concrete affected are eliminated (Fig. 3b and 3c).

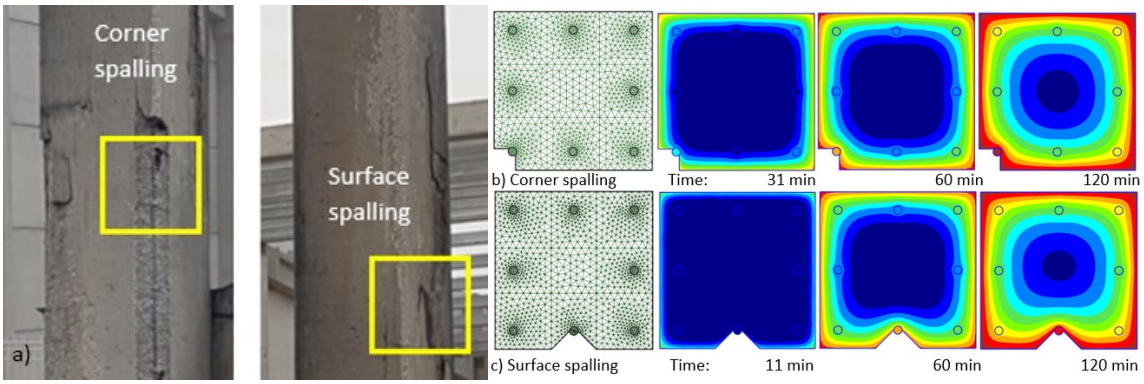

Figure 3. *a) Detail of corner and surface spalling in a RC Column; b) and c) Cross-sectional mesh and temperatures for corner and surface spalling*

The cross-sectional temperatures must be updated for the new boundary conditions, as shown in Fig. 3b and 3c. The command *RESTARTT* in SAFIR is used to that end. The new thermal file needed as an input for the mechanical analysis combines the temperatures of the section before and after spalling. This file must be created manually by the user keeping the SAFIR output file format. In order to neglect the contribution to the RC column fire resistance of the fibres that would disappear in case of spalling, they are assigned a temperature of 1200 ºC (as recommended in the technical documentation [3]).

With this model of spalling, the influence of the column slenderness, the location of spalling over the column length or the damage dimension are analysed. Fig. 4 shows some of the results obtained. In general, spalling at mid-length is more damaging (Fig. 4a) and surface spalling results more harmful

giving lower values of FRR for the RC columns. According to the model of spalling considered, its effect can be neglected for higher slenderness whereas is more significant for columns with lower slenderness (e.g. columns in dwellings or in car parks with more onerous fire requirements) (Fig. 4b).

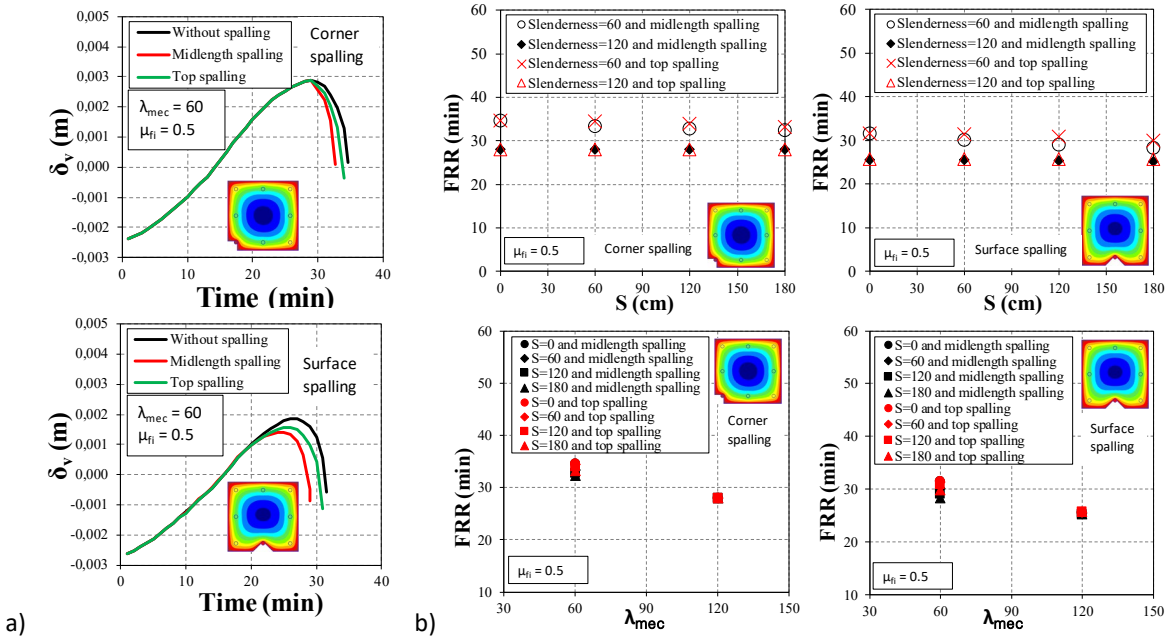

Figure 4. *a) Influence of spalling position b) Influence of slenderness and damage dimension (S)*

4. CONCLUSIONS

An advanced numerical model was developed in SAFIR for the effects of spalling in the fire response of slender RC columns and successfully validated with experiments. It was found that mid-length and surface spalling were more dangerous. Its effect is more notable for columns with lower slenderness.

ACKNOWLEDGEMENTS

The authors would like to express their sincere gratitude to the ‘‘Conselleria d’Innovació, Universitats, Ciència i Societat Digital” of the Valencian Community (Spain) for the help provided through the project CIGE/2021/002.

REFERENCES

[1] Dotreppe, J.C., Franssen, J.M., & Vanderzeipen, Y. (1999). Calculation method for design of reinforced concrete columns under fire conditions. *ACI Journal*, *96(1), 9-18.*

[2] Hertz, K.D. (2003). Limits of spalling of fire-exposed concrete. *Fire Safety Journal, 38, 103-116.*

[3] Franssen, J.M. (2005). SAFIR: A thermal-structural program for modelling structures under fire. *Engineering Journal, 42(3), 143-158.*

[4] CEN. (2004). EN 1992-1-2, Eurocode 2: design of concrete structures, Part 1.2: General rules – structural fire design. Brussels, Belgium: Comité Européen de Normalisation.

[5] Gernay, T. (2019). Fire resistance and burnout resistance of reinforced concrete columns. *Fire Safety Journal, 104, 67-78.*

Natural fuse-segmentation to arrest failure propagation in precast concrete buildings

Adam, José M[1]; Buitrago, Manuel[1]; Makoond, Nirvan[1]; Setiawan, Andri[1]; Caredda, Giacomo[1]; Marin-Vilches, Lorenzo[1]; Cetina, Diego[1]; Gerbaudo, Maria L[1]; Oliver, Marina[1]; Sempertegui, Geovanny[1]; Tasquer Val, Daniel[1]

ABSTRACT

Our previous work on precast construction has shown that sufficient structural robustness can be achieved by adequately designing the connection detailing to withstand a sudden column removal under the accidental load scenario. However, the behaviour of such a system under larger initial failure has not been investigated to date. This article presents one of the recent tests carried out by the Building Resilient research group of the Universitat Politècnica de València, where a full-scale precast building of 2 storeys (6 m) and 3 x 2 spans (15 x 12 m^2) has been tested under removal of three columns. Preliminary computational simulations were performed using the applied element method (AEM) to design the load scenarios. The test results indicated that the precast system has a natural segmentation ability, which is beneficial to arrest the failure propagation, limiting the collapse extent to a minimum.

Keywords: progressive collapse, full-scale testing, precast building, applied element method.

1. INTRODUCTION

Precast construction has several practical advantages compared to concrete cast-in-situ buildings, including faster construction time, minimum waste, and better quality control. In our past projects [1], we had proven that, with appropriate construction details, precast concrete structures are sufficiently robust to withstand several single-column removal scenarios without collapsing through an extensive tying system, which provides excellent connectivity between elements. However, the behaviour of such a structure under larger initial failure (multiple column losses) remains unknown. To better understand the phenomenon, the purpose-built precast specimen, which was used in [1] to perform several single-column removal scenarios, was retested but with larger initial failures involving the removal of three columns. Numerous preliminary computational simulations using the applied element method (AEM) were conducted to plan for this final test.

2. DESCRIPTION OF THE TEST CAMPAIGN

2.1. Test specimen

The purpose-built specimen had two 2.6 m high floors with a floor plan of 15 x 12 m^2. The longer span of the building consists of 3 bays of 5 m span whereas the shorter side is composed of 2 bays of 6 m span. All the columns were precast with a dimension of 40 x 40 cm^2 (including corbel systems) except in a few locations where the columns were made of triple-hinged steel columns, specially designed to perform the removal scenario [1]. The beams were partially precast with a depth of 60 cm (35 cm precast + 25 cm topping) and a width of 40 cm. These beams were supported on elastomeric pad

[1] *ICITECH. Universitat Politècnica de València (SPAIN). joadmar@upv.es (Corresponding author). mabuimo1@upv.es. ncmakoon@upv.es. asetiaw1@upvnet.upv.es. gcaredd@upv.es. lomavil@upv.es. dieceber@upv.es. mlgerbau@upv.es. maolca1@upv.es. gsemgal@posgrado.upv.es. datasval@upv.es.*

bearings atop the column's corbel. Hollow core slabs with a total depth of 26.5 cm (20 cm precast + 6.5 cm topping) and a unit width of 1.2 m were used as the floor system, spanning 6 m between the primary beams (see Figure 1).

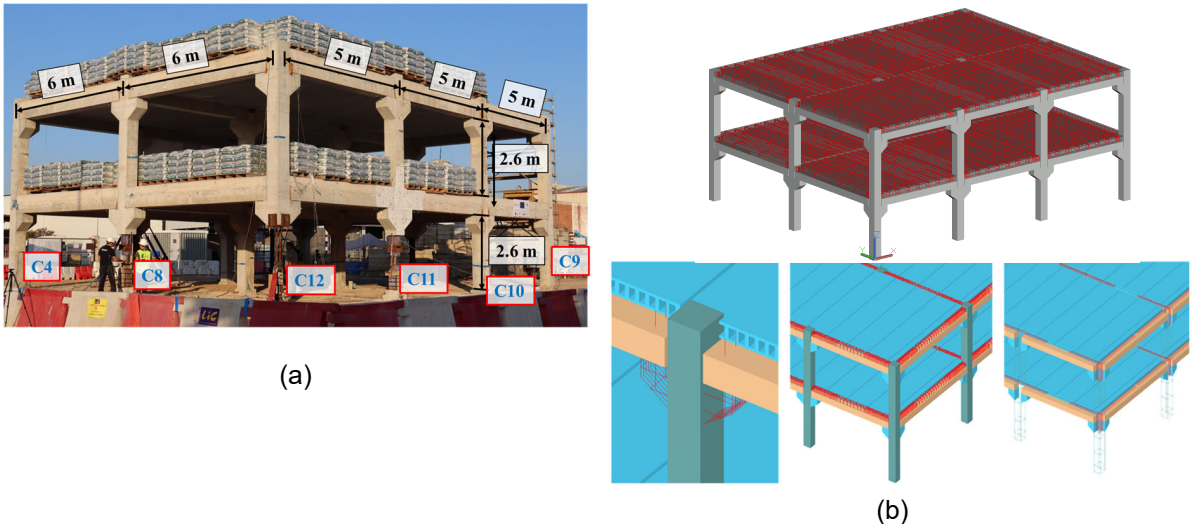

Figure 1. *(a) General overview and dimensions of the purpose-built precast specimen; (b) The numerical model of the specimen analysed using the applied element method (AEM).*

2.2. Preliminary simulations conducted using the applied element method (AEM)

The applied element method (AEM) is a numerical technique to predict the behaviour of structures based on the concept of discrete cracking as it allows accurately simulate different phases of failures from elastic, crack initiation and propagation in tension-weak materials, yielding, separation, impact (debris), and collision between separated elements or between the separated elements and the system boundaries [2]. As the present experimental test involves phenomena like separation and collision, it was decided that AEM is more appropriate to be adopted for such a purpose (see Figure 1b). The numerical model was built and initially calibrated using the test results on a single removal scenario [1]. Then, the calibrated model was utilised to explore combinations of different removal scenarios with various magnitudes of the applied gravity load (see Figure 2). The objective was to determine the optimum removal scenario that fulfils the following criteria: 1) the initial failure shall be sufficient to induce a partial collapse of the system; 2) the collapse involves (or activates) both main axes of the building; 3) the scenario requires a reasonable gravity load to trigger the local failure. After some considerations, scenario D, involving three-column removals in the corner bay of the structure, was chosen (see Figure 2d). This scenario requires the lowest failure load to reproduce while also creating a failure border in both the long and weak axes of the building.

2.3. Column removal procedure

Regarding the column removal strategy, careful planning was undertaken to ensure the safety of all people involved during the test. The procedure consists of a two-phase removal: 1st phase is the quasi-static removal of the two edge columns (adjacent to the corner column), and the 2nd phase is the sudden (dynamic) removal of the corner column.

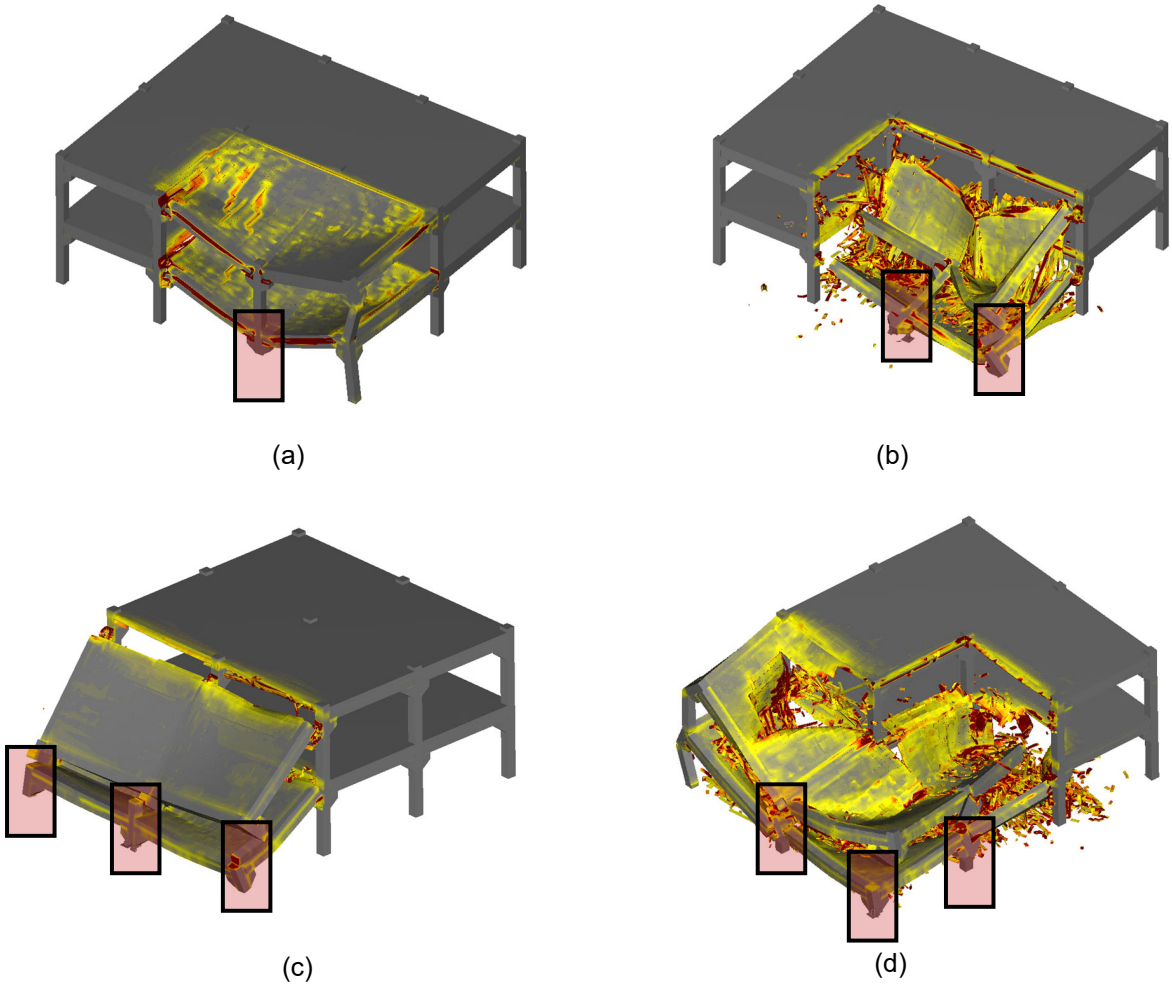

Figure 2. *Results of numerical simulations considering various initial damage scenarios: (a) single-column removal (collapse load of 19.25 kN/m^2); (b) two-column removals (12 kN/m^2); (c-d) three-column removals (load of 8.50 and 7.00 kN/m^2 respectively).*

3. RESULTS AND DISCUSSION

3.1. The structural response during the 1st testing phase (quasi-static removal of two edge columns)

After removing the two edge columns, the precast structure remained standing without any collapse. The measured beam rotations connected to the removed column location were about 0.01-0.015 radians, which were still far below the failure rotation under catenary action (0.2 radians) yet sufficiently high to induce cracking and permanent deformation. The 1st testing phase proves that the continuity provided to the system through peripheral and internal ties helps to prevent collapse under small initial failures.

3.2. The structural response during the 2nd testing phase (dynamic removal of the corner column)

After removing the corner column, the local failure was triggered, and then the failure propagated, leading to a partial collapse of the building. Interestingly, as the ties (which were supposed to provide continuity between structural members) were broken due to a significant increase in strain during the 2nd testing phase, the propagation was arrested and did not spread further to the rest of the building.

As a result, only partial collapse occurred, and a clear border could be seen between the collapsed and intact parts (refer to the boundary between the red and blue shaded regions in Figure 3a).

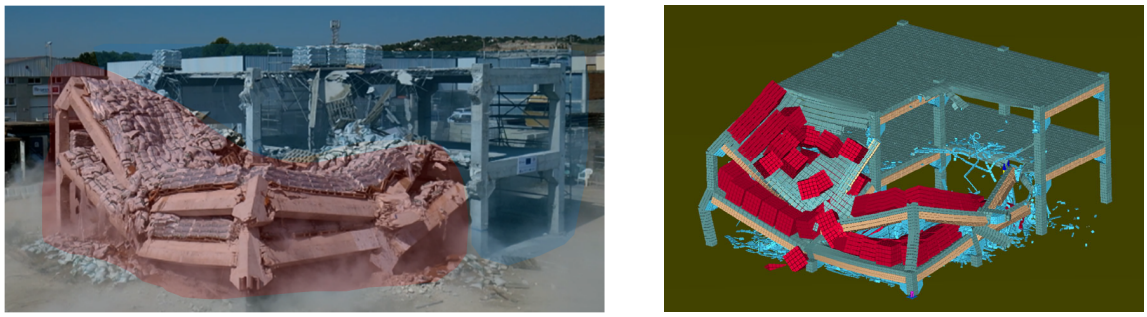

(a) (b)

Figure 3. *(a) Test specimen after the partial collapse; (b) Failure predictions obtained using the AEM.*

Comparing the collapsed state of the specimen from the test with the predictions obtained using the AEM (see Figure 3), it can be clearly observed that both are in excellent agreement.

4. CONCLUSION

The behaviour of precast concrete structures under small and large initial failures was investigated by testing a full-scale purpose-built specimen involving the removal of three columns. Results obtained from the 1st and the 2nd testing phases revealed that both continuity and segmentation could improve the robustness of building structures against abnormal events. Continuity helps redistribute the excess forces and prevent failure from occurring under small initial failures. In contrast, segmentation provides the last line of defence mechanism to arrest failure when collapse propagation becomes inevitable. An excellent agreement was found between the measured and the predicted responses obtained using the applied element method (AEM).

ACKNOWLEDGEMENTS

This article is written as a part of a research project (*Endure*) funded by the European Research Council (ERC) under the European Union's Horizon 2020 research and innovation programme (Grant Agreement No. 101000396). The authors would also like to express their gratitude for funding received under the postdoctoral program IJC2020-042642-I funded by MCIN/AEI/10.13039/501100011033 and by the "European Union NextGenerationEU/PRTR".

REFERENCES

[1] Buitrago, M., Makoond, N., Moragues, Juan J., Sagaseta, J., Adam, Jose M. 2023. Robustness of a full-scale precast building structure subjected to corner-column failure. Structures, pp. 824-841. https://doi.org/10.1016/j.istruc.2023.03.146.

[2] Meguro, K., Tagel-Din, H. 2000. Applied element method for structural analysis: Theory and application for linear materials. Structural Engineering/Earthquake Engineering. Japan: Japan Society of Civil Engineers. 17 (1): 21–35. F0028A.

New tensegrity structures based on octagonal cells

Fernández-Ruiz, Manuel Alejandro[1]; Núñez-Almagro, Javier Jacob[2]; Huerta, Milagros[2]

ABSTRACT

Tensegrity families are excellent sources of new tensegrity structures. A tensegrity family is a group of tensegrity structures that share a common connectivity pattern. The Octahedron, X-Octahedron and Z-Octahedron families are examples of them. The members of these families are constructed by assembling one-bar elementary cells. Rhombic, X-rhombic and Z-shaped cells are used to construct the members of the Octahedron, X-Octahedron and Z-Octahedron families respectively. In a recent work, a new type of elementary cell was introduced: the octagonal cell. In this work, new tensegrity structures are obtained by assembling a new octagonal cell. The values of the force:length ratio of the members of the tensegrities that lead to an equilibrium configuration have been computed analytically. The stability of the resultant tensegrity structures has been analyzed.

Keywords: tensegrity, octahedron family, form-finding, force density method, octagonal cells.

1. INTRODUCTION

Tensegrity structures are free-standing pin-jointed structures composed of pre-stressed cables (tension members) and struts (compression members) that are self-equilibrated [1]. Tensegrity structures have developed greatly in recent years due to their lightweight, controllability, deployability and ingenious forms [1].

The design of tensegrity structure is a complex process because they do not exhibit very intuitive principles. Tensegrity structures have been proved to be some excellent sources of tensegrity structures. A tensegrity family is a group of tensegrity structures that share a common connectivity pattern. The Octahedron, X-Octahedron and Z-Octahedron families are examples of them. The members of these families are constructed by assembling one-bar elementary cells. Rhombic, X-rhombic and Z-shaped cells are used to construct the members of the Octahedron [2], X-Octahedron [3] and Z-Octahedron [4] respectively. In [5] a new type of elementary cell was introduced: the octagonal cell. In this work, new tensegrity structures are obtained by assembling a new octagonal cell. The values of the force:length ratio of the members of the tensegrities that lead to an equilibrium configuration have been computed analytically. The stability of the resultant tensegrity structures has been analyzed.

[1] *Department of Civil, Materials and Manufacturing Engineering. University of Málaga (Spain). mafernandez@uma.es. (Corresponding author).*

[2] *Department of Mechanical Engineering and Industrial Design. University of Cadiz (Spain). jacob.nunez@uca.es. milagros.huerta@uca.es*

2. EQUILIBRIUM AND STABILITY OF TENSEGRITY STRUCTURES

One of the key steps in the design of tensegrity structures is to find a self-equilibrated configuration (known as the form-finding process). The Force Density Method (FDM) proposed by Schek [6] is the basis of most of form-finding methods of tensegrity structures. FDM is based on the concept of force density or force:length ratio *q*, which is defined as the ratio between the axial force and the length of each member of the tensegrity (*q* is positive for cables and negative for struts).

The equilibrium equations in the FDM for a tensegrity structure of n nodes and m members are given by Eq. (1):

$$\begin{aligned} \mathbf{D} \cdot \mathbf{x} &= \mathbf{0} \\ \mathbf{D} \cdot \mathbf{y} &= \mathbf{0} \\ \mathbf{D} \cdot \mathbf{z} &= \mathbf{0} \end{aligned} \tag{1}$$

where $\mathbf{x}$, $\mathbf{y}$, and $\mathbf{z}$ ($\in \Re^n$) are the nodal coordinate vectors, and $\mathbf{D} \in \mathbb{R}^{n \times n}$ is the force density matrix. Matrix **D** can be constructed according to Eq. (2):

$$D_{ij} = \begin{cases} \sum_{k \in \Gamma} q_k & \text{for } i = j \\ -q_k & \text{if nodes } i \text{ and } j \text{ connected by member } k \\ 0 & \text{otherwise} \end{cases} \tag{2}$$

In Eq. (2) is the set of members connected to the node *i*.

A tensegrity is fully developed in a *d*-dimensional space if the rank deficiency of matrix **D** is at least *d* + 1 (non-degeneracy condition) [1]. Regarding stability, a tensegrity is said stable if its tangent stiffness matrix **K** is positive semi-definite [1]. Super-stability (a most robust criterion) implies that the tensegrity is stable regardless of the material properties and prestress levels, and it must fulfill some conditions [1]. In this work, two cross-sectional areas of the members are considered (one for cables and one for struts) such that the maximum prestress in both cases equals 1% of the product *EA* (*E* = 200.000 MPa), as in [1].

3. TENSEGRITY STRUCTURES BASED ON OCTAGONAL CELLS

The members of the tensegrity families are constructed by assembling elementary cells following a certain topology. In [5], the Z-Octahedron family was defined based on a new type of elementary cell: the octagonal cell (see Fig. 1.a).

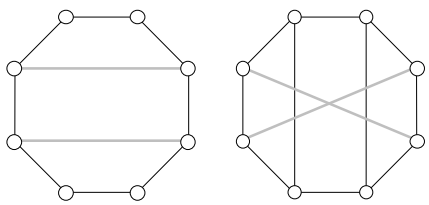

Figure 1. *Octagonal cell proposed in [5] (a) and new octagonal cell (b). Gray and black lines correspond to struts and cables respectively.*

In this work, a new octagonal cell is proposed with crossed struts and two additional cables (see Fig. 1.b). Two force:length ratios are going to be considered: q_b for struts/bars and q_c for cables.

The first tensegrity to be studied is the new expanded octahedron composed by the proposed octagonal cell, which has 24 cables, 6 struts and 12 nodes. The plane connection graph of this new tensegrity is shown in Fig. 2. This plane connection graph has been obtained by replacing the octagonal cell shown in Fig. 1.a by the new one shown in Fig. 1.b in the plane connection graph proposed in [6]. The connectivity between the nodes is one of the inputs of the form-finding method (the other is the force:length ratio assignation for the members composing the tensegrity structure).

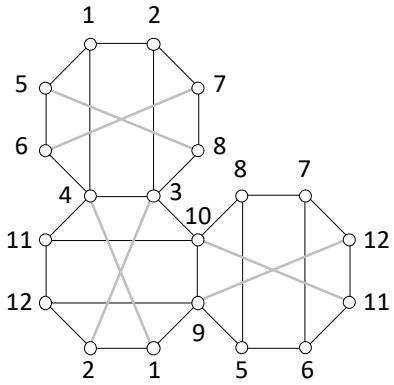

Figure 2. *Plane connection graph of the expanded octahedron composed by the new octagonal cells shown in Fig. 1. Gray and black lines correspond to struts and cables respectively.*

For the expanded octahedron case, two solutions are obtained: $q_b = \frac{1}{8}\left(-19\ q_c - \sqrt{41}\ q_c\right)$ (unstable) and $q_b = \frac{1}{8}\left(-19\ q_c + \sqrt{41}\ q_c\right)$ (super-stable). The equilibrium shape of the super-stable solution is shown in Fig. 3.a.

The double-expanded octahedron composed by the octagonal cell shown in Fig. 1.b has 48 cables, 12 struts and 24 nodes (twice the number of cables, struts and nodes than the expanded octahedron). The connectivity of the new double-expanded octahedron has been obtained as in the previous case: by replacing the octagonal cell shown in Fig. 1.a by the new one shown in Fig. 1.b in the corresponding plane connection graph proposed in [5]. The plane connection graph has not been represented in this work due to size limitations. In this case, four solutions are obtained: $q_b = \frac{1}{8}\left(-19\ q_c - \sqrt{41}\ q_c\right)$ (unstable) and $q_b = \frac{1}{8}\left(-19\ q_c + \sqrt{41}\ q_c\right)$ (stable), $q_b = \frac{1}{8}\left(-11\ q_c - \sqrt{41}\ q_c\right)$ (unstable), and $q_b = \frac{1}{8}\left(-11\ q_c + \sqrt{41}\ q_c\right)$ (super-stable). It has to be pointed out that the solutions corresponding to the expanded octahedron case are also solutions of the form-finding problem in the double-expanded octahedron case. This is because the expanded octahedron is a folded form of the double-expanded octahedron. The equilibrium shape of the super-stable solution is shown in Fig. 3.b.

Finally, the triple-expanded octahedron composed by the octagonal cell shown in Fig. 1.b has 96 cables, 24 struts and 48 nodes (twice the number of cables, struts and nodes than the double-expanded octahedron). The plane connection graph has not been represented in this work due to size limitations. In this case, four solutions are obtained: $q_b = \frac{1}{8}\left(-19\ q_c - \sqrt{41}\ q_c\right)$ (unstable) and $q_b =$

$\frac{1}{8}\left(-19\,q_c+\sqrt{41}\,q_c\right)$ (unstable), $q_b=\frac{1}{8}\left(-11\,q_c-\sqrt{41}\,q_c\right)$ (unstable), $q_b=\frac{1}{8}\left(-11\,q_c+\sqrt{41}\,q_c\right)$ (unstable), $q_b=\frac{1}{161}\left(-270\,q_c-\sqrt{31201}\,q_c\right)$ (unstable), and $q_b=\frac{1}{161}\left(-270\,q_c+\sqrt{31201}\,q_c\right)$ (stable). The equilibrium shape of the stable solution is shown in Fig. 3.c.

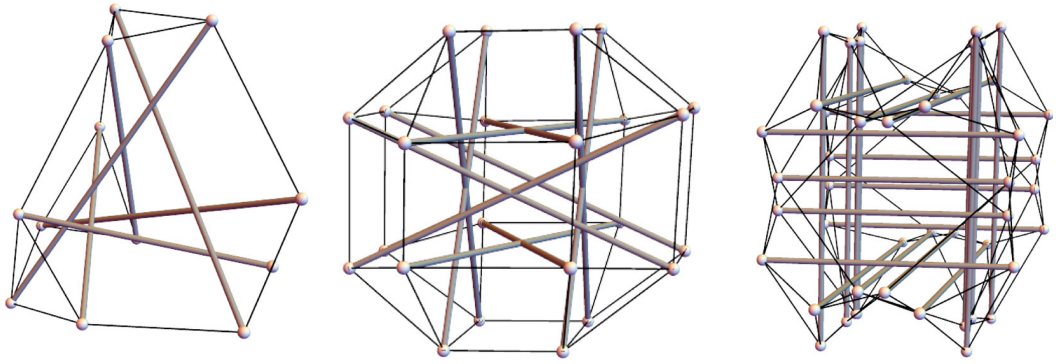

(a) (b) (c)

Figure 3. *Expanded (a), double-expanded (b) and triple-expanded (c) octahedrons composed by the new octagonal cell shown in Fig. 1.b. Gray and black lines correspond to struts and cables respectively.*

4. CONCLUSIONS

New tensegrity structures can be defined based on the cell substitution design method. In this work, a new octagonal cell formed by 10 cables and 2 struts has been defined. Three new tensegrities have been defined: the expanded octahedron, the double-expanded octahedron and the triple-expanded octahedron composed by the new octagonal cell. The first two are super-stable, and the third one is stable. It has been proved that tensegrity families are a great source of stable and super-stable tensegrity structures.

REFERENCES

[1] Zhang, J.Y., Ohsaki, M. (2015). Tensegrity Structures. Form, Stability, and Symmetry. Ed. Springer.

[2] Fernández-Ruiz, M.A., Hernández-Montes, E., Gil-Martín, L.M. (2022). Topological design of the Octahedron tensegrity family. *Engineering Structures, 259, 114211*.

[3] Fernández-Ruiz, M.A., Hernández-Montes, E., Gil-Martín, L.M. (2021). The Octahedron family as a source of tensegrity families: The X-Octahedron family. *International Journal of Solids and Structures, 208–209, 1–12*.

[4] Fernández-Ruiz, M.A., Hernández-Montes, E., Gil-Martín, L.M. (2020). The Z-octahedron family: A new tensegrity family. *Engineering Structures, 222, 111151.*

[5] Fernández-Ruiz, M.A., Hernández-Montes, E., Gil-Martín, L.M. (2022). From octagonal connection graphs belonging to the Z-Octahedron family to new tensegrity structures. *International Journal of Solids and Structures, 254–255, 111901.*

[6] Schek, H.J. (1974). The force density method for form-finding and computation of general networks. *Computer Methods in Applied Mechanics and Engineering, 3, 115–34.*

Numerical analysis of beam-to-column joints with threaded bars

López, Manuel[1]; Loureiro, Alfonso[1]; Gutiérrez, Ruth María[1]; Reinosa, José Manuel[1]

ABSTRACT

This article deals with the behaviour of an asymmetric bolted joint with threaded bars. A finite element model has been developed to obtain the stiffness and resistance of the joint. A comparison with traditional bolts has been made showing an increase in stiffness and resistance in the connection of both the minor and the major beam.

Keywords: steel joints, finite element analysis, component method, threaded bars, Eurocode 3.

1. INTRODUCCIÓN.

Las uniones atornilladas juegan un papel fundamental en el comportamiento de las estructuras de acero, por lo que continuamente se desarrollan nuevos modelos y tipologías para satisfacer las exigencias del mercado [1-3]. Las uniones con tornillos pasantes ofrecen varias ventajas con respecto a las uniones con tornillos tradicionales como son el aumento de la rigidez y de la resistencia de la unión.

En este artículo se analiza una unión asimétrica de chapa de testa con tornillos pasantes, y se compara con la misma solución realizada con tornillos tradicionales (Fig. 1). Para caracterizar la unión se calcula la rigidez y resistencia de las conexiones mayor y menor mediante un análisis numérico por elementos finitos. Los resultados muestran que el uso de tornillos pasantes incrementa la rigidez y resistencia tanto para la conexión mayor como menor. Siendo la menor la que sufre un incremento más relevante.

2. DESCRIPCIÓN DEL ESTUDIO

El estudio se centra en una unión de doble cara asimétrica con chapas de testa. En la Fig. 1 se representan las uniones estudiadas, la figura de la izquierda está resuelta con tornillos pasantes y la de la derecha con tornillos tradicionales. Las características geométricas son idénticas para ambas, siendo el perfil de la columna un HEA200, la viga mayor un IPE300 y la menor un IPE200. Los tornillos son de M20 y las chapas de testa tienen un espesor de 12mm.

3. MODELO DE ELEMENTOS FINITOS

El análisis por elementos finitos fue realizado con Abaqus. Se utilizaron elementos solidos con integración reducida y control de hourglass (C3D8R). La Fig.2 muestra los modelos, siendo el de la izquierda con tornillos pasantes y el de la derecha con tornillos tradicionales. La validación del modelo se realizó basándose en la experiencia de trabajos previos [2,4].

[1] *Laboratory of Structural Analysis. University of A Coruña. (SPAIN). manuel.lopez.lopez@udc.es (Corresponding author). a.loureiro@udc.es. ruth.gutierrez@udc.es. j.reinosa@udc.es.*

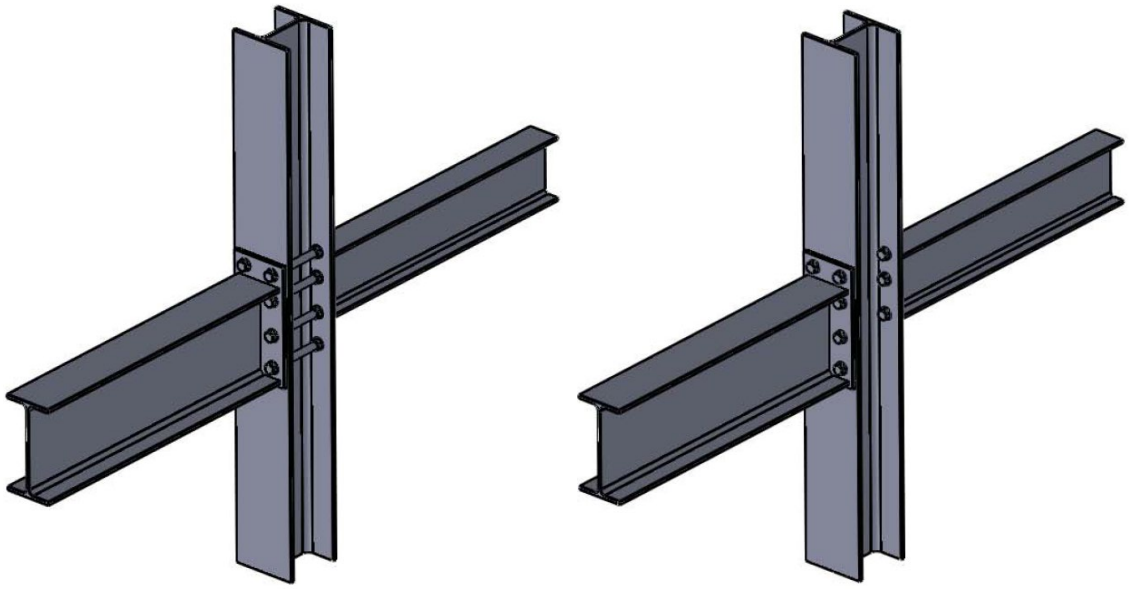

Figura 1. *Unión atornillada. Con tornillos pasantes (izquierda) con tornillos tradicionales (derecha)*

El material utilizado para la columna, vigas y chapas de testa fue S275 con valores nominales. Los tornillos fueron modelados como clase 10.9. La respuesta inelástica del material se basa en la tensión de von Mises. Se tuvieron en cuenta las no linealidades de material y geométricas.

El modelo está compuesto por columna, vigas, chapas de testa y tornillos. Los tornillos han sido modelizados como una sola pieza. Se ha utilizado una malla de densidad variable siendo el tamaño de elemento en zonas con concentración de tensiones de 10mm. Se han modelizado contactos tipo duro entre los tornillos-chapa de testa, entre pilar-chapa de testa y tornillos-pilar. El coeficiente de fricción fue de 0.25.

Las fuerzas fueron aplicadas en los extremos de las vigas considerando la sección de aplicación como rígida. El pilar se considera articulado en ambos extremos.

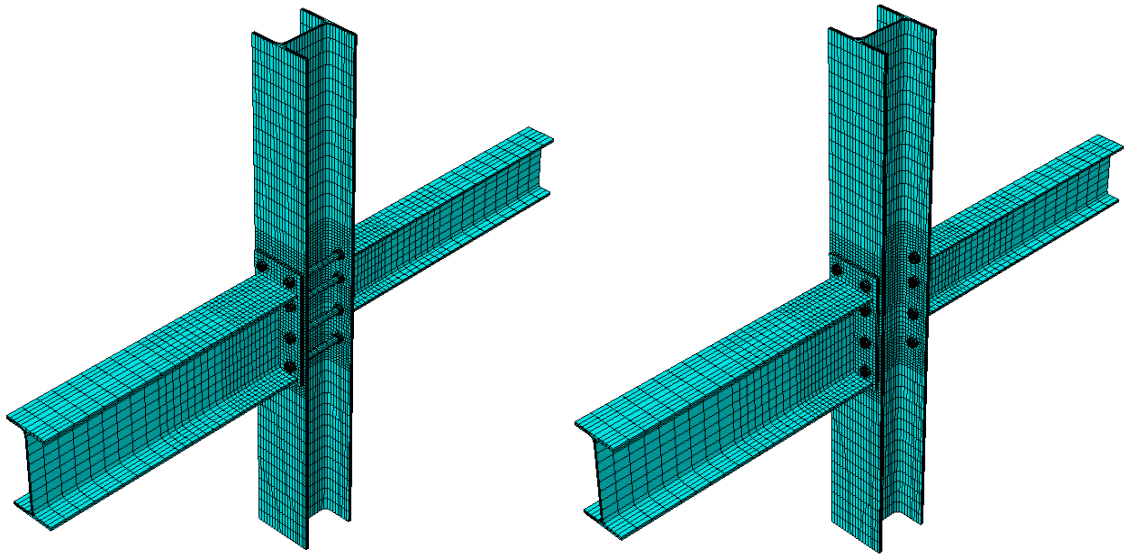

Figura 2. *Modelo de elementos finitos. Con tornillos pasantes (izquierda) con tornillos tradicionales (derecha)*

4. RESULTADOS

En la Fig. 3 se puede ver la tensión de von Mises en las dos configuraciones estudiadas, al inicio de la zona plástica. Como se puede observar en las imágenes, el caso de los tornillos tradicionales tiene una concentración de tensiones superior al caso de tornillos pasantes en la zona del ala del pilar a flexión. También se puede observar una mayor deformación del ala a flexión, lo que genera una rotación mayor en la conexión de la viga mayor.

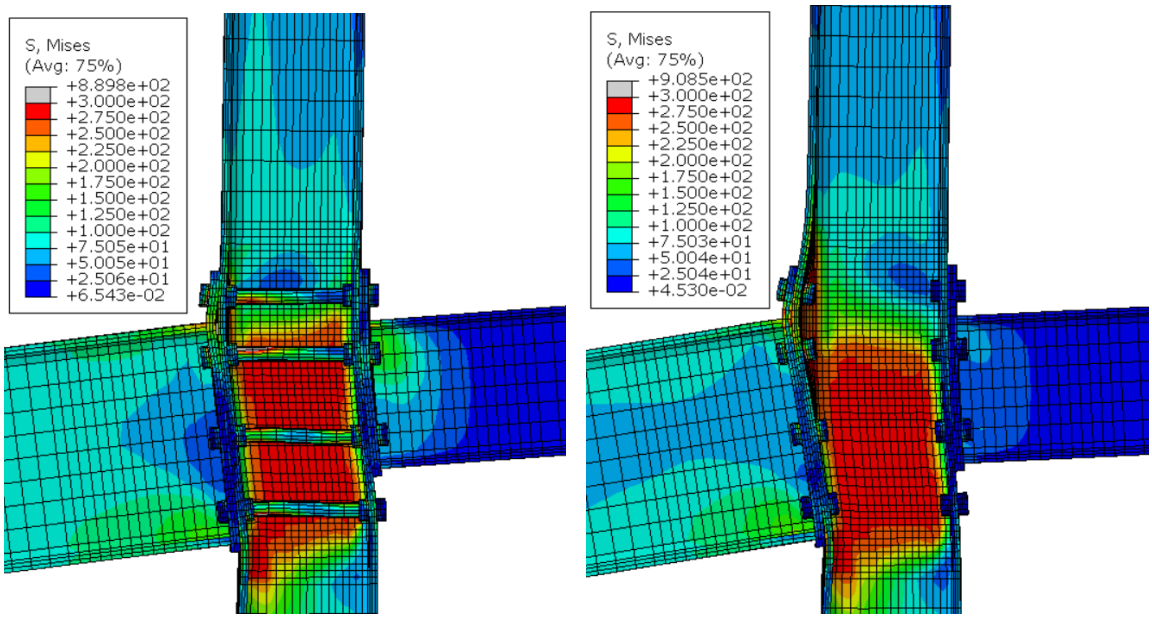

Figura 3. *Tensión de von Mises cargando en la viga mayor. Tornillos pasantes (izquierda) y tornillos tradicionales (derecha). Factor de escala 10.*

La Fig. 4 muestra las comparativa de las curvas momento rotación para la viga mayor y menor en las subfiguras de izquierda y derecha, respectivamente. El ángulo de rotación de las vigas se calcula a partir del desplazamiento vertical de dos puntos situados en el centro del alma de la viga y separados 60mm. El centro de estos puntos está situado a una distancia del ala del pilar de 90 mm, para evitar la influencia de posibles deformaciones locales del alma de la viga. El momento de la unión es la fuerza aplicada en el extremo de la viga multiplicada por la distancia al ala del perfil del pilar, que son 1000mm.

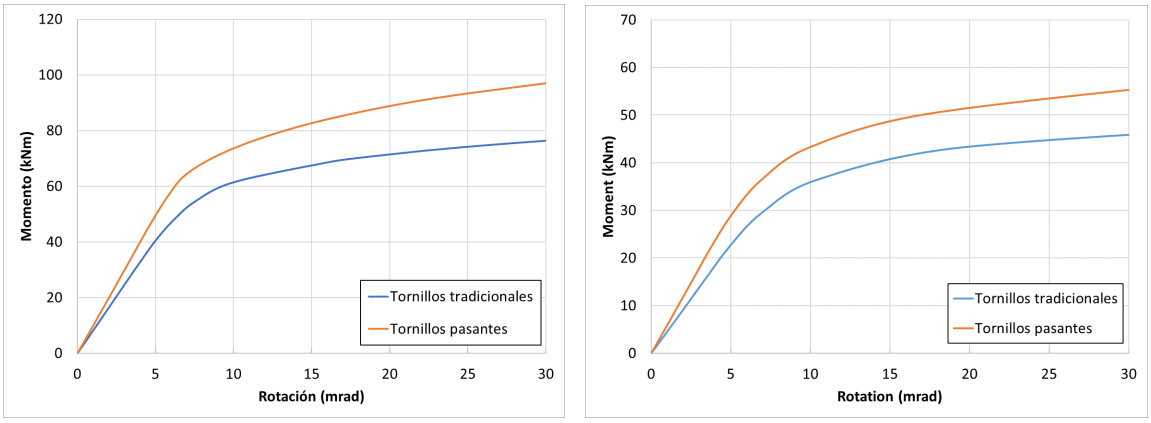

Figura 4. *Curvas Momento-Rotación. Viga mayor (izquierda) viga menor (derecha).*

En la Tabla 1 se comparan las rigideces las uniones con tornillos tradicionales y pasantes, obteniendo un incremento de 22% en la conexión mayor y 30% en la conexión de la viga menor.

La Tabla 2 analiza los efectos en la resistencia, obteniéndose un incremento de 24% de incremento para la conexión de la viga mayor y un 26% en la conexión de la viga menor

Tabla 1. Rigidez

Rigidez (kNm/mrad)	**Valor**		
	Tornillos pasantes	Tornillos tradicionales	Incremento (%)
Viga mayor	9.8	8.1	22%
Viga menor	5.9	4.5	30%

Tabla 2. Resistencia

Resistencia (kNm)	**Valor**		
	Tornillos pasantes	Tornillos tradicionales	Incremento (%)
Viga mayor	82.0	66.0	24%
Viga menor	51.5	41.0	26%

5. CONCLUSIONES

Los tornillos pasantes aumentan la resistencia y rigidizan la unión. En el caso estudiado, el incremento medio fue de aproximadamente un 25%.

Las deformaciones y tensiones, en la zona del ala del pilar a flexión de la unión con tornillos pasantes es sustancialmente menor, que en la unión con tornillos tradicionales. Lo que indica que los componentes, ala de la columna a flexión y alma del pilar a tracción, son más rígidos y resistentes.

AGRADECIMIENTOS

Los autores agradecen al Ministerio de Ciencia e Innovación y al Fondo Europeo de Desarrollo Regional el apoyo financiero recibido para este estudio (proyecto PID2020-113895GB-C31).

REFERENCIAS

[1] Faella, C.; Piluso, V.; Rizzano, G. (2000) Structural steel semirigid connections: Theory, design and software. Boca Raton (Florida): CRC Publishers.

[2] Bayo, E.; Loureiro, A.; Lopez, M.; Simões da Silva, L. (2017) General component based cruciform finite elements to model 2D steel joints with beams of equal and different depths. *Engineering Structures* 152, 698-708.

[3] Gil-Martín, L.M.; Hernández-Montes, E. (2019) A compact and simpler formulation of the component method for steel connections. *Journal of Constructional Steel Research* 164, 105782.

[4] Lopez, M.; Loureiro, A.; Gutierrez, R.; Reinosa, J.M. (2021) A new analytical formulation for the stiffness and resistance of the additional plate in bending in beam-to-beam steel joints. *Engineering Structures* 228, 111476.

Numerical modeling for the analysis of cold-formed steel joints, focused on parametric design

Gutiérrez, Ruth[1]; Loureiro, Alfonso[1]; Reinosa, José Manuel[1]; López, Manuel[1]

ABSTRACT

Joints behavior are an important element in the structural analysis, that enables more accurate results, contributing to a more rational and efficient structural design. Traditionally, numerical models of joints are carried out with brick finite elements. They are accurate models with a high computational cost. Shell finite elements models are more efficient to do parametric optimization (DOE, approximation and optimization models). In this work, a numerical model of a sleeve joint used in the assembly of roof purlins in industrial buildings is developed. The cold-formed profiles are modeled with shell finite elements. The aim is to simulate an experimental test published in the literature, including the connection behavior through fasteners and connectors.

An efficient and accurate numerical model is presented, calibrated with experimental results, which includes the joints behavior and constitutes a suitable numerical tool for parametric design.

Keywords: Modeling, steel joint, semirigid, connector, fastener.

1. INTRODUCCIÓN

Para montar las correas en las naves industriales se utilizan habitualmente dos tipos de uniones atornilladas, la unión de solape y la unión de casquillo. En trabajos previos, se han estudiado experimentalmente las uniones de casquillo [1], así como numéricamente, empleando modelos basados en elementos sólidos, tipo brick [2].

En este trabajo se desarrolla un modelo de láminas de una unión de casquillo entre perfiles de pared delgada, empleada en el montaje de correas de cubierta en edificación industrial. Estos elementos presentan ventajas relacionadas con la agilidad del modelado, del mallado y con el coste computacional. Son modelos con la agilidad necesaria para abordar el problema de diseño con optimización paramétrica (DOE, modelos de aproximación y optimización) que requiere ejecutar el modelo computacional un elevado número de veces.

Con respecto a la modelización de uniones atornilladas, los elementos lámina no pueden modelar el contacto de las paredes de los agujeros contra la superficie del perno de los tornillos. Una manera de introducir las uniones en estos modelos láminas es mediante fasteners y conectores. El objetivo es simular un ensayo experimental publicado en la literatura [1] mediante un modelo ágil, introduciendo las

[1] *Departamento de ingeniería naval e industrial. Universidade da Coruña (ESPAÑA). ruth.gutierrez@udc.es (Corresponding author). a.loureiro@udc.es. j.reinosa@udc.es. manuel.lopez.lopez@udc.es*

simplificaciones necesarias, pero con un nivel de detalle suficiente, para cuestionar el diseño de esta unión atornillada de casquillo.

2. MODELADO DE LAS UNIONES ATORNILLADAS

Los fasteners [3] son elementos que permiten aplicar una ecuación de restricción al movimiento entre los nudos situados en dos regiones con forma circular, pertenecientes a dos láminas distintas. En este trabajo se usan los fasteners discretos que van asociados con conectores. Los conectores [4] son elementos lineales que enlazan dos puntos, con 6 grados de libertad cada uno, restringiendo o permitiendo el movimiento relativo entre dichos puntos. En los grados de libertad con movimiento relativo permitido se puede aplicar un comportamiento, que permite introducir elasticidad, plasticidad, daño, parada y fallo entre los mencionados puntos. Al asociarse con los fasteners, se puede introducir el comportamiento elástico de los tornillos entre las regiones de nudos que los fasteners enlazan.

En este trabajo se emplean conectores tipo bushing [5], que no restringen ninguna componente de movimiento relativo. Las orientaciones locales del conector son la combinación de proyecciones cartesianas y proyecciones de flexo-torsión. Se introduce un comportamiento elástico en los ejes locales del conector, definidos en la línea que lo define y en el plano perpendicular a la misma.

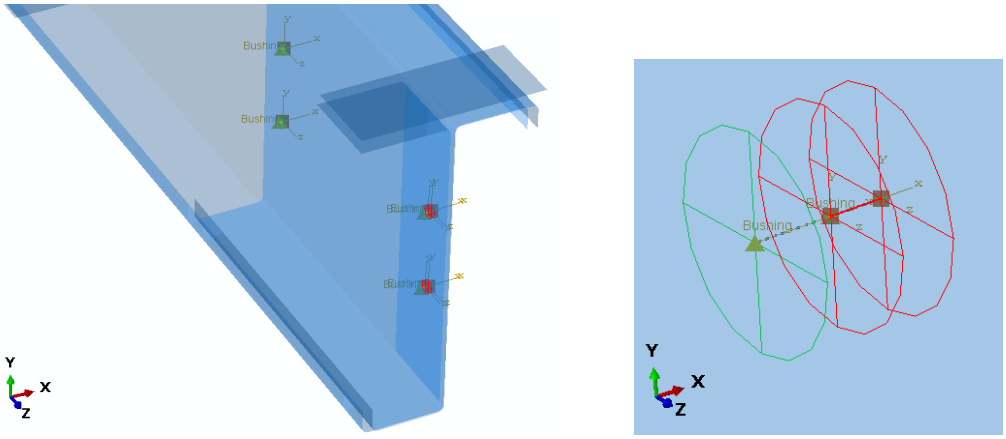

Figura 1. *Modelado de los puntos de conexión en la unión atornillada de casquillo. (a) Ensamblaje (b) Detalle de un punto de conexión entre la correa, el casquillo y el ejión.*

Los fasteners permiten aplicar la restricción del movimiento de todos los nudos incluidos en una región circular, en un sentido promedio, sin distorsionar la malla. Así tenemos un modelo en el que resulta sistemático para remallar, característica importante para estudios numéricos en los que se trabaja con una geometría parametrizada.

Este tipo de modelado no puede representar el problema de contacto/separación entre las superficies de los agujeros y de los pernos. Lo que puede resultar importante para el estudio del fallo por rasgado (por ejemplo) de los agujeros de la chapa una unión entre elementos conformados en frío. En la literatura se pueden encontrar ejemplos de modelado combinado, los elementos planos de la unión con láminas incluyendo elementos solidos alrededor de los agujeros de los tornillos y permitiendo mayor precisión para el problema de contacto [6].

El planteamiento de láminas junto con fasteners y conectores es adecuado para el estudio de la unión en régimen lineal, que es la zona de trabajo habitual. El modelo se plantea para entender y mejorar el

diseño en estudios posteriores que permitan determinar las variables geométricas y parámetros mecánicos más influyentes [7].

3. SIMULACIÓN DEL COMPORTAMIENTO DE UNA UNIÓN ATORNILLADA DE CASQUILLO

El ensayo experimental de la unión de casquillo puede verse en detalle en la referencia [1]. Se trata de un montaje especialmente diseñado para cargar la unión con unos esfuerzos similares a los que soporta en condiciones de trabajo bajo carga gravitatoria. Consiste en 2 vigas simplemente apoyadas formadas con perfil conformado en frío, con sección transversal en Z. Estas vigas se sitúan con las zetas enfrentadas y se unen superior e inferiormente en puntos discretos, para evitar el pandeo lateral (ver Fig. 2). La unión de casquillo se materializa en el centro de cada viga. Consiste en un trozo de perfil en Z que solapa ambos perfiles y va atornillado por el alma. Se sitúa invertido, para encajar en la unión.

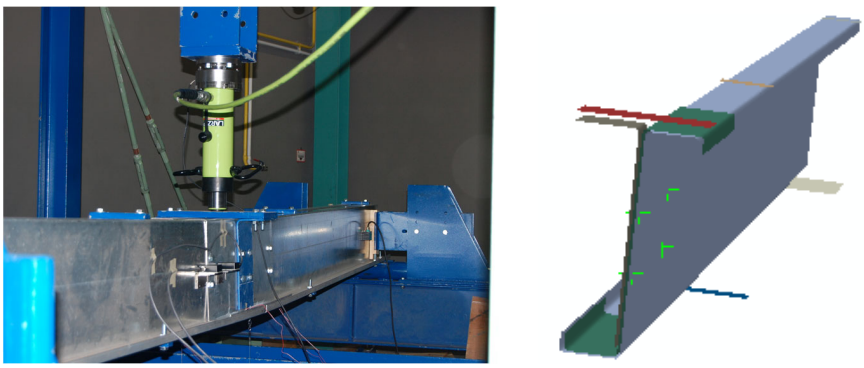

Figura 2. *Montaje experimental y modelo numérico para el estudio de una unión atornillada de casquillo.*

El modelo de elementos finitos considera el doble plano de simetría de este montaje experimental. La simulación se realiza mediante un análisis general cuasiestático, con el motor de cálculo Explicit de Abaqus, que incluye la no linealidad geométrica y del material. Se consideran las propiedades nominales de un acero S275, con un modelo de comportamiento elástico perfectamente plástico. Se resuelve el problema de contacto con fricción entre los perfiles, el casquillo, las chapas de unión, de apoyo y de carga, que se modelan con geometrías laminares.

Tabla 1. Propiedades mecánicas de los conectores

Conector 1 - Rigidez casquillo-correa		**Conector 2 - Rigidez correa-ejión**	
Axial	7.92E6 N/mm	Axial	5.28E6 N/mm
Cortante	1.18E5 N/mm	Cortante	9.71E4 N/mm

Los conectores introducen un comportamiento elástico, con los valores de rigidez axial y cortante de la tabla 1. Se considera la deformación axial, por cortadura y por flexión del perno además de las deformaciones por aplastamiento de la chapa.

4. RESULTADOS Y CONCLUSIONES

La Fig. 3 muestra la curva fuerza desplazamiento de la unión de atornillada de casquillo del modelo de láminas presentado. En ella se comparan los resultados de un ensayo experimental y con un modelo teórico tradicional de viga continua (sin unión en el centro) con un comportamiento elástico perfectamente plástico.

Esta unión tiene una longitud de casquillo reducida, lo que implica un comportamiento semirrígido con una zona de comportamiento lineal muy pequeña. El comportamiento real de la unión es distinto del predicho por modelos tradicionales de cálculo de correas, que consideran una viga continua con múltiples apoyos. Así, la rigidez experimental es menor que la del modelo tradicional (viga continua) por lo que el análisis que no considere la rigidez de la unión quedará del lado de la inseguridad.

El modelo de láminas presentado, reproduce correctamente los resultados experimentales en la zona de diseño, la zona elástica y lineal de la unión, incluyendo el comportamiento de las uniones, con lo que resulta una herramienta útil para cuestionar y mejorar el diseño de la unión, con herramientas que permitan abordar estos estudios de forma automatizada.

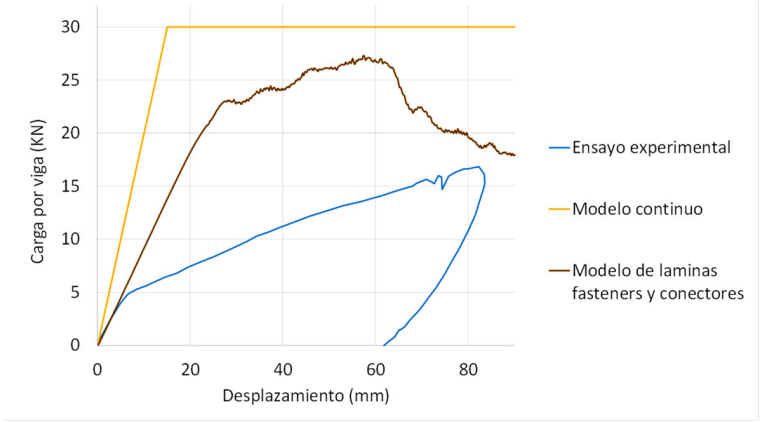

Figura 3. *Curva fuerza-desplazamiento de una unión atornillada de casquillo; comparación del modelo teórico tradicional, del modelo de láminas presentado y de un ensayo experimental.*

AGRADECIMIENTOS

Los autores agradecen el apoyo financiero proporcionado a través del proyecto PID2020-113895GB-C31 del MCIN/AEI/10.13039/501100011033.

REFERENCIAS

[1] Gutierrez, R., Loureiro, A., Lopez, M., & Moreno, A. (2011). Analysis of cold-formed purlins with slotted sleeve connections. *Thin-Walled Structures*, 49, 7, 833–841.

[2] Gutierrez, R., Loureiro, A., Reinosa, J. M., & Lopez, M. (2015). Numerical study of purlin joints with sleeve connections. *Thin-Walled Structures*, 94, 214–224.

[3] Dassault Systemes Simulia Corp. © 1995-2023 Dassault Systèmes. Abaqus CAE, Modelling techniques, Fasteners. *Fasteners - 2022 - dssimulia_established*.

[4] Dassault Systemes Simulia Corp. © 1995-2023 Dassault Systèmes. Abaqus CAE, Modelling techniques, Connectors. *Connectors - 2022 - dssimulia_established*, 3.

[5] Dassault Systémes Simulia Corp. (2014). Abaqus Analisys User's Guide, Volumne IV, 31 Connector Elements. *Providence, RI, USA: Abaqus Documentation*.

[6] Ye, J., Quan, G., Yun, X., Guo, X., & Chen J. (2022). An improved and robust finite element model for simulation of thin-walled steel bolted connections, *Engineering Structures*, 250, 113368.

[7] Kyvelou, P., Kyprianou, C., Gardner, L., & Nethercot, D. A. (2019). Challenges and solutions associated with the simulation and design of cold-formed steel structural systems. *Thin-Walled Structures*, 141, April, 526–539.

Numerical study on the dynamic response of external post-tensioning tendons under strand breakages

Vecino, Belén[1]; Naranjo-Pérez, Javier[1,2]; M.C. Renedo, Carlos[1]; García-Palacios, Jaime H.[1]; M. Díaz, Iván[1]

ABSTRACT

Non-destructive testing (NDT) techniques based on vibration methods can be used to detect anomalies in external post-tensioning tendons. In this sense, a numerical study on the dynamic response of a tendon is carried out under strand breakages. In order to quantify the sensitivity of several performance indicators (PIs) to strand breakage. The indicators are: the natural frequencies, the ratios between them and the modal shape symmetry. Thus, firstly, the partial differential equation that governs the cable displacement including bending stiffness is solved. Secondly, a detailed 3D finite element (FE) model of a seven-strand tendon is developed. An elastic contact model between strands and grout has been assumed. Finally, the performance indicators together with the effective tension force are assessed for the simulation steps in such a way that their effectiveness as damage indicator tool for vibration-based NDT is assessed.

Keywords: Post-tensioned tendon, Finite element, Cable dynamics; Vibration based monitoring, Non-destructive testing.

1. INTRODUCTION

Recently, several failures have been detected in external post-tensioning tendons due to brittle breakage in stress corrosion cracking situations (interaction of corrosion and mechanical stress) [1]. Tendon failures can affect both serviceability and safety. Two examples of bridge collapses are: Viaducto O Castro A-6 (Lugo), 2022 and Morandi bridge, Genova (Italy), 2018. Thus, the use of non-destructive testing (NDT) techniques to detect potential tendon deterioration is essential to plan the tendon maintenance and anticipate damage. A vibration-based NDT technique can be used in intermittent and continuous monitoring for damage detection. This NDT technique relies on the sensitivity of some structural performance indicators (PIs) to damage, such as: the natural frequencies, the ratios between them and the modal shape symmetry. Structural damage can be represented by deviations of these indicator's normal values during the monitoring process.

2. ANALYTICAL MODEL

A tendon can be analysed as a cable with non-negligible bending stiffness. To quantify the PI sensitivity to tendon damage, an analytical model of a 10-meter cable with non-negligible bending stiffness is studied. Using taut spring theory, considering a uniform cable and constant tension force, the partial equation governing the tendon free response is:

[1] *Department of Continuum Mechanics and Theory of Structures. E.T.S.I. Caminos, Canales y Puertos, Universidad Politécnica de Madrid (SPAIN). b.vecino@alumnos.upm.es (Corresponding author), javier.naranjo@externos.upm.es, carlos.martindelaconcha@upm.es, jaime.garcia.palacios@upm.es, ivan.munoz@upm.es.*

$$EI\,\frac{\partial^4 u(x,t)}{\partial x^4} - T\frac{\partial^2 u(x,t)}{\partial x^2} + m\frac{\partial^2 u(x,t)}{\partial t^2} = 0 \qquad (1)$$

where $u(x,t)$ is the transverse displacement, $m(x)$ is the mass per unit linear length, *T(x)* is the tension force, E is Young's modulus and $I(x)$ is the moment of inertia of the cross-section [2]. This partial equation is solved considering three tendon segments to simulate damage by varying the bending stiffness (EI) or the tension (T) in the central section (Fig. 1).

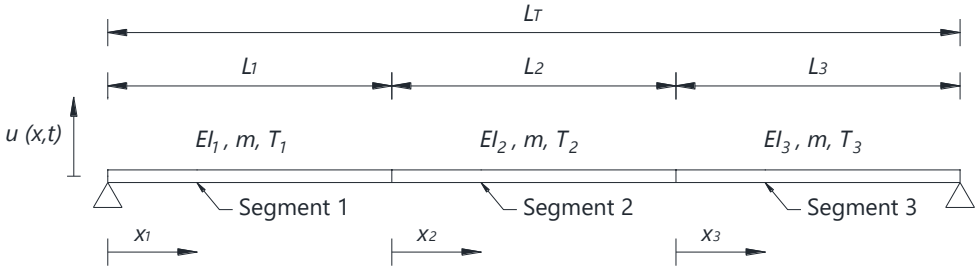

Figure 1. *Cable with non-negligible bending stiffness considering three different segments.*

Considering perfect continuity between segments, thus displacements, rotations, bending moments and shear forces are equal, the partial equation can be solved. The central part's length is considered as 10% of the total cable length, its parameters (EI_2 and T_2) are modified to simulate damage. Two analyses are carried out: i) bending stiffness reduction, ii) tension force reduction.

3. DETAILED FE MODEL

A detailed FE model of a seven-strand and horizontal tendon of 10 m length is developed considering the strand-grout interaction (an elastic contact model is assumed). Both, the tendon behaviour under strand breakages and the variations are analysed.

Thus, the strands are designed with a split element in their central section to simulate strand breakages by deactivating the contact between the two sides of the strand (strand-strand contact), which initially are modelled with a bonded contact to guarantee its continuity before breakage. 3D Solid elements are used for this model. Sweep meshing method has been used so that the positions of the nodes match with those of the grout in each section. Both ends of the seven strands are modelled with fixed support. The stress states reached by stressing the strands are modelled by thermal loads. Two stressing states are considered: 40% and 70% of the minimum ultimate load of a prestressing strand [3]. The stressing forces considered are 775 kN and 1241 kN, respectively. A lineal elastic surface-to-surface contact model between the grout and the strands is assumed. Considering self-anchoring and the 30 cm transfer length [4] the contact stiffness adopted is $k = 1 \cdot 10^{15}$ N/m^2/m.

A non-linear analysis by load steps is then performed. A sparse direct solver and the Newton-Raphson algorithm with convergence in forces and displacements are used. The non-linearity is caused by the activation and deactivation of contacts, which is solved by the "Pure Penalty" methodology, whereas materials are kept elastic. The followed steps are: i) Stressing of strands by applying a thermal load, ii) Activation of strand-grout contacts to simulate the grout injection and iii) Successive breakage of strands by deactivating the strand-strand contacts (Fig. 2). A modal analysis is carried out following each strand breakage.

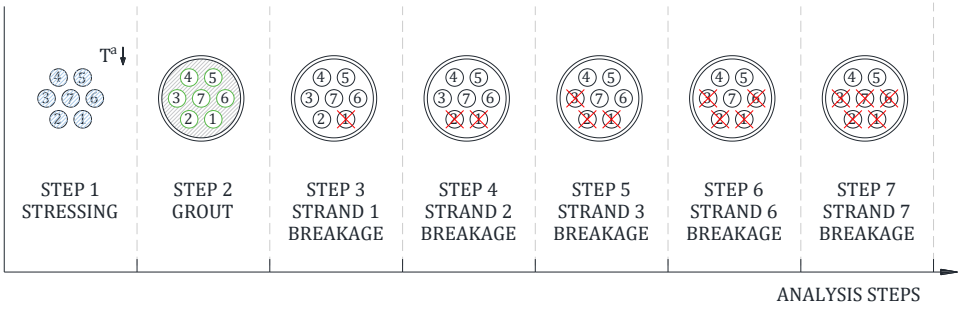

Figure 2. *FE analysis steps*

4. DISCUSSION OF RESULTS

4.1. Analytical model

The changes on PIs obtained by reducing the bending stiffness are negligible. Thus, the tension reduction results are discussed. Both the frequencies and the ratios are representative of damage presence as tension reduction occurs. Frequencies are the most sensitive indicator, especially the higher frequencies. Fig. 3 shows the results for the ninth frequency.

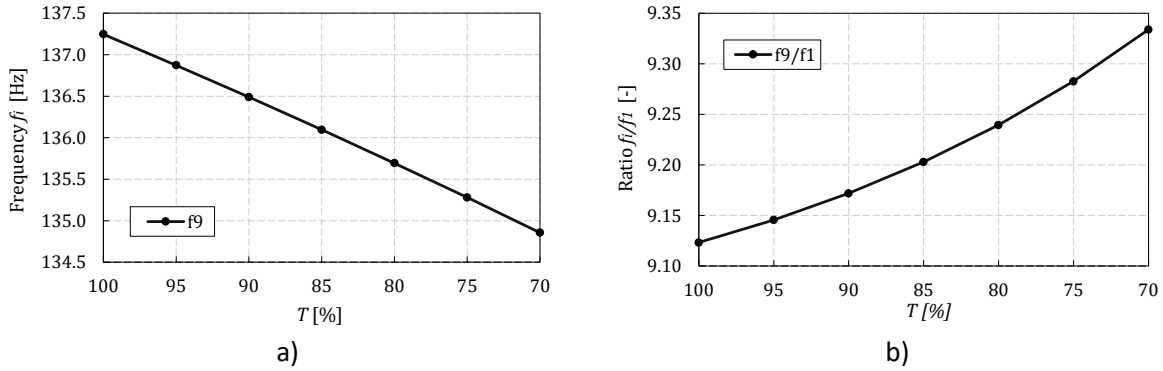

Figure 3. *Analytical model tension reduction results. a) Frequency b) Ratios*

4.2. FE model

The frequencies and stressing force values are compared with the experimental results obtained in [3]. The results follow similar trends; however, differences arise in the damage intermediate levels mainly due to the high stiffness contact and the purely elastic materials assumed. The results show that a tendon anomaly is detected, as both the frequencies and the stressing force are lower as the damage increases (Fig. 4a and Fig. 4b).

The normal stresses along the strand 2 with successive strand breakages (strands 1,2,3,6 and 7) is shown in Fig. 4c. The results show that stress of a strand increases when a neighbour strand breaks. When breakage occurs, the broken strand normal stress is only lost in the surroundings of the broken section because of the self-anchorage phenomena. Due to the high stiffness of the elastic grout-strand contact assumed, the relative sliding only takes place in the transfer length, the remaining length approximately keeps its stresses. The FE model reproduces with some limitations the mechanical behaviour of a prestressed tendon under successive breakages. Self-anchoring is fundamental to understanding why stressing forces do not decrease proportionally with the area of steel lost in the strand. The high stiffness contact may not be the most suitable, leading to an overestimation of the results compared to reality. The non-consideration of plasticity causes the stress redistribution when a strand breaks to be non-uniform,

which seems to conclude that the stress redistribution in the strand is governed by the plastic nature of the steel.

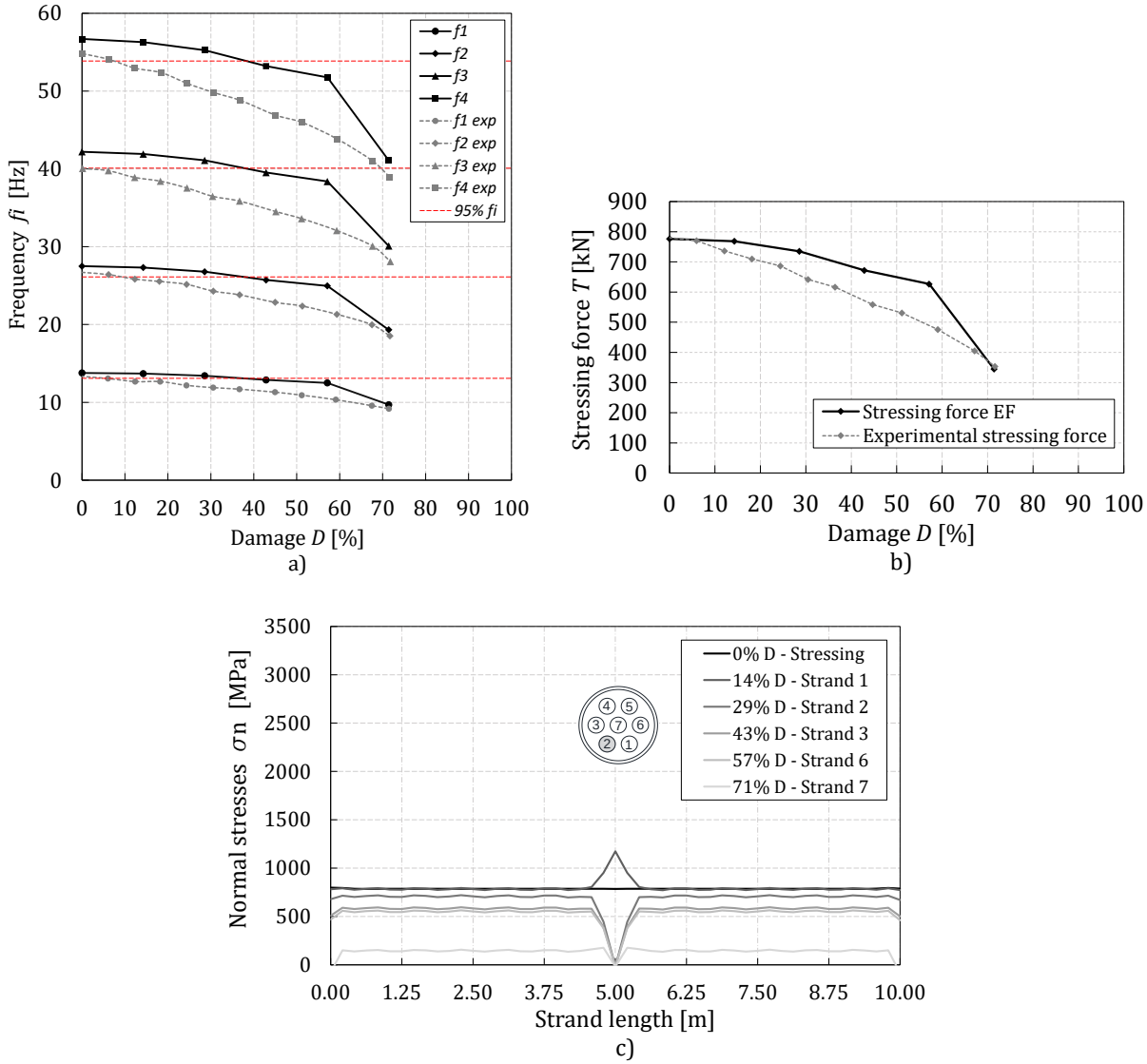

Figure 4. *FE results. a) Frequency b) Stressing force c) Normal stress along the strand 2*

ACKNOLEDGEMENTS

Research project PID2021-127627OB-I00 funded by MCIN/ AEI / 10.13039/501100011033 / FEDER, EU

REFERENCES

[1] Texas Transportation Institute (2009). Effect of voids in grouted, post-tensioned concrete bridge construction: Volume 1 – Electrochemical testing and reliability assessment. College Station, Texas.

[2] Rao, S. S. (2007). Vibration of Continuous Systems. Coral Gables, Florida: John Wiley & Sons.

[3] Lee, J. K., & Kang, J. W. (2019). Experimental Evaluation of Vibration Response of External Post-Tensioned Tendons with Corrosion. KSCE Journal of Civil Engineering, Volume 23, 2561-2572. doi: https://doi.org/10.1007/s12205-019-0735-5

[4] Russell, B., & Burns, N. (1993). Design guidelines for transfer, development and debonding of large

Performance characteristics of concrete packaged with electric arc furnace slag to replace average aggregate

Parrón-Rubio, María Eugenia[1]; Pérez-García, Francisca[1]; Oliveira, Miguel José[2]; Rubio-Cintas, María Dolores[3]

ABSTRACT

One of the objectives sought today is the reuse of any type of waste and converting it into raw material for reuse. The study of different components in concrete for materials that go to landfill, minimizing the impact it causes on the environment can be a solution in civil engineering, minimizing risks and carrying out the study of different dosages to obtain an optimal result. This article studies the replacement of cement with different types of slag GGBFS (Ground Granulated Blast Furnace Slag) and LFS (Ground Granulated Blast Furnace Slag), at a percentage of 50%, with aggregates.

Keywords: Concrete, electric arc furnace, ecological concrete, steel slag.

1. INTRODUCCIÓN

Uno de los principales factores a estudiar hoy día, en la producción de cualquier producto, es garantizar un planeta sostenible, en un contexto tanto de vida, como de trabajo saludable y seguro, causando el menor impacto en el medio ambiente.

Durante muchos años, en nuestra sociedad ha predominado la economía lineal, utilizando materias primas para fabricar productos, desechando los residuos que se generaban. Poco a poco, en los procesos de fabricación, se han ido introduciendo residuos como materia prima, para la generación de productos nuevos, como ejemplo, en las dosificaciones de hormigón. Lo interesante es que todo aquel residuo que se genere en la industria, tenga una segunda vida, y que poco a poco, se vayan incluyendo en otro tipo de productos, y así, reducir los vertederos hasta su casi posible extinción[1].

Por otro lado, uno de los principales problemas de la industria siderúrgica, es la generación de residuos y subproductos que deben procesarse o reutilizarse adecuadamente para promover la sostenibilidad ambiental, siendo uno de estos subproductos, la escoria de acero. La estrategia de sustitución de estos subproductos tiene dos objetivos; la reducción del consumo de materias primas y la gestión de residuos.

El objetivo de este estudio, es sustituir dos tipos distintos de escorias de acerías; una de ellas por el 50% cemento y la otra por el 100% del árido intermedio, y ver los resultados que se obtienen, tanto en su resistencia a flexión, como a compresión.

[1] *Departamento de Ingeniería Civil, Materiales y Fabricación. Universidad de Málaga. (ESPAÑA). mariaeugenia.parrón@uma.es (Corresponding author), perez@uma.es*
[2] *Departamento de Ingeniería Civil. Universidad de Algarve (Portugal). mjolivei@ualg.pt*
[3] *Departamento de Ingeniería Industrial e Ingeniería Civil. Escuela Politécnica Superior de Algeciras, Universidad de Cádiz. (ESPAÑA). mariadolores.rubio@uca.es*

2. MATERIALES

Para la realización de este trabajo se han utilizado los materiales que se describen a continuación.

2.1. Escorias

Según la sociedad de Administraciones Públicas del Gobierno de España, las escorias son residuos "no tóxicos" que pueden ser sólidos o pastosos, no siendo residuos peligrosos, obtenidos de diferentes procesos industriales. Se definen los dos tipos de escorias que se utilizarán, las escorias GGBFS (Ground Granulated Blast Furnace Slag) tal como muestra la Fig. 1. (a) y las escorias LFS (Ground Granulated Blast furnace slag), Fig. 1. (b).

(a) (b)

Figura 1. *Escoria GGBFS (a) y Escoria LFS (b)*

Las GGBFS o escoria de alto horno, es un subproducto del proceso de producción de hierro fundido, durante el cual se forman grandes cantidades de escoria líquida de composición cercana a la del cemento Portland. Se muelen para obtener un polvo de finura comparable a la del cemento.

La escoria granulada de alto horno es un material vítreo granular que varía según la composición química y el método de producción. Debido a sus propiedades cementosas, las escorias GGBFS se pueden utilizar como material cementante complementario [2].

La escoria de horno de arco eléctrico o "escoria negra" se produce durante la fabricación de acero bruto mediante el proceso de horno de arco eléctrico (EAF). La escoria líquida se deja enfriar lentamente al aire formando escoria cristalina. El subproducto EAFS se convierte en un material pedregoso, cohesivo, ligeramente poroso, pesado, duro y tenaz, cuyo color inicial es casi negro, debido a la presencia de óxidos de hierro. Con un posterior refinamiento de dicho acero en el horno cuchara se produce un tipo diferente de escoria, la Ladle Furnace Slag (LFS) o "escoria blanca".

2.2. Cemento y áridos

El cemento utilizado para la preparación de todas las mezclas, ha sido Cemento Portland CEM I 52,5 R, cemento de alta resistencia y sin ningún tipo de añadido. Los áridos utilizados fueron: áridos gruesos (4-16 mm), áridos intermedios (0-4 mm), áridos finos (0-2 mm), agua para consumo doméstico, sin ningún ingrediente que pueda afectar las propiedades del hormigón, aditivo (Aditivo superplastificante).

2.3. Dosificación

La dosificación del hormigón proviene de trabajos previos con distintos tipos de escorias o porcentajes de sustitución [4,5]. Para este trabajo se han realizado dos relaciones diferentes, una para hormigón convencional, definiéndolo como D1 y otra, en la que se sustituye el 50% de cemento por escorias

GGBFS, y el 100% de escorias LFS por el árido intermedio, definiéndolo como D2. Dichas dosificaciones se muestran en la Tabla 1.

Tabla 1. Dosificación del hormigón

Dosificación del hormigón		
Material	**Convencional (D1)Kg/m³**	**GGBFS y LGS (D2)Kg/m³**
Cemento	14,63	7,32
GGBFS	-	7,32
Agua	7,32	7,32
Aditivo	0,25	0,25
Árido 0-2	14,88	14,88
Árido 0-4	34,72	-
Árido 4-16	49,6	49,6
LGS 0-4	-	34,72

3. RESULTADO Y DISCUSIÓN

Las muestras se han sometido a dos tipos de ensayos, resistencia a compresión y resistencia a flexión, cuyos resultados se muestran a continuación.

3.1. Resistencia a compresión.

Los ensayos a compresión se realizaron a 1, 3, 7, 28, 60 y 90 días según las normas EN 12390-3 y EN 12390-4. Se utilizaron 6 probetas por cada mezcla fabricada, por día se utilizaron de promedio 2 probetas por cada ensayo, realizando la rotura mediante una prensa hidráulica, obteniendo los resultados que se muestran en la Fig.2.

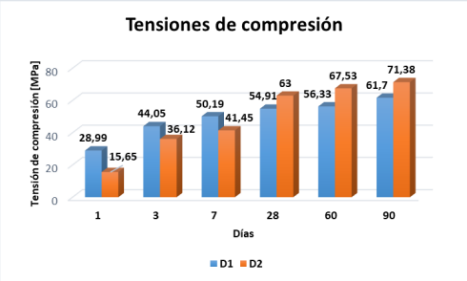

Figura 2. *Tensiones de compresión*

Se observa, que en un principio la capacidad resistente de D1, hormigón convencional, aumenta con respecto a hormigón con adición en un 46,01%. Por el contrario, conforme va aumentando el curado del material, la capacidad resistente de D2 va aumentando, reduciéndose la diferencia a un 17,17%, observando que, a 28 días, supera el hormigón con adición al convencional en un 12,84% y en un 13,56% a 90 días. El aumento de la capacidad resistente con respecto al tiempo, es debido a la hidratación del cemento, puesto que la escoria es un material con características hidráulicas latentes, garantizando por tanto la hidratación del cemento.

3.2. Resistencia a flexión

Para el estudio de la resistencia a flexión se parte de la norma UNE EN 12390-5. Para el desarrollo de este ensayo se han utilizado probetas prismáticas de 40x40x160 mm. Los datos obtenidos se muestran en la Fig. 3.

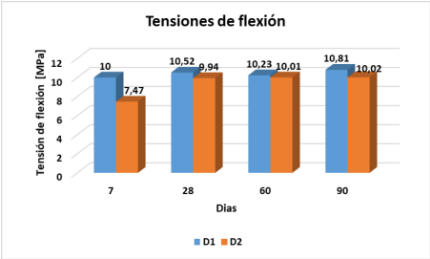

Figura 3. *Resultados de esfuerzos a flexión*

Se observa que a edades tempranas, la capacidad de resistencia a flexión es del 25,3% mayor en el hormigón convencional que en el de sustitución de escorias. Sin embargo, conforme va pasando el tiempo, la capacidad resistente se iguala a todas las edades, estando por debajo del 5% de diferencia prácticamente en todos ensayos realizados.

4. CONCLUSIONES

En este trabajo se refleja que el uso de escorias (GGBFS y LFS) como sustitución de áridos y cemento, es factible para la fabricación de hormigón ecológico, ya que no sólo mantiene la misma capacidad resistente, sino que, en el caso de la resistencia a compresión, la aumenta, siendo éste el resultado más característico del estudio.

De este modo se contribuye a una economía circular y sostenible, ya que es posible utilizar un material de desecho, en la producción de acero que reduce el consumo de materias primas, para la elaboración del hormigón.

REFERENCIAS

[1] Instituto Nacional de Estadística. (Spanish Statistical Office). https://www.ine.es

[2] Duran Atis,C., Bilim, C., (2007). Wet and dry cured compressive strength of concrete containing ground granulated blast-furnace slag. *Building and Environment*, *29, 3060–3065.*

[3] Özalp, F., (2022). Effects of electric arc furnace (EAF) slags on mechanical and permeability properties of paving stone, kerb and concrete pipes. *Construction and Building Materials, 329.*

[4] Rubio-Cintas, M.D., Parrón-Rubio, M.E., Pérez-García, F., Bettencourt-Ribeiro, A., Oliveira, M.J., (2020). Influence of steel slag type on concrete shrinkage. *Sustainability,13.*

[5] Rubio-Cintas, M.D., Barnett, S.J., Pérez-García, F., Parrón-Rubio, M.E., (2019). Mechanical-strength characteristics of concrete made with stainless steel industry wastes as binders. *Construction and Building Materials, 204, 675–683*.

Piezoresistive laminates for structural monitoring. Laboratory application.

Castillo-López, Germán[1]; García-Sánchez, Felipe[1]; Beltrán-Ramos, Jose Bernardo[1]; Germán-Ayuso, Lorena[2]; Neira-Hernández, Santiago[2]

ABSTRACT

The need to reinforce existing structures (degraded structures, modifications in the working conditions of the structure, etc.) is quite common. One of the most commonly used types of reinforcement is laminated composite reinforcement. In previous works, the authors have analyzed the piezoresistive response of nanocomposites based on carbon nanotubes and nanofibers and glass fiber laminates made with nanocomposites. The results have shown their piezoresistive capability. In this work, the ability of these laminates to provide information on the structural state of laboratory demonstrators has been tested. For this purpose, sensitive laminates have been fabricated and bonded to commercial pultrusion beams and subjected to (i) cyclic loading in undamaged and damaged situations and (ii) increased loading until structural failure. The results show that the functionalized resin has a sensitive capability and that the laminates have both sensitive and reinforcing capabilities. Therefore, both solutions are valid for monitoring structural health.

Keywords: Carbon nanofibers, nanocomposites, piezoresistive laminates, structural health monitoring.

1. INTRODUCCIÓN

El ciclo de vida de una estructura se ve comúnmente limitada bien sea por su degradación, bien por los cambios de uso a los se ven sometidas, siendo necesario reforzarlas si se desea alargar su vida útil. Entre las técnicas de refuerzo comúnmente empleadas destaca el uso de laminados de polímeros reforzados (FRP) [1], debido a sus propiedades mecánicas específicas. Por otro lado, durante los últimos veinticinco años se han desarrollado técnicas de monitorizado, [2] [3] por ejemplo, que permiten conocer la salud estructural en tiempo real. La aparición de resinas funcionalizadas con nanocompuestos de carbono que muestran un comportamiento piezorresistivo podría ser un camino para conseguir ese doble objetivo, sensorizar y reforzar una estructura [4].

En un trabajo previo [5], se ha puesto a punto un nanocompuesto de resina comercial epoxi vinilester (DERAKANE® 8084) dopada con un 2% de nanofibras GANF ® (Grupo Antolin Ingeniería). Para analizar la calidad como sensor, se ha utilizado como parámetro, el factor de galga (S_g), definido mediante la Eq. (1), siendo $\Delta R/R_o$ la variación unitaria de resistencia del sensor y ε la deformación unitaria que sufre.

$$S_g = \frac{\Delta R/R_o}{\varepsilon} \quad (1)$$

[1] *Departamento Ingeniería Civil, de Materiales y Fabricación. Escuela de Ingenierías Industriales (ESPAÑA). gcastillo@uma.es (Corresponding author). fgsanchez@uma.es. jbbeltran@uma.es.*

[2] *Gaiker Technology Centre. Basque Research and Tehnology Alliance (BRTA) (ESPAÑA). german@gaiker.es. neira@gaiker.es.*

En este nanocompuesto se observó una buena dispersión de la nanofibra en la resina, una viscosidad compatible con procesos de fabricación de materiales compuestos, polarización prácticamente nula y un factor de galga comparable a los valores de sensores comerciales: $S_g = 3{,}60 \pm 0{,}18$, con un buen comportamiento tras un proceso de envejecimiento medioambiental: $S_g = 2{,}80 \pm 0{,}04$.

Posteriormente [6], se estudió el comportamiento de placas de fibra de vidrio fabricadas mediante infusión del nanocompuesto desarrollado. Se eligió un laminado de fibra de vidrio unidireccional UD C1000 SE 1500), $[0]_{2s}$. Estos laminados no presentaban polarización, mostraban una buena linealidad frente a la deformación y su factor de galga aumentó con respecto al del nanocompuesto: $S_g = 6{,}36 \pm 0{,}3$.

En el presente trabajo se presenta la aplicación de (i) la resina piezorresistiva como película sensible y (ii) los laminados sensitivos desarrollados, a la monitorización y/o refuerzo de un demostrador de laboratorio.

2. TÉCNICAS EXPERIMENTALES

Como estructura de laboratorio, se ha seleccionado un perfil de fibra de vidrio de $50 \times 50 \times 5$ mm (FIBERLINE), utilizado en sectores como la construcción, offshore y ferroviario. Para la medición de la variación superficial de resistencia se ha utilizado pintura de plata RS Pro123-9911 y un multímetro digital de 7 ½ dígitos Keithley DMM7510-901-01 (ver Fig. 1). Los perfiles han sido sometidos a flexión en cuatro puntos mediante una máquina universal de ensayos Servosis ME 405, equipada con una célula de carga de 100 kN. Los parámetros de ensayo se muestran en la *Tabla 1* para los especímenes ensayados: probetas sensorizadas con resina piezorresistiva (Fig. 1. Centro) y probetas reforzadas con laminados piezorresistivos (Fig. 1 Dcha.). Los ensayos realizados han sido de dos tipos: ciclados de carga y descarga a velocidad constante, dentro de la zona elástica y ensayos hasta rotura.

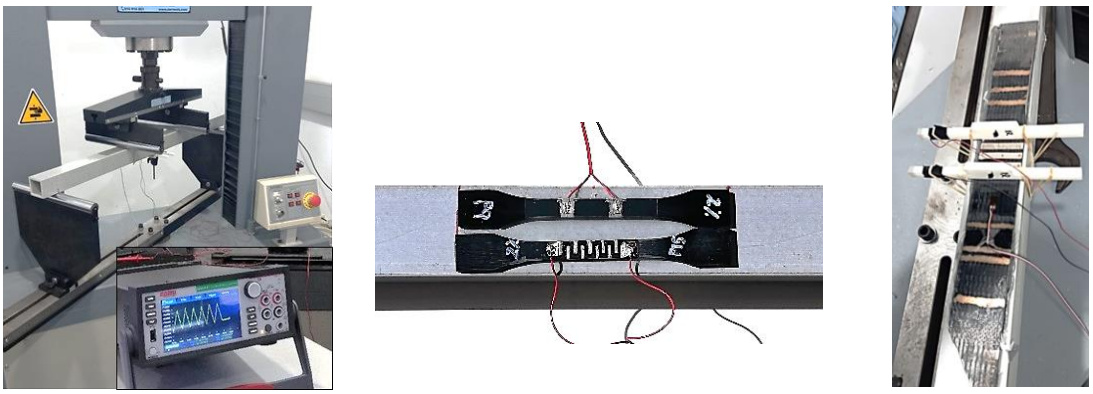

Figura 1. Ensayo de flexión (Izda.). Resina piezorresistiva (Centro). Laminado piezorresistivo (Dcha.)

Tabla 1. Condiciones de ensayos de flexión cuatro puntos

Espécimen	Resina	Laminado
Distancia entre apoyos [mm]	450	900
Distancia entre puntos de carga [mm]	200	400
Fuerzas de ciclado [kN]	$0{,}5 - 6$	$0 - 5$
Velocidad de desplazamiento [mm/min]	1,5	1,5

La deformación en el vano central, tanto de la viga como del sensor, se han medido mediante galgas extensométricas comerciales. Como film sensor se han utilizado probetas de nanocompuesto de $150 \times 10 \times 4$ mm, Fig. 1 Centro, mientras que como laminado sensor se han utilizado placas laminadas de $350 \times 40 \times 3$ mm, Fig. 1 Dcha. Como adhesivo se ha utilizado una resina epoxi. Con el objetivo de estudiar la sensibilidad de detección de daño, en el caso de las vigas sensorizadas con resina piezorresistiva, se han introducido daños progresivos antes de llevar a rotura la viga.

3. RESINA PIEZORRESISTIVA COMO PELÍCULA SENSORA

La Fig. 2 Izda. muestra la variación de deformación y resistencia del film sensor. Se observa que no hay polarización, así como una buena correlación entre las deformaciones y resistencia del sensor.

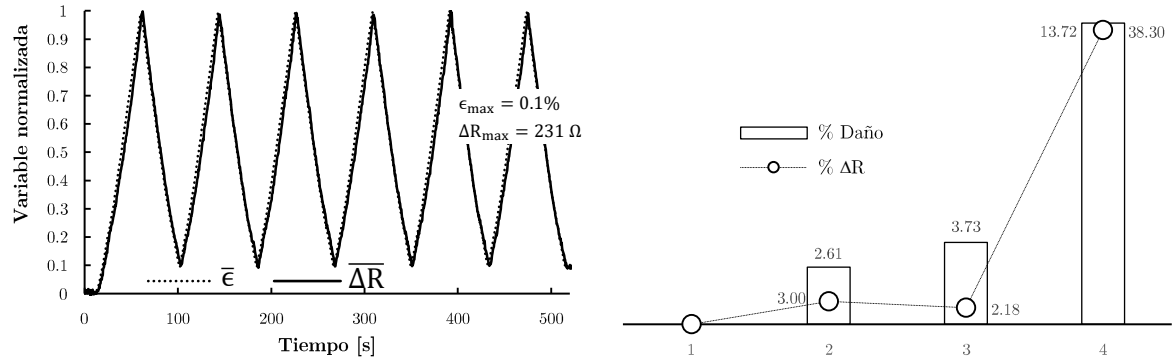

Figura 2. Film sensor: variación de deformación y resistencia (Izda.), daño vs variación de resistencia (Dcha.).

La Fig. 2 Dcha., muestra la variación de resistencia durante el ciclado en función del porcentaje de daño inducido en la sección central de la viga. Se observa que el sensor es capaz de detectar la existencia de daño. La Fig.3 muestra los resultados del ensayo a rotura. Se observa que el sensor no es capaz de monitorizar la viga hasta la rotura ya que, con anterioridad a esta, se produce su despegue.

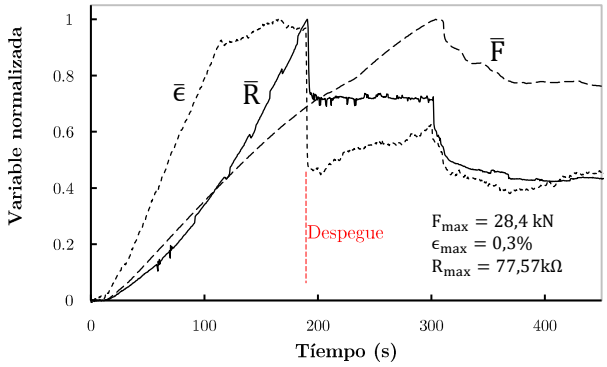

Figura 3. Ensayo a rotura, film sensor.

4. LAMINADO PIEZORRESISITVO COMO SENSOR Y REFUERZO ESTRUCTURAL

La Fig. 4 Izda. muestra una buena correlación entre la variación de fuerza aplicada y la variación correspondiente de resistencia. La Fig. 4 Dcha. muestra el ensayo a rotura. En este caso, el ensayo no ha sido monotónico sino ciclos de carga creciente. Se observa que al igual que en el caso del film sensor, se produce el despegue del laminado sensitivo.

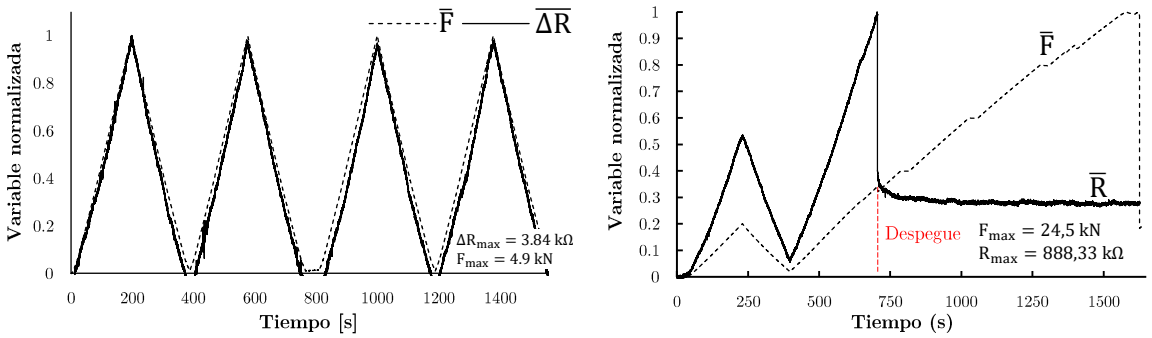

Figura 4. Refuerzo piezorresistivo: variación de resistencia con la carga (Izda.), ensayo hasta rotura (Dcha.).

5. CONCLUSIONES

Este trabajo muestra que la utilización de nanorrefuerzos de carbono permite funcionalizar la resina empleada confiriéndole propiedades piezorresistivas. Su empleo tanto como film sensor como laminado de refuerzo ha sido validado en un demostrador de laboratorio. Sin embargo, la adhesión del elemento sensor/refuerzo a la estructura resulta crítica.

AGRADECIMIENTOS

Este trabajo ha sido financiado por el Ministerio de Economía y Competitividad y por el Fondo Europeo de Desarrollo Regional, bajo el título Ciencia, Innovación y Universidades de España a través del proyecto “Monitorización de la salud estructural autoabastecida mediante refuerzos inteligentes de nanocompuestos (MSEAARINC)” de referencia RTI2018-094945-B-C21.

REFERENCIAS

[1] Mukhtar, F. M., & Faysal, R.M. (2018). A review of test methods for studying the FRP-concrete interfacial bond behaviour. *Construction and Building Materials, vol. 169.*

[2] Eskew, E. & Jang, S. (2017). Optimal sensor placement for parameter estimation of bridges, *Health Monitoring of Structural and Biological Systems*. vol. 10170.

[3] Pachón, P., Castro, R., García-Macías, E., Compan, V., & Puertas, E. (2018). E. Torroja’s bridge: Tailored experimental setup for SHM of a historical bridge with a reduced number of sensors. *Eng. Struct., vol. 162*.

[4] Schumacher T., & Thostenson, E.T. (2014). Development of structural carbon nanotube-based sensing composites for concrete structures. *J. Intell. Mater. Syst. Struct., vol. 25, no. 11*.

[5] Pérez Martínez, L. (2021), Sistema de resina polimérica cargada con nanoderivados de carbono. De su comportamiento piezorresistivo y aplicabilidad a la monitorización de estructuras, Trabajo Fin de Master, Universidad de Málaga.

[6] Moral Ortiz de Urbina, A., (2022). Evaluación del uso de una resina polimérica funcionalizada con nanofibras de carbono para la monitorización de deformaciones, Trabajo Fin de Grado, Universidad de Málaga.

Quantifying the damping performance of magnet arrays using kinematic methods

Fernández, Guillermo[1]; Iglesias Pordomingo, Álvaro[1]; Cacho Pérez, Mariano[1] and Lorenzana, Antolín[1]

ABSTRACT

The vibration mitigation devices known as tuned mass dampers (TMD) comprise basically a frame that houses a mass suspended on elastic elements and dampers. Ideally, the device behaves as a SDOF system. It is also known that the interaction, without contact, between permanent magnets and non-ferromagnetic metallic materials (copper, aluminum…) behaves as a linear damper because of Eddy currents. The energy dissipation depends on factors like the magnet arrangement. One interesting task is to quantify the associated damping constant. This work aims at finding the optimal arrangement of the magnets for a design of a TMD in which the magnets move parallel to the moving mass. As the motion is like a vehicle rolling down on an inclined plane, a simple scenario is conceived in which its terminal velocity can be related to the damping constant. After processing and understanding the experimental results, several conclusions are drawn.

Keywords: TMD, Eddy current damping, permanent magnets, magnet arrangement, optimum design.

1. INTRODUCTION

Passive vibration mitigation devices in structural engineering are also known as tuned mass dampers (TMD). Mostly, these devices comprise basically a frame that houses a mass suspended on both elastic elements and dampers, ideally behaving as single degree of freedom (SDOF) systems. The damper must apply a force proportional to the velocity, so a specific amount of viscous damping is achieved, along with the rest of tuning parameters of the whole TMD system. The traditional way of manufacturing such a damper is by means of pistons that transfer oil from one chamber to another. This mechanical arrangement inevitably adds friction as a consequence of oil seals. Since friction leads to a non-linear behavior, the actual operation of the TMD can be impaired. Note that the TMD is installed in the vibrating structure and the movement of the structure is what causes the TMD to move and dissipate energy. For small oscillations, friction can cause the TMD not to start up, conditioning the efficiency of the assembly.

It is also known that the interaction, without contact, between permanent magnets (PMs) and non-ferromagnetic metallic materials such as aluminum or copper behaves as a viscous damper by the effect of induced Eddy currents in the conductor material. Electromagnetic induction theory establishes the possibility of inducing Eddy currents on non-ferromagnetic materials as a countereffect of magnetic flux variations in two scenarios: a time varying magnetic inductor field in a

[1] *ITAP. University of Valladolid (SPAIN). guillermo.fernandez.ordonez@estudiantes.uva.es (Corresponding author), alvaro.iglesias@uva.es, mariano.cacho@uva.es, ali@eii.uva.es*

static situation or by moving a constant magnetic field at a certain speed causing a change in the flux associated to a surface crossed by vector magnetic lines. The second scenario is the one that gives a chance to incorporate a source of viscous damping in the TMD device without friction, because PMs can be arranged and establish a relative motion between the moving mass and themselves by leaving a certain amount of air gap which leads to a non-contact interaction. Some vibration control devices are only focused on damping, and if they are based in the induction of Eddy current to obtain a force which opposes motion, they are called Eddy current dampers (ECD) ([1], [2]).

In this work, a simple scenario to test different type of magnet arrangements has been conceived. As the motion is similar to that between a vehicle and the inclined plane on which it rolls, its terminal velocity can be related to the damping constant. The optimal magnet arrangement corresponds to the maximum damping achieved. This time-domain study using simple kinematic methods aims at identifying the qualitative optimal arrangement applied in both a TMD and an ECD, by means of obtaining a quantitative indicator which can lead to place the PMs in a specific way in the final device.

2. MAGNET HOLDER DESIGN, MAGNET ARRANGEMENT AND CONFIGURATION

Different types of magnet arrangements are obtained by designing a specific magnet holder, which provides the possibility of placing PMs in different relative ways. Fig. 1 shows a modular holder designed in CATIA® V5 and later 3D printed (using PLA) from a previous fixed design. This final model has corner chamfers to identify the magnet's north, can be attached to other holders of the same type with no magnet contact (with possible and simple 180-degree rotations to invert poles) and finally creates an arrangement in two directions assumed as a matrix.

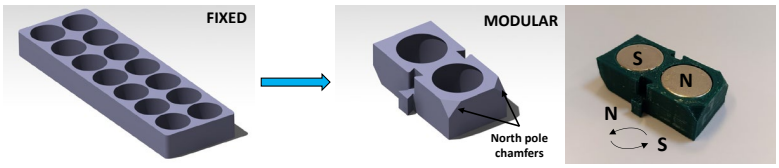

Figure 1. *Magnet holder CAD models in CATIA® V5 and 3D printed final modular design.*

With the holder described above, now different magnet arrangements are feasible. In Fig. 2, a total of four cases are proposed considering 8 D15xH10 (mm) NdFeB PMs (so 4 modules are needed). Alternated (A), north (N), equal (E) and bands (B) arrangements provide different inductor magnetic fields by means of different vector lines spatial distribution. Special care has to be taken when placing the magnets following N and B patterns, because a 180-degree fixed relative rotation is needed to have the same poles within the same face.

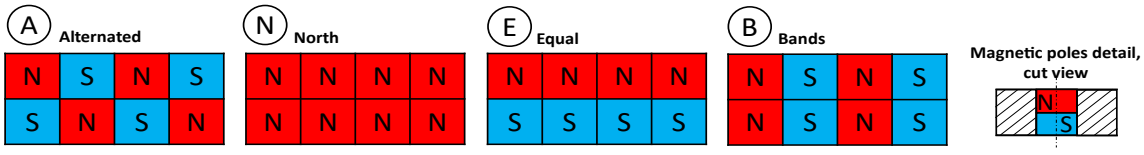

Figure 2. *Different types of permanent magnet arrangements (N=8).*

3. EXPERIMENTAL METHODOLOGY AND RESULTS

The simple experimental scenario conceived to measure the corresponding damping constant for every magnet arrangement described in section 2 is shown in Fig. 3, where a custom-built LEGO® car rolls down on an inclined plane made up by a copper plate. PMs are placed under the car's chassis leaving an air gap. Both Vertical (V) and Horizontal (H) directions are tested for every arrangement, with V meaning that the prevailing magnet array dimension is parallel to the movement's direction. In every case, the car's terminal motion occurs at a constant speed v as a consequence of a damping force F opposing movement. This force is caused by the induced Eddy currents in the copper and the corresponding magnetic field component in the plate's normal direction. Measuring v is possible by timing the car's motion using a laser displacement sensor (Panasonic® HL-G1) and DAQ system (Dewesoft SIRIUS®). Then, once v has been obtained, Newton's second law of motion is applied to the movement's direction and c is obtained, as shown in Eq. (1). Parameters and constants involved in the study are given in Table 1. This procedure is repeated five times for each configuration (magnet arrangement and direction) so an average result can be computed.

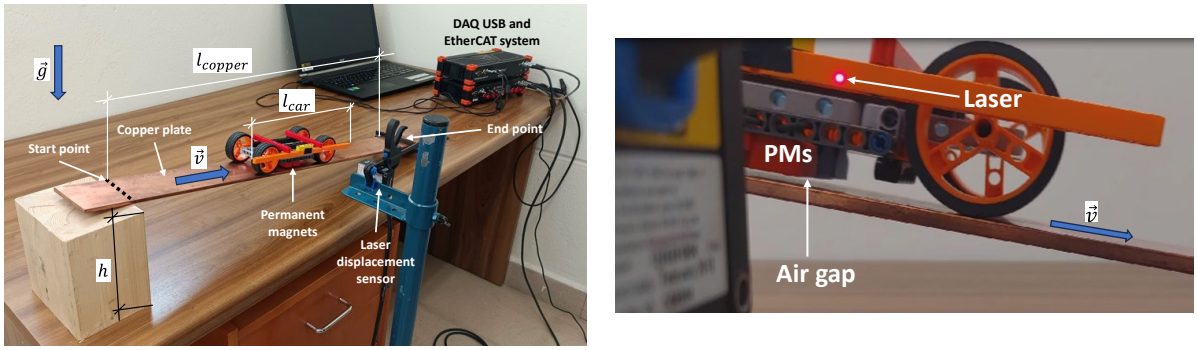

Figure 3. *Experimental set-up (left) and detail of the laser measuring displacement (right).*

Table 1. Parameters and constants involved in the study.

Parameter	Meaning	Value
$\boldsymbol{m_{car}}$	LEGO® car mass	0,148 kg
$\boldsymbol{l_{car}}$	LEGO® car length	0,239 m
$\boldsymbol{m_{mag}}$	Single magnet mass + half of the magnet holder's mass	0,015 kg
$\boldsymbol{N_{mag}}$	Total number of magnets used	8
$\boldsymbol{l_{copper}}$	Copper plate length	0,875 m
$\boldsymbol{N_{tests}}$	Total number of tests per configuration	5
$\boldsymbol{h}$	Ramp height	0,15 m
$\boldsymbol{g}$	Gravitational acceleration	9,81 m/s^2
$\boldsymbol{a}$	Air gap	2,5 mm

$$F = c \cdot v = \frac{mgh}{l_{copper}} \rightarrow c = \frac{mgh\Delta t}{l_{car} \cdot l_{copper}}, \quad \begin{cases} v = \dfrac{l_{car}}{\Delta t} \\ m = m_{car} + N_{mag} m_{mag} \end{cases} \tag{1}$$

By using the available geometric information and the damping force expression, the damping constants are obtained using Eq. (1) and are shown in Table 2.

Table 2. Obtained damping constants c (in Ns/m) for every configuration (magnet arrangement and V / H direction). Average over $N_{tests} = 5$ for each case.

Direction	Magnet arrangement			
	A	**E**	**N**	**B**
V	6,99	2,24	4,53	10,35
H	5,45	11,17	7,11	2,08

As seen in the table above, the damping constant is highly dependent on both the magnet arrangement and direction. It is observed that the best configuration in terms of the best damping constant achieved is an Equal (E) magnet arrangement in a horizontal (H) direction, with the prevailing magnet array dimension perpendicular to the movement direction. Almost the same amount of damping can be achieved using a Bands (B) configuration in a Vertical (V) direction. The damping constant in both aforementioned situations only differs in 7,34%, much less than the other ones.

4. CONCLUSIONS

The experimental time-domain study carried out in this work shows that when using PMs and non-ferromagnetic metallic materials such as copper to provide both a TMD or an ECD with a source of linear viscous damping without contact interaction is highly dependent on different types of magnet arrangements and their prevailing dimension with respect to the movement's direction. Eddy currents are induced in the conductor plate and a force opposing the movement originates. The simple scenario conceived with a LEGO® car rolling down in an inclined plane with the magnets attached under its chassis is of great interest, as it is based on the SDOF concept. Qualitative deductions have been made using quantitative values of the damping constants, not only showing a relationship with the PMs relative arrangement (A, N, E, or B), but also with their direction (V or H) regarding the car's motion (assumed as the TMD's and ECD's) to complete a full configuration. The best results are obtained with both E in H and B in V, so those configurations are desirable when incorporated to the final device. Future studies can be focused at finding more specific relationships between damping and other parameters that are now fixed, like the air gap, the number and the type of magnets.

ACKNOWLEDGEMENTS

The authors wish to acknowledge to the AEI, Spanish Government (10.13039/501100011033), and to "ERDF A way of making Europe", for the partial support through the grant PID2022-140117NB-I00.

REFERENCES

[1] Diez-Jimenez, E., Rizzo, R., Gómez-García, M.J. & E. Corral-Abad (2019), Review of Passive Electromagnetic Devices for Vibration Damping and Isolation. *Shock and Vibration, 16 pages.*

[2] Sodano, H.A., Bae, J. S., Inman, D.J. & Keith Belvin, W. (2005). Concept and model of eddy current damper for vibration suppression of a beam. *J Sound Vib, 288, 1177–1196.*

Recent advances in piezocomposites: towards eco-friendly and enhanced performance materials via computational modelling

Cañamero, Francisco J.[1]; Buroni, Federico C.[2]; Rodríguez-Tembleque, Luis[3]

ABSTRACT

This paper presents a critical review of the latest developments in piezocomposites [1-9], with a focus on eco-friendly, high-performing materials. The study emphasizes the use of lead-free materials and how the carbon nanotubes (CNTs) in the composite matrix enhance the piezoelectric response. The influence of the texture of the active phase [1-8] and the optimal CNT concentration on piezocomposite performance is also discussed when two types of the piezocomposites configurations, namely, 1-3 (fiber) and 0-3 (particle), are considered.

Keywords: Lead-free piezocomposites, 1-3 piezocomposites, 0-3 piezocomposites, Effective properties.

1. INTRODUCTION

Eco-friendly and lead-free piezoelectric materials have recently begun to be studied and have undergone a remarkable development in recent years. In the last decade, environmental concerns have led to attempts to eliminate lead-based materials from consumer items, including piezoelectric transducers, sensors and actuators. Therefore, the market for lead-free piezoelectric materials and devices is expected to grow in the coming years, driven by increasing demand for environmentally friendly and safe technologies as well as the growing adoption of piezoelectric devices.

Recently, the works developed by Krishnaswamy et al. [1-7] have studied lead-free piezocomposites based on powder of microparticles of polycrystalline barium titanate (BTO) randomly dispersed in relatively soft polymeric matrices, such as polydimethylsiloxane (PDMS) or polyvinylidene fluoride (PVDF). In those works, numerical studies have analysed the impact of several microstructural characteristics in improving the performance of such lead-free piezoelectric composites. Their results have contributed -among others- to understand the role of tuning the dielectric environment of the matrix by adding nanoinclusions, such as graphene and carbon nanotubes (CNTs), showing an improvement on the piezoelectric properties. However, recent studies in 0–3 and 1-3 lead-free piezocomposites [8,9] have showed that the values of the electromechanical coupling factors are largely affected by the CNTs volume fraction.

[1] *Fundación Centro Tecnológico Metalmecánico y del Transporte, Parque Empresarial Santana (SPAIN). javier.canamero@cetemet.es.*

[2] *Departamento de Ingeniería Mecánica y de Fabricación, Escuela Técnica Superior de Ingeniería y Escuela Politécnica Superior, Universidad de Sevilla (SPAIN). fburoni@us.es*

[3] *Departamento de Mecánica de Medios Continuos y Teoría de Estructuras, Escuela Técnica Superior de Ingeniería, Universidad de Sevilla (SPAIN). luisroteso@us.es (Corresponding author).*

In this context, this work studies the performance of 1–3 and 0-3 leadfree piezoelectric composites, where parallelly-aligned BTO fibres or uniform distributed powder are embedded, respectively, in a three-dimensional CNT-enriched PDMS matrix (see Fig.1). The influence of the texture of the active phase and the optimal CNT concentration on the planar electromechanical coupling factor performance is discussed for these two pattern configurations.

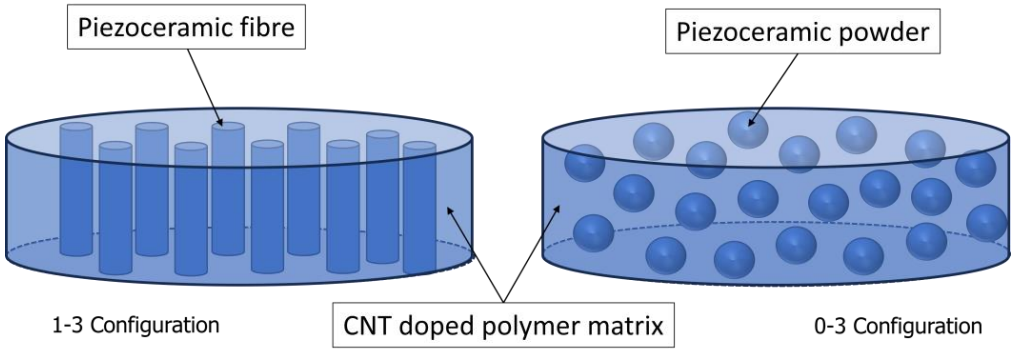

Figure 1. *Representation of the 1-3 and 0-3 connectivity of two phases composites (i.e., the piezoceramic active phase and the polymer matrix passive phase).*

2. ANALYSIS AND METHODOLOGY

The constitutive equations of piezoelectric materials can be written -assuming linear piezoelectric theory- in the following form:

$$\begin{aligned} \sigma_{ij} &= C_{ijkl}\,\varepsilon_{kl} - e_{kij}\,E_k \\ D_i &= e_{ikl}\,\varepsilon_{kl} + \kappa_{ik}\,E_k \end{aligned} \tag{1}$$

where σ_{ij} is the stresses, ε_{kl} is the strains, E_k is the electric field and D_i is the electrical displacements. In the expressions above, C_{ijkl} is the fourth-order elasticity tensor, κ_{ik} is the second-order free body electric tensor, and e_{ikl} is the third-order piezoelectric stress tensor. Another widely used alternative and equivalent representation consists in writing the constitutive Eq. (1) in the following form:

$$\begin{aligned} \varepsilon_{ij} &= S_{ijkl}\,\sigma_{kl} + d_{kij}\,E_k \\ D_i &= d_{ikl}\,\sigma_{kl} + \epsilon_{ik}\,E_k \end{aligned} \tag{2}$$

where S_{ijkl} is the elastic compliance tensor, ϵ_{ik} is the dielectric permittivity tensor, and d_{ikl} is the piezoelectric strain tensor.

The effective properties of the resulting piezoelectric composite are evaluated in this work by using a Representative Volume Element (RVE) based homogenization methodology, taking into account corresponding periodic unit cells (see Fig.2). Once the effective properties of the piezoelectric composite are numerically computed, the planar electromechanical coupling factor (k_p) can be found, according to [10], as

$$k_p = \left(1 - (\kappa_{33}/\epsilon_{33})(C_{33}^D/C_{33})\right)^{1/2}, \tag{3}$$

where $C_{33}^D = C_{33} + e_{33}^2/\kappa_{33}$.

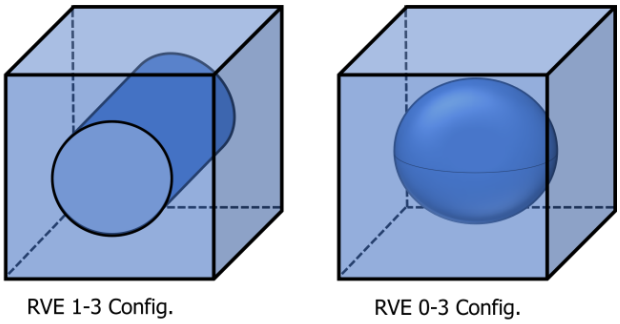

Figure 2. *RVE geometry of a 1–3 and 0-3 piezocomposite homogenization.*

3. RESULTS CONCLUSIONS

This work considers the BTO for the lead-free active phase and the PDMS polymer for the matrix. The texture of the active phase (BTO) [1-8] is analyzed, together with the CNT concentration on the PDMS polymer. The properties of each phase of the piezoelectric composite, i.e., the textured BTO and the PDMS polymer doped with CNTs, have been obtained from [8] for several values of the texture parameter (α) and CNT volume fraction (f_{CNT}), respectively.

After homogenization, the computed planar electromechanical coupling factor (k_p) is presented in Figs.3 as a function of α and the ratio f_{CNT}/f_c, being f_c the percolation threshold of the nanotubes ($f_c = 0.608\%$). The performance of k_p is presented for the 1-3 (fiber) and 0-3 (particle) piezocomposite configurations, for a BTO volume fraction of 33.33%.

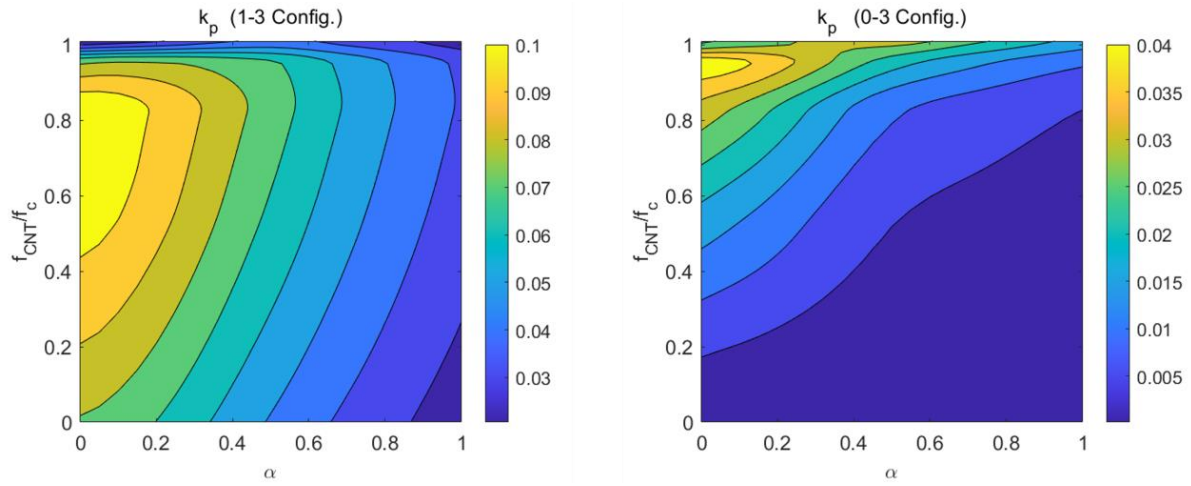

Figure 3. *Electromechanical coupling factor (k_p) performance as a function of BTO texture parameter (α) and the CNT volume fraction (f_{CNT}/f_c), being f_c the percolation threshold of the CNTs ($f_c = 0.608\%$), for BTO volume fraction of 33.33%.*

After evaluating the energy conversion efficiency through the electromechanical coupling factor k_p, the following observations are made. First, 1-3 configuration presents a significant greater value of k_p that the 0-3 configuration. Moreover, for both 1-3 and 0-3 configurations, the optimal performance of k_p is obtained for $\alpha = 0$. However, these configurations behave differently when the PDMS matrix is doped with CNTs. For the 1-3 configuration, k_p enhances with the addition of CNTs, being the optimal values located in the range $f_{CNT} \in (0.45 f_c 0.85 f_c)$. However, for the 0-3 configuration, the optimal value

of k_p is obtained for $f_{CNT} \approx 0.95 f_c$. Consequently, in lead-free BTO/PDMS piezocomposites, the addition of CNTs in the PDMS matrix does not always improve the performance of the piezocomposite. The optimal CNTs volume fraction is highly dependent on the configuration of the piezoelectric composite.

ACKNOWLEDGEMENTS

This work was supported by the Ministerio de Ciencia e Innovación (Spain) through the research project DIP2022-137903OB-I00.

REFERENCES

[1] Krishnaswamy, J.A., Buroni, F.C., Garcia-Sanchez, F., Melnik, R., Rodriguez-Tembleque, L., Saez, A. (2019) Improving the performance of lead-free piezoelectric composites by using polycrystalline inclusions and tuning the dielectric matrix environment. Smart Mater. Struct., 28: 075032.

[2] Krishnaswamy, J.A., Buroni, F.C., Garcia-Sanchez, F., Melnik, R., Rodriguez-Tembleque, L., Saez, A. (2019) Lead-free piezocomposites with CNT-modified matrices: Accounting for agglomerations and molecular defects. Composite Structures, 224: 111033.

[3] Krishnaswamy, J.A., Buroni, F.C., Garcia-Macias, E Melnik, R., Rodriguez-Tembleque, L., Saez, A. (2020) Design of lead-free pvdf/cnt/batio3 piezocomposites for sensing and energy harvesting: the role of polycrystallinity, nanoadditives and anisotropy. Smart Mater. Struct., 29: 015021.

[4] Krishnaswamy, J.A., Buroni, F.C., Garcia-Macias, E., Melnik, R., Rodriguez-Tembleque, L., Saez, A. (2020) Design of nano-modified pvdf matrices for lead-free piezocomposites: Graphene vs carbon nanotube nano-additions. Mechanics of Materials, 142: 103275.

[5] Krishnaswamy, J.A., Buroni, F.C., Melnik, R., Rodriguez-Tembleque, L., Saez, A. (2020) Advanced modeling of lead-free piezocomposites: The role of nonlocal and nonlinear effects. *Composite Structures*, 238: 111967.

[6] Krishnaswamy, J.A., Buroni, F.C., Melnik, R., Rodriguez-Tembleque, L., Saez, A. (2020) Design of polymeric auxetic matrices for improved mechanical coupling in lead-free piezocomposites. *Smart Mater. Struct.*, 29:054002.

[7] Krishnaswamy, J.A., Buroni, F.C., Melnik, R., Rodriguez-Tembleque, L., Saez, A. (2021) Multiscale design of nanoengineered matrices for lead-free piezocomposites: Improved performance via controlling auxeticity and anisotropy. Composite Structures, 255: 112909.

[8] Cañamero, F.J., Buroni, F.C., Aliabadi, F.M.H., Rodriguez-Tembleque, L. (2023) Piezoelectric performance of lead-free PDMS/CNT/BaTiO3 piezocomposites with imperfect interphases and cnt agglomerations. *Smart Materials and Structures,* 32(3):035005.

[9] Cañamero, F.J., Buroni, F.C., Aliabadi, F.M.H., Rodriguez-Tembleque, L. (2023) Enhancing the performance of 1-3 lead-free piezoelectric composites using a CNT doped matrix. *Journal of Multiscale Modelling,* 14(2): 2350003.

[10] European standard, EN 50324-2: (2002) "Piezoelectric properties of ceramic materials and components, Part 2: Methods of measurement - Low power," CENELEC European Committee for Electrotechnical Standardization.

Reflections and methodological proposals about the inclusion of the Sustainable Development Goals in the teaching of subjects related to structural engineering

Lapuebla-Ferri, Andrés[1]; Espinós, Ana[1]; Ibáñez, Carmen[2]; Pons, David[1]

ABSTRACT

The United Nations General Assembly adopted in 2015 the 2030 Agenda, a global scale agreement aimed to achieve the peace and prosperity of Humanity and to protect the planet. 2030 Agenda hinges in 17 Sustainable Development Goals (SDGs) and 169 targets related to social, environmental and economic issues. Since the role of universities is relevant to achieve the SDGs, these must be incorporated in the curricular design of Higher Education degrees. In spite of this, the inclusion of SDGs in the contents of the technological subjects is challenging because both lecturers and students are generally not trained in 2030 Agenda and SDGs. In this work, a reflection is made in order to identify the most suitable SDGs to be included in the contents of subjects related to Structural Engineering at bachelor and master degree levels. The use of several teaching-learning activities is proposed to support the training in SDGs.

Keywords: 2030 Agenda, Sustainable Development Goals (SDG), Higher Education, Structures, Concrete Structures

1. INTRODUCTION

Universities have been always identified as transforming agents to the society. Since the adoption of 2030 Agenda [1] (Fig. 1) universities were prompted to implement the SDGs in their major activities (teaching, research, transfer and management) [2]. Besides, Spanish regulation RD 822/2021 [3] stablishes the organization and quality assurance of higher education, stating that *one of the guiding principles in the design of academic programmes must have as a reference the principles and the democratic values, as well as the SDGs.* Since all academic areas of knowledge have implications for sustainability and developments problems, it is mandatory to include SDGs in the curricula of the university degrees.

Nevertheless, the paradigm of a Higher Education based in the SDGs can suppose a challenge to implement in the existing degrees, especially in those of technical or scientific nature. The lecturers have little or no training in this matter [4-6] and the students are not enough aware of the principles

[1] *Dpt. of Continuum Mechanics and Theory of Structures. Universitat Politècnica de València (SPAIN). anlafer0@mes.upv.es (Corresponding author), aespinos@mes.upv.es, dpons@upv.es*
[2] *Dpt. of Construction Engineering. Universitat Politècnica de València (SPAIN). caribus@upv.es*

of 2030 Agenda [7-8]. These works evidence that there is a lot to do to include SDGs in the technical careers before an SDG-based training could be transferred to the professional activity [9].

Figure 1. *Though SDGs are interrelated, they can be integrated in the following areas: people (SDG1 to SDG5), planet (SDG6, SDG12-SDG15), prosperity (SDG7-SDG11), peace (SDG16) and alliances (SDG17).*

The present work exemplifies the incorporation of the SDGs in two subjects of bachelor and master degree belonging to the industrial field. Moreover, in order to train properly the students in 2030 Agenda, the application of some teaching and learning methodologies is proposed.

2. METHODOLOGY

In this work, two subjects were chosen. Firstly, Structures (STR, Bachelor's Degree in Industrial Engineering) and, secondly, Concrete Structures (CST, Master's Degree in Industrial Engineering). Both degrees are taught in the School of Industrial Engineering, Universitat Politècnica de València (Valencia, Spain). These subjects are mandatory in the curricula of Civil Engineering and Architecture degrees. A brief listing of the contents of the two subjects can be found in Table 1.

Table 1. Contents of the two subjects involved in the present study.

Structures (STR) **Bachelor degree**	**Concrete structures (CST)** **Master's degree**
Typological classification of structures	Materials: concrete and steel
Methods of movement calculation	Durability
Trusses	Ultimate Limit States
Slope-deflection method	Serviceability Limit States
Simplifications in structures	Buckling
Matrix method	Detailing

Prior to design training activities and evaluation methods the SDGs that are aligned with their contents must be identified. It has to be taken into account that each SDG comprises 8-12 targets, which are written in a concrete and focused way. Targets allow SDGs to be implemented in the form of teaching-learning activities and evaluation methods.

3. RESULTS

All of the 169 targets of the 17 SDGs were mapped to the contents of the involved subjects in order to check their alignment. The results are presented in Table 2.

Table 2. Number of targets in each SDG that are aligned with the subjects analysed.

SDG		Total	Number of aligned targets	
			STR	CST
SDG1	No poverty	7	0	**1**
SDG2	Zero hunger	8	0	0
SDG3	Good health and well-being	13	0	0
SDG4	Quality education	10	**1**	**1**
SDG5	Gender equality	9	**1**	**1**
SDG6	Clean water and sanitation	8	0	2
SDG7	Affordable and clean energy	5	0	**1**
SDG8	Decent work and economic growth	12	0	2
SDG9	**Industry, innovation and infrastructure**	**8**	**5**	**5**
SDG10	Reduced inequalities	10	**1**	**1**
SDG11	Sustainable cities and communities	10	**1**	0
SDG12	Responsible consumption and production	11	0	3
SDG13	Climate action	5	0	0
SDG14	Life below water	10	0	0
SDG15	Life on land	12	0	0
SDG16	Peace, justice and strong institutions	12	0	0
SDG17	Partnerships for the goals	19	**1**	**1**
		169	**10**	**18**

According to Table 2, it is found that not every SDG is suitable to be included in structural engineering-related subjects. Besides, master's degree is more suitable to train students in SDGs than the bachelor degree. In fact, CST is framed within the speciality of construction and industrial facilities of the last course, and involves many aspects of the professional practice. SDG9 is the goal that is more suitable to be translated into teaching activities (5 out to 8 targets are aligned to the contents of both subjects). SDG12 has 3 targets aligned with the subject CST, but none with STR. CST contents are also suitable to incorporate SDG6 and SDG8 (2 targets each). SDG4 and SDG5 are considered transversal goals that can be treated in any subject independently on its knowledge area. Finally, other SDG that are tangentially related to both subjects are SDG10, SDG11 and SDG17, and probably they are not suitable to be translated into learning activities.

Once the targets that match the best the contents of the subjects have been identified, it should be performed a common overview of the subjects of the entire degree to verify that the students will be trained in all the SDGs along their studies. This should be the starting point for the lecturers to design activities related to the SDGs in their subjects. Experiences of collaborative work, such as Aronson's Puzzle [10] followed by co-evaluation or peer reviewing may be encouraging for the students in their training of SDGs.

4. CONCLUSIONS

2030 Agenda and SDGs must be incorporated to higher education. In the framework of a certain subject, the targets of the SDGs can be regarded as learning outcomes as well as conventional skills, knowledge and abilities. Training in SDGs must be done in a reflexive manner, taking into account that the 2030 Agenda is still a new topic for university subjects. Schools and Faculties must coordinate that the entire subjects of a degree perform actions aimed to train the students in all the SDGs.

REFERENCES

[1] United Nations General Assembly. Transforming our world: the 2030 Agenda and Sustainable Development, 21 October 2015, A/RES/70/1. Available at: https://sdgs.un.org/2030agenda. Accessed 20 July 2023.

[2] SDSN Australia/Pacific (2017): Getting started with the SDGs in universities: A guide for universities, higher education institutions, and the academic sector. Australia, New Zealand and Pacific Edition. Sustainable Development Solutions Network – Australia/Pacific, Melbourne. Available at: https://resources.unsdsn.org/. Accessed 20 July 2023.

[3] Boletín Oficial del Estado nº 233, de 29/09/2021 (BOE-A-2021-15781). Madrid: Ministerio de la Presidencia, Relaciones con las Cortes y Memoria Democrática. Gobierno de España.

[4] Vallés-Lluch, A.; Lapuebla-Ferri, A.; Alemany, M. M. E.; Villanueva, J. F.; Esteso, A.; Gallardo, S.; Fuster, M. V.; Andrés, J.; Sancho, M.; García-Serra, J. (2022). Mapping the implementation of Sustainable Development Goals in engineering university studies. In 16th International Technology, Education and Development Conference (INTED 2022). Valencia: IATED.

[5] Villanueva, J. F.; Fuster, M. V.; Esteso, A.; Andrés, J.; Vallés-Lluch, A.; Lapuebla-Ferri, A.; Gallardo, S.; Alemany, M. M. E.; Sancho, M.; García-Serra, J. (2022). The point of view of teachers before the Sustainable Development Goals: a review prior to its implementation in a school of engineering. In 16th International Technology, Education and Development Conference (INTED 2022). Valencia: IATED.

[6] Martínez-Gómez, M.; Gallardo, S.; Villanueva, J. F.; Sancho, M.; Lull, C.; Esteso, A.; Vallés-Lluch, A.; Lapuebla-Ferri, A.; Alemany, M. M. E.; Ortiz, A. (2023). Diagnosis of training in Sustainable Development Goals in the Higher Technical School of Industrial Engineering (ETSII). In 17th International Technology, Education and Development Conference (INTED 2023). Valencia: IATED.

[7] Esteso, A.; Gallardo, S.; Villanueva, J. F.; Alemany, M. M. E.; Vallés-Lluch, A.; Fuster, M. V.; Andrés, J.; Lapuebla-Ferri, A.; García-Serra, J. (2022). How to know the awareness of Sustainable Development Goals among students? A revision of questionnaire surveys. In 16th International Technology, Education and Development Conference (INTED 2022). Valencia: IATED.

[8] Esteso, A.; Lull, C.; Lapuebla-Ferri, A.; Villanueva, J. F.; Sancho, M.; Gallardo, S.; Vallés-Lluch, A.; Martínez-Gómez, M.; Alemany, M. M. E.; Ortiz, A. (2023). Diagnosis of awareness of the Sustainable Development Goals among students and lecturers in higher education engineering school. In 17th International Technology, Education and Development Conference (INTED 2023). Valencia: IATED.

[9] Andrés, J.; Alemany, M. M. E.; Fuster, M. V.; Vallés-Lluch, A.; Lapuebla-Ferri, A.; Gallardo, S.; Esteso, A.; Villanueva, J. F.; Sancho, M.; García-Serra, J. (2022). Employer's perception of the Sustainable Development Goals in Higher Technical Education: a revision. In 16th International Technology, Education and Development Conference (INTED 2022). Valencia: IATED.

[10] Lázaro-Carrascosa, C., Hernán-Losada, I., Palacios-Alonso, D., Velázquez-Iturbide, Ángel. (2021). Flipped Classroom and Aronson´s Puzzle: a combined evaluation in the master´s degree in pre universitary teaching, *Education in the Knowledge Society*, 22, e23617. https://doi.org/10.14201/eks.23617.

Review of optimal design procedures for submerged arches.

LLamosas-Mayca, W. H.[1]; Hernández-Díaz, A.M. [2]; Pérez-Aracil, J.[3]; García-Román, M.D.[1]; Fister, I. Jr.[4]; Salcedo-Sanz, S. [3]

ABSTRACT

The submerged arches are widely used in different fields of civil engineering and their optimization procedure involves several parameters. They were traditionally designed pointing to funicular structures (i.e., minimizing their bending moments).

Recently, previous works have introduced the shape parameterization of the arch's centerline as an efficient alternative for the optimal structural design of this type of underwater installations. In this line, the present work approaches the comparative analysis of the shape optimization in submerged arches considering to this aim three specific parametric families: conics, elliptic and Bézier curves, and the optimization procedure is performed in the context of the CRO-SL evolutionary strategy.

The results obtained so far points out that several structural designs are feasible. Moreover, the choice of the shape parameterization function is not relevant for some design scenarios, pointing out the convenience of an unified approach for the optimization of submerged arches.

Keywords: submerged arches, geometric optimization, evolutionary algorithms.

1. INTRODUCTION

The submerged arches were traditionally underwater installations designed pointing to funicular types. Some works in the last years proposed to define the shape of submerged arches with a linear combination of conic curves (in particular, ellipse and parabola) and obtain the optimal shape using metaheuristics techniques in order to minimize bending moments (close to funicular condition) and maximize serviceability design conditions (such as the enclosed airspace). In this work we propose a review of the shape parameterization procedures for the optimization of the submerged arches via evolutionary algorithms, involving thus two additional geometrical types, the so called elliptic curves and Bézier curves.

[1] *Department of Civil, Nautical and Maritime Engineering. University of La Laguna (SPAIN). wllamosa@ull.edu.es (Corresponding author), mroman@ull.edu.es.*

[2] *Department of Techniques and Projects in Engineering and Architecture. University of La Laguna (SPAIN). ahernadi@ull.edu.es*

[3] *Department of Signal Processing and Communications. University of Alcalá (SPAIN). jorge.perezaracil@uah.es, sancho.salcedo@uah.es*

[4] *Faculty of Electrical Engineering and Computer Science. University of Maribor (SLOVENIA). iztok@iztok-jr-fister.eu*

1.1. Physical approach to the problem

For this analysis we adopt a general scheme for a symmetrical submerged arch, considering the coordinate system and the external loads represented in Fig. 1. The spam or distance between the supports of the arch is 2*B* and it has a height of *H* measured on the axis of symmetry. The distance between the water surface and the line of supports is *D*.

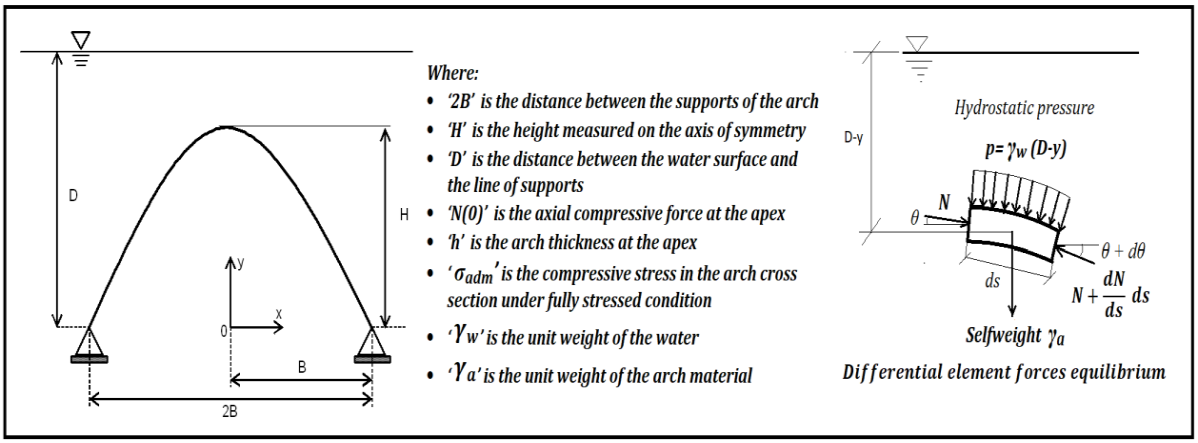

Figure 1. *Coordinate system, geometry of submerged arch and differential element under forces equilibrium.*

The centerline of the funicular shape corresponds to *y*(*x*), and it is obtained by solving the boundary conditions problem shown in [1]. The shapes of the submerged arches analyzed in this work were parameterized using parabola-ellipse conic, elliptic and Bézier curves.

1.2. Parabola-Ellipse curves

This parameterization consists of the linear combination of the conics parabola and ellipse, as shown in Eq. (2) [1]. Thus, for a given set of values *B, H, H'* and *t,* each curve is completely defined in terms of its radial coordinate r_{pe} and its angular coordinate φ.

$$r_{pe}\,(t,\varphi,B,H,H') = (1-t).r_p + t.r_e \tag{1}$$

1.3. Elliptic curves

Let K be a (commutative) field. An elliptic curve E is an algebraic plane curve defined by a Weierstrass equation [2, 3], Eq. (2) and Eq. (3):

$$E: y^2 + a_1xy + a_3y = x^3 + a_2x^2 + a_4x + a_6, \text{where } a_1, a_2, a_3, a_4, a_6 \in K, \text{with discriminant } \Delta \neq 0 \tag{2}$$

$$x^2 = -(\lambda y)^3 - p\lambda y + q, \quad p, q, \lambda \in K, where \;\; p, q \; are \; parameters \; and \; \lambda \; is \; a \; dilation \; factor \tag{3}$$

1.4. Bézier curves

Bézier curves are polynomial curves expressed using Bernstein's polynomials in a way analogous to Newton's binomial and the Casteljau algorithm [4], such as follows:

$$x(t) = \sum_{0}^{n} b_i \, B_i^n(t), \quad t \in [0,1] \in R, \ \ where \ B_i^n(t) = \binom{i}{n}(1-t)^{n-1} \, . \, t^i \, , \qquad (4)$$
$$is \ a \ Bernstein \ polynomial$$

The control points coordinates are defined by *P1=(0,0), P2=(p2x,p2y), P3=(p3x,p3y), P4=(p4x,p4y=p3y), P5=P2, P6=(2B,0)*.

2. OPTIMIZATION ALGORITHM

For this purpose we use the Coral Reefs Optimization with Substrate Layers (CRO-SL) algorithm which is a multi-method ensemble meta-heuristic for optimization.

Five operators have been used in the CRO-SL. This combination of operators has been obtained by practical experience. They are described as follows [5]: a) Harmony Search (HS): this technique emulates the improvisation of musicians composing a melody); b) Differential Evolution (DE): with a probability CR, the offspring is generated by introducing a perturbation in the individual, with a mutation factor. Otherwise, a random value within the bounds is generated; c) Multi-point and two-point crossover (2Px, MPx): this operators swap component values of two individuals (parents) to generate two offspring individuals, d) Gaussian Mutation (GM): this type of mutation is based on a Gaussian probability density function.

3. NUMERICAL RESULTS

The reinforced concrete arch's structural response (maximum absolute values of bending stress (Ms), compressive stress and vertical displacement), subjected to the corresponding hydrostatic load and its selfweight, is calculated using the finite element software ANSYS [6, 7]. A symmetric plane simply supported arch has been modeled using BEAM188 elements, with a Young's modulus *E* = 27664.49 MPa and Poisson's ratio *v*=0.30. The area (As) of the arch's enclosed airspace is also determined, and the functional to be optimized (minimized in this case) is calculated using the following expression Eq. (5), with weighting values p_m=0.80 and p_a=0.20:

$$f = p_m . max(|Ms|) + p_a . \left(\frac{1}{As}\right). \qquad (5)$$

The best individual parameters and fitness obtained are shown in Table 1.

Table 1. Numerical results for each optimization strategy

Parameterization	**Parameters**						**Fitness**
Parabola-Ellipse	**H' (m)**	**B (m)**	**H (m)**	**t**	**h (m)**		***f***
	82.6338	38.6725	6.0	0	3.08		0.0006464
Elliptic	**p**	**q**	**H (m)**	**λ**	**h (m)**		***f***
	-4837.5125	3932.0684	6.0	0.0253	3.06		0.0006578
Bezier	**p2x (m)**	**p2y (m)**	**p3x (m)**	**p3y (m)**	**p4x (m)**	**h (m)**	***f***
	8.7734	2.5425	21.6418	6.0	38.4992	3.85	0.0006536

The shapes of the optimal arches obtained are shown in Fig. 2.

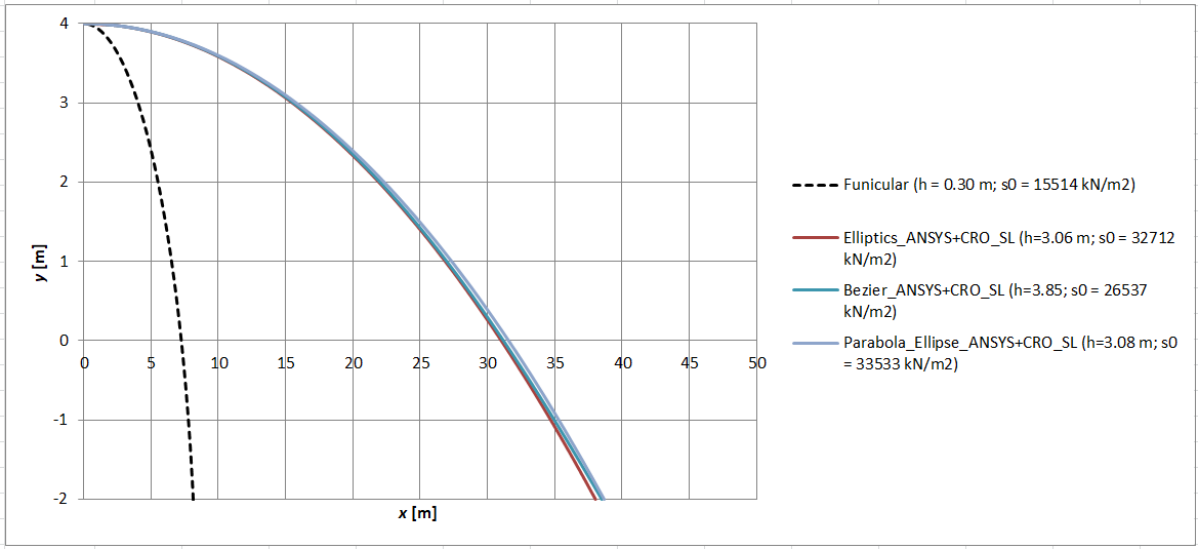

Figure 2. *Optimal parametrical shapes for deep waters (D = 60 m; H = 6 m). s0: compressive stress at the apex.*

4. CONCLUSIONS

The results obtained show that the optimal structural design of submerged arches admits several design contexts depending on the level of compressive stresses in the arch, specially when other serviceability parameters are involved in the optimization process. Moreover, in this work the optimization process based on shape parameterization is approached over three different geometrical types (conics, elliptic and Bézier curves), resulting in a convergence of their shapes and their fitness values. This points out that the optimal shape of a submerged arch in deep waters may be independent of the geometrical type adopted for defining its shapes and leads to search an unified parameterization model for such structures.

REFERENCES

[1] Alejandro M Hernández-Díaz, Andrés Bueno-Crespo, Jorge Pérez-Aracil, and José M Cecilia. (2018). Multi-objective optimal design of submerged arches using extreme learning machine and evolutionary algorithms. Applied Soft Computing, 71:826–834.

[2] William Fulton. (2008). Algebraic curves. An Introduction to Algebraic Geom, 54.

[3] Joseph H Silverman. (2009). The arithmetic of elliptic curves, volume 106. Springer.

[4] G. Farin, J. Hoschek, M. S Kim, and M. S Kim. (2002). Handbook of Computer Aided Geometric Design. Elsevier Science I& Technology, Amsterdam. ID: 31144.

[5] Pérez-Aracil, J., Camacho-Gómez, C., Hernández-Díaz, A. M., Pereira, E., Camacho, D., & Salcedo-Sanz, S. (2021). Memetic coral reefs optimization algorithms for optimal geometrical design of submerged arches. Swarm and Evolutionary Computation, 67, 100958.

[6] Tadeusz Stolarski, Yuji Nakasone, and Shigeka Yoshimoto. (2018). Engineering analysis with ANSYS software. Butterworth-Heinemann.

[7] Jiménez-Alonso, J. F., Pérez-Aracil, J., Hernández Díaz, A. M., & Sáez, A. (2019). Effect of Vinyl flooring on the modal properties of a steel footbridge. Applied Sciences, 9(7), 1374.

Service behaviour and shear strength of concrete members strengthened with Iron-based Shape Memory Alloys

del Río-Bonnín, Sandra[1]; Cladera, Antoni[1]; Montoya-Coronado, Luis A.[1]; Ruiz-Pinilla, Joaquín G.[1]; Ribas, Carlos[1]

ABSTRACT

Iron-based Shape Memory Alloys (Fe-SMA) have the ability to return to their initial shape after suffering large deformations by being heated and cooled afterwards (activation process). This characteristic is known as the shape memory effect and it allows Fe-SMAs to be used in the construction sector as prestressing material in new buildings or for rehabilitation. An experimental campaign on the service behaviour and shear strength of concrete members strengthened using 11 mm diameter Fe-SMA rebars has been carried out. In this work, a concrete member with activated (prestressed) Fe-SMA and a member with non-activated Fe-SMA will be preliminary compared to evaluate this technology's effectiveness. The preliminary results confirm the suitability of using this material for an active strengthening method since they demonstrate an improvement in Service Limit State, supporting higher load for identical deflection, with fewer and narrower cracks. No significant change is observed in Ultimate Limit State.

Keywords: Fe-SMA, shear strength, SLS, concrete, active prestress.

1. INTRODUCCIÓN

Las aleaciones con memoria de forma en base hierro (Fe-SMA) se utilizan en el sector de la construcción gracias a sus singulares propiedades. Entre ellas se encuentra el efecto de memoria de forma como resultado de la transformación martensítica [1]. Dicha propiedad permite utilizar este material para el pretensado y refuerzo de estructuras existentes y/o nueva construcción [2] gracias a la generación de tensiones de recuperación [3] al colocar el Fe-SMA preestirado, anclar los extremos y proceder a calentarlo y enfriarlo (activación). El objetivo de la campaña experimental que se presenta de forma preliminar es evaluar la mejora del comportamiento de elementos de hormigón pretensados con barras corrugadas ϕ11 mm de Fe-SMA frente al estado límite de servicio (ELS), así como su resistencia a cortante.

2. METODOLOGÍA

2.1. Caracterización Fe-SMA

La empresa suiza re-fer AG suministró las barras corrugadas de ϕ11 mm de Fe-SMA prestiradas entre el 2% y el 4% (en fase martensita). Para llevar a cabo la caracterización del material se cortaron muestras de 300 mm de longitud para proceder a su ensayo. Se llevaron a cabo varios ensayos para determinar la tensión de recuperación (ver Fig. 1a), en los cuales se puede apreciar que al fijar los extremos de la muestra y proceder a calentarla entre 250 y 300 °C, las tensiones de recuperación obtenidas rondaban los 300 MPa de media de 4 ensayos. La Fig. 1b compara el comportamiento del Fe-SMA activo (A), es

[1]*Departamento de ingeniería industrial y de la construcción. Universidad de las Islas Baleares UIB (España). s.del-rio@uib.es (Corresponding author). antoni.cladera@uib.es. luisal12@gmail.com. joaquin.ruiz@uib.es. carlos.ribas@uib.es.*

decir, preestirado y tras la generación de las tensiones de recuperación (curva roja de la Fig. 1a) y pasivo (P), solo preestirado, mediante un ensayo monotónico. En la Fig. 1b se aprecia claramente el marcado carácter no lineal del Fe-SMA.

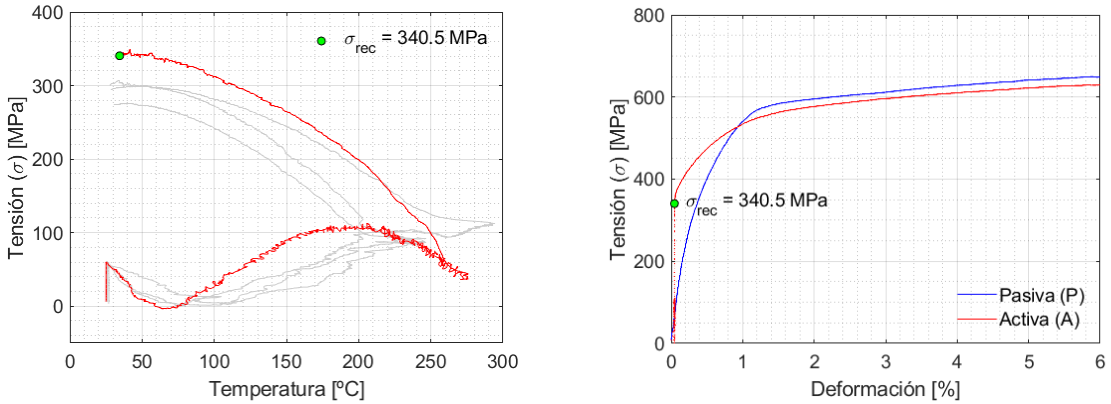

Figura 1. *Caracterización de las barras corrugadas de Fe-SMA:* **(a)** *Ensayos de tensión de recuperación en el proceso de activación* **(b)** *Ensayos monotónicos del Fe-SMA activo vs pasivo.*

2.2. Diseño de los especímenes de ensayo

La Fig. 2 muestra la geometría de los especímenes diseñados, cuya sección transversal tenía una base de 120 mm y un canto de 200 mm. La longitud total de 2940 mm estaba formada por el sumatorio de las longitudes de anclaje del Fe-SMA (840 mm) y 3 veces "*a*" (siendo *a* = 420 mm). El armado longitudinal constaba de 2 barras de ϕ11 mm de Fe-SMA en la cara inferior y 2 barras de ϕ10 de acero B500SD en la cara superior, mientras que el armado transversal se componía de un estribo de ϕ6 mm cada 100 mm dispuesto a lo largo del espécimen dejando exenta la zona prevista de rotura a cortante.

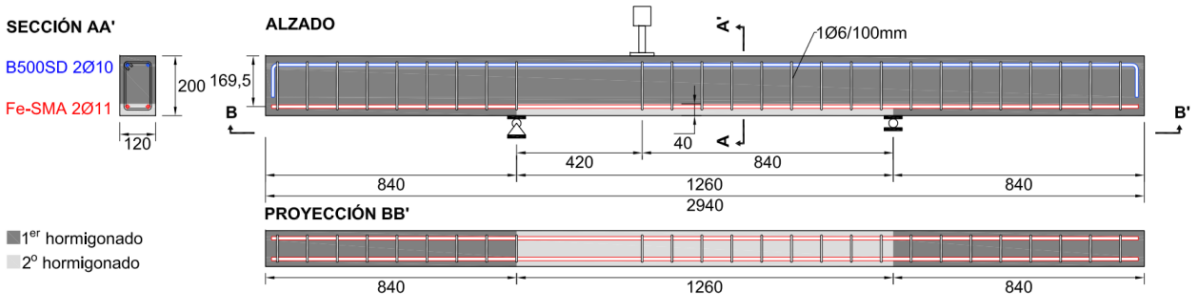

Figura 2. *Detalle de la geometría de los especímenes ensayados.*

2.3. Proceso constructivo

En primer lugar, se encofraron los laterales y la base. A continuación, se introdujo el armado (situando el Fe-SMA en la cara superior), y se pusieron unos tapones de poliestireno expandido de 4 cm de grosor a 840 mm de cada borde del espécimen. Luego se vertió y vibró el primer hormigón. Una vez adquirió la resistencia suficiente (48 MPa), se instrumentó y se procedió a activar el Fe-SMA del espécimen A, calentando con un soplete cada barra y controlando que la temperatura alcanzada estuviera entre 250

y 300 °C con una pistola de temperatura. Seguidamente se dejaron enfriar las barras a temperatura ambiente. Se vertió y vibró el segundo hormigón (ver Fig. 2) y una vez fraguado se voltearon los especímenes y se transportaron al laboratorio para su ensayo.

2.4. Ensayo: configuración e instrumentación

Se llevaron a cabo ensayos asimétricos a tres puntos (ver Fig. 2) con control por deformación. Durante el ensayo se midió la flecha debajo del punto de carga, las deformaciones del armado longitudinal, la apertura de la fisura crítica a cortante y el patrón de fisuración.

3. RESULTADOS Y DISCUSIÓN

La Fig. 3a compara las gráficas obtenidas de cortante – flecha bajo el punto de carga de los especímenes A (rojo) y P (azul). El espécimen A comienza desde una flecha negativa debido a la contraflecha de activación. Además, se indica como ELS la deformación correspondiente a L/300 tal como establece el CTE [5]. La Fig. 3b muestra el cortante comparado con la deformación del armado longitudinal B500SD (línea discontinua) y Fe-SMA (línea continua). Nótese que, debido a la contraflecha de activación, la deformación de las barras B500SD parte de una deformación positiva. Obsérvese también que para ELS-P las barras de Fe-SMA del especímen A presentan menor deformación que las del espécimen P.

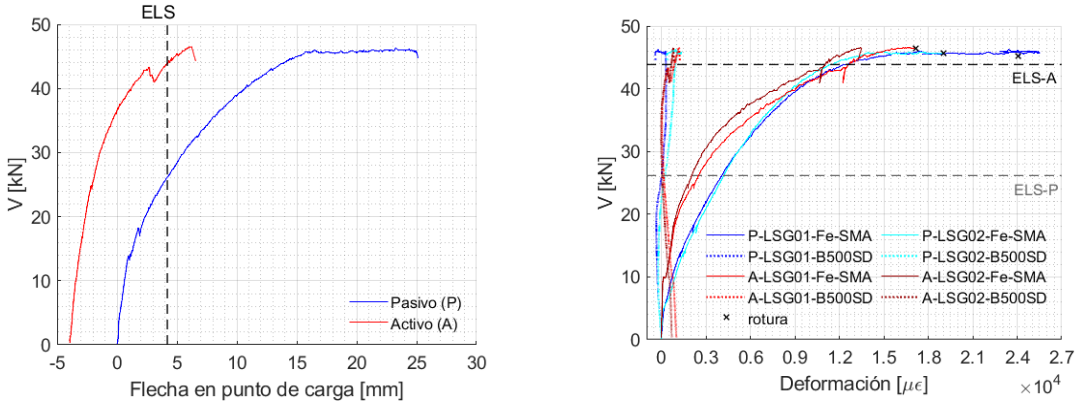

(a) Cortante – flecha bajo punto de carga **(b)** Cortante – deformación Fe-SMA y B500SD

Figura 3. *Gráficas de los resultados.*

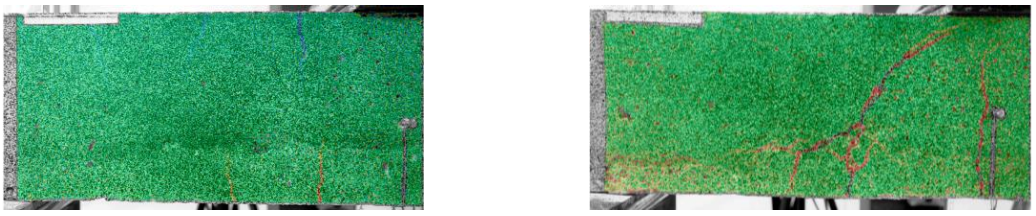

(a) *Activo* **(b)** *Pasivo*

Figura 4. *Patrón de fisuración en ELS (V = 26.19 kN).*

Las fotografías tomadas durante el ensayo se postprocesaron usando la metodología de correlación de imágenes digital (DIC), obteniéndose los patrones de fisuración. La Fig. 4 compara el estado de ambos especímenes para la carga en la que el P llegó a la deformación del ELS, es decir, para una fuerza cortante de 26.19 kN. En estas imágenes, el color rojo indica una deformación positiva (apertura de fisuras), el color verde es neutro y el color azul una deformación negativa (cierre de fisuras de activación). Como puede apreciarse, al llegar al ELS, el espécimen A solo había desarrollado fisuras de flexión

que no llegaban a atravesar el segundo hormigonado, mientras que el P ya presentaba la primera y segunda rama de la fisura crítica a cortante.

4. CONCLUSIONES

El uso de barras corrugadas de Fe-SMA como pretensado en elementos de hormigón mejora el comportamiento en ELS. Al comparar ambos especímenes para la misma carga, se observa que:

- El espécimen activo presenta menor flecha que el pasivo gracias a la contraflecha inicial generada al pretensar.
- Las barras de Fe-SMA del espécimen activo presentan menor deformación que las del pasivo.
- En el espécimen activo hay menor cantidad de fisuras, las cuales son menos profundas y no se observa ninguna fisura a cortante.

En todo caso, es importante resaltar que la campaña experimental involucró el ensayo de 4 pares de especímenes de ensayo (8 elementos), y en estos momentos se está realizando el análisis completo de resultados. Este análisis servirá para respaldar, o posiblemente modificar, las conclusiones presentadas aquí.

AGRADECIMIENTOS

Esta investigación forma parte del proyecto PRD2020/39 financiado por la *Comunitat Autònoma de les Illes Balears* a través de la *Conselleria de Fons Europeus, Universitat i Cultura* y la *Direcció General de Política Universitària i Recerca* con fondos de la Ley de Impuesto de Estancia Turística nº ITS 2017-006, y de los proyectos TED2021-130272B-C22 y PID2021-123701OB-C22 financiados por el *Ministerio de Ciencia e Innovación (MICINN)*. Los autores agradecen la colaboración de re-fer AG Strengthening Solution Company, Pastor S.A y Labartec S.L. También a *Vicepresidència i Conselleria d'Innovació, Recerca i Turisme del Govern de les Illes Balears* por conceder una beca FPI a la primera autora.

REFERENCIAS

[1] Cladera, A., Weber, B., Leinenbach, C., Czaderski, C., Shahverdi, M., & Motavalli, M. (Jul. 2014). Iron-based shape memory alloys for civil engineering structures: An overview. *Constr Build Mater*, *vol. 63, pp. 281–293*, doi: 10.1016/J.CONBUILDMAT.2014.04.032.

[2] Schranz, B., Michels, J., Shahverdi, M., & Czaderski, C. (2019). Strengthening of concrete structures with iron-based shape memory alloy elements: Case studies. *SMAR 2019 - Fifth Conference on Smart Monitoring, Assessment and Rehabilitation of Civil Structures.*

[3] Lee, W. J., Weber, B., Feltrin, G., Czaderski, C., Motavalli, M., & Leinenbach, C. (Nov. 2013) Stress recovery behaviour of an Fe–Mn–Si–Cr–Ni–VC shape memory alloy used for prestressing. *Smart Mater Struct, vol. 22, no. 12, p. 125037*, doi: 10.1088/0964-1726/22/12/125037.

[4] Centro de Publicaciones, Secretaría General Técnica, Ministerio de Fomento, and Gobierno de España, Eds. (2008). EHE-08. Instrucción de Hormigón Estructural.

[5] Ministerio de Fomento, T. y V. Secretaría de Estado de Infraestructuras, Secretaría General de Vivienda, and V. y S. Dirección General de Arquitectura. (2019). Código Técnico de la Edificación (CTE): Documento Básico SE.

Simplified model for joints between partially sleeved hollow sections with self-drilling screws

Vigón, Paula[1]; López-Colina, Carlos[1]; García, Ismael[1]; G.Picallo, Diego[1]; Serrano, Miguel A.[1];

ABSTRACT

Partially sleeved connections between similar rectangular tubes using self-drilling screws under shear as a means of joining are being studied. The feasibility of using self-drilling screws is being evaluated to improve sustainability and disassembly. These connections are semi-rigid and suitable for lightweight structures. This piece of work presents the preliminary experimental results, comparing them with a simplified mechanical model for strength and stiffness and classifying the joints.

Keywords: Joints, Hollow Sections, Self-drilling Screws, Stiffness, Connections.

1. INTRODUCCIÓN

La caracterización de uniones es importante en las regulaciones recientes [1,2]. Las uniones estructurales se diseñan habitualmente como rígidas o articuladas, pero puede no ajustarse a la realidad [3]. El Eurocódigo 3-1.8 [1] aborda mediante el método de los componentes la resistencia y rigidez de uniones entre perfiles I o H, pero no entre perfiles huecos [3], y menos si son atornilladas [4]. Aquí se estudia el uso de tornillos autotaladrantes para unir tubos rectangulares de tamaño similar por encaje parcial.

2. TRABAJO EXPERIMENTAL

Se ensayan uniones por encaje parcial con tornillos autotaladrantes entre secciones rectangulares huecas (RHS), obteniendo su momento resistente (M_R) y rigidez inicial ($S_{j,ini}$). También se ensayaron los tornillos autotaladrantes a cortadura simple. Las mediciones de desplazamientos y giros se realizaron con un sistema de correlación digital de imágenes (DIC).

2.1. Materiales

Se utilizaron tubos RHS de 140×70×6 insertados parcialmente en RHS de 140×80×4, ambos perfiles de grado S355 y conformados en frio. En cada unión se usaron 18 tornillos autotaladrantes AUTO de Indefix, de diámetro 5,5 mm y longitud 32 mm, con recubrimiento de zinc.

2.2. Ensayos de uniones viga-pilar

Se ensayaron 3 probetas de unión viga-pilar (BC) por encaje entre los perfiles, sometiendo la viga a momentos flectores y esfuerzos cortantes mediante la aplicación de una carga vertical a 684 mm de la cara de la columna. Se probaron uniones por encaje interior o exterior de la viga, ver Fig. 1.

1 Departamento de Construcción e Ingeniería de fabricación. Universidad de Oviedo (ESPAÑA). uo194830@uniovi.es (Corresponding author), lopezpcarlos@uniovi.es, garciamael@uniovi.es, uo265194@uniovi.es, serrano@uniovi.es

La carga en los ensayos se aplicó mediante control de desplazamiento. Se distribuyeron 9 tornillos en cada lado de la unión con una separación de 43 mm en dirección vertical y horizontal. Se obtuvieron las curvas momento-rotación, calculando a parir de ellas la rigidez rotacional $S_{j,ini}$ y momento resistente M_R, ver *Tabla 1*. Los resultados mostraron un fallo final debido a la rotura de los tornillos, sin observarse deformaciones plásticas significativas en los agujeros o los perfiles.

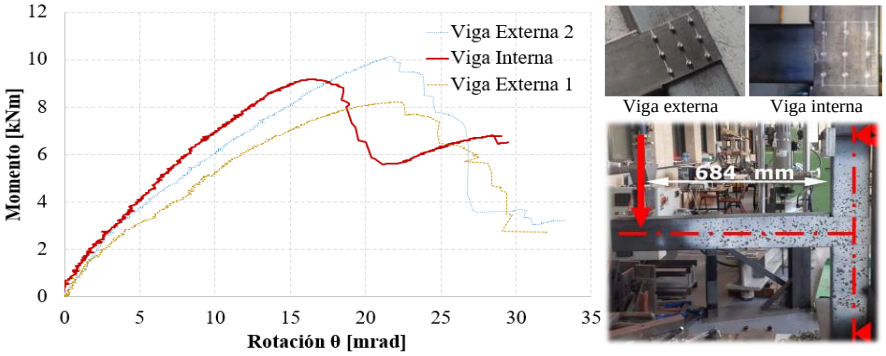

Figura 1. *Tipos de encaje, ensayo y curvas momento-rotación de las uniones BC*

Tabla 1. Resistencia al momento y rigidez experimental

Ensayo	**$S_{j,ini}$ [kNm/rad]**	**$M_{j,R}$ [kNm]**
BC Viga Externa 1	803	8,20
BC Viga Externa 2	867	10,12
BC Viga interna	841	9,17
Media (Desviación estándar relativa)	837 (RSD=3,1%)	9,16 (RSD=8,6%)

2.3. Ensayos del componente tornillo autotaladrante

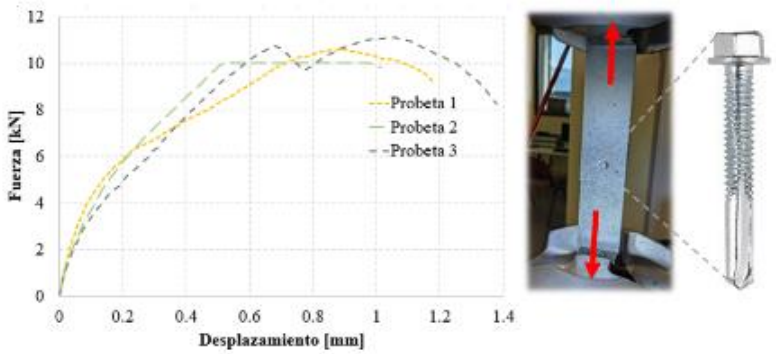

Figura 2. *Ensayo de tornillos SDS y curvas fuerza-desplazamiento resultante*

Se evaluaron la resistencia y rigidez a cortante del componente individual consistente en un tornillo autotaladrante (SDS) a cortadura simple y su entorno. Las probetas constan de dos placas de 100 ×200 extraídas de ambos perfiles RHS unidas con un tornillo autotaladrante colocado a 50 mm de los bordes. El ensayo, el tornillo y las curvas fuerza-desplazamiento resultantes se muestran en la Fig. 2. En la *Tabla 2* se presenta la resistencia máxima, F_R y rigidez inicial, K_{ini}. Al observar un comportamiento no-lineal

temprano, también se ha obtenido la rigidez secante a 2/3 del momento resistente (K_{sec}) como posible valor a usar en el cálculo analítico.

Tabla 2. Rigidez y Resistencia obtenidas en ensayos SDS

Ensayo	K_{ini} [kN/mm]	K_{sec} [kN/mm]	F_R [kN]
SDS 1	69,41	25,88	10,60
SDS 2	67,89	23,76	-
SDS 3	59,62	19,83	11,12
Media (Desviación estándar relativa)	65,64 RSD=6,5%	23,16 RSD=10,8%	10,86 RSD=2,4%

3. RESULTADOS

Se clasifican las uniones por su rigidez rotacional y resistencia y se evalúan modelos mecánicos analíticos simples para calcular ambas propiedades.

3.1. Clasificación según rigidez y resistencia

De acuerdo con los resultados experimentales obtenidos y la clasificación propuesta por el Eurocódigo 3, las uniones viga-columna estudiadas son semirrígidas para luces habituales en estructuras ligeras, pero se podrían considerar rígidas [1] para luces de vigas mayores a 9,6 metros en pórticos intraslacionales. Debido al diseño de las probetas, la resistencia promedio de la unión fue de 9,16 kNm, que es un 34% de la resistencia a flexión de la pieza conectada más débil, clasificándose como de resistencia parcial. Esto puede ser suficiente si se considera la rigidez real de la unión en el cálculo global de la estructura que corresponda.

3.2. Modelo mecánico simplificado

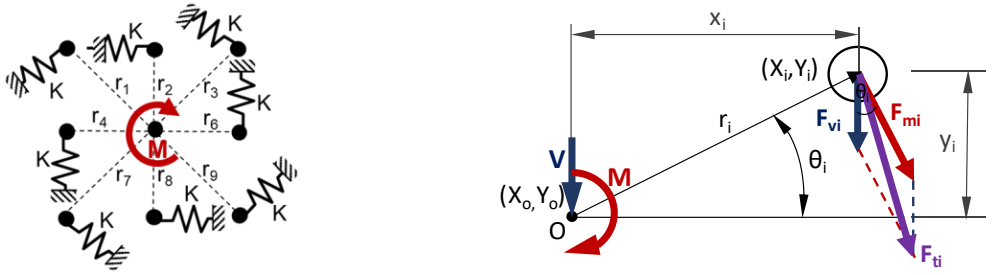

Figura 3. *Modelo de componentes para rigidez (a) y suma vectorial de fuerzas en un tornillo genérico (b)*

En el estudio de las uniones (BC) se empleó una distribución tradicional elástica de fuerzas en una conexión atornillada con carga excéntrica en el plano, Fig. 3. Dado que en el montaje de la unión se dejó un espacio entre las piezas que evita el contacto en el borde cortado, el baricentro de la unión (tornillo central) puede considerarse centro de rotación. Asumiendo esto y conocida la rigidez lineal del componente "tornillo autotaladrante y su entorno"(K) podría calcularse la rigidez rotacional con la Eq. (1).

$$S_{j,ini} = K \sum r_i^2 \qquad (1)$$

El esfuerzo cortante en el tornillo más cargado puede predecirse mediante una distribución de fuerzas en la que un tornillo genérico *i* del conjunto de *n* tornillos esté sometido a la suma vectorial de la fuerza de cortadura debida al momento *M* Eq. (2) y la debida al cortante *V* Eq. (3).

$$F_{mi} = M \cdot r_i / \sum_{j=1}^{n} r_j^2 \quad (2)$$

$$F_{vi} = V/n \quad (3)$$

Dado el comportamiento no lineal observado en los componentes individuales, para *K* se utilizó la rigidez secante a 2/3 del momento resistente K_{sec}, en la *Tabla 2* en lugar de la rigidez inicial. Además, se consideró el efecto de grupo al ajustar el cálculo de rigidez, usando el factor Ψ propuesto por LaBoube y Sokol [5] de la Eq. (4).

$$\Psi = 0{,}535 + 0{,}467/\sqrt{n} \quad (4)$$

La rigidez rotacional inicial que se obtiene analíticamente ensamblando por este método las rigideces individuales de los tornillos es de 690 kNm/rad, lo que representa una diferencia del 17,6% respecto al valor experimental. El fallo se predijo de acuerdo con la resistencia al corte del tornillo más solicitado, lo que resultó en una predicción de fallo cuando se alcanza el momento de 7,77 kNm (actuando conjuntamente en el ensayo BC con un esfuerzo cortante de 10,31 kN). Esto representa una diferencia del 15,0% respecto al valor observado experimentalmente.

4. CONCLUSIONES

Las uniones propuestas son aptas para estructuras ligeras y fáciles de ejecutar, clasificadas como semirrígidas, pudiendo volverse rígidas según el contexto. Las uniones ensayadas tienen resistencia parcial, suficiente al considerar su rigidez parcial en el cálculo global. Se puede usar un modelo simple de distribución elástica de fuerzas si se tienen datos apropiados sobre resistencia y rigidez de componentes, sin contactos complicados entre piezas. Debe considerarse una rigidez reducida en los componentes debido a su comportamiento no lineal temprano, y también el efecto de grupo en los cálculos. Estas uniones son ideales para estructuras ligeras y simplifican el análisis estructural.

AGRADECIMIENTOS

Se agradece el apoyo del Gobierno de España con el proyecto en curso PID2021-126636NB-I0.

REFERENCIAS

[1] CEN. Eurocode 3 (2005) Design of Steel Structures Part 1-8- Design of Joints. (EN-1993-18:2005).

[2] American Institute of Steel Construction AISC. (2005) Specification for structural steel buildings. AISC. Chicago IL, USA.

[3] Weynand, W.; Jaspart, J.P.; Steenhuis, M. (1998) Economy Studies of Steel Building Frames with Semi-Rigid Joints. *Journal of Constructional Steel Research* 1998, No. 46 (1-3), p.85.

[4] Wardenier, J.; Packer, J.A.; Zhao, X.L.; Van der Vegte, G.J. (2010) Hollow Sections in Structural Applications. 2nd Edition. Geneva, Switzerland: ISBN 978-90-72830-86-9. CIDECT.

[5] LaBoube, R.A.; Sokol, M.A. (2002) Behaviour of Screw Connections in Residential Construction. *J. Struct. Eng.* 2002, p.115-118.

Stochastic surrogate modelling of short fiber-reinforced composite materials

García Merino, José Carlos[1]; Calvo Jurado, Carmen[2]; García Macías, Enrique[3]

ABSTRACT

Recent advances in Nanotechnology have unlocked potential in high-performance composite materials. In particular, carbon nanotubes (CNTs) are of interest in enhancing cement-based composites. Studies demonstrate that adding small CNT quantities (below 1% of total volume) yields significant increases in compression, flexural strength, and Young's moduli compared to the base matrix. These properties depend on factors like reinforcement volume fraction, orientation, and interactions among composite constituents. Predicting the mechanical properties of these composites poses formidable challenges, requiring the implementation of complex numerical approaches like multi-scale finite element methods or dynamics molecular simulations. However, their computational demands hinder intensive analyses such as sensitivity or stochastic propagation studies. To this aim, non-intrusive surrogate models may offer efficient approximations, although the consideration of both intrinsic/extrinsic uncertainties remains a challenge. To address this issue, this study implements stochastic Kriging as a meta-model with great potential for conducting stochastic numerical homogenization of CNT-reinforced cement mortars.

Keywords: Surrogate modelling, Stochastic Kriging, Homogenisation, Composites, CNTs.

1. INTRODUCCIÓN.

Los recientes avances en nanotecnología han abierto nuevas posibilidades para el desarrollo de materiales compuestos de alto rendimiento. Uno de los materiales destacados en la actualidad son los nanotubos de carbono o CNTs (siglas en inglés de Carbon NanoTubes). Los CNTs han demostrado tener un enorme potencial para desarrollar materiales compuestos de alto rendimiento a base de cemento. Investigaciones recientes han mostrado que, añadiendo cantidades relativamente bajas de CNTs (menos del 1% del volumen total) es posible lograr aumentos de alrededor del 10%, 25% y 30% respectivamente en la resistencia a compresión, flexión y módulo de Young con respecto a la matriz prístina [1]. Las propiedades de estos materiales compuestos dependen de muchos factores, como la fracción de volumen de fibras, su orientación, distribución y geometría, así como la interacción entre las diferentes fases del compuesto. En general, la predicción de las propiedades mecánicas efectivas de los materiales compuestos suele ser un problema complejo, para el cual se han propuesto diversas soluciones en la literatura. Los métodos numéricos son particularmente populares debido a su capacidad para representar la geometría exacta de microestructuras complejas, mientras que a su vez mantienen

[1] *Departamento de matemáticas, Universidad de Extremadura (Spain). jcgarcia@unex.es (Corresponding author)*
[2] *Departamento de Matemáticas. Universidad de Extremadura (Spain). ccalvo@unex.es*
[3] *ETSI de Caminos, Canales y Puertos, Universidad de Granada (Spain). enriquegm@ugr.es*

mínimo el número de suposiciones y simplificaciones de la microestructura subyacente. Sin embargo, este enfoque conlleva altos costos computacionales que limitan su uso en análisis intensivos como los métodos Montecarlo.

Para superar estas dificultades, el uso de modelos subrogados ha demostrado ser de gran utilidad. Un modelo subrogado o metamodelo es una representación computacionalmente más ligera del modelo original de interés [2]. Uno de los métodos de construcción de metamodelos más populares es Kriging. A partir de un conjunto de evaluaciones del modelo original llamado *diseño experimental*, Kriging emplea un proceso gaussiano para obtener una aproximación continua del comportamiento del modelo de interés. No obstante, Kriging es un método interpolador, esto es, el metamodelo toma exactamente el mismo valor sobre los puntos de entrenamiento que el modelo original. Esto puede no ser adecuado en situaciones como la simulación de materiales compuestos en que el refuerzo del material está distribuido aleatoriamente, y en que por tanto dos simulaciones con la misma entrada pueden arrojar valores ligeramente diferentes de las propiedades consideradas. Una manera de tratar este problema es emplear una extensión de Kriging conocida como *Kriging estocástico*. El objetivo de este trabajo será utilizar Kriging estocástico para analizar las propiedades mecánicas efectivas de un mortero de cemento reforzado con CNT a escala nanométrica.

2. DESARROLLO TEÓRICO.

2.1 Homogenización numérica de materiales compuestos.

La homogenización numérica de las propiedades efectivas de un material compuesto se basa en la experimentación virtual de un *elemento representativo de volumen* (Representative Volumen Element, RVE). Un RVE debe cumplir dos requisitos: ser característico de todo el compuesto en términos medios, y ser un volumen que contenga un número suficiente de inclusiones para lograr homogeneidad estadística en el comportamiento global [3].

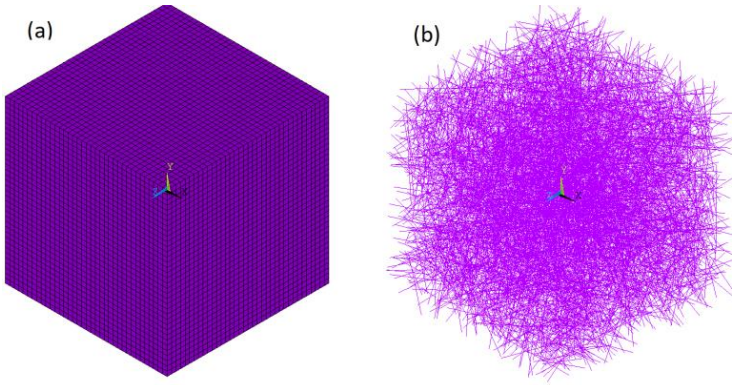

Figura 1: RVE de un compuesto de cemento reforzado con CNTs. (a): matriz de cemento; (b) CNTs.

Para el análisis del compuesto de cemento/CNT se ha considerado un RVE cúbico constituido por una matriz de cemento en la que se han incluido CNTs orientados aleatoriamente. La geometría del modelo se ha construido mediante el software Matlab (versión 2019a) añadiendo CNTs de manera secuencial en una celda cúbica hasta que se ha alcanzado el volumen deseado, teniendo en cuenta que no haya colisiones entre los mismos. Para la elaboración del modelo del modelo de elementos finitos se empleó el software ANSYS (versión R1 2023). Se ha asumido en el modelo que tanto la matriz como el refuerzo son materiales isotrópicos. La matriz ha sido modelada empleando elementos cúbicos sólidos

(SOLID185) mientras que los CNTs han sido representados mediante modelos de viga 3D (BEAM188). Un ejemplo de RVE conteniendo aproximadamente un 0.5% de CNTs puede observarse en la figura (1).

Respecto a la homogenización numérica, para calcular las propiedades elásticas efectivas de un RVE concreto de volumen *V*, debemos resolver:

$$\overline{\sigma}_{ij} = \frac{1}{V}\int_V \sigma_{ij}\,\mathrm{d}V, \qquad \overline{\varepsilon}_{ij} = \frac{1}{V}\int_V \varepsilon_{ij}\,\mathrm{d}V, \tag{1}$$

donde $\hat{\sigma}_{ij}$ y $\hat{\varepsilon}_{ij}$ representan las tensiones y deformaciones medias del volumen, respectivamente. Además, aplicaremos las siguientes condiciones de contorno sobre el RVE:

$$u_i = \overline{\varepsilon}_{ij}x_j + \nu_i\,, \forall x \in \Gamma, \tag{2}$$

donde Γ denota la frontera del RVE, ν_i representa la parte periódica local de las componentes de desplazamiento u_i en la superficie, y los índices i y j denotan las direcciones cartesianas globales. Una vez se han aplicado las condiciones de contorno, podemos estimar el tensor de elasticidad C como:

$$\overline{\sigma}_{ij} = C_{ijkl}\overline{\varepsilon}_{ij}. \tag{3}$$

2.2 Kriging estocástico.

Kriging estocástico es una extensión de Kriging que aborda situaciones en que el comportamiento del modelo original presenta incertidumbre. Para ajustar un modelo Kriging se requiere de un conjunto de puntos de entrenamiento y de un modelo de correlación dependiente de ciertos parámetros cuya adecuada determinación determinará la calidad del metamodelo. Por otro lado, Kriging estocástico requiere determinar además un término que capture la incertidumbre del modelo original. En base a lo anterior, la predicción de un metamodelo Kriging estocástico en un punto x viene dada por [4]:

$$\widehat{\mathcal{M}}(x) = f(x)^{\mathrm{T}}\hat{\beta} + r(x)^{\mathrm{T}}(R + \Sigma_\varepsilon)\big(y - F\hat{\beta}\big), \tag{4}$$

donde $f(x)^{\mathrm{T}}\hat{\beta}$ es un modelo de regresión lineal determinado por el usuario, y es el vector de evaluaciones del modelo sobre el conjunto de entrenamiento, $F_{ij} = f_j\big(x^i\big)$ es la llamada matriz de información del modelo de regresión lineal. Los términos $r(x)^T$ y R denotan la correlación del punto de predicción con los puntos de entrenamiento y la correlación entre los propios puntos de entrenamiento, respectivamente. Finalmente, la matriz Σ_ε representa la incertidumbre del modelo original. Cuando $\Sigma_\varepsilon = 0$, el modelo subrogado se reduce a un Kriging clásico.

3. RESULTADOS NUMÉRICOS, DISCUSIÓN Y CONCLUSIONES.

Como material de estudio, se ha escogido un compuesto de cemento reforzado con CNTs. Los parámetros de las fases constitutivas empleados en el posterior análisis se recogen en la tabla 1. Estos valores cubren los más habituales de los materiales considerados [5]. Para la construcción del metamodelo se ha empleado un diseño experimental de 30 puntos muestreados mediante el método del *hipercubo latino* para garantizar su representatividad. Dado que tenemos dos variables de interés (el módulo de elasticidad y el coeficiente de Poisson del compuesto), se ha ajustado un modelo subrogado para cada una de ellas. Como puede apreciarse en la figura 2, la calidad de ambos metamodelos es excepcional, obteniendo un coeficiente de determinación R^2=0.99. Respecto al tiempo de evaluación, mientras que

cada modelo de elementos finitos requiere de entre dos y seis horas dependiendo de la cantidad de CNTs considerada, la evaluación del modelo subrogado es de aproximadamente 0.01 segundos.

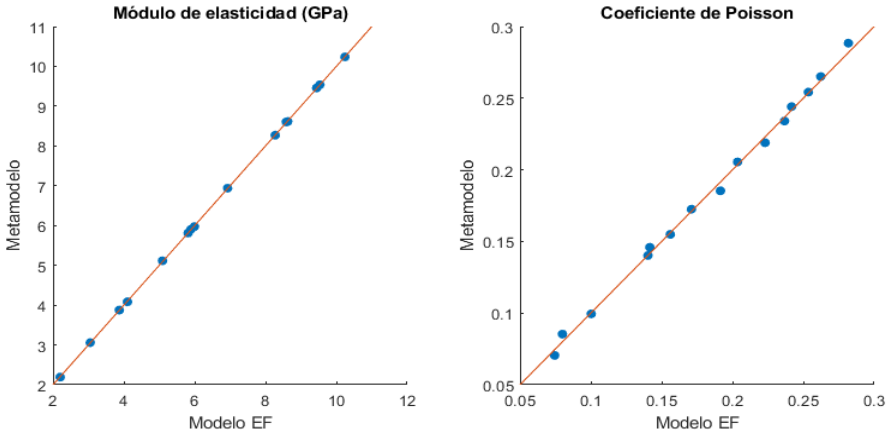

Figura 2: Predicciones de las cantidades de interés predichas por los metamodelos frente a los valores obtenidos por homogenización numérica sobre un conjunto de validación independiente de quince puntos.

En vista a lo expuesto anteriormente, podemos concluir que el modelo subrogado de Kriging estocástico resulta una metodología de gran interés para el estudio de las propiedades elásticas efectivas de materiales compuestos cuya modelización tenga un componente estocástico o de incertidumbre.

Tabla 1. Propiedades constitutivas de los materiales base considerados

Variable	Material	
	Matriz cemento	CNTs
Módulo de Young	2-10 GPa	0.23-1.22 TPa
Coeficiente de Poisson	0.05-0.3	0.1-0.275
Fracción de volumen	-	0-1.2%

REFERENCIAS

[1] El-Gamal, S., Hashem F., & Amin, M. (2017). Influence of carbon nanotubes, nanosilica and nano-metakaolin on some morphological-mechanical properties of oil well cement pastes subjected to elevated water curing temperature and regular room air curing temperature. *Construction and Building Materials, 146, 531-546.*

[2] García-Merino, J. C., Calvo-Jurado, C. & García-Macías, E. (2022). Polynomial chaos expansion for uncertainty propagation analysis in numerical homogenization of 2D/3D periodic composite microstructures. *Composite Structures*, *300*, 116130.

[3] Ostoja-Starzewski, M. (2002). Microstructural randomness versus representative volume element in thermomechanics, *Journal of Applied Mechanics, 69, 25-35.*

[4] Ankenmann, B., Nelson, B.L. & Staum, J. (2010). Stochastic Kriging for simulation metamodeling. *Operations Research*, 58, 371-382.

[5] Drougkas, A., Verstrynge, E., Hayen, R. & Van Balen, K. (2019). The confinement of mortar in masonry under compression: experimental data and micro-mechanical analysis. *International Journal of Solids and Structures, 162, 105–120*.

Strategic approach for the engineering analysis and design teaching courses

Gutiérrez, Ruth[1]; Loureiro, Alfonso[1]; Reinosa, José Manuel[1]; López, Manuel[1]

ABSTRACT

Future engineers are going to face their professional development in a rather uncertain environment. It becomes more and more necessary to enhance competences in simulation, in tune with traditional concepts. The development of these skills is carried out through project-based learning using professional software. This approach presents several challenges, such as professional software training along with exposing how the theoretical principles are integrated into and the numerical methods under the interface. It is an intensive work plan with a four-month-time constraint. This approach results in a highly effective teaching-learning process, with students motivated and inclined to question the computer results, based on the physics. Finding answers provided by different approaches and providing conclusions, they work on essential skills for a future where they may have to question solutions coming from algorithms not based on physics or from artificial intelligence, with untraceable or unknown origin.

Keywords: In-depth knowledge, Professional software, Competencies, Activities for learning.

1. INTRODUCCION

En septiembre de 2021 se publicó legislación relevante (RD 822/2021) sobre la organización y la calidad de las enseñanzas universitarias, que exige una adaptación de las actuales titulaciones de grado y máster. Se refuerza el papel de los resultados de aprendizaje en los títulos universitarios. En este marco, desde distintos ámbitos de conocimiento se reconoce la importancia de seleccionar las competencias de lo/as futuro/as profesionales desde una perspectiva académica e industrial [1] [2] y volver a analizar cuáles son los resultados de aprendizaje más convenientes en el marco actual [3]. Este trabajo se centra en las asignaturas de diseño y análisis de sistemas estructurales, en relación con la formación necesaria para los desafíos que los ingeniero/as de estructuras van en enfrentar en su futuro desarrollo profesional.

2. COMPETENCIAS ESPECIFICAS EN MECANICA COMPUTACIONAL

Actualmente, los estudios de ingeniería se reorganizan para incorporar la adquisición de competencias básicas en simulación y en CT (computational thinking) [4]. Se trata de que el estudiantado adquiera las competencias básicas en mecánica computacional modificando el enfoque de materias con contenidos más tradicionales, como por ejemplo elasticidad, resistencia de materiales o estática y dinámica estructural. En las primeras materias mencionadas se trabajan las competencias relacionadas con la capacidad de analizar estados de tensión y de deformación en sólidos y estructuras. En dinámica estructural se trabajan competencias sobre el análisis de estructuras y elementos mecánicos sometidos a vibración y

[1] *Departamento de ingeniería naval e industrial. Universidade da Coruña (ESPAÑA). ruth.gutierrez@udc.es (Corresponding author). a.loureiro@udc.es. j.reinosa@udc.es. manuel.lopez.lopez@udc.es.*

el diseño de estos sistemas bajo cargas dinámicas. Las tablas 1 y 2 muestran los resultados de aprendizaje que se pueden desarrollar paralelamente.

Tabla 1. Resultados de aprendizaje básicos en mecánica computacional para problemas estáticos

Competencias	Resultados de aprendizaje
Manejar las leyes básicas que regulan el análisis de sólidos elásticos y estructuras. Conocer el método de rigidez. Exponer el Principio de los desplazamientos Virtuales. Clasificación de los problemas elásticos	Conocer los fundamentos teóricos de un programa de Elementos Finitos. Identificar familias de elementos. Explicar el proceso de ensamblaje y aplicación de cargas. Discutir equilibrio elemental, nodal y global.
Manejar los principios básicos del análisis estructural por ordenador. Modelar matemáticamente sistemas mecánicos y estructurales. Aplicar de forma adecuada los conceptos teóricos.	Conocer los elementos continuos y estructurales. Crear piezas para análisis. Definir las propiedades y asignación a las piezas. Ensamblar las piezas. Aplicar cargas y condiciones de contorno. Mallar. Exponer y manejar algunos métodos numéricos de integración.
Resolver ejercicios y problemas de modo completo y razonado	Configurar diversos procedimientos de análisis y compararlos. Discutir los análisis en varios pasos. Solicitud de resultados. Visualización y análisis de resultados.
Usar un lenguaje riguroso en el campo de la ingeniería estructural para presentar e interpretar datos y resultados	Comparar resultados analíticos y numéricos. Analizar la precisión y las aproximaciones realizadas. Explicar diferencias. Elaboración de informes

Tabla 2. Resultados de aprendizaje básicos en mecánica computacional para problemas dinámicos.

Competencias	Resultados de aprendizaje
Manejar los principios básicos de la teoría de vibraciones para analizar sistemas dinámicos de 1 y N grados de libertad.	Plantear modelos matemáticos de sistemas de 1 y N grados de libertad. Identificar y discutir distintos tipos de carga y diversos procedimientos de análisis.
Aplicar adecuadamente los conceptos teóricos en el laboratorio. Comprender y aplicar algunas técnicas computacionales de solución.	Identificar y aplicar métodos analíticos para obtener la respuesta ante vibración libre y forzada para sistemas de 1 y N grados de libertad. Analizar sistemas de 1 y N grados de libertad con un programa de elementos finitos y modelos masa-muelle-amortiguador. Describir algunos métodos numéricos de integración de las ecuaciones dinámicas y configurarlos en un programa. Conocer los métodos lineales y no lineales. Describir distintos modelos de amortiguamiento.
Usar un lenguaje rigoroso en dinámica estructural para presentar e interpretar datos y resultados.	Comparar resultados analíticos y numéricos. Analizar la precisión y las aproximaciones realizadas. Explicar diferencias. Elaboración de un informe.

El aprendizaje basado en un software profesional presenta algunos desafíos, como un periodo de aprendizaje largo e interfaces pensadas para la práctica profesional y/o la investigación [5, 6]. Con una adecuada coordinación entre asignaturas del mismo ámbito de conocimiento, se puede amortizar el periodo de aprendizaje usándolo en distintas asignaturas y para trabajos fin de grado o máster. Este tipo de software permite proponer actividades docentes más realistas, de mayor motivación y se aprende una herramienta que facilita la incorporación de lo/as ingeniero/as en proyectos de investigación.

3. APRENDIZAJE BASADO EN PROYECTOS

Como metodología se utiliza el aprendizaje basado en proyectos, que se resuelven por una doble vía, de un modo tradicional, es decir, analíticamente, para reforzar el aprendizaje de los conceptos teóricos

y numéricamente, con ayuda del software, para comparar las soluciones. Esta aproximación exige un esfuerzo doble a lo/as estudiantes, pero resulta muy beneficioso a largo plazo, porque relaciona el bagaje teórico aprendido en su trayectoria académica, introduce a el estudiantado en la comparación de varias soluciones y el análisis de las aproximaciones realizadas en los modelos, así como el alcance de los distintos métodos de cálculo, el rango de validez y la precisión de los mismos. Por ejemplo, lo/as estudiantes abordan problemas de análisis de sistemas mecánicos pasando por todo el rango de comportamiento, elástico y plástico hasta el fallo, a través de un programa de elementos finitos, estudiando y comprobando la validez del modelo prismático para obtención de la distribución de tensiones, la influencia del considerar el comportamiento del material y las consecuencias de la formación de una rótula plástica.

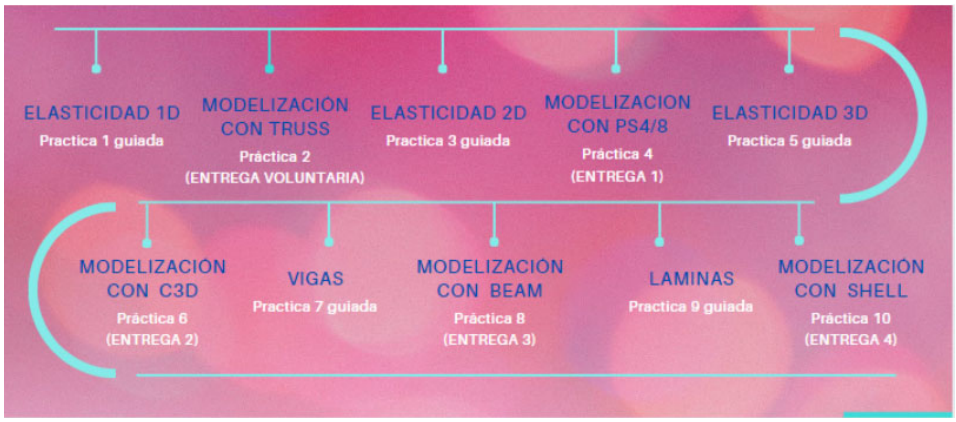

Figura 1. *Pasos en el desarrollo de las competencias básicas en estática computacional.*

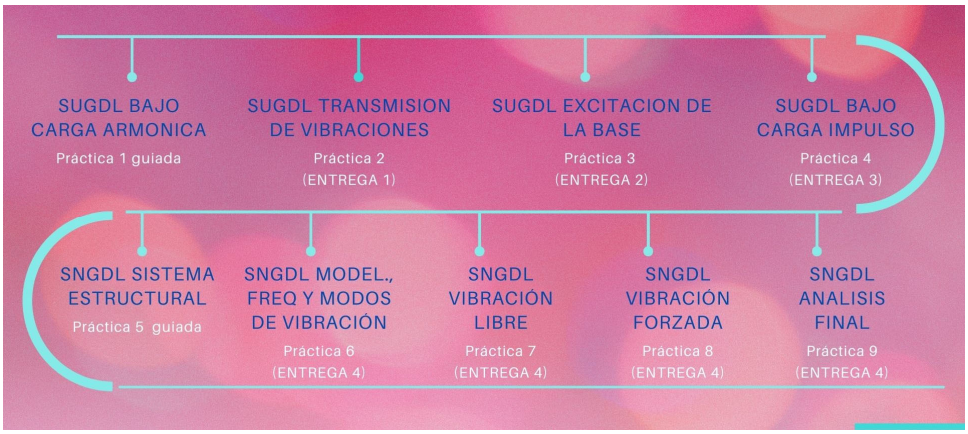

Figura 2. *Pasos en el desarrollo de las competencias básicas en dinámica computacional.*

Este planteamiento docente resulta a la larga muy efectivo; involucra conocimientos teóricos y prácticos de otras materias, resistencia de materiales, estructuras, mecanismos, la comparación obliga a buscar las diferencias de planteamiento y a adquirir un conocimiento más profundo de los métodos de resolución. Cuestiona los resultados numéricos basándose en la física de los problemas, y permite un ejercicio de análisis sobre la precisión y la adecuación de los métodos numéricos y algoritmos que están detrás de este tipo de programas.

El ultimo reto es la limitación de tiempo de un cuatrimestre. El plan de trabajo se muestra en las Fig. 1 y 2. Se consideran dos ítems diferentes, las prácticas guiadas y las propuestas. En las primeras se trabaja el aprendizaje del software profesional con clases demostrativas que lo/as estudiantes van

reproduciendo en sus portátiles y las segundas son proyectos que trabajan un aspecto teórico del programa, y manejan la parte asociada del programa cuyo aprendizaje se ha acelerado en la sesión demostrativa anterior.

Finalmente, se solicita la comparación, el análisis, la explicación razonada de los resultados obtenidos y la elaboración de un informe con todas estas reflexiones.

4. CONCLUSIONES

En este trabajo se han revisado algunos resultados de aprendizaje que pueden resultar de utilidad para el futuro ingeniero de estructuras, en asignaturas relacionadas con la mecánica computacional y el diseño. El futuro depende fundamentalmente del talento humano, de su capacidad de trabajo y de su creatividad. Se trata de vislumbrar la mejor educación para potenciar este talento, ante la velocidad de cambio de la tecnología y de la sociedad. Las herramientas que usarán los ingenieros estructurales cambian a la misma velocidad que la tecnología, evolucionando en un aspecto importante: cada vez más se basan en datos (sensores, monitorización, estadística e inteligencia artificial) en vez de en la física de los problemas. Mas que nunca hay que incorporar en nuestras asignaturas competencias para el análisis crítico y el contraste de modelos, para que nuestro/as estudiantes guíen el progreso de la industria hacia soluciones innovadoras ante el desafío que supondrán los complejos procesos de diseño, análisis y gestión que tendrán que enfrentar.

AGRADECIMIENTOS

Los autores agradecen el apoyo financiero proporcionado a través del proyecto PID2020-113895GB-C31 del MCIN/AEI/10.13039/501100011033.

REFERENCIAS

[1] Ninan, J., Hertogh, M., & Liu, Y. (2022). Educating engineers of the future: T-shaped professionals for managing infrastructure projects. *Project Leadership & Society*, 3, November, 100071.

[2] Kiss, A. A., & Grievink, J. (2020). Process systems engineering developments in Europe from an industrial and academic perspective. *Computers & Chemical Engineering*, 138, 106823.

[3] Muñoz-Cantero, J. M., Espiñeira-Bellón, E. M., & Pérez-Crego, M. C. (2023). Perceptions about the evaluation of learning outcomes in master's degrees. *Revista de Investigación Educativa*, 41, 1, 243–261.

[4] Wang, Y. (2023). The role of computer supported project-based learning in students' computational thinking and engagement in robotics courses. *Thinking Skills and Creativity*, 48, March.

[5] Loureiro, A., Lopez, M., Gutiérrez, R., & Reinosa, J. M. (2018). Análisis estructural con software comercial vs programación propia: propuesta docente. *Investigación práctica en la educación superor,* pp. 153–156. Membiela P, Casado N, Cebreiros MI, Vidal M, Eds.

[6] Gutiérrez, R., Loureiro, A., Reinosa, J. M., & Lopez, M. (2019). El aprendizaje apoyado en el software profesional. *Perspectivas docentes en la educación superior,* pp. 115–119. Membiela P, Ed.

Tension force estimation of post-tensioning external tendons from measured natural frequencies: validation from full modal testing

Naranjo-Pérez, Javier[1]; Renedo, Carlos M.C.[2]; García-Palacios, Jaime H.[3]; Díaz, Iván M.[2]

ABSTRACT

Cables and tendons are crucial elements in bridge engineering due to their susceptibility to fatigue and corrosion problems. Tension force is probably the main parameter to be analysed to assess their structural performance. Among the different methods to obtain the tension, vibration-based method is the most common. It is based on the measurement of their experimental modal properties in order to calibrate a mathematical model defined in terms of the tension, among other parameters. In such a way, the tension is inferred as function of real known values. The experimental parameters can vary according to the position and number of accelerometers employed and the number of vibration modes extracted. In this study, a sensitivity analysis is conducted to assess the influence on the estimated tension force of the number of both test points and considered modes.

Keywords: vibration-based monitoring, post-tensioning tendons, tension force estimation, cable dynamics, modal testing.

1. INTRODUCTION

Cables and tendons have become key elements in current civil structural engineering as they are employed in the construction and rehabilitation of several structures, such as, cable-stayed, suspension or post-tensioned concrete bridges. Besides, they constitute critical components of these structures because of their vulnerability to corrosion and fatigue. The control of tension forces may be used to evaluate the structural performance of these elements. Thus, the application of an economical, accurate and reliable method is a current trend [1]. In this study, the indirect estimation method based on vibration monitoring is applied. This method relies on the relationship between tension and natural frequencies, which are experimentally obtained from acceleration measurements. Hence, the estimation accuracy depends directly on the quality of the extracted experimental modal properties which, indeed, depend on the number and position of accelerometers and the number of extracted vibration modes. To shed light on this, two external post-tensioning tendons of a continuous 12-span railway bridge are herein analysed considering different number and position of sensors to infer their tension. The estimation is achieved via a minimization problem which is solved using genetic algorithms. The objective function to be minimized is defined in terms of the errors between numerical and experimental natural frequencies. The numerical ones are calculated

[1] *Department of Continuum Mechanics and Structural Analysis. Universidad de Sevilla (SPAIN). jnaranjo3@us.es (Corresponding author)*
[2] *Department of Continuum Mechanics and Structural Analysis. Universidad Politécnica de Madrid (SPAIN). carlos.martindelaconcha@upm.es. ivan.munoz@upm.es*
[3] *Department of Hydraulics, Energy and Environmental Engineering. Universidad Politécnica de Madrid (SPAIN). jaime.garcia.palacios@upm.es*

considering the taut string theory including bending stiffness for tendon modelling. Finally, the results are compared in terms of the weighted mean and standard deviation to find the minimum number of sensors and modes that must be taken into account, which is an important point to be considered in cost-effective monitoring systems.

2. TENSION FORCE ESTIMATION METHODOLOGY

In order to estimate the tendon tension, a constrained single-objective optimization problem whose aim is to minimize the differences between analytical and experimental modal properties is solved. The mathematical formulation is as follows:

$$\begin{array}{l} \text{find } \boldsymbol{\theta} = [L, EI, T] \\ to\ minimise\ J(\boldsymbol{\theta}) \quad s.t.: \boldsymbol{\theta}_l \leq \boldsymbol{\theta} \leq \boldsymbol{\theta}_u \end{array} \tag{1}$$

where L, EI and T are the length, bending stiffness and tension of the tendon, θ_l and θ_u are the lower and upper possible values that those design variables can adopt and $J(\boldsymbol{\theta})$ is the objective function defined as follows:

$$J(\boldsymbol{\theta}) = \frac{1}{2}\left[\sum w_f \cdot \left(\frac{f_{num} - f_{exp}}{f_{exp}}\right)^2 + \sum w_m \cdot \frac{\left(1 - \sqrt{MAC}\right)^2}{MAC}\right] \tag{2}$$

with f_{num} and f_{exp} being the numerical and experimental natural frequencies, w_f and w_m the weights associated to natural frequencies and mode shapes and MAC the Modal Assurance Criterion. The numerical natural frequencies and mode shapes are obtained from the mathematical model of the tendon. The theoretical model is built by solving the partial differential equation that governs the in-plane transverse displacement of taut cables including bending stiffness [2]:

$$EI\frac{\partial^4 v(x,t)}{\partial x^4} - T\frac{\partial^2 v(x,t)}{\partial x^2} + \rho\frac{\partial^2 v(x,t)}{\partial t^2} = 0 \tag{3}$$

$v(x,t)$ being the transversal displacement and ρ the linear mass of the tendon (considered known in this study). Under the assumption of pinned-pinned supports, the natural frequency and mode shape have the following closed-form expression:

$$f_{num,i} = \frac{i}{2L}\sqrt{\frac{T}{\rho} + \frac{\pi^2 EI i^2}{L^2\rho}}; \qquad \phi_{num,i}(x) = \sin\left(\frac{i\pi x}{L}\right) \qquad i = 1, 2, \dots N \tag{4}$$

However, real tendons can have some rotational stiffness at their ends giving this model a poor approximation of the actual mode shape near the ends. For this reason, an equivalent pinned tendon with a reduced length (equivalent length as shown in Fig. 1) is considered [3]. Therefore, in the analytical model (Eqs. (4)) and Eq. (1), length L is the equivalent length L_{eq}.

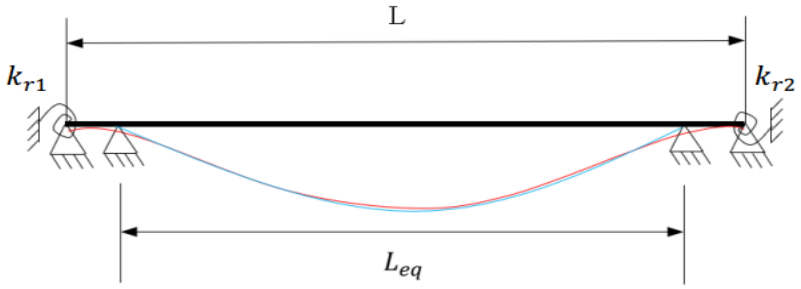

Figure 1. *Representation of the pinned joints tendon model with the equivalent length.*

3. EXPERIMENTAL TEST AND SENSITIVITY ANALYSIS

The studied tendons have a length of 22 meters and are formed by 22 strands. The accelerations of the tendon are measured with PCB seismic accelerometers installed with ad-hoc braces attached to the external polyethylene pipe. The recorded ambient vibrations, with a sampling frequency of 1651 Hz, are employed to perform an Operational Modal Analysis (OMA). The Stochastic Subspace Identification method, SSI-cov algorithm, is used for modal extraction. Previously, signals have been detrended and pre-processed with a low-pass Butterworth filter with a cut-off frequency of 80 Hz. As result, the natural frequencies and modal shapes are obtained. The estimation is performed in Matlab using the genetic algorithm function. In order to obtain a mean value of the tension and the standard deviation, 20 simulations are run. The mean and standard deviation are weighted through the inverse value of the objective function reached at the end of each simulation.

The following sensitivity analysis is conducted to evaluate the effect of the extracted data on the estimated tension force of the tendon. The number of vibration modes are: 2, 3, 4 and 7. The number of accelerometers and their position are: 1 (placed at L/10 from the midspan of the tendon), 2 (one at L/10 from midspan and the other placed at midspan) and 5 and 9 (both equidistant). In addition, the objective function is modified to account only for the contribution of the natural frequencies, excluding the mode shapes, for the cases of 5 and 9 accelerometers (for 1 and 2 the mode shape is always neglected as there are not enough points). Thus, 24 cases are run to conduct the sensitivity analysis of each tendon.

3.1. Results

Figure 2 shows the results of two analyses for two different tendons. It can be observed that the medium value of the tension force varies for the same test according to the number of accelerometers and vibration modes and the objective function definition. When the contribution of the mode shape is considered, the estimated value is higher. Besides, the standard deviation decreases with the number of vibration modes and not with the number of accelerometers. With only one accelerometer, the number of modes has been up to 4. Finally, in both cases can be observed that the influence of the number of modes is higher than the number of measuring points. It is noticeable that the mean value is very similar for 2, 5 and 9 accelerometers except for 2 vibration modes. Finally, it may be concluded that at least four modes must be considered for the estimation.

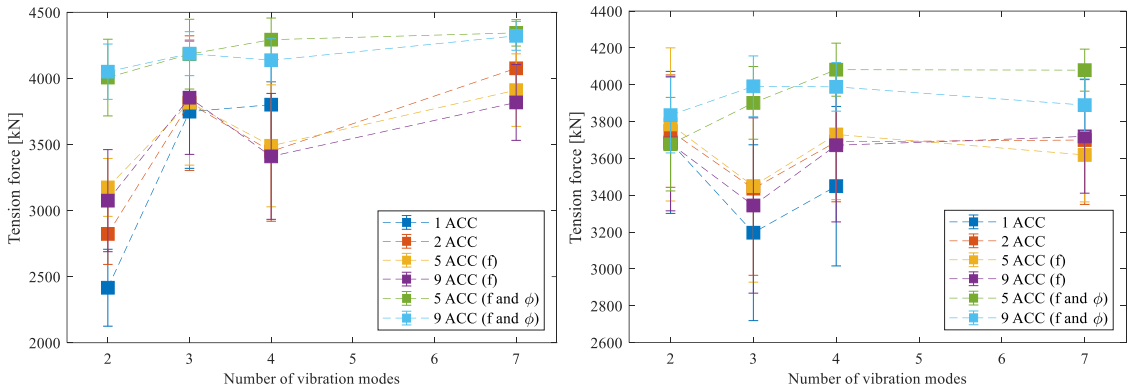

Figure 2. *Results of the two sensitivity analyses.*

4. CONCLUSIONS

The tension of cables and tendons plays an important role in their structural assessment. In this study, the vibration-based method which uses the experimental modal properties has been applied for the estimation. As the accuracy of the method relies directly on the experimental characterization, the instrumented points and devices are key elements. Herein, a sensitivity analysis considering different number of accelerometers, vibration modes and definitions of the objective function has been conducted. The results have shown that, the higher number of vibration modes the lower values of the standard deviation. In addition, it can be concluded that 2 accelerometers and 4 vibration modes are enough to obtain an accurate value of the tension.

ACKNOWLEDGEMENTS

The authors acknowledge the grant PID2021-127627OB-I00 funded by MCIN, AEI and 10.13039/501100011033 by "ERDF A way of making Europe". Javier Naranjo-Pérez thanks Ministerio de Universidades for the Margarita Salas grant funded through the program "European Union NextGenerationEU/PRTR".

REFERENCES

[1] Caetano, E. (2022). Characterisation and assessment of damage in cable structures. *Journal of Civil Structural Health Monitoring*, *12(6), 1267-1283*.

[2] Morse, P. M., Ingard, K. U. (1986). Theoretical acoustics. Princeton university press.

[3] Chen, C. C., Wu, W. H., Chen, S. Y., Lai, G. (2018). A novel tension estimation approach for elastic cables by elimination of complex boundary condition effects employing mode shape functions. *Engineering Structures, 166, 152-166.*

Author index


ESCUELA DE INGENIERÍAS INDUSTRIALES
Spanish Group IABSE
cemosa Ingeniería y Control
málaga CONVENTION BUREAU
MAPEI
copicentro www.copicentro.net
metro Málaga
COPITI Colegio Oficial de Peritos e Ingenieros Técnicos Industriales de Málaga
Colegio Oficial de Ingenieros Industriales de Andalucía Oriental